Applications of Small Unmanned Aerial Systems (sUAS) and Photogrammetry to Monitor and Inspect Structural Health and Construction Sites

A thesis submitted to the Graduate School of the

University of Cincinnati in partial fulfillment of the

requirement for the degree of

Master of Science

in the Department of Electrical Engineering and Computer Science

of the College of Engineering and Applied Science

by

Aswin Balasubramaniam

Bachelor of Science, University of Cincinnati

May 2019

Committee Chair: Arthur Helmicki, Ph.D.

Committee Members:

Victor Hunt, Ph.D.

Richard Beck Ph.D.

Abstract

The rapid advancements in the development of small unmanned aerial systems (sUAS) and their availability allow various inspection and construction surveying businesses to implement them in their daily functions reasonably and economically. These systems give users access to a wide range of low altitudes, high resolution and geo-referenced visual and thermal image datasets that were not easily available in the past. This research uses available sUAS systems, visual and thermal cameras, and photogrammetry software to develop standard operating procedures, using the best practices found through experimentation, to augment monitoring and inspection of infrastructure health and construction sites.

The purpose of this research is to document the applications of sUAS to augment infrastructure and construction site inspection process and ensure that the generated outputs can be easily perceived and replicated by trained engineers and professionals in their respective surveying fields. This research work details the development of flight planning, image capture, 3D/2D outputs processing, and post-processing procedures to aid in the inspection of facilities, bridges, and construction sites. The research process used off-the-shelf unmanned aerial systems, cameras and photogrammetry tools to develop procedures that would generate accurate results. The research work involved learning and applying mixed scientific disciplines that included but not limited to aerospace engineering, image processing, civil engineering and systems engineering.

First, the various photogrammetry software and hardware are discussed. Second, the workflow designed and the breakdown of the workflow to produce the desired outputs using photogrammetry tools are presented. This includes the research work conducted to study the effects of these parameters on the outputs produced. Third, the results obtained using the

ii

workflow is presented in the form of case studies. The study included inspecting two bridges,

one facility and two construction sites in the state of Ohio. Finally, the conclusion and scope for

future work are presented. The future work involves developing tools and techniques that would

automate the process to identify cracks on concrete bridges, detect thermal delamination on road

surfaces, and filter point clouds and build applications that would help streamline the information

present in the standard operating procedure documents to users interactively.

Acknowledgments

I am immensely grateful for Dr. Arthur Helmicki and Dr. Victor Hunt, my advisors, and mentors, for providing me this massive opportunity to work on such a large-scale project with the Ohio Department of Transportation (ODOT). Their support and motivation have inspired me to keep moving forward and never give up until my goals were achieved.

I would like to express my humble gratitude to Dr. Mahdi Norouzi and Dr. Chandrasekar Venkatesh for referring me to Dr. Helmicki and Dr. Hunt to work on the UAS project with ODOT. I would also like to thank them for their continued support and guided mentorship during their time at UCII.

I would like to thank Dr. Richard Beck for taking the time to preside on my defense committee and for reviewing my work.

I would like to thank Bryan Brown and Austin Wessels for their help to collect the necessary images and data to conduct this research work.

I am extremely thankful to the students of the UCII lab, Niranjan Rao, Arjun Chiddarwar, Parashmani Timilsina, Nikita Saraf, Sudhamsh Korrapati, Sohan Karkera, Pranav Khekare, and Sana Rajani, for their invaluable support and aid along the course of the research project.

I would also like to take the opportunity to acknowledge all my friends for their invaluable support and tolerating me over the course of my stay at the University of Cincinnati. Your silent contributions have been immense and key to making Cincinnati an enjoyable place to stay.

Last but not the least I would like to my Mom, Dad, and Sister for always believing in me, for their endless support and encouragement.

Table of Contents

List of Figures

xvi

List of Abbreviations

ODOT   Ohio Department of Transportation

sUAS   Small Unmanned Aerial Systems

SfM   Structure from Motion

GPS   Global Positioning System

RTK   Real-time Kinematic

GSD   Ground Sampling Distance

GCP   Ground Control Point

GIS   Geographic Information System

DSM   Digital Surface Model

MTP   Manual Tie Point

DTM   Digital Terrain Model

IR   Infrared

SC   Scale Constraint

SPC   State Plane Coordinates

ME   Mean Error

MAE   Mean Absolute Error

RMSE   Root Mean Square Error

SD   Standard Deviation

FOV   Field of View

CP   Control/Check Point

VRS   Virtual Reference Station

Chapter 1 : Introduction

The thesis document presents the research work conducted to develop a standard operating procedure that would allow ODOT personnel to utilize sUAS and photogrammetry to inspect and monitor infrastructure and construction sites.

Chapter 1 gives a brief introduction to the topic of photogrammetry, small unmanned aerial systems (sUAS) and their applications relevant to the scope of the presented research work. It also discusses, in brief, the research objectives and emphasizes the main goals of the research work carried out.

Chapter 2 reviews the hardware components involved in undertaking the research project and the relevant photogrammetric parameters and terminologies. This chapter also briefly discusses the various software and tools used to accomplish the objectives of the research.

Chapter 3 describes in detail the approach and overall structure of the workflow followed. In this chapter, the various experiments generated to test the effect of select parameters, under every step of the research workflow, that effect the outputs generated using Pix4D Mapper and Context Capture, are presented. The chapter concludes with the discussion of various types of outputs generated using Pix4D Mapper and Context Capture for the research work presented.

Chapter 4 presents the results obtained following the generated research workflow in the form of case studies conducted at various buildings, bridges and construction sites.

Chapter 5 presents the conclusions for the research work and discusses opportunities for future work that can be conducted.

1.1 Problem Statement

An increasing number of structures constructed year-round require an equal amount of logistics to maintain and inspect their health. Traditional surveying and inspecting methods lack the necessary efficiency to keep up with the growing number of structures being built every year. Bridges, buildings, and construction sites are an important sector of the infrastructure network and therefore require continuous monitoring to detect damages or progress at early stages. Early detections and progress monitoring would allow authorities to avoid downtimes and additional costs [1]. Traditional surveying and inspection work are performed via visual inspection and measurements recorded manually using expensive tools by trained personnel. This inspection process tends to consume time which is a crucial factor when it comes to accessing infrastructure health [2]. With the advancements in small unmanned aerial systems (sUAS) and imaging, inspectors can employ commercially available sUAS to conduct their inspection process efficiently while complementing their traditional surveying techniques and procedures. The work presented in this document discusses a workflow that would help inspectors automate the process of inspection and presents tests conducted to explain the effect of various photogrammetry parameters on the outputs that will be analyzed by a trained inspector and compared to results obtained through a manual process. The suggestions and recommendations to extend and improve the workflow are also presented and discussed.

1.2 Photogrammetry Overview

Photogrammetry is the branch of science and technology that allows users to gain surface data of a region using 2D images without direct contacts [3]. Photogrammetry concept uses two dimensional (2D) images to create three dimensional (3D) outputs (3D point clouds, and mesh) as well as detailed two-dimensional (2D) images (orthomosaic and facades). The underlying

concept utilizes image matching by triangulation to extract three-dimensional (3D) points from different images. The scale-invariant distances can be calculated using the spatial relation of points between images [4]. The techniques involved in extracting points and positions for the 3D point cloud, generating 3D mesh and orthomosaics vary with the photogrammetry tools used. Photogrammetric tools allow one to determine the size, shape, and positions of objects using the 3D point clouds, mesh and 3D orthomosaics.

1.2.1 Photogrammetry History

Photogrammetry dates back to 1839, with its beginning in stereophotogrammetry where images were taken from offset positions and viewed with stereoscopic equipment. The invention of airborne systems made this technique more applicable and further fine-tuned with the invention of computers. The invention and development of visual and thermal camera systems and computers aided the creation of the present state of photogrammetry. With the rapid development of storage device capacities and computational power, the photogrammetry process is becoming an automated process enabling users to handle and process large quantities of digital photographic information [3][5].

Recent developments of the structure from motion (SfM) approach contributed to the further development of digital photogrammetry field. This approach, adopted by a majority of photogrammetry tools available in the market, automates the process of solving the orientation and positions of images without the requirement of a priori targets with known 3D positions [6]–[8]. The parameters that determine the orientation and position of images are calculated through a redundant and iterative adjustment process based on the features automatically extracted using overlapping image datasets [7], [9], [10]. This approach thus requires images to be captured with high overlaps and in various patterns to generate a 3D model of the object of interest. Coupled

with the advancement in airborne systems and computational power modern photogrammetry software packages require minimal manual inputs to automatically orient image positions, match features, and generate complex 3D models. This allows the analysis of images from handheld cameras and sUAS surveys to be practical and accurate [11].

1.2.2 Photogrammetry Classification

Photogrammetry can be classified in multiple ways based on various factors [12]. These factors are, but not limited to:

1. Camera position and object distance

2. Number of images

3. Methods of recording and processing

4. Availability of measurement results

5. Application or specialist area

For the purpose of this research, the primary factor taken into consideration is the camera position and object distance. Using the camera's position as photogrammetry is classified as follows [12]:

1. Satellite photogrammetry: This is used when the processed images are captured using a satellite where the camera systems or sensors are positioned at altitudes greater than 200km.

2. Aerial photogrammetry: This is used when the processed images are captured using an aerial system that is positioned at an altitude greater than 300m. Aerial photogrammetry is commonly conducted using sUAS to which a visual or thermal camera to capture images at the required altitudes [13].

4

3. Terrestrial photogrammetry: This is used when the processed images are used to take measurements from a fixed terrestrial location.

4. Close range photogrammetry: This is used when the processed images are captured using camera systems positioned at a distance less than 300m from the object.

5. Macro photogrammetry: This is used when the processed images are of macroscopic scales.

The work presented in this document falls under the category of aerial and close-range photogrammetry because of the use of sUAS to capture images at distances less than 300m from the object.

1.2.3 Photogrammetry Applications

Applications of photogrammetry are not limited to a specific field like infrastructure or construction site monitoring as presented in this document. For the longest time photogrammetry was limited to aerial and architecture surveying. The advancements in technology have enabled users to apply its principles in the following industries [12]:

1. Automotive industries: To inspect manufacturing processes.

2. Security and defense industry: To acquire military intelligence.

3. Architecture and archaeology industry: To interpret the geology of areas of interest and monitor the conditions of historic buildings.

4. Medical industry: To aid in surgery and measure parts of the body through non-contact methods

5. Forensics industry: To aid in the scene of crime measurements

The list of industries that use photogrammetry for their function keeps growing as technology becomes more accessible and with it the advantage of photogrammetric surveys is becoming clear for their ability to increase safety and accuracy in measurements while limiting cost [14].

1.3 Small Unmanned Aerial Systems (sUAS) Overview

sUAS is any aircraft vehicle that can be operated remotely or autonomously without the need for a human operator on board. sUAS comprises of a number of components and subsystems that includes but not limited to a ground control system (a remote controller), camera system (visual or thermal), camera gimbals, global positioning system (GPS) or real-time kinematic (RTK) systems, and data collection tools [15].

At present, sUAS has been gaining significant traction due to its significant advancements and hence its varied range of applications. The benefits of utilizing sUAS are far-reaching and are impacting nearly all aspects of infrastructure. Using sUAS provides users high-quality surveying and data mapping capabilities that can be collected automatically or remotely. This technology allows users to map large areas relatively quickly when compared to traditional surveying practices [16].

In addition to the broad applications discussed under the photogrammetry section, sUAS along with the theories of photogrammetry is being used by several state DOTs for various specific purposes that include surveying construction sites, monitor bridge conditions, manage traffic and improve safety [15]. Ohio DOT has demonstrated the use of sUAS by collecting data on freeway conditions, intersection movement, and traffic monitoring [17][18]. Virginia DOT has demonstrated the application of sUAS for real-time traffic surveillance, monitoring traffic incidents, signals and environmental condition assessment of roadside areas [19]. New Jersey

DOT has shown the use of sUAS to support structural inspections, real-time construction project monitoring, 3D corridor mapping and assessment of traffic congestion [16].

The studies on sUAS referred and reviewed provide vital information to understand the state-of-the-art practice in using emerging sUAS technologies to aid in infrastructure and construction site inspection and monitoring. Using these practices users can augment their inspections by processing sUAS images using photogrammetry tools and interpret the high-resolution 3D outputs generated as opposed to analyzing 2D planar images and CAD generated model [20].

1.4 Research Objectives

The primary objective of this research is to assist the Ohio Department of Transportation (ODOT) personnel to use photogrammetry and small unmanned aerial systems (sUAS) as part of their inspection procedure. To achieve this, the presented research discusses the effect of common photogrammetry parameters on the outputs generated using photogrammetry tools. The outputs generated using the photogrammetry tools are evaluated using planimetric and pointwise measurements and the effect on the accuracies due to various photogrammetry parameters are analyzed in this research. Moreover, the efficiency and effectiveness achieved using sUAS and photogrammetry to monitor infrastructure health and construction site monitoring are presented in this document. This is presented in the form of case studies conducted at active bridges, building and construction sites around the state of Ohio.

The research questions discussed in this thesis are as follows:

- What is the effect of various photogrammetry factors (ground sampling distances (GSD), image overlap percentage, mode of capture, camera triggering interval, the pattern of

flight, thermal camera settings, and ground control points (GCPs)) on the outputs

generated using the photogrammetry tools?

- Can close-range photogrammetry and sUAS methods aid in documenting crack widths in

  the range of 0.3mm?

- Can close-range photogrammetry and thermal camera systems aid in documenting

  delamination on road surfaces with the same level of accuracies when compared to

  contact-based inspections?

Chapter 2 : Literature Review

In this chapter, a brief literature review of the hardware and software tools used to conduct the

research is presented.

2.1 Photogrammetry Hardware

This section reviews all the hardware system used to undertake the research. It is divided into

three subsections that discusses the small unmanned aerial systems (sUAS) or drones, cameras,

and computer system used for this research. The research work presented in this document used

off-the-shelf hardware

2.1.1 Small Unmanned Aerial Systems (sUAS)

DJI's [21] UAS systems were primarily used for the research work presented in this document.

DJI Matrice 100 [22], DJI Matrice 210 RTK [23], and DJI Phantom 4 RTK [24] were used to

collect the data. DJI Matrice 100 [22] is developer-friendly sUAS and was used extensively for

this research study due to its compatibility with the majority of camera systems, flight planning

applications and its customizable framework [25]. The DJI Matrice 100 [22] gimbal supports the

DJI Zenmuse Z3 [26], DJI Zenmuse X5 [27], DJI Zenmuse Z30 [28], and DJI Zenmuse XTR

[29] cameras.

Figure 2.1: DJI Matrice 100 sUAS [22]

DJI Matrice 210 RTK [23] is a commercial sUAS that has two bottom gimbals that supports two

cameras at a time and a top gimbal that would allow users to fly below bridges and inspect the

underside of a bridge's superstructure. The DJI Matrice 210 [30] provides a longer flight time

compared to the DJI Matrice 100 [25] and has a real-time kinematic (RTK) system that improves

the precision of the image coordinates when compared to GPS. The Matrice 210 RTK [30]

gimbal support the DJI Zenmuse X5s [31], and DJI Zenmuse Z30 [28] camera.

Figure 2.2: DJI Matrice 210 RTK sUAS [23]

DJI Phantom 4 RTK [24] is an enterprise version sUAS that has a fixed 20MP camera, that cannot be swapped, and an RTK system that connects to the local virtual reference station (VRS) that would help in improving the precision of the image coordinates recorded by the sUAS [32]. The sUAS also has a terrain awareness function that is useful when mapping regions of uneven terrain elevation, as this would lead to the capture of images with consistent overlaps and ground sampling distance (GSD) [32].

Figure 2.3: DJI Phantom 4 RTK sUAS [24]

2.1.2 Camera

DJI's [21] camera systems were primarily used for the research work presented in this document. DJI's Zenmuse Z3 [26], Zenmuse X5 [27], Zenmuse X5s [31], Zenmuse Z30 [28], Zenmuse XTR [29] and Phantom 4 RTK cameras [24] were used to capture the images required for this research. The Zenmuse Z3, X5, X5s, and Phantom 4 RTK cameras are visual cameras and were used primarily to capture images [32]–[35]. The Zenmuse X5 and X5s cameras have an interchangeable lens system that allowed the use of 15mm and 45mm lenses [34], [35]. The Zenmuse Z30 is a visual video camera that has a 30x optical zoom lens and was primarily used to capture videos [36]. The Zenmuse XTR is a thermal radiometric camera and was used to capture thermal images and the temperature of the objects covered in the image frame [37]. Figures 2.4 to 2.9 provides a summary of the cameras' specifications used for the project. Understanding the specifications of an sUAS camera is extremely important when it comes to planning automated missions to capture images as this would help in determining the height and speed the sUAS must be flown and the mode of image capture. Other than the values of field of view, rest of the values listed in Figures 2.4 to 2.9 were populated using the information present in their respective user manuals [32]–[37]. The values for field of view was calculated using Equation 1 [38].

$$\text{FOV (rectilinear)} = 2 \arctan\left[\frac{\text{frame size}}{F_r * 2 * (m + 1)}\right] (\text{deg}) \qquad 1$$

DJI Z3

Specifications	Value
Horizontal Field of View (deg):	76.36
Vertical Field of View (deg):	60.22
Diagonal Field of View (deg):	97.25
Sensor Width (mm):	6.17
Sensor Height (mm):	4.55
Sensor Diagonal (mm):	7.67
Real Focal Length (mm):	3.92
Focal Length (35 mm equ.) (mm):	22
Image Width (pixels):	4000
Image Height (pixels):	3000
Image Resolution (MP):	12
Type of Camera:	Visual

Figure 2.4: DJI Zenmuse Z3 Camera Specifications [26]

DJI X5

Specifications	Value
Horizontal Field of View (deg):	59.94
Vertical Field of View (deg):	35.84
Diagonal Field of View (deg):	66.94
Sensor Width (mm):	17.30
Sensor Height (mm):	9.70
Sensor Diagonal (mm):	19.83
Real Focal Length (mm):	15/45
Focal Length (35 mm equ.) (mm):	30/90
Image Width (pixels):	4608
Image Height (pixels):	3456
Image Resolution (MP):	16
Type of Camera:	Visual

Figure 2.5: DJI Zenmuse X5 Camera Specifications [27]

DJI X5s

Specifications	Value
Horizontal Field of View (deg):	59.94
Vertical Field of View (deg):	46.86
Diagonal Field of View (deg):	71.61
Sensor Width (mm):	17.30
Sensor Height (mm):	13.00
Sensor Diagonal (mm):	21.64
Real Focal Length (mm):	15/45
Focal Length (35 mm equ.) (mm):	30/90
Image Width (pixels):	5280
Image Height (pixels):	3956
Image Resolution (MP):	21
Type of Camera:	Visual

Figure 2.6: DJI Zenmuse X5s Camera Specifications [31]

DJI Z30 (30x Optical Zoom Lens)

Specifications	Value
Horizontal Field of View (deg):	57.42
Vertical Field of View (deg):	44.75
Diagonal Field of View (deg):	68.83
Sensor Width (mm):	4.71
Sensor Height (mm):	3.54
Sensor Diagonal (mm):	5.92
Real Focal Length (mm):	4.3 - 129
Focal Length (35 mm equ.) (mm):	31.59 - 947.64
Image Width (pixels):	1920
Image Height (pixels):	1080
Image Resolution (MP):	2
Type of Camera:	Visual

Figure 2.7: DJI Zenmuse Z30 Camera Specifications [28]

DJI Phantom 4 RTK Camera

Specifications	Value
Horizontal Field of View (deg):	73.74
Vertical Field of View (deg):	53.13
Diagonal Field of View (deg):	84.05
Sensor Width (mm):	13.20
Sensor Height (mm):	8.80
Sensor Diagonal (mm):	15.86
Real Focal Length (mm):	8.8
Focal Length (35 mm equ.) (mm):	24
Image Width (pixels):	5472
Image Height (pixels):	3648
Image Resolution (MP):	19.9
Type of Camera:	Visual

Figure 2.8: DJI Phantom 4 RTK Camera Specifications [24]

DJI XTR

Specifications	Value
Horizontal Field of View (deg):	31.95
Vertical Field of View (deg):	25.80
Diagonal Field of View (deg):	40.27
Sensor Width (mm):	10.88
Sensor Height (mm):	8.70
Sensor Diagonal (mm):	13.93
Real Focal Length (mm):	19
Focal Length (35 mm equ.) (mm):	60.42
Image Width (pixels):	640
Image Height (pixels):	512
Image Resolution (MP):	0.33
Type of Camera:	Thermal

Figure 2.9: DJI Zenmuse XTR Camera Specifications [29]

2.1.3 Computer System

Following the studies conducted by Pix4D [39], presented in the form of an article [40] and the Pix4D Mapper user manual [41], a desktop computer system with the following configurations was built for the research work presented.

- CPU   :   Intel® Core™ i7-8700K CPU [42]

- RAM   :   64GB DDR4

- GPU   :   NVIDIA GeForce GTX 1060 6GB [43]

- Memory   :   Samsung 960 Pro PCIe NVMe 512 GB SSD [44]

                        Western Digital Black 4TB Performance Hard Disk Drive [45] (x2)

The SSD was used as the primary storage device where the images to be processed and all the necessary software was stored and installed. The two hard disk drives were used for secondary storage and backups. The processed images and outputs were transferred to the secondary storage device and the backup of the secondary storage was scheduled on a weekly basis.

2.2 Software

This section reviews all the software used to undertake the research. It is divided into four subsections that discusses the flight planning, image analysis, survey point analysis, and photogrammetry & GIS software used for this research. The research work presented in this document used both open source and commercial software packages.

2.2.1 Flight Planning Software

Flight planning software is used to automate the sUAS and image capture. The DJI GS Pro [46] flight planning software was used to automate this process. The GS Pro application works with

the all the three sUAS (Matrice 100, Matrice 210 RTK, and Phantom 4 RTK) and the six

cameras (Z3, X5, X5s, Z30, Phantom 4 RTK, and XTR) used for the research presented in this

document. The application provides users the interface to select the boundary of the area, camera

and sUAS, and the flight parameters for the area being mapped. The application allows users to

modify the following parameters: flight height/altitude, image capture mode, camera

triggering/shutter interval, camera shooting angle, front and side overlaps of images captured,

flight course angle, and the gimbal pitch angle [47]. The application also generates a summary of

useful mission statistics that includes the length of the flight path, the area covered by the flight

boundary, total flight time and the number of batteries required for the mission. Figure 2.10

shows the screenshot of the interface of the application loaded with a sample mission. The

following chapters present the research work conducted to understand the effect of flight height,

image capture modes, camera triggering interval, and pattern of image capture on the 3D and 2D

outputs generated using photogrammetry software.
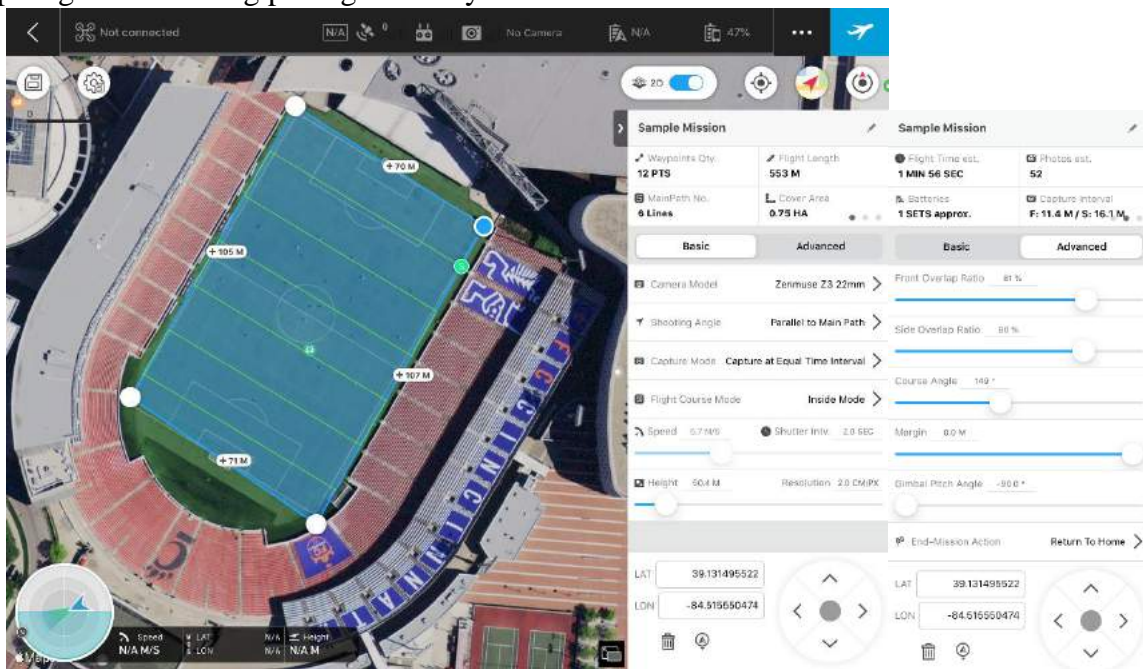
Figure 2.10: DJI GS Pro Flight Planning Application

The application provides users the option to input a custom camera model if the required camera is not available in the application's database. Under the custom camera option, the users will need to input the camera's sensor size and camera lens' focal length. These values impact the calculation of flight height and speed, which directly impact the resolution of objects in the image and the overlap between images [47]. Information about a camera's specification thus becomes extremely important and users will have to ensure the correct information is entered when setting up a camera that is not present in the application's database.
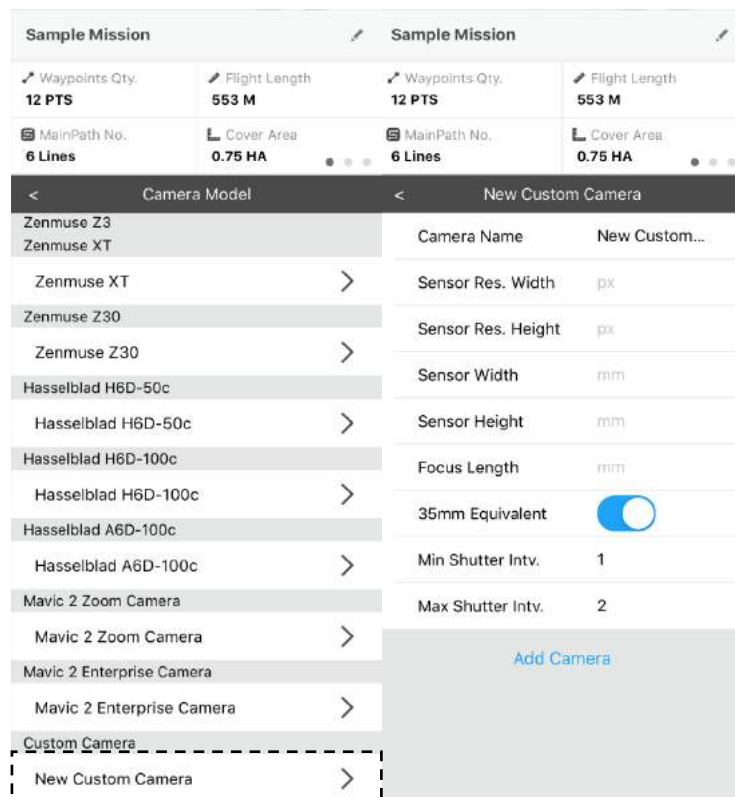
Figure 2.11: DJI GS Pro Creating New Camera Model

When a user sets a flight altitude the application calculates a value listed in the application called resolution. This is commonly called the ground sampling distance (GSD) which is the distance covered by each pixel in the image [47]. This effects the resolution of objects seen in the image and the GSD value varies proportionally with flight height [41]. The following chapters discuss this parameter in detail.

The shooting angle parameter determines the alignment of the camera with respect to the path followed by the sUAS. The application provides the option of parallel to the main path and perpendicular to the main path. Parallel to the main path option positions the camera to capture images whose height is parallel to the flight path. Perpendicular to the main path positions the camera to capture images whose height is perpendicular to the flight path [47].

Figure 2.12: Shooting Angle Illustrations; Parallel to Main Path (Left) and Perpendicular to Main Path (Right) [47]

The capture mode parameter determines the way images are captured using the sUAS and the application provides two options, hover & capture and equal timed. The hover & capture mode captures images in a stop and go pattern whereas the equal timed mode captures images at equal time intervals without stopping. For the same region mapped hover & capture mode takes a longer time than the equal timed mode of capture [47].

The shutter triggering interval parameter is activated when the capture mode is set to equal timed capture mode. The shutter triggering is the time elapsed between image capture. This value and the image overlap values determine the flight speed [47].

The front and side overlap parameters determine the overlap of two consecutive images in the same row and nearby images in the adjacent row respectively [47].

The gimbal pitch angle parameter determines the pitch angle of the camera that captures images. The angle is measured with respect to the horizon where -90° points the camera downward and 0° points the camera forward. When the camera is pointed downward the obtained image is called a nadir image whereas when the camera is pointed at an angle greater than -90° the

18

obtained image is called an oblique image [47]. The following chapters discuss this is in further detail.

2.2.2 Image Analysis Software

The images obtained after an automated flight are analyzed to ensure they were captured at the correct altitude and position and have the required overlaps. GeoSetter and Microsoft Word were used to conduct this analysis.

GeoSetter is a freeware application that helps to read and modify geo-data or other metadata of image files [48]. GeoSetter's user interface allows users to view the coordinates of images on a map as thumbnails as shown in Figure 2.13. Viewing the coordinates on the map helps users to check if the images were captured uniformly and at the correct location. The application also reads image metadata formats like IPTC, XMP and Exif [48] which contains detailed information about camera settings and location. The metadata information read by the application also helps to confirm the values of the altitude at which the image was captured.
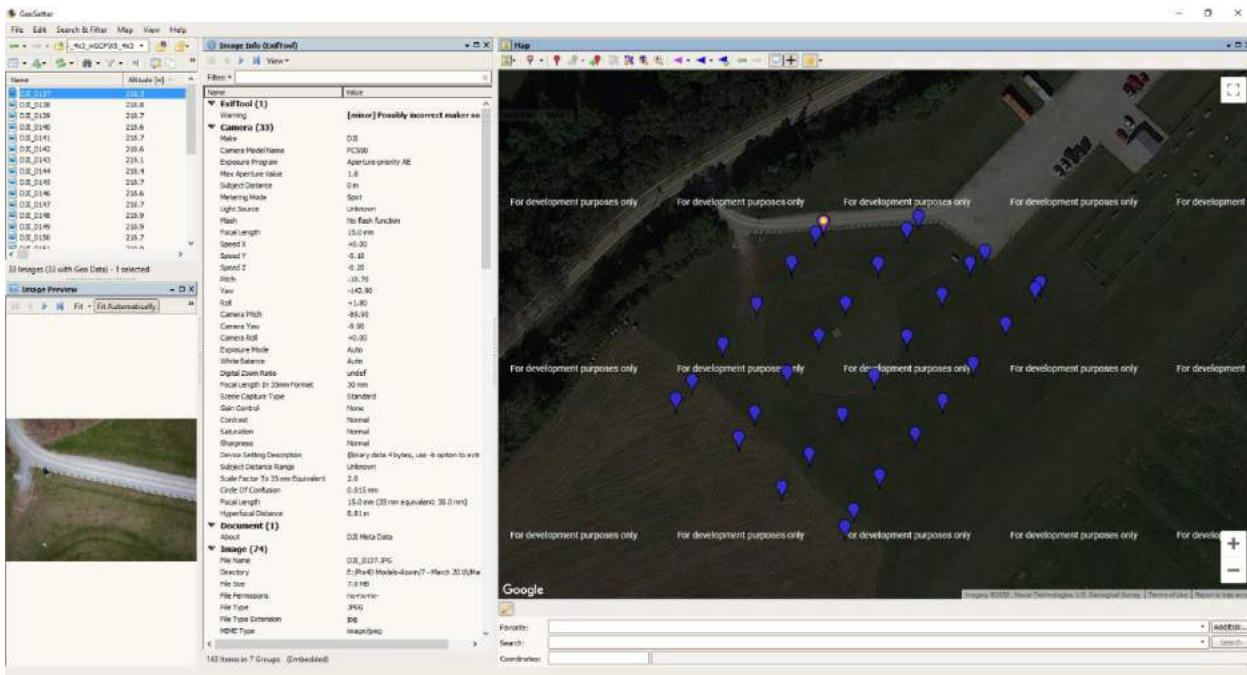
Figure 2.13: GeoSetter Application Interface

19

Microsoft Word is a commercial word processor application that is widely available and was used to analyze the overlap between images captured [49]. The various image formatting tools available on Word was used to conduct this analysis and estimate the overlap between the images. Figure 2.14 shows the screenshot of the analysis conducted on a sample dataset to estimate the relative overlap percentages between images. The measurements shown in the figure were recorded using the information provided under the picture and shape format option in the application.

Front Overlap = (1 − 0.8"/3") x 100 % = 73.33%   Side Overlap = (1 − 1.03"/4") x 100 % = 74.25%
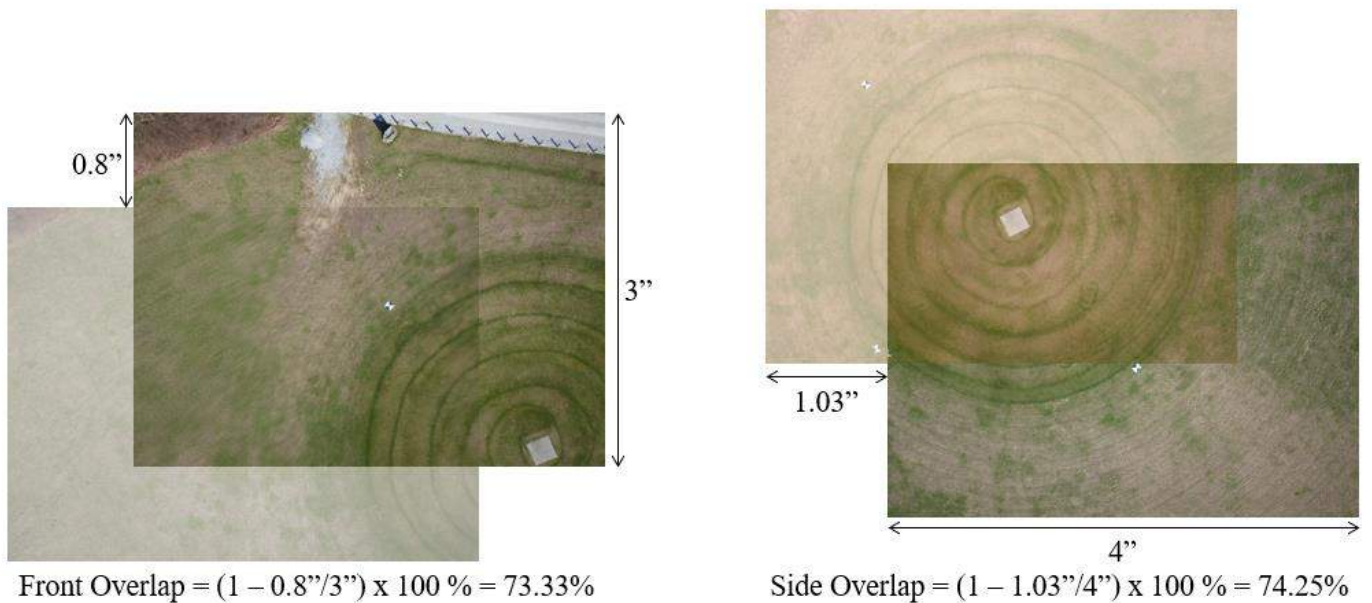
Figure 2.14: Image Overlap Calculations Using Microsoft Word

2.2.3 Survey Point Analysis Software

Survey points are landmarks or monuments present in the mapped region of interest whose coordinates are recorded using highly accurate and precise surveying equipment. Survey points help improve the quality and check the accuracies of the 3D and 2D outputs obtained using the photogrammetry software. Survey points and their locations in the real world are analyzed using Google Earth, an application that maps the Earth by superimposing satellite images, aerial photography, and GIS data onto a 3D globe [50]. Google Earth allows users to load co-ordinates

of survey points and displays them on the 3D representation of the earth. This application

provides users a reference about the location of these survey points and would allow users to

locate the points easily on the 3D and 2D outputs generated using Pix4D. Figure 2.15 shows the

screenshot of a sample set of survey points loaded on Google Earth.
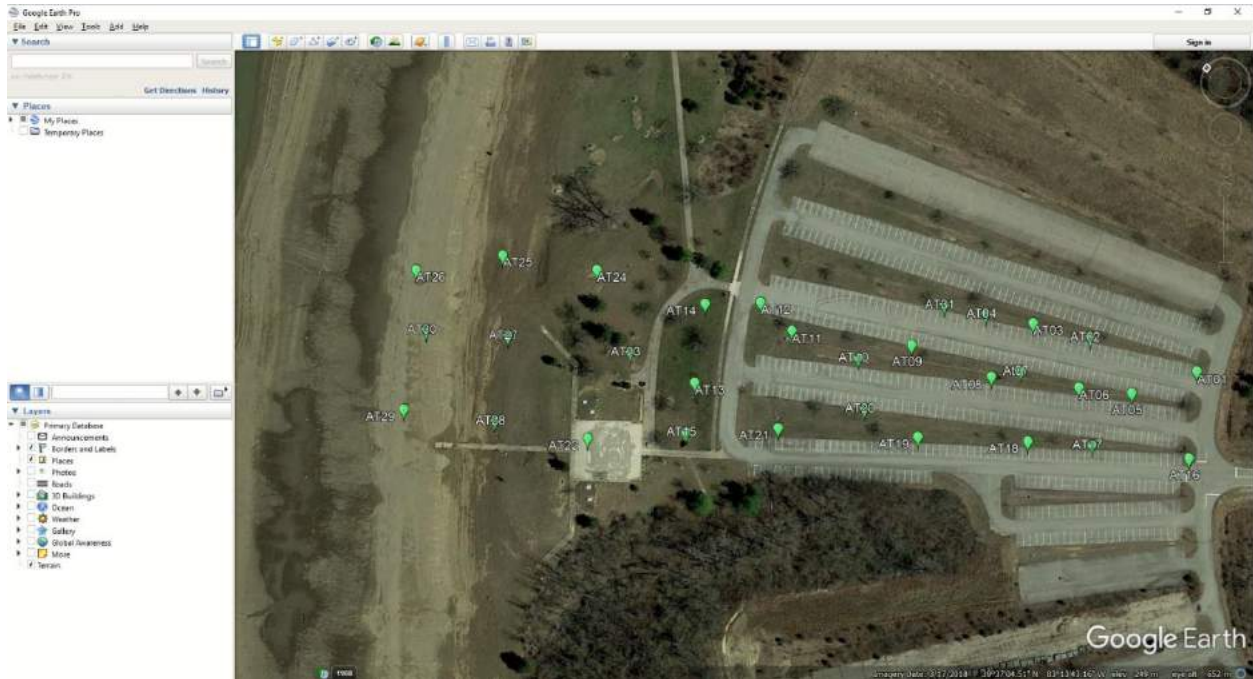
Figure 2.15: Survey Points Loaded on Google Earth Application

2.2.4 Photogrammetry and GIS Software

This section reviews the photogrammetry software used and their general workflow to create the

3D point clouds, 3D mesh and 2D orthomosaic outputs generated for the research work

presented in this document. The photogrammetry software used for the research included Pix4D

Mapper [51], Bentley's Context Capture [52] and FLIR Studio. QGIS [53], an open-source

geographic information system (GIS) software, was used to analyze the orthomosaic and DSM

generated using Pix4D Mapper.

2.2.4.1 Pix4D Mapper

Pix4D Mapper [51] is a photogrammetry software that converts aerial images to 3D point clouds

and mesh and 2D orthomosaics [41]. Pix4D Mapper software enables users to use any sUAS to

augment their surveying and inspection process. The software provides users an intuitive

interface that allows them to interact with the outputs generated, edit and analyze them. Pix4D

Mapper's general processing workflow is shown in Figure 2.16 [41].
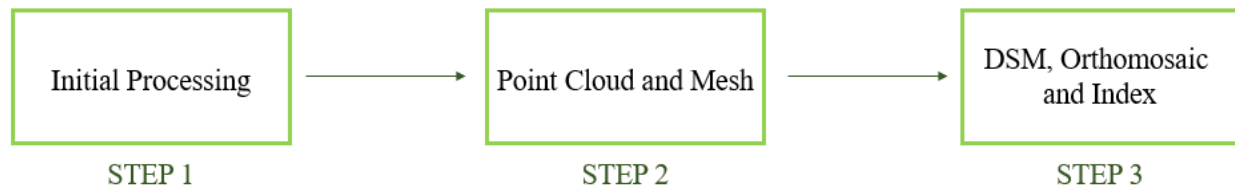
Figure 2.16: Pix4D Mapper General Processing Workflow

The acquired image dataset is imported into Pix4D as a new project and the software extracts the

geolocation of the images and the parameters of the camera are extracted using the metadata

information embedded in images. These parameters, available in the software's database, include

the values of image pixel size, sensor size, lens focal length, and correction factors of the images

captured using the camera. Pix4D Mapper provides the option to input image geolocations

recorded using auxiliary GPS/RTK systems [41]. Figure 2.17 shows the window with the list of

imported images with their extracted image geolocations and camera parameters.
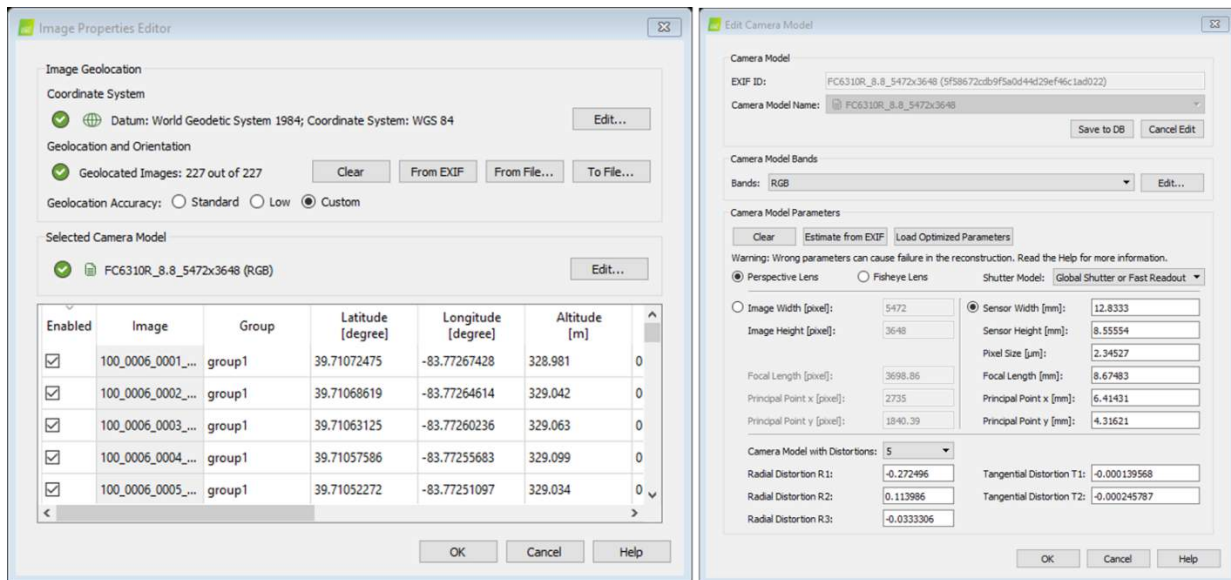
Figure 2.17: Pix4D Image Properties Window

Pix4D Mapper allows users to select their preferred coordinate frame of reference for the 3D and 2D outputs generated. The software provides multiple options for the horizontal coordinate reference system but has a limited number of options for the vertical coordinate system. The results presented in this document was obtained using the following coordinate reference system [54]:

- Horizontal Coordinate System: NAD83 (2011) Ohio South or Ohio North (survey US ft)
- Vertical Coordinate System: Arbitrary

The preferred vertical coordinate system NAVD88 Geoid 12A was not available in the list of options in Pix4D. When the vertical coordinate system is set to arbitrary Pix4D uses the vertical coordinate system of the image geolocations or the ground control point's (GCPs) altitude to values to set the vertical reference system of the 3D outputs generated [55]. Figure 2.18 shows Pix4D Mapper's output coordinate systems window.

23
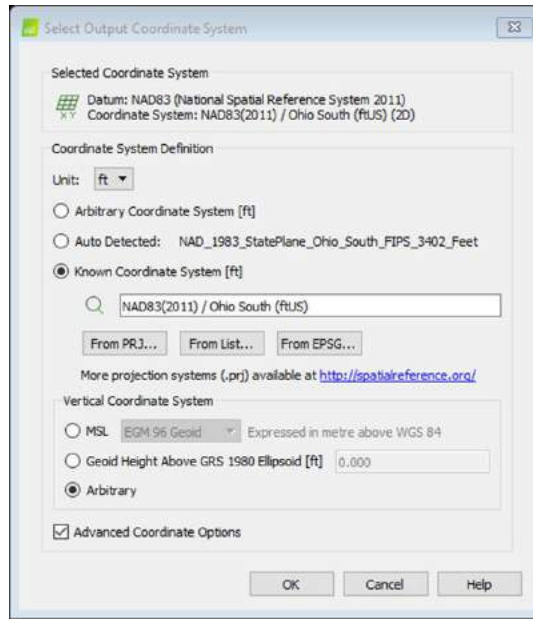
Figure 2.18: Pix4D GCP/MTP Editor Window

Pix4D Mapper allows users to import ground control points (GCPs), points whose coordinates are recorded using highly accurate and precise surveying equipment, or add manual tie points (MTPs) both which improve the matching between images and the accuracy of the outputs generated using Pix4D Mapper [41]. The Pix4D window shown in Figure 2.19, allows users to select the GCP's coordinate frame of reference, import and export control points, mark images that cover the GCPs and export the marks created on images.
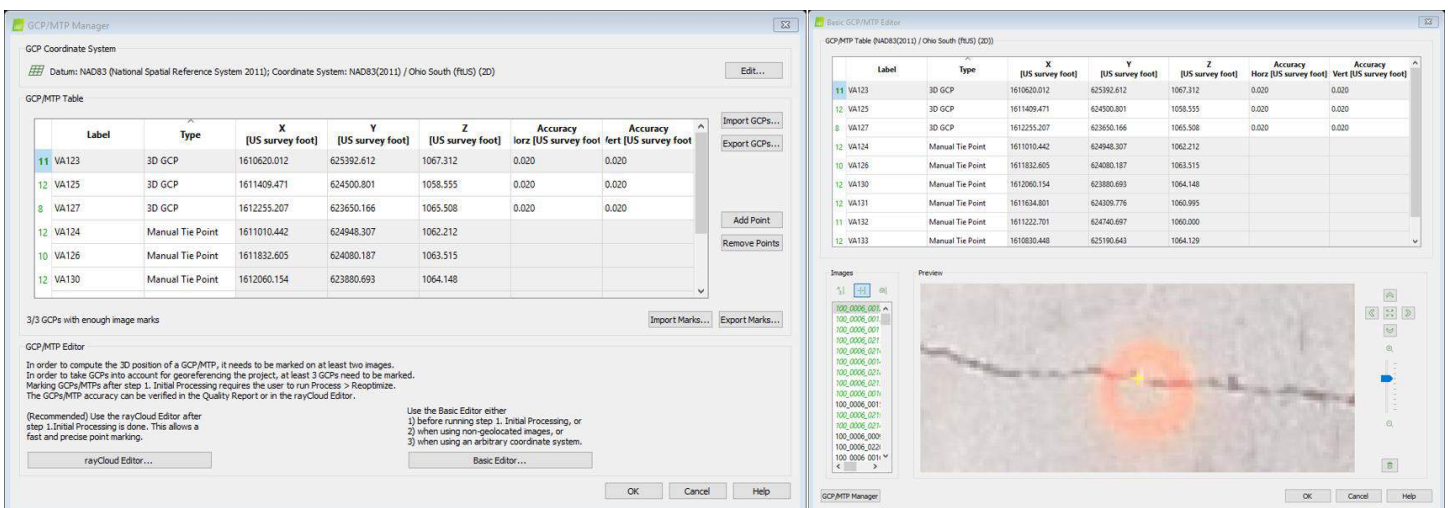
Figure 2.19: Pix4D Output Coordinate System Window

In step 1, Pix4D Mapper's algorithm automatically finds thousands of common points between images to generate a 3D point. Each characteristic point found ion an image is called a key point. When there is a high overlap between two images the common area captured is larger which leads to the generation of many key points. Greater the number of key points extracted, a more accurate 3D representation of the object of interest can be generated. The recommended overlap between images for most cases is at least 75% front overlap and 70% side overlap [41]. The application allows users to adjust the initial processing parameters after the project is setup. These parameters include matching image pairs by flight path, time at which images were captured, using image geolocations or image features for similarity matching, and camera calibration option as shown in Figure 2.20. The results presented in this document were generated using the default values set by Pix4D Mapper in step 1 [41]. The camera calibration is also done in step 1 where the optimized camera parameters are calculated and compared with original values [41]. This is crucial as it helps to understand the accuracies achieved in the final outputs. Users can select the parameters, external, internal or both, to be calibrated.
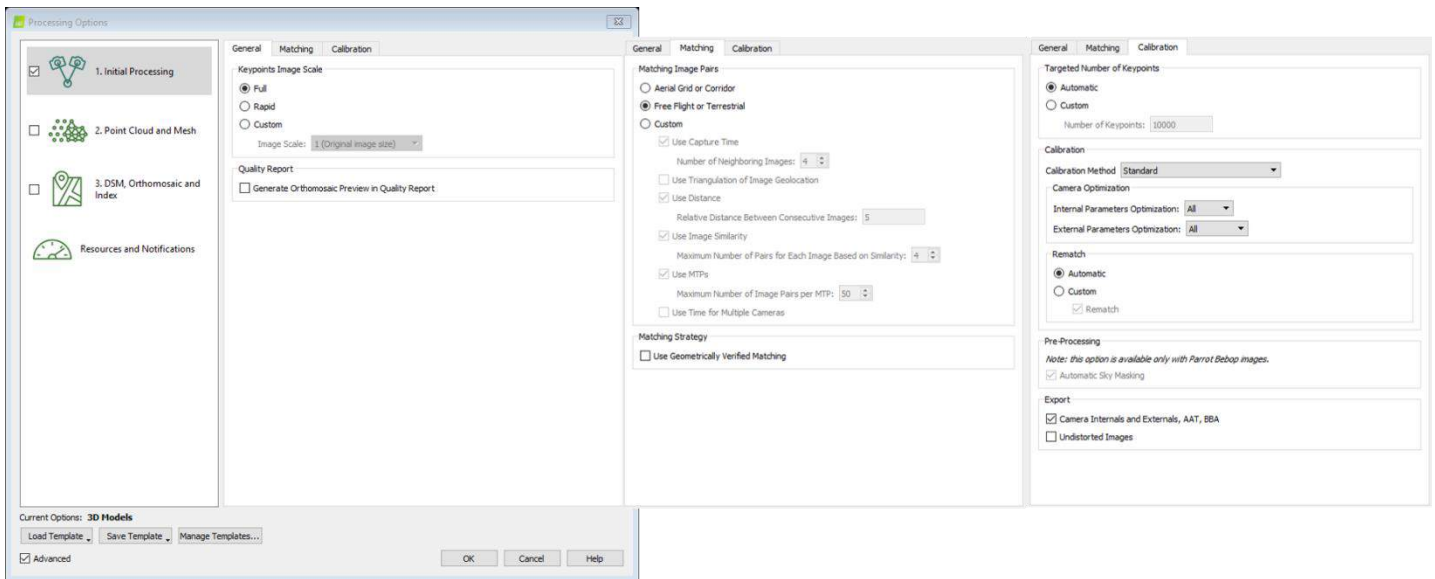
Figure 2.20: Pix4D Mapper Step 1 Processing Options

The second step in the workflow performs the 3D point cloud densification, followed by the

generation of the textured 3D mesh. Pix4D provides users the option to change the parameters

that produce 3D point clouds and mesh. Some of these options include image scales at which the

points are computed, point density and the number of minimum matches between images [41].

The output file formats for the 3D point clouds and mesh can also be chosen. Figure 2.21 shows

the list of all the options a user could tweak to generate the desired output after step 2.
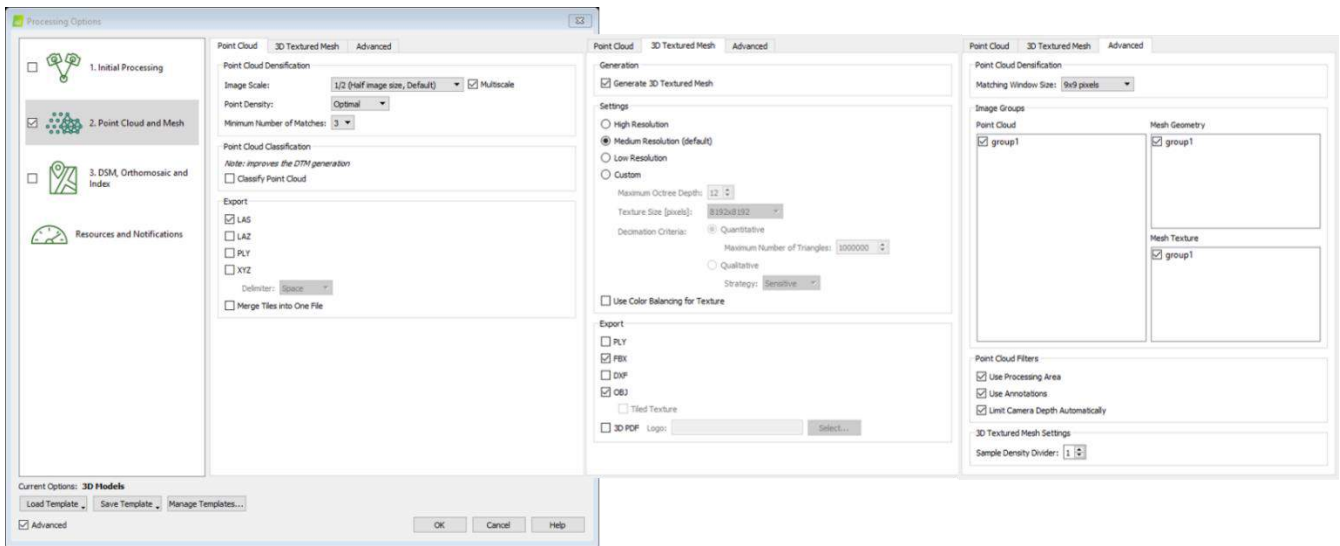
Figure 2.21: Pix4D Mapper Step 2 Processing Options

The last step in the workflow creates the digital surface model (DSM), orthomosaic, digital

terrain model (DTM) and reflectance map. Like the first two steps of the workflow Pix4D also

gives users the option to modify the parameters of the third step. This includes filtering DSM to

delete noise and avoid erroneous data, surface smoothing options, merging orthomosaic tiles,

determining the output file formats, generating derivative file formats and setting the resolution

of the orthomosaic [41]. Figure 2.22 shows the list of all the options a user could tweak to

generate the desired output after step 3.
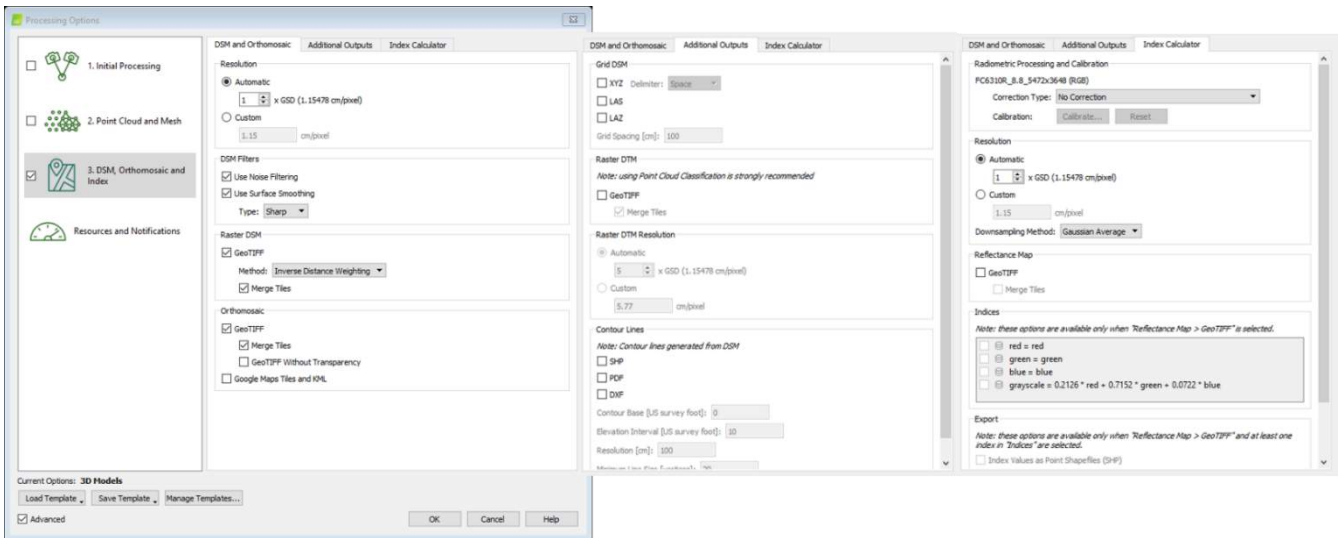
Figure 2.22: Pix4D Mapper Step 3 Processing Options

The work presented in this document used Pix4D Mapper primarily to test the effect of various

photogrammetry parameters on 3D point clouds. Pix4D Mapper allows users to make

planimetric and point measurements of the 3D point clouds. These measurements are used to

report the accuracies of the 3D point clouds generated using Pix4D. Objects of known

dimensions or survey points are laid out in the region of interest before the images are captured

to conduct the accuracy tests. Planimetric measurements are recorded using the polyline and

surface area tools available in Pix4D Mapper (Figure 2.23).
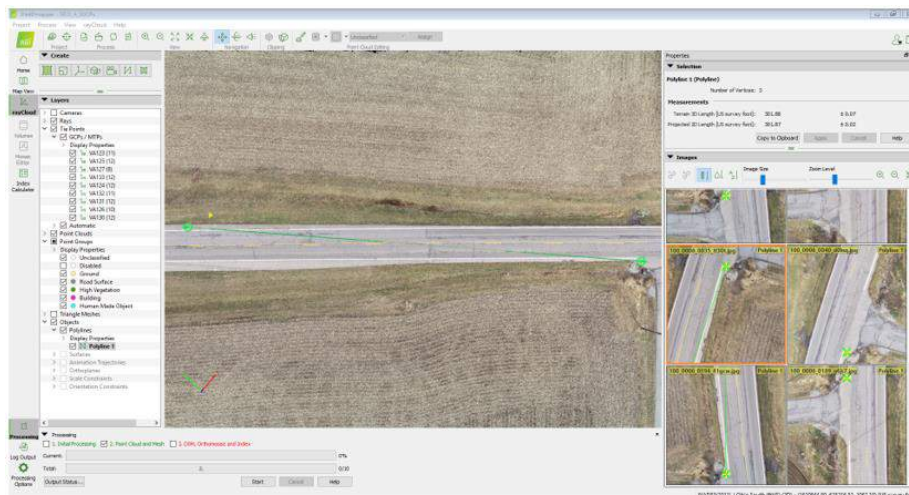
Figure 2.23: Pix4D Mapper Polyline Tool to Record Planimetric Measurements

Point measurements are taken by adding manual tie points at the location of survey points and recording their computed coordinates (Figure 2.24).
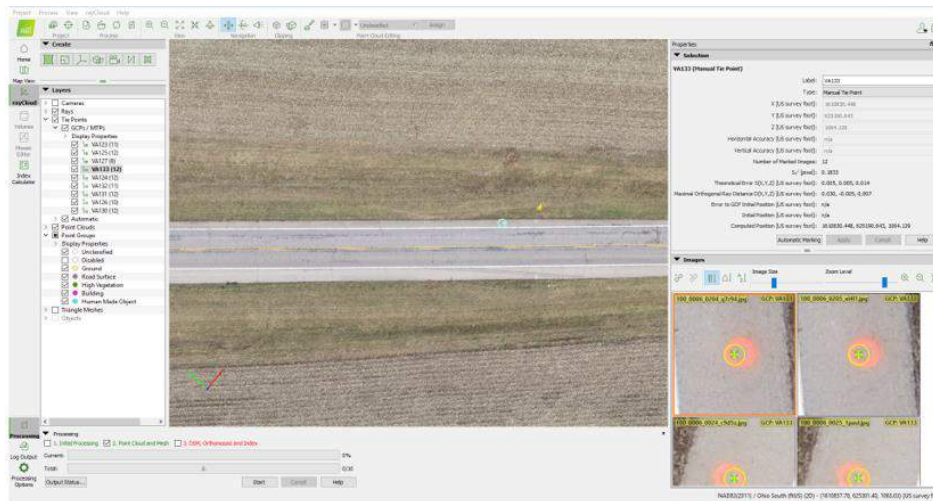
Figure 2.24: Pix4D Mapper Manual Tie Point Tool to Record Point Measurements

2.2.4.2 Bentley Context Capture

Bentley Context Capture is a photogrammetry software that converts aerial images to 3D mesh, point cloud and 2D Orthomosaic [52]. This software was primarily used to create 3D mesh outputs as it does not have the functionalities to test the accuracies of generated 3D point clouds. Context Capture's general workflow is shown in Figure 2.25 [56].
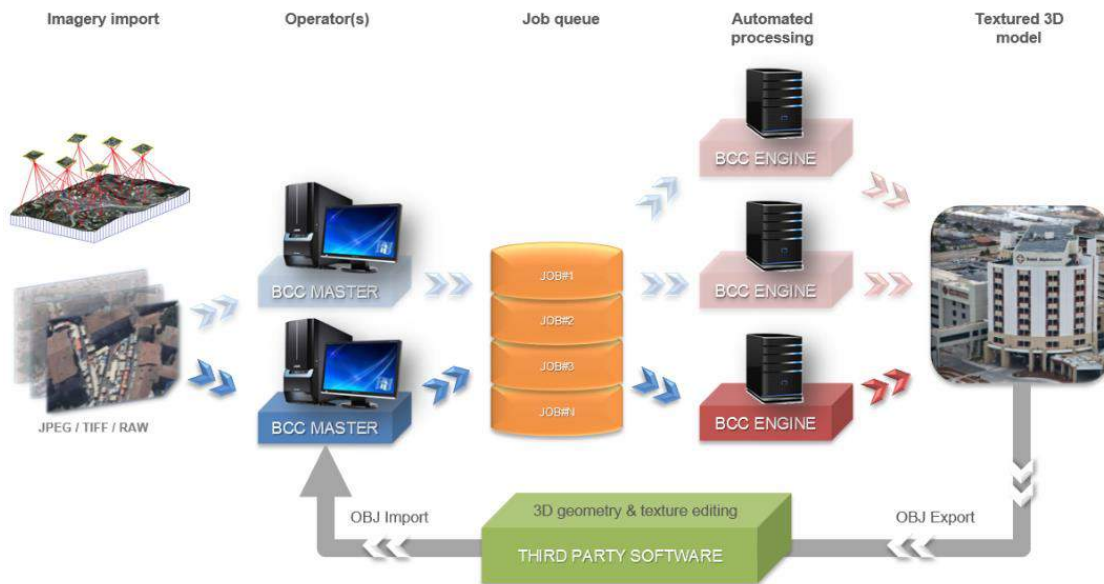
Figure 2.25: Bentley Context Capture's General Workflow [56]

Bentley's Context Capture software is divided into two components Bentley Context Capture

Master and Bentley Context Capture Engine as shown in Figure 2.25. Context Capture Master is

the user interface that allows users to import data sets, modify parameter settings, submit and

monitor tasks, and visualize results. Context Capture Master does not perform the processing

tasks instead, it decomposes tasks into elementary jobs which it submits to a job queue [56]. The

interface manages the different steps shown in the workflow above through a project.

A project created using Context Capture Master is organized as a tree structure and can be

described as a three-step process as shown in Figure 2.26.

Figure 2.26: Context Capture Master Project's Workflow

In the first step, a block manages the images and their properties (image group properties: sensor

size, focal length, principal point, lens distortion/pose: position, rotation), based on which one or

several reconstructions are created. These reconstructions are represented as sub-items of the

block in the tree structure [56].

In the second step, reconstruction manages a 3D reconstruction framework (spatial reference

system, region-of-interest, tiling, retouching, processing settings), based on which one or several

productions can be started. These productions are represented as sub-items of the reconstruction

in the tree structure [56].

In the third step, production manages the generation of 3D models, with error feedback, progress

monitoring and notifications about updates of the underlying reconstruction (e.g. retouching)

[56]. Context Capture Master's main interface window is shown in Figure 2.27 [56].
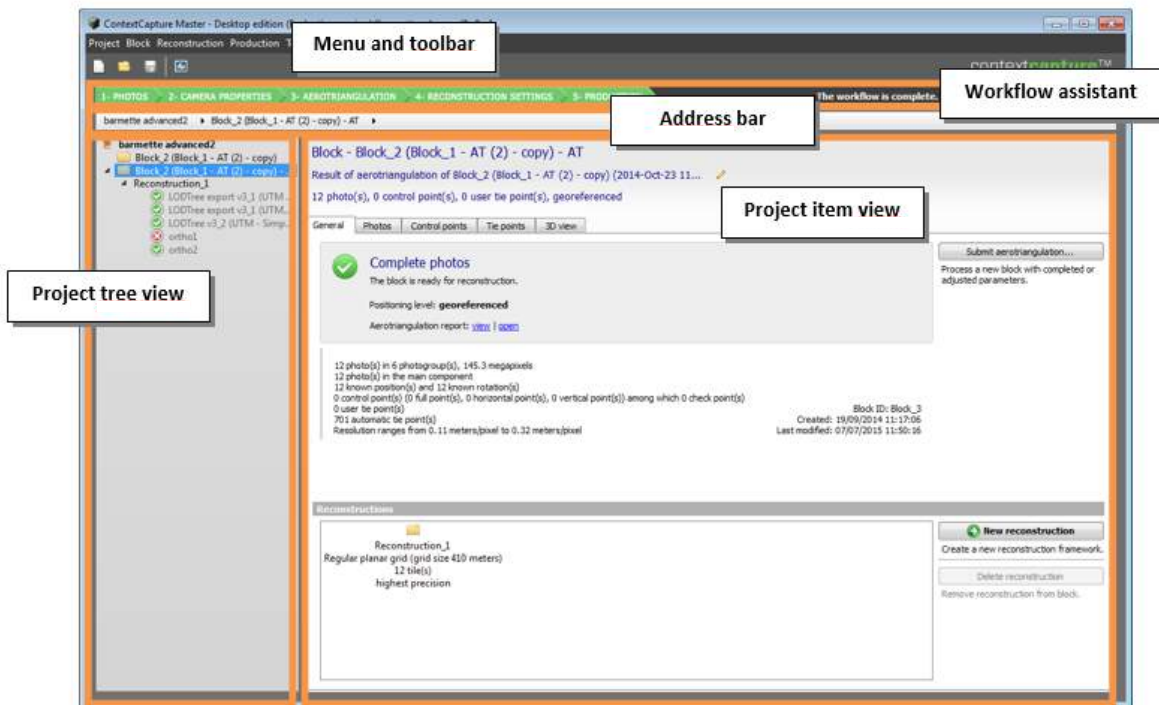
Figure 2.27: Context Capture Master's Main Interface Window [56]

Context Capture Engine is the worker module that runs in the background without any user intervention. The engine takes a pending job in the queue and executes it. Context Capture Engine is a separate application that must be run on the computer in order to start processing the jobs in the queue. A job usually consists of an aero triangulation or 3D reconstruction process, using various computationally intensive algorithms (keypoint extraction, automatic tie point matching, bundle adjustment, dense image matching, robust 3D reconstruction, seamless texture mapping, texture atlas packing, level-of-detail generation, etc.) [56].

2.2.4.3 FLIR Tools

FLIR Tools [57] is a thermal image analysis and reporting software. The software is used to analyze the thermal images captured for the research presented in this document. The software interface allows users to import thermal images in the radiometric JPEG (.rjpeg) file format. RJPEG image file format stores the temperature measured using the IR sensor in each pixel.

Using this information embedded in each pixel, FLIR tools allow users to measure the temperatures of various objects in the image using the spot measurement tool (Figure 2.28). Using the auto adjust region tool the temperature scale of the image can be constrained to regions of interest (Figure 2.29). This produces an image that would allow users to visually see the small temperature changes in the region. This tool was used extensively to analyze thermal images captured for the work presented in this document. The application also allows users to correct the emissivity value of images to correct the temperatures of objects with emissivity values different from the one embedded in the image.

Figure 2.28: FLIR Tools Interface to Measure Temperature Using Spot Measurement Tool
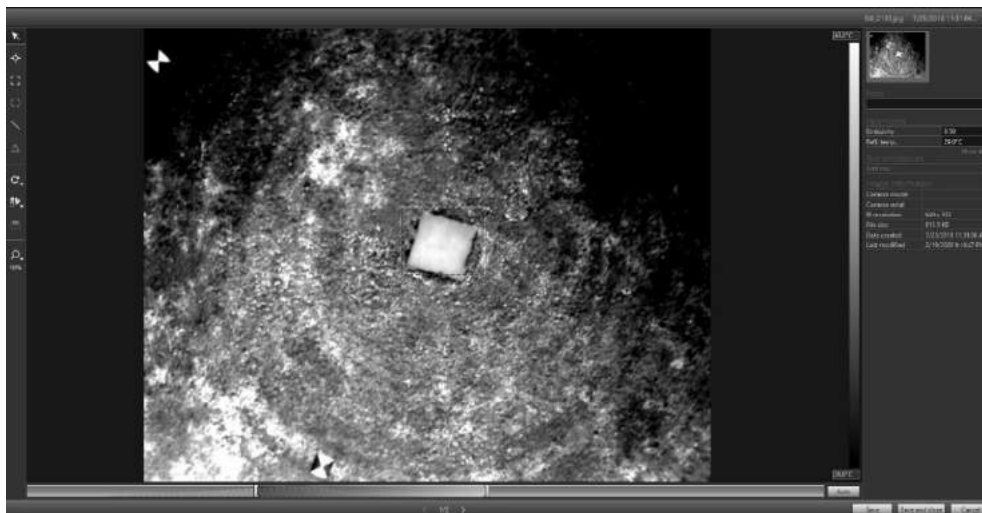
Figure 2.29: FLIR Tools Interface to Adjust Temperature Values Based Regions of Selection

31

2.2.4.4 QGIS GIS Software

Quantum GIS (QGIS) is an open-source GIS software where georeferenced data like an orthomosaic can be viewed and analyzed [53]. QGIS offers users a growing number of tools in the application itself and through the installation of open-source plugins. QGIS was primarily used to analyze the accuracies of the orthomosaic and DSM generated using Pix4D Mapper. The georeferenced 2D outputs were imported and analyzed using the point sampling and distance measurement tools available in QGIS.

2.3 Photogrammetry Parameters and Terminology

This section reviews the various photogrammetry parameters and terminologies introduced in this document, along with their definitions and theories.

2.3.1 Nadir and Oblique Images

Images captured using an sUAS are classified into nadir or oblique based on the orientation of the camera axis with respect to the ground/object captured. Nadir or vertical images are defined as images captured by a camera pointing to the nadir direction, where the nadir direction means the camera axis is perpendicular to the ground/object captured [58]. Figure 2.30 shows the illustration of a nadir image and its footprint.
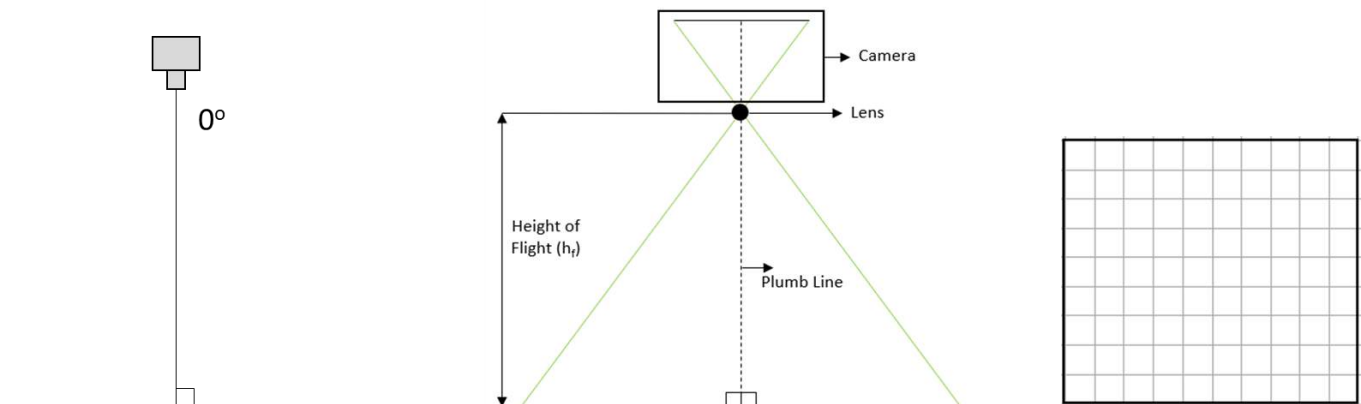
Figure 2.30: Nadir Image Illustration (Left to Right: Camera Angle, Image and Camera Illustration, Nadir Image Footprint)

Oblique images are defined as images captured by a camera that is not perpendicular to the ground/object captured. Oblique images are further classified into low and high oblique images based on the angle at which image is captured [59]. Low oblique images are defined using the relation shown in Equation 2 [59] and high oblique images are defined using the relation shown in Equation 3 [59]. Figure 2.31 shows the illustration of an oblique image and its footprint.

$$\text{Low Oblique Images: (Angle} - 90) > \frac{\text{Field of View}}{2} \qquad 2$$

$$\text{High Oblique Images: (Angle} - 90) < \frac{\text{Field of View}}{2} \qquad 3$$

The work presented in this document makes use of both nadir and oblique images to process 3D and 2D outputs.

Low Oblique Image: (Angle – 90) > FOV/2
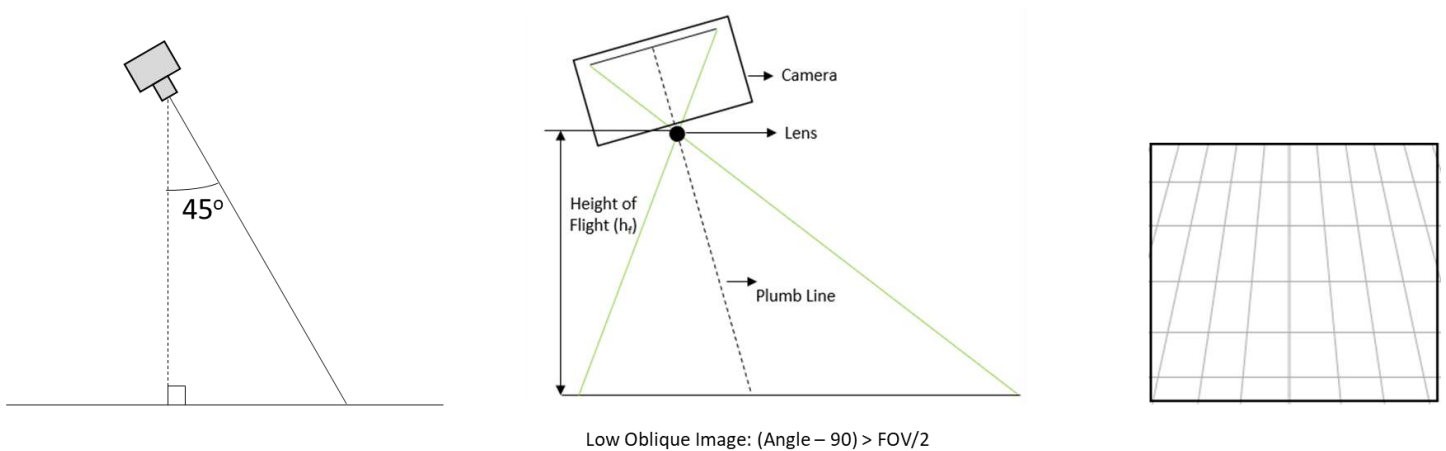
Figure 2.31: Low Oblique Image Illustration (Left to Right: Camera Angle, Image and Camera Illustration, Oblique Image Footprint)

2.3.2 Ground Sampling Distance

Ground sampling distance (GSD) is the distance covered by each pixel on the ground/object in the image [41]. GSD is commonly measured in the units of centimeters/pixel. GSD is an important parameter in photogrammetry as it can affect the accuracies of the 3D point clouds generated using Pix4D Mapper and as an extension affect the survey/inspection process. The

expected accuracies from a 3D output generated using Pix4D Mapper is generally 1-2 GSD

horizontally and 1-3 GSD vertically for a correctly constructed project [60]. The average GSD of

a nadir image is calculated using the formula shown as Equation 4 [41].

$$\text{Ground Sampling Distance (GSD)} = \frac{H \text{ (m)} * \text{Sensor}_{\text{size}} \text{ (mm)} * 100}{Fr(\text{mm}) * \text{Image}_{\text{size}}(px)} \qquad 4$$

The variables shown in Equation 4 are defined as follows:

Ground sampling distance (GSD): The distance covered by each pixel in an image, in

centimeters/pixel

H: Height of flight/sUAS where the image is captured, in meters

$\text{Sensor}_{\text{size}}$: The size (width/height) of the camera's sensor, in millimeters

F_R: The real focal length of the camera lens, in millimeters

$\text{Image}_{\text{size}}$: The size (width/height) of the image, in pixels

Figure 2.32 shows the illustration of a nadir image that aided in deriving the formula shown in

Equation 4.
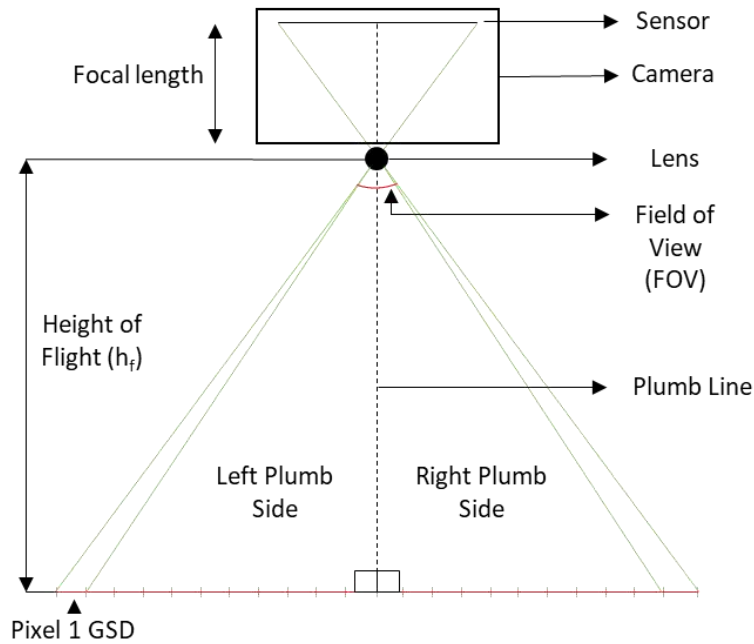
Figure 2.32: Nadir Image Illustration to Calculate the GSD Formula

For a camera, the GSD value varies proportional with flight height and as the GSD affects the accuracies of the 3D point clouds generated using Pix4D Mapper it is important to decide the height of flight before images are captured. Figure 2.33 illustrates the effect on GSD with varying flight altitudes [61].
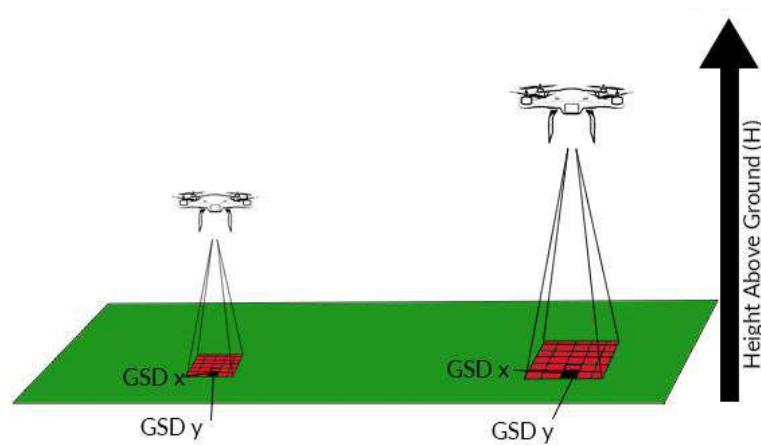
Figure 2.33: Nadir Image Illustration to Visualize Effect on GSD with Varying
Flight Altitudes [61]

The work presented in the following chapters investigates the effect of varying GSD on the accuracies measured using the Pix4D generated 3D point clouds and 2D orthomosaics.

35

Moreover, the study conducted on deriving the GSD equations for oblique and nadir images, and the relation between image pixel location and GSD is also presented.

2.3.3 Image Overlap

As the name suggests image overlap is the percentage of overlap between two images, i.e. the amount by which one image includes the area covered by the next image. There are two types of image overlaps in photogrammetry, front overlap and side overlap. The front overlap is the percentage of overlap between consecutive images captured in the same path of flight direction. Side overlap is the percentage of overlap between images on consecutive flight paths [41]. Figure 2.34 illustrates the front and side overlaps between images [62].
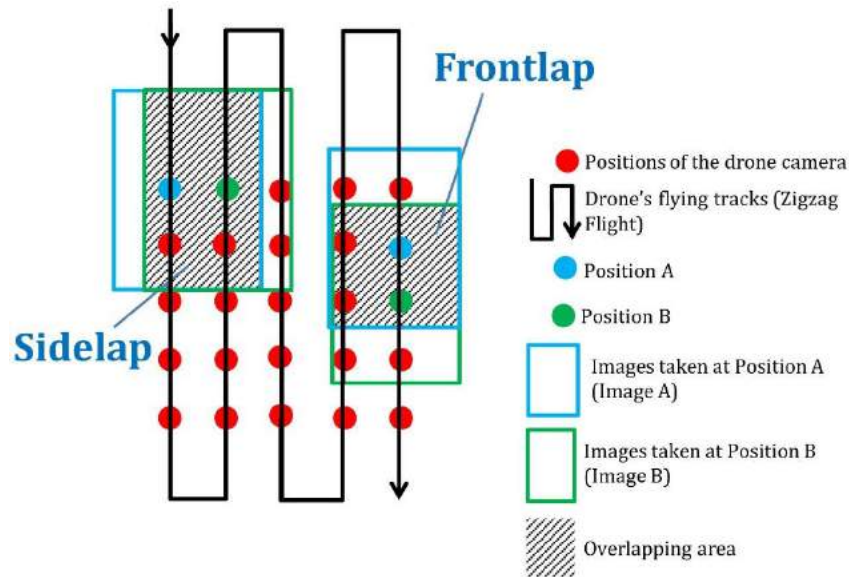
Figure 2.34: Illustration of Image Overlaps [62]

High overlap percentages between images help in computing a greater number of matched key points which leads to the generation of an accurate 3D model [41]. And the recommended overlap between images for most cases is at least 75% front overlap and 70% side overlap [41]. Maintaining consistent high overlap values becomes difficult when the terrain has varying elevations as illustrated in Figure 2.35 [63]. When the terrain has varying elevations it is

recommended to take-off point at each plateau or increase the takeoff overlap percentages to compensate for the loss [63].
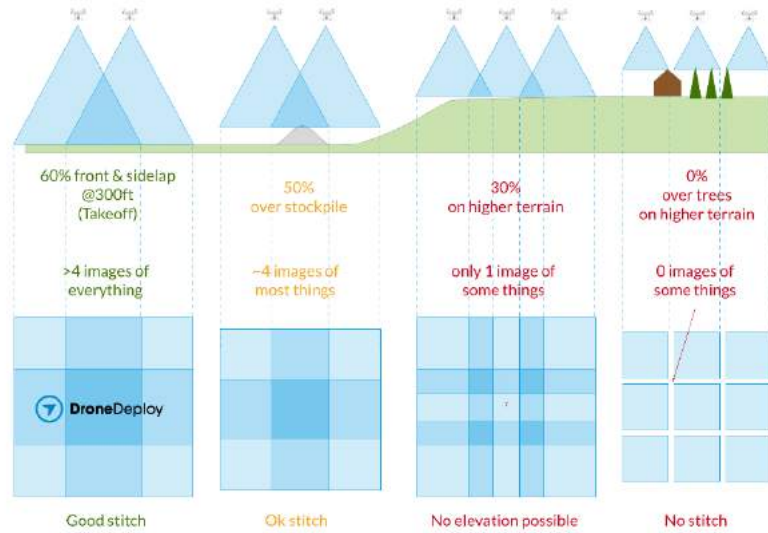
Figure 2.35: Image Overlap with Varying Terrain Elevation [63]

The study conducted on deriving an equation to compensate for the varying elevation of terrain or the presence of a tall structure in the area of interest is presented in the following chapters.

2.3.4 Mode of Capture

The majority of flight planning applications provide users two modes to capture images using sUAS. These are hover & capture equal timed modes. The hover & capture mode captures images in a stop and go pattern whereas the equal timed mode captures images at equal time intervals without stopping. For the same region mapped hover & capture mode takes a longer time than the equal timed mode of capture [41]. The study conducted to compare the results obtained by varying the modes of image capture is presented in the following chapters.

37

2.3.5 Camera Triggering Interval

The camera triggering interval is the time elapsed between image capture. This value and the image overlap values determine the flight speed [47]. The relation between speed of flight (v; m/s), image height (imH; pixels), GSD (cm/px), image overlap (fraction), and triggering time (t; seconds) is shown in Equation 5 [41].

$$v = \frac{imH * GSD}{100} * \frac{1 - overlap}{t} \qquad\qquad 5$$

Most flight applications provide the user the option to capture images in stop and capture fashion (hover and capture) or capture images while in motion (equal timed mode). Capturing images while in motion is always preferred over stop and capture as it reduces the flight time considerably when mapping large structures. When images are captured while in motion users are provided with the option of triggering interval, the time elapsed between the capture of two consecutive images, which also affects the speed of flight.

For a selected camera, if the desired flight parameter inputs (GSD, overlap, and triggering interval) generates a flight speed less than 1m/s, most flight planning applications change the mode of image capture to hover and capture. Also, if a camera's limitations with respect to triggering intervals are not known images may not be captured as per user's requirements. Due to the plethora of options available in the application users tend to adjust the flight parameters until the application agrees with values selected. The following chapters present the study conducted to identify DJI XTR and X5 camera's triggering interval limitations.

2.3.6 Pattern of Flight

The path/pattern sUAS follows to capture images can be altered using the course angle parameter available on flight planning applications. Users can plan missions where the sUAS follow paths that are either parallel or perpendicular to the width of the mission boundary [41]. The obtained images can then be processed on Pix4D separately (parallel or perpendicular) and together (grid pattern). The study conducted to test the effect of images obtained using various flight patterns (parallel, perpendicular, and grid) on the outputs generated using Pix4D is presented in the following chapters.

2.3.7 Infrared Imagery

Materials above the absolute zero (-230°C) temperature radiate infrared (IR) energy in the electromagnetic spectrum [64]. Systems that capture this energy radiated and convert it to images with different shades of grey or color, corresponding to different temperatures, are called infrared systems. Infrared imaging is a non-contact approach used to detect anomalies in the radiant heat patterns emitting from the material of investigation. The defects are identified by comparing the heat emissions of a hot or cold spot with the predicted amount [65].

IR wavelength, in the electromagnetic spectrum, lies between the visible and microwave wavelengths of about 10^{-6} m and 10^{-3} m, as shown in Figure 2.36 [66].
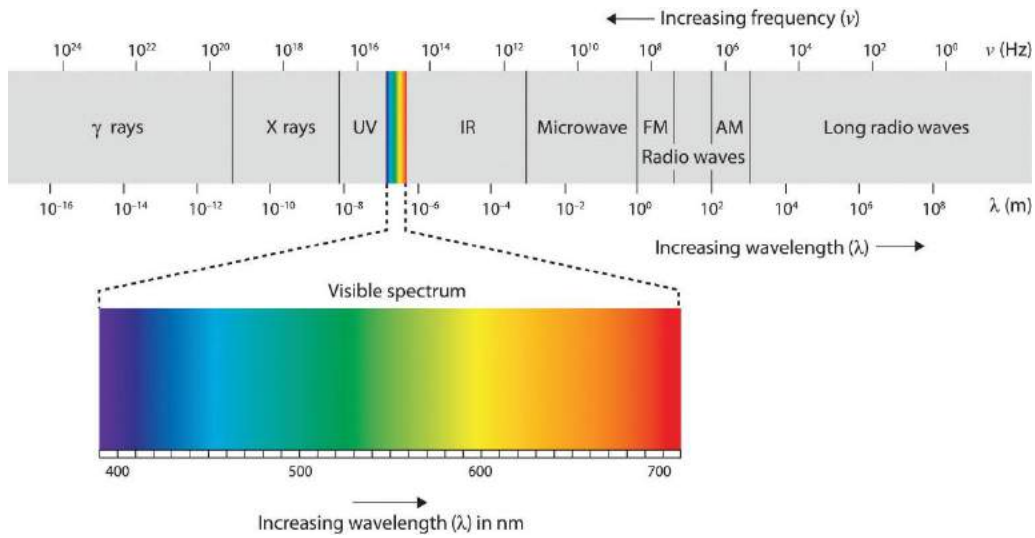
Figure 2.36: Electromagnetic Spectrum [66]

IR cameras calculate the temperature of an object by measuring the energy radiated from the object and a parameter called emissivity determined by the nature of the object's surface. Emissivity is the ratio of a body at a given temperature to that of a black body at the same temperature [67]. Emissivity values lie between 0 and 1 and are determined by the object's color, finish, and intrinsic material properties [67]. A black body is a material that absorbs all the incident radiation regardless of the wavelength and direction and, does not reflect any radiations [67].

The radiation detected by an IR camera includes two components; radiation emitted directly by the target surface and the reflected radiation from the background (sky, atmosphere, etc.) [67]. The ratio of the two components detected by the IR camera is weighted according to the emissivity of the target surface as shown in Equation 6 [67].

$$E_{sensor} = \varepsilon . E_{target} + (1 - \varepsilon) . E_{background} \hspace{3cm} 6$$

40

E_{sensor} is the radiant energy detected by the IR camera in Wm^{-2}, E_{target} is the radiant energy emitted by the target surface, $E_{background}$ is the radiant energy emitted by the background and ε is the emissivity of target surface [67].

After substituting the Stefan-Boltzmann law (Equation 7) and rearranging produces the formula (Equation 8) used to calculate the temperatures using the data recorded by IR cameras [67].

$$E = \sigma T^4 \qquad\qquad\qquad 7$$

$$T_{target} = \sqrt[4]{\frac{T_{sensor}^4 - (1 - \varepsilon).T_{background}^4}{\varepsilon}} \qquad\qquad 8$$

T_{target} is the corrected surface temperature of the target in kelvin, T_{sensor} is the temperature recorded by the IR camera in kelvin, $T_{background}$ is the brightest temperature of the background in kelvin and σ is the Stefan-Boltzman constant which is equal to 5.67 x10^{-8} Wm^{-2}K^{-4} [67].

The following chapters present the work conducted to derive an equation, based on Equations 7 and 8, to correct temperature values recorded in a thermal image that have objects of varying emissivity values.

DJI XTR, the thermal camera used for the work presented in this document, uses a FLIR Tau 2 sensor [37]. The camera can detect temperature values ranging from -25°C to 100°C, which is radiometrically calibrated to measure absolute temperatures [37]. The camera has a sensitivity of <50mK and can measure temperatures with an accuracy of ±10°C and an accuracy of ±5°C when the environmental and image capture conditions are ideal [37].

The list of the recommended ideal conditions populated by Pix4D [51], the American Society for Testing and Materials (ASTM) [68], and FLIR [69] is given below [41][70] [71].

1. The recommended overlap of objects in thermal images must be 90% if the images are processed using Pix4D Mapper.

2. Thermal images must be captured at an angle less than 35º with respect to the camera's perpendicular axis as Pix4D Mapper cannot calibrate thermal images with angles greater than 35º.

3. When thermal images objects of high reflectivity and low emissivity are captured position the camera at angles lower than 60º with respect to the camera's perpendicular axis.

4. To negate the effects of spot size, the region of interest in the image should cover at least 10 pixels.

5. If atmospheric conditions are not well-characterized images need to be recorded at 10m or less

6. Thermal images must not be collected at speeds greater than 10mph (16km/h)

The work presented in this document uses IR imagery to detect shallow delamination on bridge decks and detect temperature variations in roof thermal images.

2.3.8 Manual Tie Points

Manual tie points (MTPs) are 3D points marked by a user on the images that correspond to a key point. Employing MTPs is one of many methods used to calibrate and improve the accuracies of Pix4D outputs. MTPs are points that do not have coordinate information about the points marked in the images [41]. MTPs are typically used to assess and improve the accuracies of the reconstructed Pix4D outputs [41]. Figure 2.37 shows the example of an MTP used in a Pix4D project.
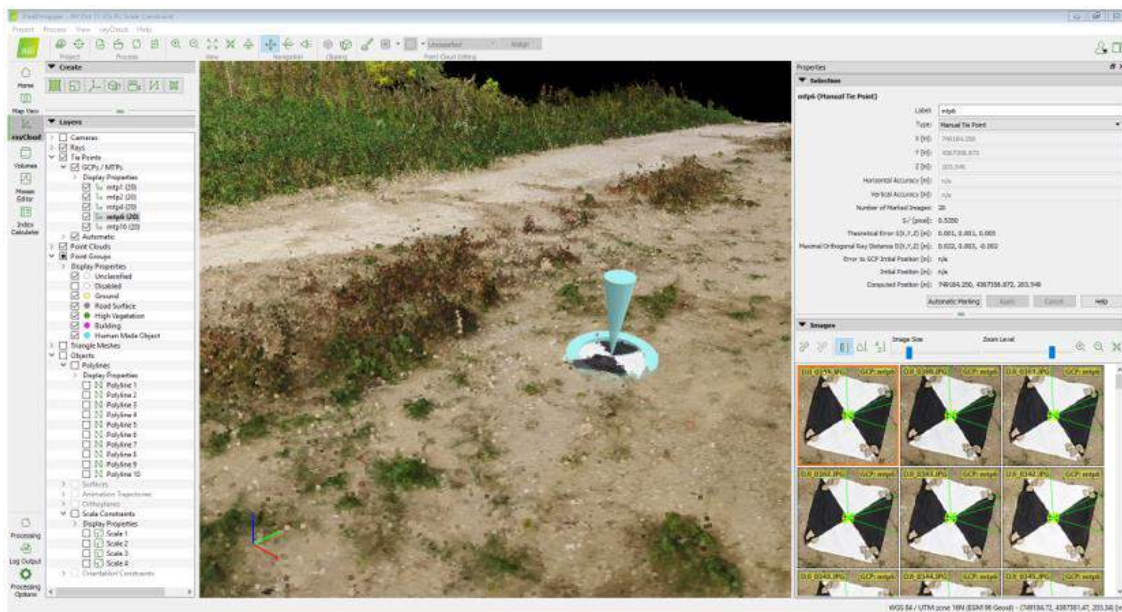
Figure 2.37: Manual Tie Points used in Pix4D Mapper

2.3.9 Scale Constraints

Scale constraints (SCs) is a known length of measurement between two points in the mapped area. Employing SCs is one of many methods used to calibrate and improve the accuracies of Pix4D outputs. SCs in Pix4D Mapper aids in setting up the scale of the outputs generated and therefore impacts the accuracies recorded [41]. SCs are usually used to improve the accuracies of

the outputs when ground control points (GCPs) are not used or the images processed do not have

geolocations [41]. Figure 2.38 shows the example of an SC used in a Pix4D project.
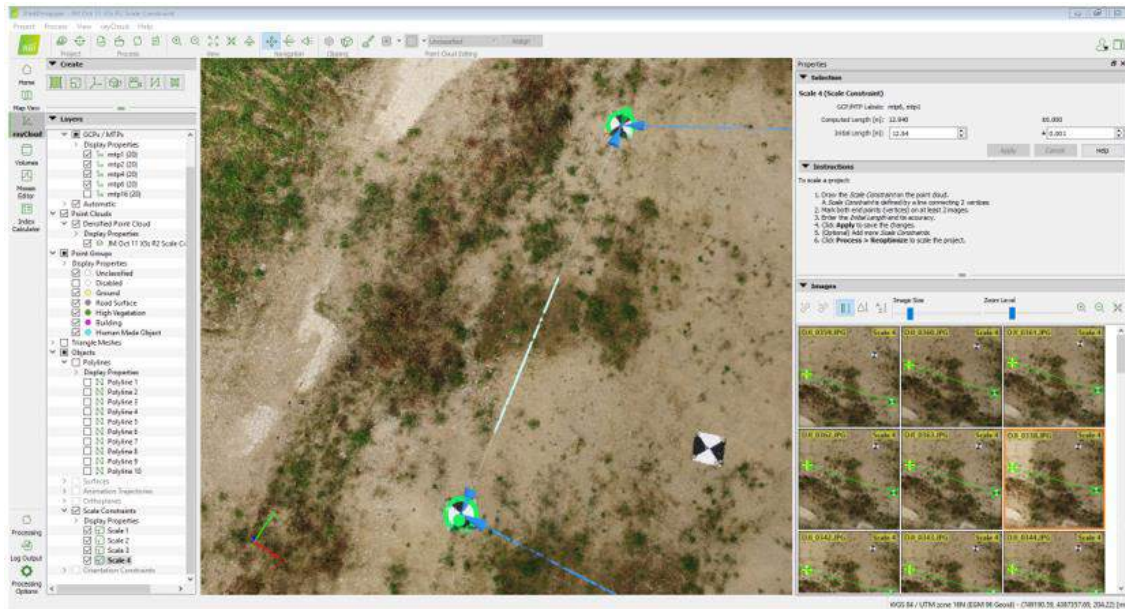
Figure 2.38: Scale Constraints used in Pix4D Mapper

2.3.10 Ground Control Points

Ground control points (GCPs) are points in the mapped region whose coordinates are recorded

using highly accurate and precise surveying equipment. Employing GCPs is one of many

methods used to calibrate and improve the accuracies of Pix4D outputs [41]. GCPs are usually

large marked or contrasting targets that are distributed strategically and uniformly throughout the

mapped area. Examples of target shapes and designs used as ground control points are shown in

Figure 2.39 [41]. GCPs and their corresponding coordinates are used to help Pix4D Mapper to

accurately position the 3D point cloud in relation to the real world. GCPs are not necessary to

process a project with Pix4D mapper but they help to significantly increase the absolute accuracy

of the outputs generated [41]. In projects where the images have geolocations, GCPs increase the

absolute accuracy of the model and reduces the shift due to the image GPS coordinates from

meters to centimeters [72]. In projects where the images do not have geolocations, GCPs help to

georeferenced, scale, orient and position the outputs [72]. Laying out a minimum of five GPCs is recommended when mapping large areas, where four GCPs are laid uniformly near the corners and the fifth one is placed in the center of the area, as shown in Figure 2.40 [72]. Using more GCPs does not aid to significantly increase the accuracies obtained. The study conducted to test the effect of a varying number of GCPs on the outputs obtained using Pix4D Mapper is presented in the following chapters.

Figure 2.39: Examples of GCP Target Shapes and Designs [41]
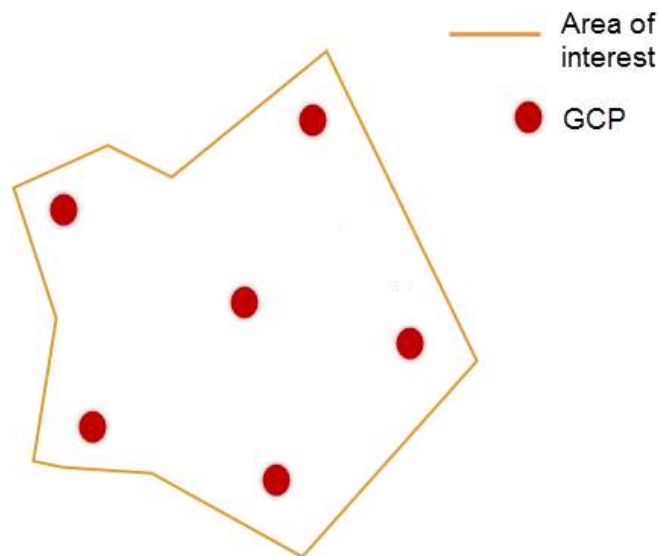
Figure 2.40: Suggested Distribution of Five GCPs in Area of Interest [72]

2.3.11 Ohio State Plane Coordinate System and VDatum

The coordinates embedded in the images captured using sUAS is in the form of latitude (degrees), longitude (degrees), and altitude (meters) referenced in the World Geodetic Coordinate System (WGS). Whereas, the coordinates of the survey points (GCPs and checkpoints), laid out in the field, are recorded in the Ohio State Plane Coordinate (SPC) system. Where the horizontal system used is called NAD83 2011 Ohio South or North and the vertical system is called the NAVD88 Geoid 12A or 12B [54]. Figure 2.41 shows the boundary line that decides the horizontal and vertical frame for each county in Ohio [73]. These coordinates are in the form of northing (US survey feet), easting (US survey feet), and altitude (US survey feet).
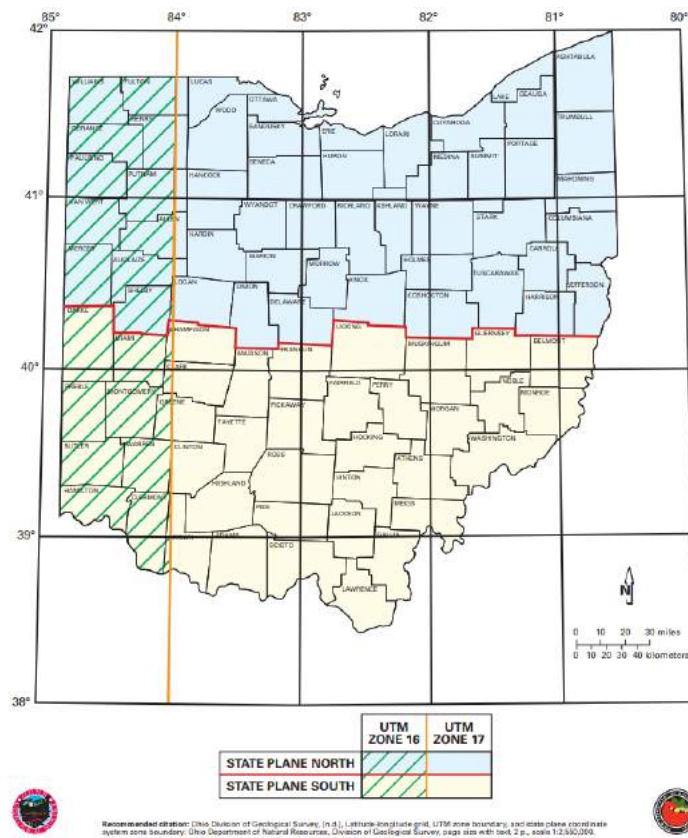
Figure 2.41: State Plane Coordinate System Zone Boundary Map

Pix4D Mapper provides users options to set the required coordinate systems and can handle multiple coordinates systems (images referenced in WGS and GCPs referenced in SPC) in the

horizontal frame but does not have enough options to set the required vertical frame [41]. This becomes an issue when testing a model processed without GCP as the model will be referenced to two different coordinate systems: horizontal in SPC and vertical in WGS.

To test the altitudes of the points, the survey point in SPC is converted to the WGS reference system using the free software tool called VDatum [74]. VDatum is a software tool developed jointly by the National Oceanic and Atmospheric Administration's (NOAA) National Geodetic Survey (NGS), Office of Coast Survey (OCS), and Center for Operational Oceanographic Products and Services (CO-OPS) [74]. VDatum is designed to vertically transform geospatial data among a variety of tidal, orthometric, and ellipsoidal vertical datums. This allows users to convert data from different horizontal/vertical references to a preferred system [74]. Figure 2.42 shows the VDatum software interface. The application allows users to batch convert survey point coordinates to the desired frame of reference using the file conversion tool. Once the survey points are converted to the WGS reference frame the new altitude in feet can be used to compare the altitude values obtained using Pix4D Mapper.
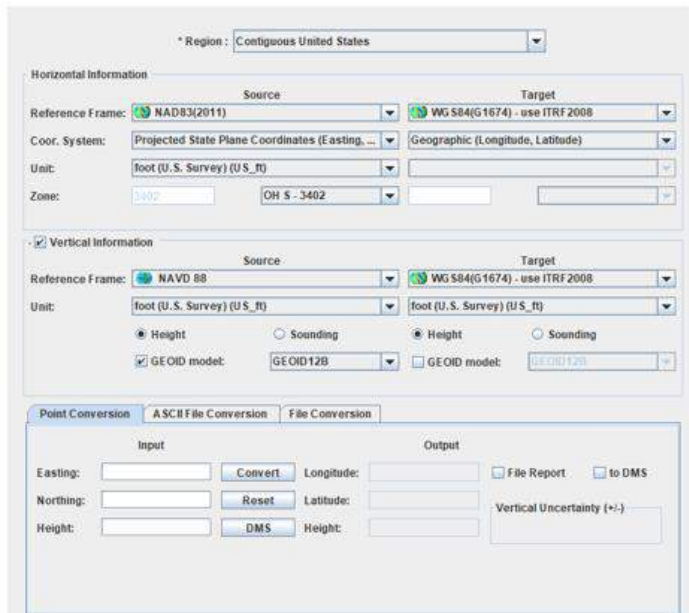
Figure 2.42: VDatum Software Interface

Chapter 3 : Approach and System Design

This chapter introduces the workflow designed for the research work presented in this document and breaks down each step of the workflow. The subsections break down each step of the workflow and presents the work done to investigate the effect on Pix4D output accuracies due to various parameters and settings that can be altered at each step of the workflow.

3.1 General Workflow

Figure 3.1 shows the general workflow that was designed to illustrate the overall process that was followed to generate the work presented in this document. The workflow is divided into four steps.

The first step involves planning missions to capture images using available DJI sUAS and applications, the second step involves processing the captured images using GeoSetter, Pix4D Mapper, Context Capture and FLIR Studio, the third step involves analyzing the generated outputs (3D Point Cloud, 3D Mesh, Orthomosaic, and DSM) and the fourth and final step involves post-processing the generated outputs. The fourth step is reserved for work that can be conducted in the future and the examples include automatic crack detection using orthomosaics and filtering point clouds. The preliminary work conducted to detect cracks is presented in the future scope section of this document.

Figure 3.1: General Workflow Followed for the Research Work Conducted

3.2 Accuracy Checks

The accuracies of the outputs generated by Pix4D are calculated using the accuracy metrics shown in Equations 9-15. Using the equations given below the error values for individual measurements (planimetric and pointwise) and the model were calculated.

$$\text{Error } (E_i) = d_i - \widehat{d_i} \tag{9}$$

$$\text{Absolute Error } (AE_i) = \left| d_i - \widehat{d_i} \right| \tag{10}$$

$$\text{Mean Error } (ME) = \frac{1}{N} \sum_{i=1}^{N} d_i - \widehat{d_i} \tag{11}$$

$$\text{Mean Absolute Error } (MAE) = \frac{1}{N} \sum_{i=1}^{N} \left| d_i - \widehat{d_i} \right| \tag{12}$$

$$\text{Root Mean Square error } (RMSE) = \sqrt{\frac{1}{N} \sum_{i=1}^{N} (d_i - \widehat{d_i})^2} \tag{13}$$

49

$$\text{Standard Deviation (SD)} = \sqrt{\frac{1}{N}\sum_{i=1}^{N}(E_i - \bar{E})^2} \qquad\qquad 14$$

$$\text{Variance} = \text{SD}^2 \qquad\qquad 15$$

The variables seen in Equation 9-15 are defined as follows:

- d_i: Actual measurement/output

- $\widehat{d_i}$: 3D point cloud measurement/output

- N: Total number of measurements

- E_i: Observed error

- $\bar{E}$: Mean of error values

The calculated error values are presented in a plot and the colors of the points in the plot are formatted based on the error values. When the measured error values are greater than 0.7 feet the points in the plots are colored red and when the error values are less than 0.7 feet the points are colored green. The 0.7 feet constraint value was set to ensure the recorded error values agree with the accepted 3D model error values required by ODOT surveyors [75]. Figure 3.2 shows ODOT's allowable error values for varying surveying classes in the horizontal and vertical planes [75].

Planimetric Accuracy Class	Recommended Use	Maximum Allowable RMSE (ft.)
Class I	Projects that require Class I planimetric features listed in Appendix A to be identified and mapped (i.e.: design engineering projects)	0.30
Class II	Projects that require Class II planimetric features listed in Appendix A to be identified and mapped (i.e.: planning studies)	1.00

DTM Accuracy Class	Recommended Use	Maximum Allowable Average Dz (feet)	Maximum Allowable RMSE (feet)
Class A	Paved areas	± 0.07	0.16
Class B	Vegetated areas outside of pavement that are maintained at a minimum biannual frequency (i.e.: farm fields, residential yards, roadside R/W, etcetera)	± 0.25	0.32
Class C	Vegetated areas that are not maintained	± 0.50	0.50
Class D	Areas where vertical accuracy is not critical or warranted (i.e.: planning engineering projects)	± 1.00	1.00

Figure 3.2: ODOT's Maximum Allowable Horizontal (Left) and Vertical (Right) Surveying Error Measurements

3.3 Flight Planning and Image Capture

Flight planning and image capture were conducted using DJI's sUAS and flight planning applications. DJI GS Pro was used to plan the required flights and the application allows users to modify multiple flight parameters. This section presents the work done to document the effect of a few of the parameters and the equations derived to aid in planning the desired flights.

3.3.1 Ground Sampling Distance (GSD)

GSD is the distance covered by each pixel on the ground/object in the image, and for a given camera, the value depends on the height at which the image was captured, as seen in Equation 4. This section presents the work conducted to derive the equation to calculate the distance covered by each pixel in a nadir and oblique image, and the effect of varying GSD values on the accuracies of 3D point clouds, on the temperature measured using thermal images and in the detection of defects using thermal images.

3.3.1.1 GSD Equations

The GSD equations presented in this section was derived to understand the relation between the distance covered by each pixel and the pixel location, and to calculate the average GSDs of
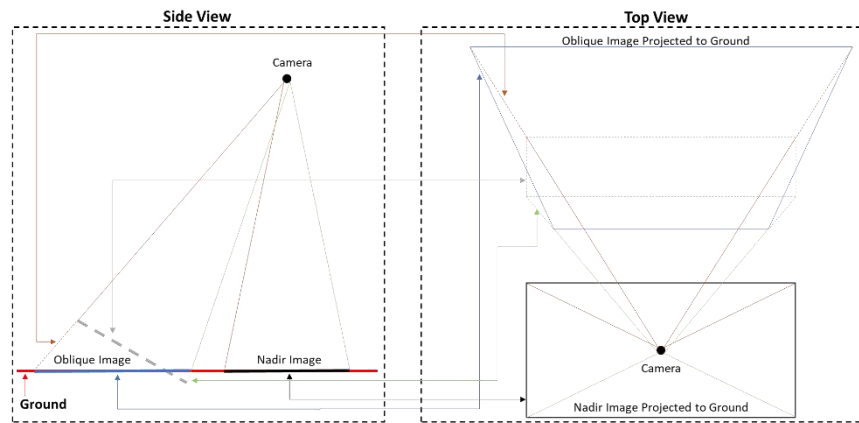
Figure 3.3: Side and Top Views of Nadir and Oblique Image Projected to Ground

oblique images. Figure 3.3 shows the illustration of a nadir and oblique image's side and top view when projected to ground.

The illustration in Figure 3.3 helped understand the geometry of a nadir and oblique image's footprint which helped in deriving the following equations.

Figure 3.4 shows the illustration of a nadir image's footprint, where the small boxes indicate pixels. Each pixel consists of two dimensions, one along its height (GSD_h) and the second along its width (GSD_w).
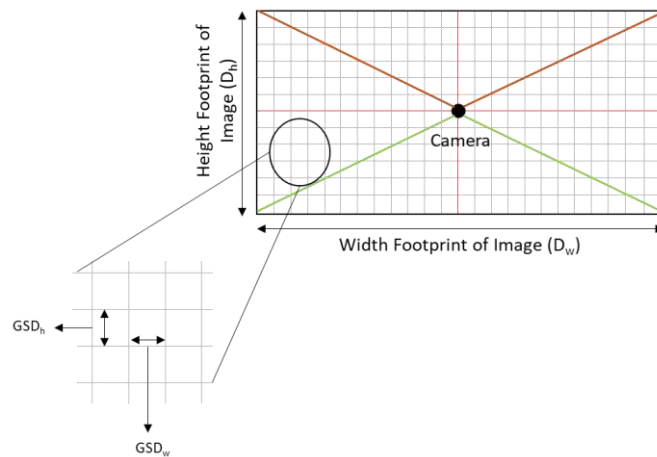
Figure 3.4: Top View of Nadir Image Projected to Ground with Pixels

Figure 3.5 shows the cross-section (front view) of a nadir image with respect to the centerline that lies along the width of the image, and the breakdown of this view that helped in deriving the equation that calculates the distance covered by each pixel.
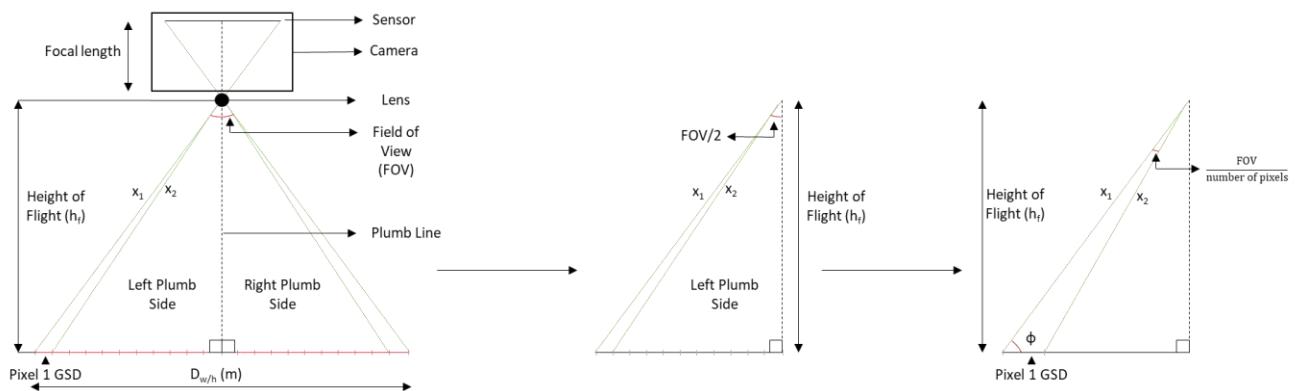
Figure 3.5: Front View of Nadir Image with Respect to Center Line Along Image Width

52

Using Figure 3.5, the equation of GSD of a pixel in a nadir image was derived in the following way (Equations 16-19).

$$x_2(n) = \frac{h_f}{\sin\left(90 - \left(\frac{FOV}{2} - \frac{n \cdot FOV}{\text{number of pixels}}\right)\right)} \qquad 16$$

$$\emptyset(n) = 90 - \left(\frac{FOV}{2} - \frac{(n-1) \cdot FOV}{\text{number of pixels}}\right) \qquad 17$$

$$GSD_{nadir}(n) = \frac{x_2(n) \cdot \sin\left(\frac{FOV}{\text{number of pixels}}\right)}{\sin(\emptyset(n))} \qquad 18$$

$$GSD_{nadir}(n) = \frac{h_f \cdot \sin\left[\frac{FOV}{\text{number of pixels}}\right] \cdot 100}{\sin\left[\left(\frac{180 - FOV}{2}\right) + \left(\frac{FOV \cdot (n-1)}{\text{number of pixels}}\right)\right] \cdot \sin\left[\left(\frac{180 - FOV}{2}\right) + \left(\frac{FOV \cdot n}{\text{number of pixels}}\right)\right]} \qquad 19$$

The above equations were derived using basic trigonometric functions and sine rule. The variables seen in Equations 16-19 are defined as follows:

- $GSD_{nadir}(n)$: Ground sampling distance of nth pixel from the edge in cm/px

- n: Pixel number from the edge from 1 to image width/2 or image height /2

- h_f: Flight height in meters

- FOV: Field of view; Horizontal Field of View (HFOV) relates to the angle formed with the width of image; Vertical Field of View (VFOV) relates to the angle formed with the height of the image, in degrees

- Number of pixels: The number of pixels that cover the width or height of the image, in pixels

Using the camera parameters for the DJI XTR camera and flight height of 20 meters the GSD values for each pixel vs the pixel number were plotted as shown in Figure 3.6.
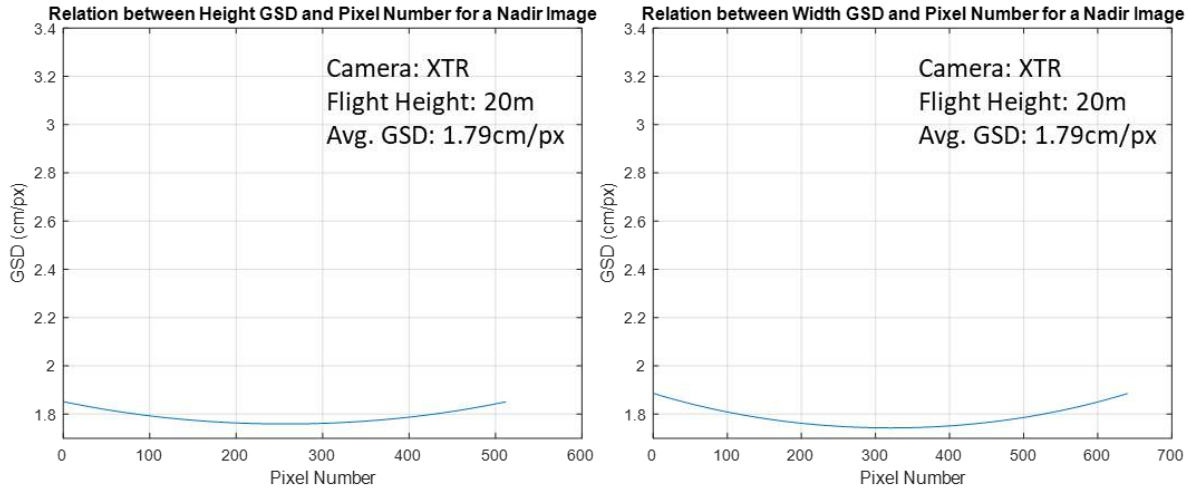
Figure 3.6: Relation Between GSD Value Per Pixel vs. Pixel Number for a Nadir Image for DJI XTR Camera where hf = 20m

The plot in Figure 3.6 shows that the GSD value, for a nadir image, is not constant throughout the image and varies parabolically. The average of the plotted point, in Figure 3.6, gives the same value if the GSD was computed using the formula in Equation 4 (average GSD equation).

Using Figure 3.5 the equation for distance/footprint (height and width) covered by a nadir image was derived as follows (Equation 20).

$$D_{w/h} = 2 \cdot \tan \left(\frac{FOV}{2} \right) \cdot h_f \qquad 20$$

The variables seen in Equation 20 are defined as follows:

- $D_{w/h}$: Distance covered on the ground along the height/width of a nadir image in meters

- Image footprint the distance (width or height) covered on the ground in meters

- h_f (m): Flight height in meters

- FOV: Field of view; Horizontal Field of View (HFOV) relates to the angle formed with the width of image; Vertical Field of View (VFOV) relates to the angle formed with the height of the image, in degrees

54

Figure 3.7 shows the illustration of an oblique image's footprint, where the small boxes indicate pixels. Due to its trapezoid shape each pixel, in an oblique image, consists of three dimensions, one along its leg (GSD_l), second along its bottom width (GSD_{wb}), and third along its top width (GSD_{wt}).
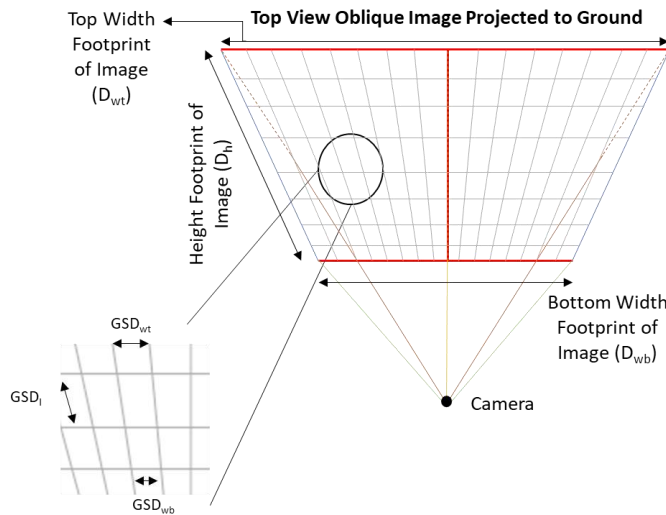
Figure 3.7: Top View of Oblique Image Projected to Ground with Pixels

Figure 3.8 shows the cross-section (side view) of an oblique image with respect to the centerline (yellow line) that lies along the height of the image, and the breakdown of this view (left plumb side and right plumb side) that helped in deriving the equation that calculates the distance covered by each pixel.
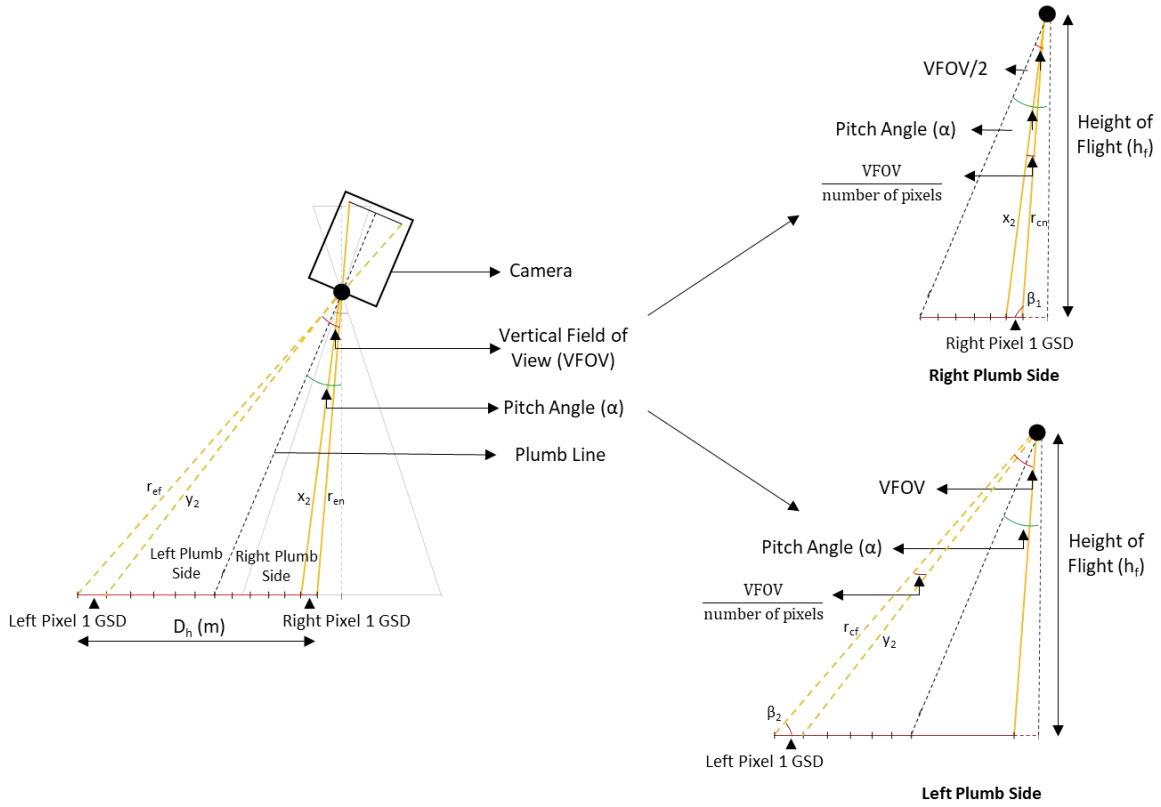
Figure 3.8: Side View of an Oblique Image with Respect to the Center Line Along Image Height

Using Figure 3.8, the equation of GSD of a pixel, along the leg, in an oblique image was derived in the following way (Equations 21-30).

$$x_2(n) = \frac{h_f}{\sin\left(90 - \left(\propto -\frac{VFOV}{2} + \frac{n \cdot VFOV}{number\ of\ pixels}\right)\right)} \quad\quad 21$$

$$y_2(n) = \frac{h_f}{\sin\left(90 - \left(\propto +\frac{VFOV}{2} - \frac{n \cdot VFOV}{number\ of\ pixels}\right)\right)} \quad\quad 22$$

$$\beta_1(n) = 90 + \left(\propto -\frac{VFOV}{2} + \frac{(n-1) \cdot VFOV}{number\ of\ pixels}\right) \quad\quad 23$$

$$\beta_2(n) = 90 - \left(\propto +\frac{VFOV}{2} - \frac{(n-1) \cdot VFOV}{number\ of\ pixels}\right) \quad\quad 24$$

$$RGSD_H(n) = \frac{x_2(n) \cdot \sin\left(\frac{FOV}{number\ of\ pixels}\right)}{\sin(\beta_1(n))} \quad\quad 25$$

56

$$LGSD_H(n) = \frac{y_2(n) \cdot \sin\left(\frac{FOV}{\text{number of pixels}}\right)}{\sin(\beta_2(n))}$$

26

$$RGSD_H(n) = \frac{h_f \cdot \sin\left[\frac{VFOV}{\text{number of pixels}}\right] \cdot 100}{\sin\left[\left(\frac{180 - (VFOV - 2\alpha)}{2}\right) + \left(\frac{VFOV \cdot (n-1)}{\text{number of pixels}}\right)\right] \cdot \sin\left[\left(\frac{180 - (2\alpha - VFOV)}{2}\right) - \left(\frac{VFOV \cdot n}{\text{number of pixels}}\right)\right]}$$

27

$$LGSD_H(n) = \frac{h_f \cdot \sin\left[\frac{VFOV}{\text{number of pixels}}\right] \cdot 100}{\sin\left[\left(\frac{180 - (VFOV + 2\alpha)}{2}\right) + \left(\frac{VFOV \cdot (n-1)}{\text{number of pixels}}\right)\right] \cdot \sin\left[\left(\frac{180 - (2\alpha + VFOV)}{2}\right) + \left(\frac{VFOV \cdot n}{\text{number of pixels}}\right)\right]}$$

28

$$r_{cn} = \frac{h_f}{\cos\left[\alpha - \left(\frac{VFOV}{2}\right)\right]}$$

29

$$r_{cf} = \frac{h_f}{\cos\left[\alpha + \left(\frac{VFOV}{2}\right)\right]}$$

30

The above equations were derived using basic trigonometric functions and sine rule. The variables seen in Equations 21-30 are defined as follows:

- $RGSD_H(n)$: Ground sampling distance (height) of the nth pixel from edge for the right plumb side in cm/px

- $LGSD_H(n)$: Ground Sampling Distance (height) of the nth pixel from edge for the left plumb side in cm/px

- n: Pixel number from the edge from 1 to image height/2

- h_f: Flight height in meters

- α: Camera pitch angle (90-α>FOV/2) in degrees

- VFOV: Vertical Field of View relates to the angle formed with the height of the image in degrees

- Number of pixels: The number of pixels that cover the height of the image, in pixels

- r_{cn}: Length of near center ray in meters (solid yellow line)

- r_{cf}: Length of far center ray in meters (dotted yellow line)

57

Figure 3.9 shows the cross-section (front view, green lines) of an oblique image with respect to the bottom line that lies along the bottom width of the image, and the breakdown of this view that helped in deriving the equation that calculates the distance covered by each pixel.
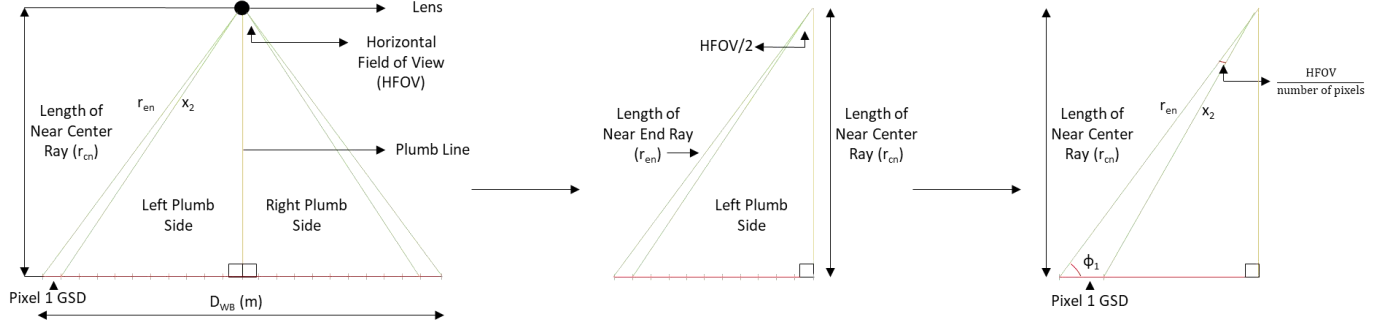
Figure 3.9: Front View of an Oblique Image with Respect to the Bottom Line Along Image Bottom Width

Using Figure 3.9, the equation of GSD of a pixel, along the bottom width, in an oblique image was derived in the following way (Equations 31-35).

$$x_2(n) = \frac{r_{cn}}{\sin\left(90 - \left(\frac{FOV}{2} - \frac{n \cdot HFOV}{\text{number of pixels}}\right)\right)} \tag{31}$$

$$\emptyset_1(n) = 90 - \left(\frac{FOV}{2} - \frac{(n-1) \cdot HFOV}{\text{number of pixels}}\right) \tag{32}$$

$$GSD_{WB}(n) = \frac{x_2(n) \cdot \sin\left(\frac{HFOV}{\text{number of pixels}}\right)}{\sin(\emptyset_1(n))} \tag{33}$$

$$GSD_{WB}(n) = \frac{r_{cn} \cdot \sin\left[\frac{HFOV}{\text{number of pixels}}\right] \cdot 100}{\sin\left[\left(\frac{180 - HFOV}{2}\right) + \left(\frac{HFOV \cdot (n-1)}{\text{number of pixels}}\right)\right] \cdot \sin\left[\left(\frac{180 - HFOV}{2}\right) + \left(\frac{HFOV \cdot n}{\text{number of pixels}}\right)\right]} \tag{34}$$

$$r_{en} = \frac{r_{cn}}{\cos\left[\left(\frac{HFOV}{2}\right)\right]} \tag{35}$$

The above equations were derived using basic trigonometric functions and sine rule. The variables seen in Equations 31-35 are defined as follows:

- $GSD_{WB}(n)$: Ground sampling distance of nth pixel (bottom width) from edge

58

- n: Pixel number from the edge from 1 to image width /2

- h_f: Flight height in meters

- Number of pixels: The number of pixels that cover the height of the image, in pixels

- HFOV: Horizontal Field of View relates to the angle formed with the width of the image in degrees

- r_{en}: Length of near-end ray in meters (solid green line)

- r_{cn}: Length of near center ray in meters (solid yellow line)

Figure 3.10 shows the cross-section (back view, brown lines) of an oblique image with respect to the top line that lies along the top width of the image, and the breakdown of this view that helped in deriving the equation that calculates the distance covered by each pixel.
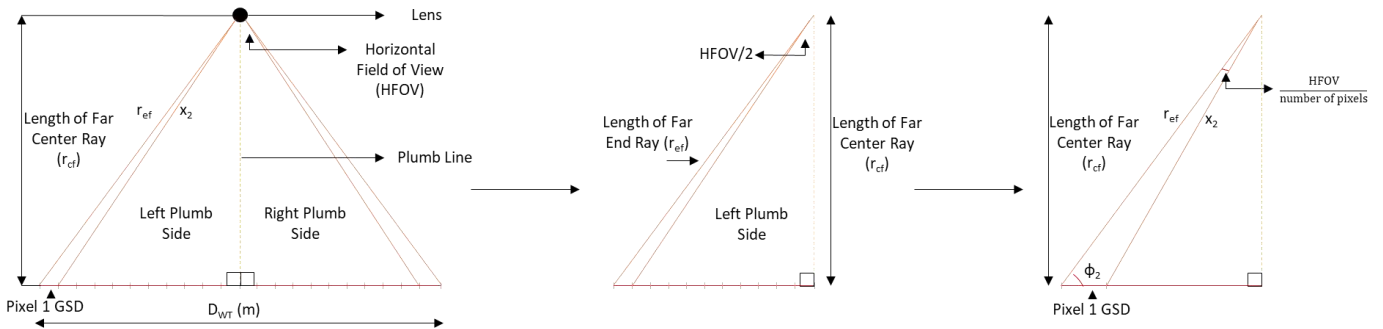
Figure 3.10: Back View of an Oblique Image with Respect to the Top Line Along Image Top Width

Using Figure 3.10, the equation of GSD of a pixel, along the top width, in an oblique image was derived in the following way (Equations 36-40).

$$x_2(n) = \frac{r_{cf}}{\sin\left(90 - \left(\frac{FOV}{2} - \frac{n \cdot HFOV}{\text{number of pixels}}\right)\right)} \qquad 36$$

$$\emptyset_2(n) = 90 - \left(\frac{HFOV}{2} - \frac{(n-1) \cdot HFOV}{\text{number of pixels}}\right) \qquad 37$$

59

$$GSD_{WT}(n) = \frac{x_2(n) \cdot \sin\left(\frac{HFOV}{\text{number of pixels}}\right)}{\sin(\emptyset_2(n))}$$

38

$$GSD_{WT}(n) = \frac{r_{cf} \cdot \sin\left[\frac{HFOV}{\text{number of pixels}}\right] \cdot 100}{\sin\left[\left(\frac{180 - HFOV}{2}\right) + \left(\frac{HFOV \cdot (n-1)}{\text{number of pixels}}\right)\right] \cdot \sin\left[\left(\frac{180 - HFOV}{2}\right) + \left(\frac{HFOV \cdot n}{\text{number of pixels}}\right)\right]}$$

39

$$r_{ef} = \frac{r_{cf}}{\cos\left[\left(\frac{HFOV}{2}\right)\right]}$$

40

The above equations were derived using basic trigonometric functions and sine rule. The variables seen in Equations 36-40 are defined as follows:

- $GSD_{WT}(n)$: Ground sampling distance of nth pixel (top width) from edge

- n: Pixel number from the edge from 1 to image width /2

- h_f: Flight height in meters

- Number of pixels: The number of pixels that cover the height of the image, in pixels

- HFOV: Horizontal Field of View relates to the angle formed with the width of the image in degrees

- r_{ef}: Length of far end ray in meters (solid brown line)

- r_{cf}: Length of far center ray in meters (dotted yellow line)

Using the camera parameters for the DJI XTR camera and flight height of 20 meters and a pitch angle of 20° the GSD values for each pixel vs the pixel number were plotted as shown in Figure 3.11.

The plot in Figure 3.11 shows that the GSD value for an oblique image is not constant throughout the image and the GSD increases when location of the pixel analyzed moves further

away from the image's centerline. The average GSD of an oblique image can be calculated by integrating the derived equations.
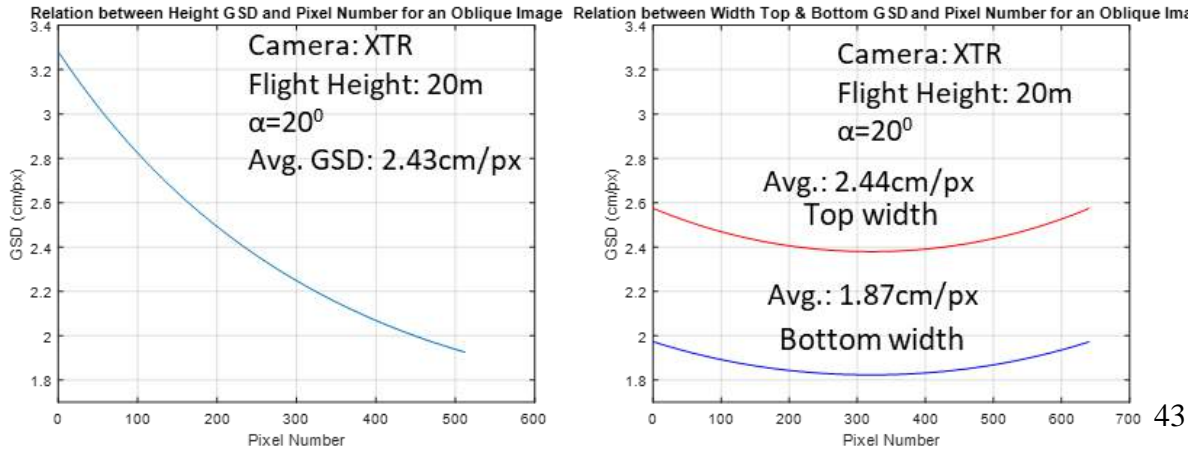
Figure 3.11: Relation Between GSD Value Per Pixel vs. Pixel Number for an Oblique Image for DJI XTR Camera where hf = 20m and α=20°

Using Figures 3.8, 3.9 and 3.10 the equation for distance/footprint (height and width) covered by an oblique image was derived in the following way (Equations 41-43).

$$D_h = \sqrt{r_{en}^2 + r_{ef}^2 + 2 \cdot r_{en} \cdot r_{ef} \cdot \cos{(VFOV)}}$$
$$\text{41}$$

$$D_{wb} = 2 \cdot r_{en} \cdot \tan\left(\frac{HFOV}{2}\right)$$
$$\text{42}$$

$$D_{wt} = 2 \cdot r_{ef} \cdot \tan\left(\frac{HFOV}{2}\right)$$

The above equations were derived using basic trigonometric functions and cosine rule. The variables seen in Equations 41-43 are defined as follows:

- VFOV: Vertical Field of View, the angle formed with height of the image in degrees

- HFOV: Horizontal Field of View, the angle formed with width of the image in degrees

- r_{en}: Length of near-end ray in meters (solid green line in Figure 3.9)

- r_{ef}: Length of far end ray in meters (solid brown line in Figure 3.10)

3.3.1.2 Effect of Varying GSD on 3D Point Clouds Accuracies

This section presents the results obtained to study the effect of varying GSD values, on the planimetric measurement accuracies, recorded using a 3D point cloud. The section is divided into three paragraphs where the first paragraph presents information about the experiment setup and the data captured, the second paragraph presents the processed output and the compiled accuracy results, and the third paragraph presents the conclusion obtained.

The test was conducted at an empty field beside i75 in the city of Toledo, Ohio. Five objects of known dimensions were laid out in the mapped region. These objects included vinyl targets of varying sizes and a metal ruler. Figure 3.12 shows the illustrations of these objects along with the measurements recorded on-field and their images. Images of the field were captured using the DJI X5 camera and the DJI M100 sUAS. Images were captured in a grid pattern with two different GSD values, 1cm/px and 2cm/px, keeping all the other flight parameters the same. Figure 3.13 shows screenshots obtained using the GeoSetter application showing the image locations of the two datasets, on a map.

On-field Measurements																		
Number	1	2	3	4	5	6	7	8	9	10	11	12	13	14	15	16	17	18
Name	S1 - S2	S2-S3	S3-S4	S4-S1	Long	Small	M1 - M2	M2-M3	M3-M4	M4-M1	M2 1-M2 2	M2 2-M2 3	M2 3-M2 4	M2 4-M2 1	L1-L2	L2-L3	L3-L4	L4-L1
Value (ft)	2.58	2.6	2.63	2.58	2	1.33	9.67	7.83	9.88	7.67	7.75	9.65	7.71	9.71	12.1	19.79	12.17	19.81
Object	Small Target				Metal Ruler		Medium Target 1				Medium Target 2				Large Target			
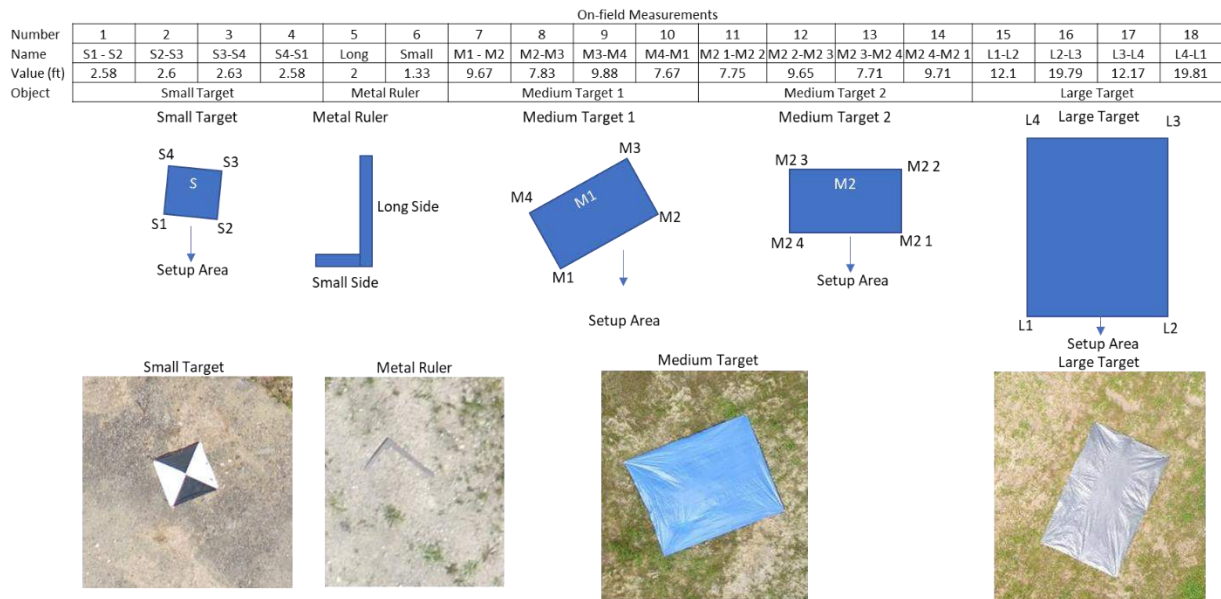
Figure 3.12: i75 Experiment Test Objects and Measurements
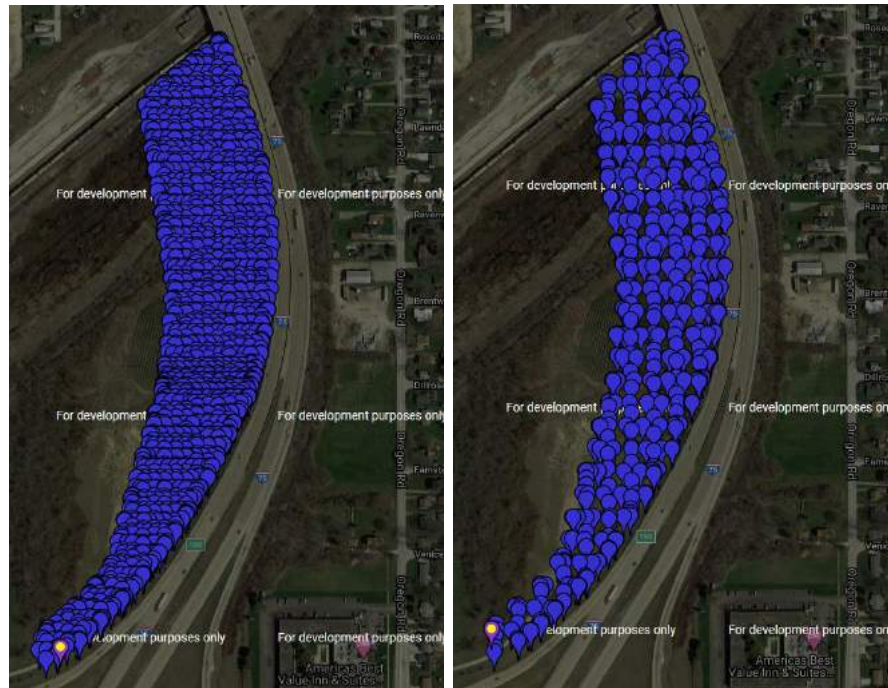
Figure 3.13: Image Locations; Left: 1cm/px Dataset, Right: 2cm/px Dataset

The datasets were processed separately using Pix4D Mapper without any GCPs and with their

geotags. The models were processed using the default 3D model template available on Pix4D

Mapper. The generated 3D point clouds met the required quality checks recommended by Pix4D

Mapper and were shown in the quality report. The generated 3D point clouds were analyzed by

measuring the objects laid out in the field using the polyline line tool and the computed values

were compared to the values recorded on the field. Figure 3.14 shows the 3D point cloud

generated using the 1cm/px dataset. Figure 3.15 shows the 3D point cloud generated using the

2cm/px dataset. The plots in Figure 3.16 show the individual absolute error measurements, and

their mean absolute and root mean square errors.
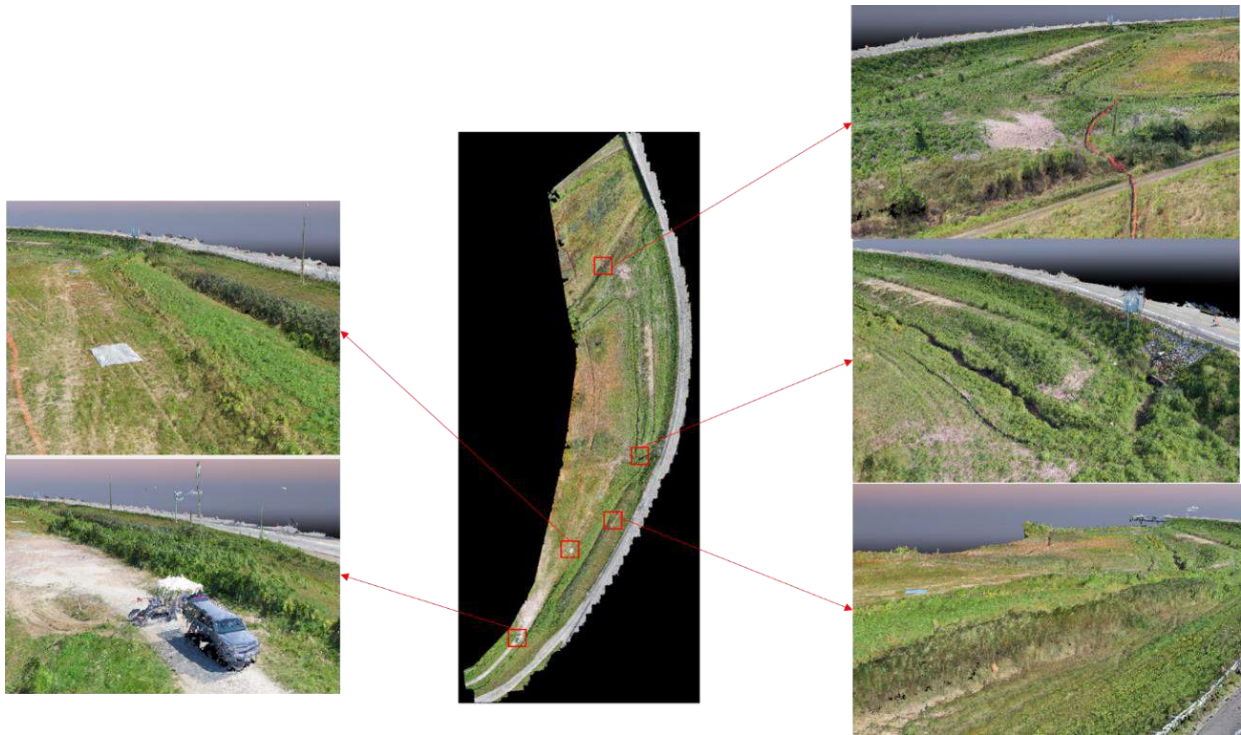
Figure 3.14: 3D Point Cloud Generated Using 1cm/px GSD Dataset

Figure 3.15: 3D Point Cloud Generated Using 2cm/px GSD Dataset
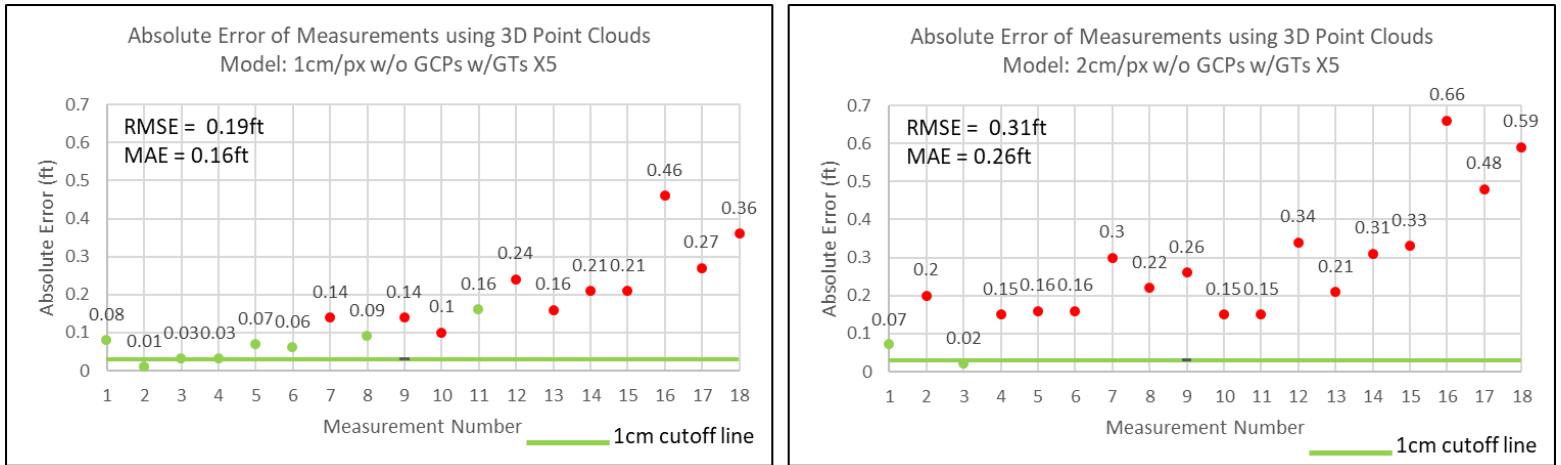
Figure 3.16: Absolute Error Measurement Plots of Generated 3D Point Clouds

The results presented in Figure 3.16 clearly show that individual as well as average error values reduce as the GSD value reduces. This is mainly because the corners of the objects measured can be easily and accurately selected as the resolution of the objects in the image increase. Based on acceptable error values users will have to decide the required GSD values when planning automated missions, as the error values recorded are directly proportional to the GSD value.

3.3.1.3 Effect of Varying GSD on Temperature Measured using Thermal Images

This section presents the results obtained to study the effect of varying GSD values on the temperature accuracies recorded using thermal images and thermal orthomosaic. The section is divided into three paragraphs where the first paragraph presents information about the experiment setup and the data captured, the second paragraph presents the processed output and the compiled accuracy results, and the third paragraph presents the conclusion obtained.

The test was conducted at Air Master RC Flying Park an empty field in North Bend, Ohio. The objective of this experiment was to compare the temperatures obtained using an IR Thermometer and the temperatures obtained using thermal images at varying GSDs. Temperatures of various

objects in the field, a concrete slab, green grass, and a vinyl target, were recorded using FLUKE 62 Max+ infrared thermometer. The IR thermometer has an accuracy of ±1°C and a measurement range of -30°C to 650°C [76]. Thermal images of the field were captured at 4 different GSD values (4cm/px, 4.4cm/px, 5.4cm/px, and 8.5 cm/px) using the DJI XTR camera and the DJI M100 sUAS. The obtained thermal images were analyzed and processed using FLIR Tools and Pix4D Mapper. Pix4D Mapper was used to generate thermal orthomosaics and the temperatures of the various objects were measured using Pix4D Mapper. FLIR Tools was used to analyze individual images and measure the temperature of analyzed objects. The emissivity was set to 0.94 (emissivity value for dry concrete [77], [78]) in both the IR thermometer and DJI XTR camera. The temperature of the objects was measured using the IR thermometer before each flight and is shown in Figure 3.17, along with the visual images of the objects analyzed. The red circles in the visual images indicate the spot where the temperature was measured using the IR thermometer. Figure 3.18 shows the screenshot obtained using the GeoSetter application showing the image locations of the 5.4cm/px dataset, on a map.

IR Thermometer On-field Measurements (in degree Celsius)				
Objects	GSD: 4cm/px	GSD: 4.4cm/px	GSD: 5.4cm/px	GSD: 8.5cm/px
Dry Concrete	36.11°C	38.33°C	37.22°C	24.22°C
Green Grass	32.24°C	34.98°C	30.56°C	19.11°C
Vinyl Target	35.81°C	36.67°C	31.11°C	13.11°C

Figure 3.17: Air Masters Experiment Test Objects and Measurements

66

Figure 3.18: Image Locations of the 5.4cm/px Dataset

The datasets were processed separately using Pix4D Mapper without any GCPs and with their

geotags and also analyzed using FLIR Tools. The models were processed using the default

thermal image template available on Pix4D Mapper. The generated outputs met the required

quality checks recommended by Pix4D Mapper and were shown in the quality report. The

generated 2D orthomosaics were analyzed by measuring the temperatures using the available

Pix4D tools and were compared to the values recorded on the field. Figure 3.19 shows the 2D

orthomosaic generated using the 5.4cm/px dataset and the temperature scale of the orthomosaic.

Figure 3.20 shows the breakdown of orthomosaic and temperature measurements obtained for

each of the objects using Pix4D Mapper. Pix4D Mapper allows users to select regions of interest

and scale the temperature bar bases on the selected region. Figure 3.21 shows the analysis of the

5.4cm/px dataset and the measurements recorded using FLIR tools. The box measurement tool

available in FLIR Tools was used to measure the temperature values. The plots in Figure 3.22

show the absolute error measurements of the temperature recorded using Pix4D Mapper and FLIR Tools. Each plot shows the trend in temperature error values recorded for each object (concrete, green grass, and vinyl target) with varying GSD values.
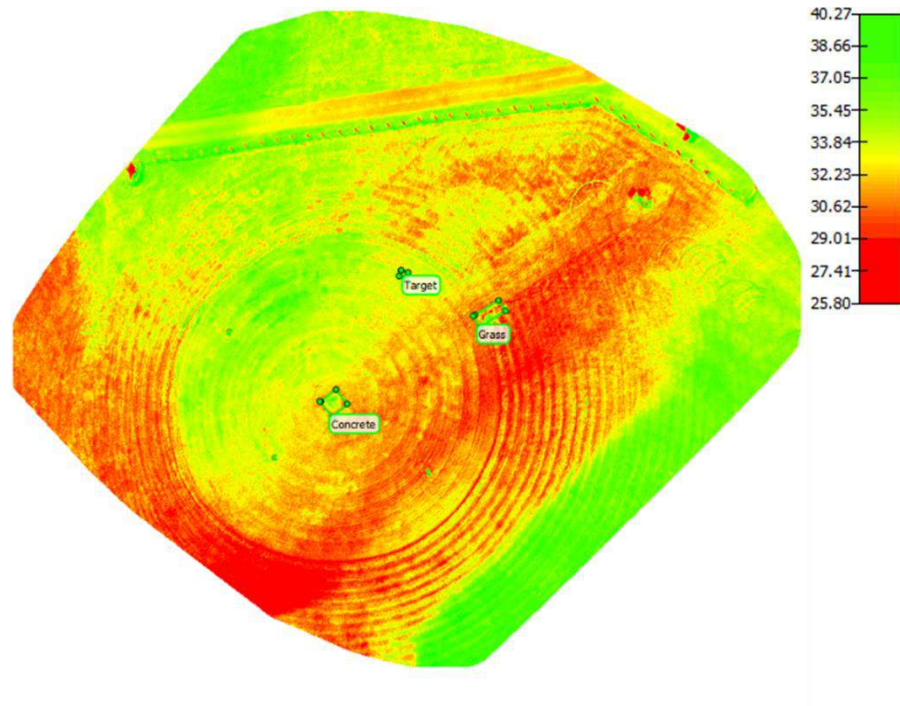
Figure 3.19: Thermal Orthomosaic of the 5.4cm/px Dataset Generated Using Pix4D Mapper
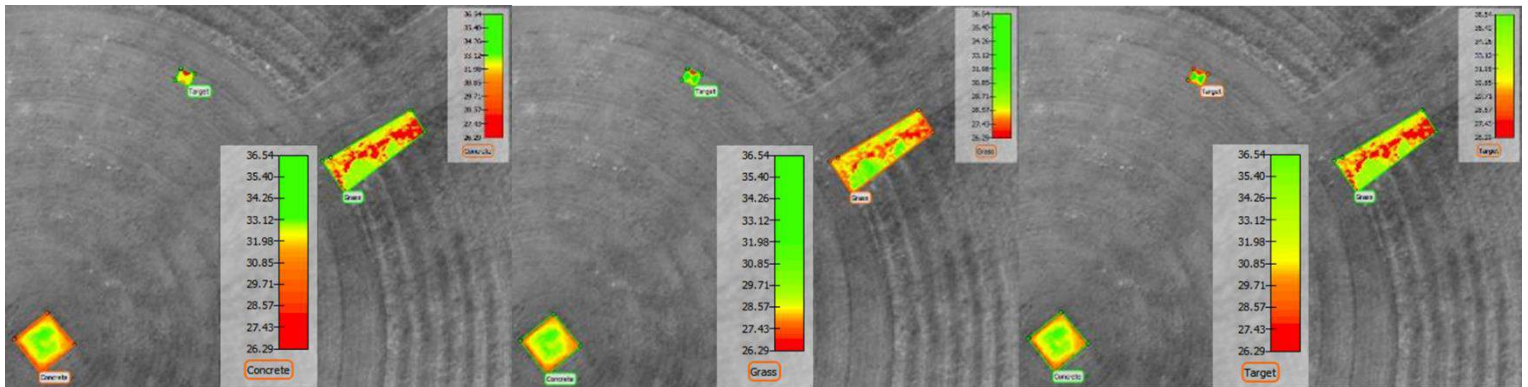
Figure 3.20: Breakdown of the Thermal Orthomosaic of the 5.4cm/px Dataset Using Pix4D Mapper
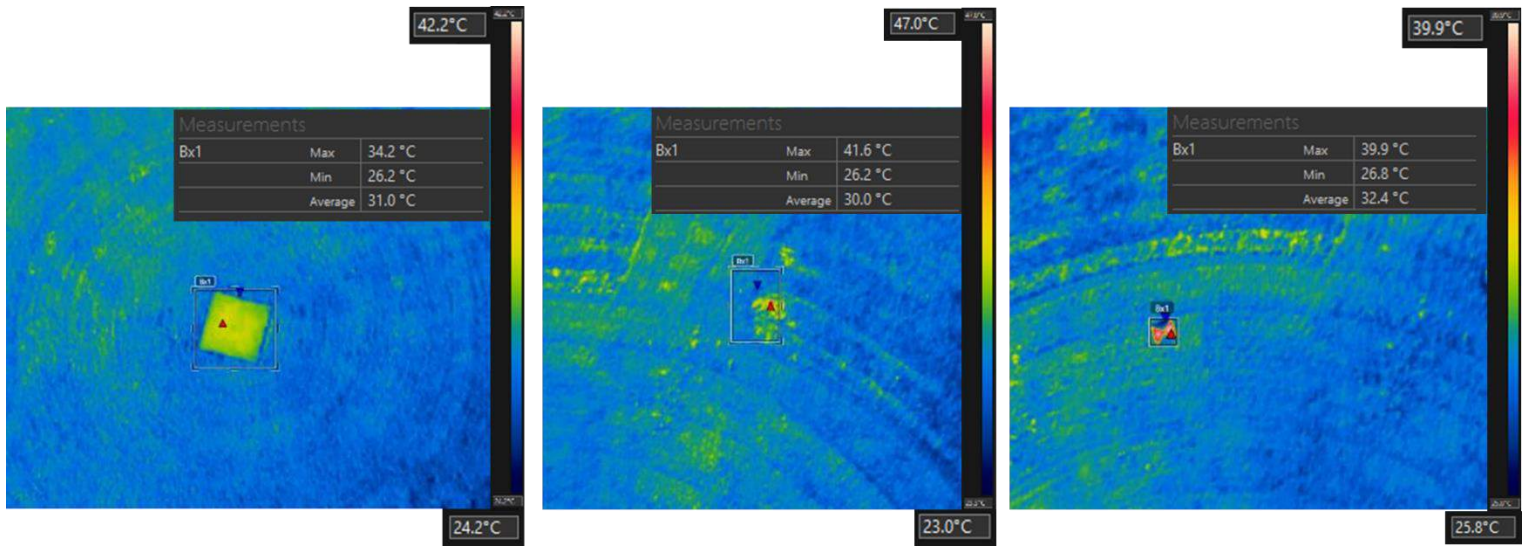
Figure 3.21: Analysis of Individual 5.4cm/px Thermal Dataset Using FLIR Tools
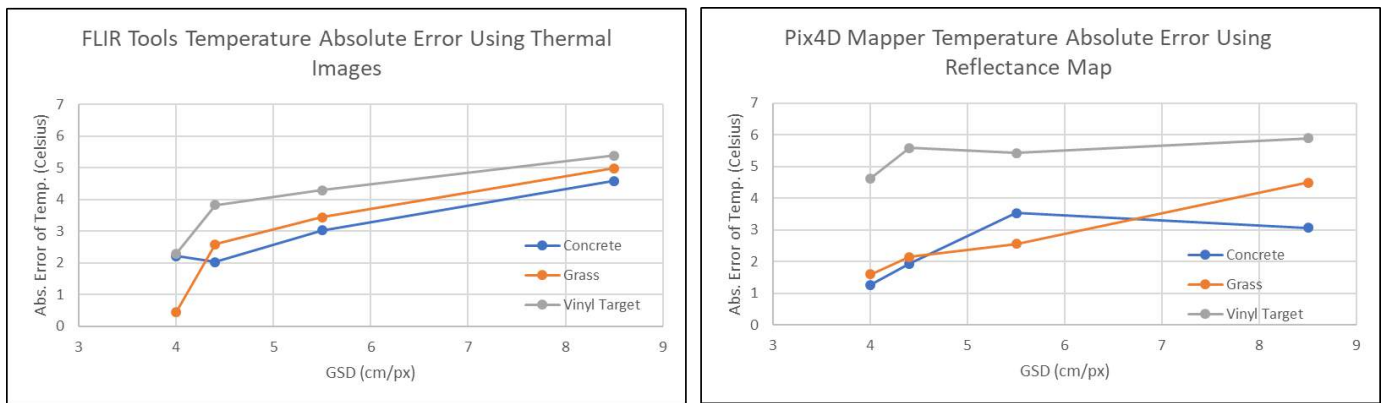
Figure 3.22: Absolute Error Plots of 5.4cm/px Thermal Dataset; Left: FLIR Tools Error Analysis, Right: Pix4D Mapper Error Analysis

The results presented in Figure 3.22 clearly show that individual temperature error values increase as the GSD value increases. A thermal image of a surface provides the radiometric temperature measurement for each pixel. As the GSD increases, measuring the temperature of different points on the surface will become exceedingly difficult since the number of pixels covering the surface diminishes. Based on acceptable error values users will have to decide the required GSD values when planning automated missions, as the error values recorded are directly proportional to the GSD value.

3.3.1.4 Effect of Varying GSD in Detecting Defects using Thermal Images

This section presents the results obtained to study the effect of varying GSD values, in detecting defects using thermal images and as an extension to understand the effect of spot size with varying GSD values. The spot-size effect causes degradation in measurement accuracy because of optical distortion, diffraction, stray light, and sensor image processing that result in a washed-out image. Not accounting for the spot-size effect will yield results that may be highly influenced by nearby surfaces [71]. To negate the effects of spot size, the desired region of interest in the image should cover at least 10 pixels [71]. In other words, to know the temperature value of a region or to distinguish a region clearly in a thermal image (without the interference of spot size) that covers 6", the region should be covered by at least 10 pixels, where the GSD required needs to be set as; 15.24cm/10pixels = 1.5cm/px. The section is divided into three paragraphs where the first paragraph presents information about the experiment setup and the data captured, the second paragraph presents the processed output and the compiled accuracy results, and the third paragraph presents the conclusion obtained.

As seen in the previous section GSD influences the temperature measured in thermal images. As an extension, this in turn, affects the contrast of the thermal images and the ability to identify unusual temperature differences. The test was conducted at Fosters bridge in Mainville, Ohio. Oblique thermal images with varying GSDs (1.89cm/px, 2.05cm/px, 2.27cm/px, 2.34cm/px, 2.45cm/px, 2.64cm/px, 2.81cm/px, 2.86cm/px, 3.02cm/px, 3.27cm/px, 3.39cm/px, 3.68cm/px, and 3.74cm/px) were collected and analyzed to detect unusual temperature changes, indicating the presence of delamination. Thermal images of the bridge deck were analyzed to visually compare the density of the identified defects for the extreme GSD cases (1.89 cm/px and 3.39cm/px) and the detection of defects of varying sizes ($1.8m^2$, $1m^2$, $0.76m^2$, $0.5m^2$, $0.18m^2$)

were compared for each GSD case. The bridge was manually inspected, by an ODOT inspector, using the chain dragging method and the detected delaminations were marked in white paint. The markings on the bridge's deck were used to compare the defects identified using thermal images.

The obtained thermal images were analyzed using FLIR Tools and the detected defects were marked on the visual orthomosaic of the deck. Figures 3.23 and 3.24 show the marked visual orthomosaics using the information obtained by analyzing the 1.89cm/px and 3.39cm/px dataset. Thermal images of varying GSDs, covering selective regions of the defect, were analyzed separately. Figures 3.25 – 3.29 show the screenshots of thermal images (of varying GSDs) covering delaminated areas of varying sizes with their visual image.
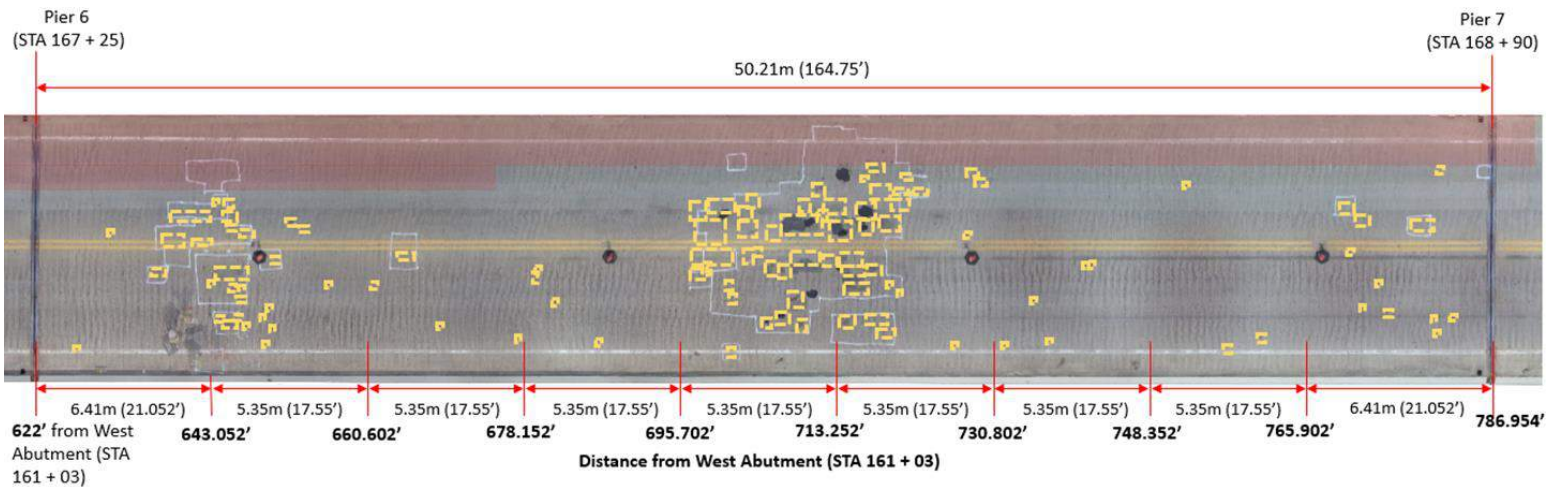
Figure 3.23: Defects Detected Using Thermal Images with a GSD of 1.89cm/px Marked on the Bridge Deck's Visual Orthomosaic
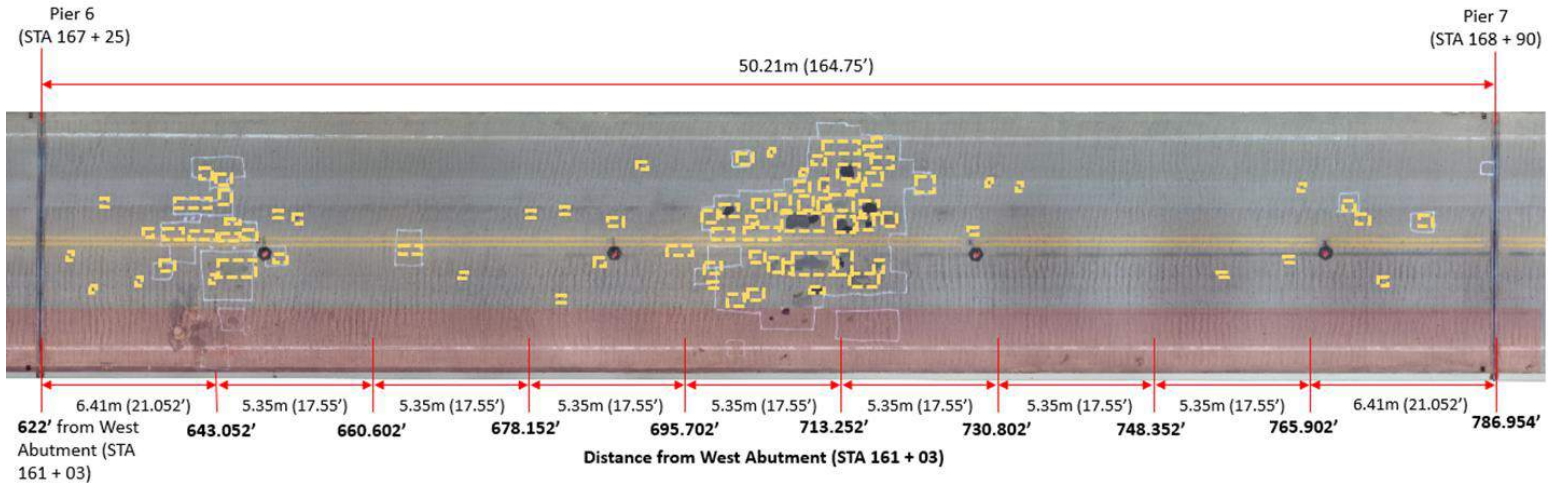
Figure 3.24: Defects Detected Using Thermal Images with a GSD of 3.39cm/px Marked on the Bridge Deck's Visual Orthomosaic

1.89cm/px 2.05cm/px 2.27cm/px 2.34cm/px 2.45cm/px

2.64cm/px 2.81cm/px 2.86cm/px 3.02cm/px 3.27cm/px

3.39cm/px 3.68cm/px 3.74cm/px

Area covered by defect = 1.8m²/19.4ft²
Visual Image of Area Shown Above
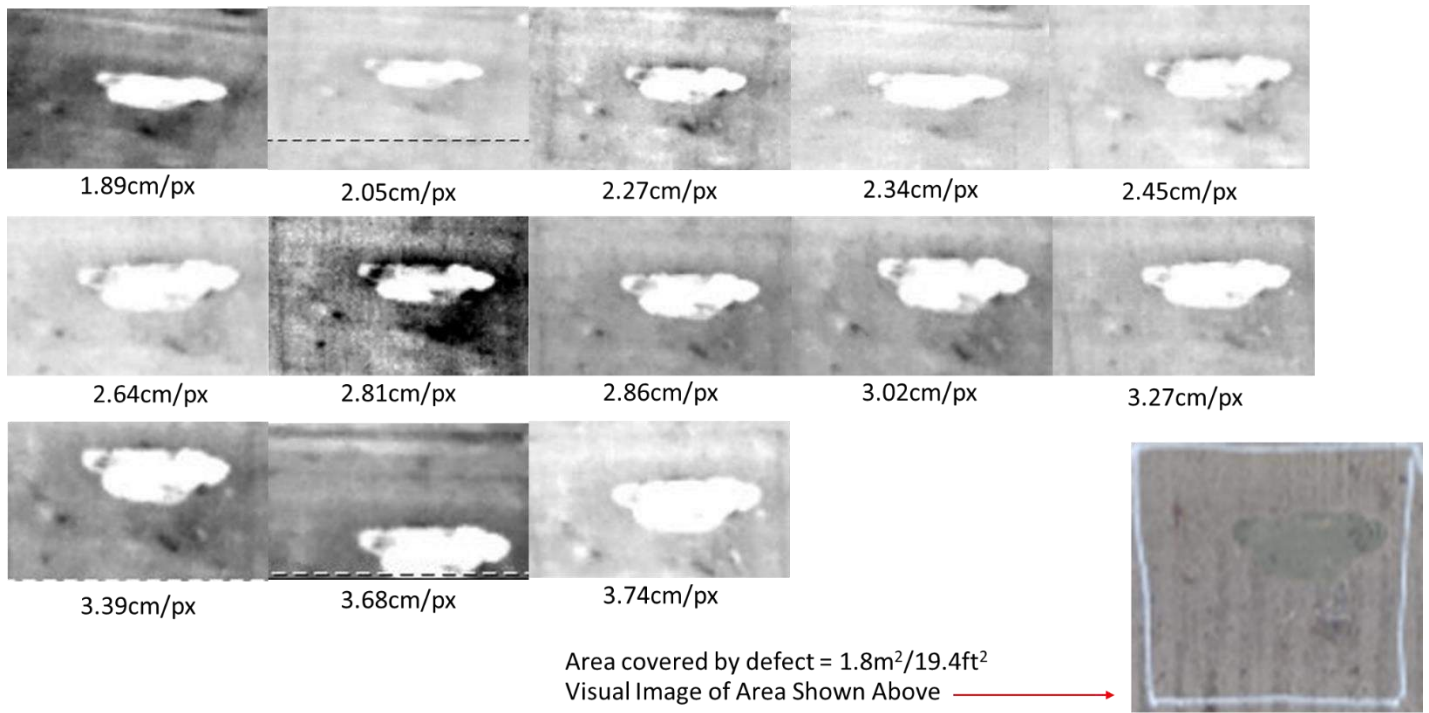
Figure 3.25: Analysis of Thermal Images with Varying GSDs for a Defective Area of 1.8m^2

1.89cm/px   2.05cm/px   2.27cm/px   2.34cm/px   2.45cm/px

2.64cm/px   2.81cm/px   2.86cm/px   3.02cm/px   3.27cm/px

3.39cm/px   3.68cm/px   3.74cm/px

Area covered by defect = 1m^2/10.8ft^2
Visual Image of Area Shown Above
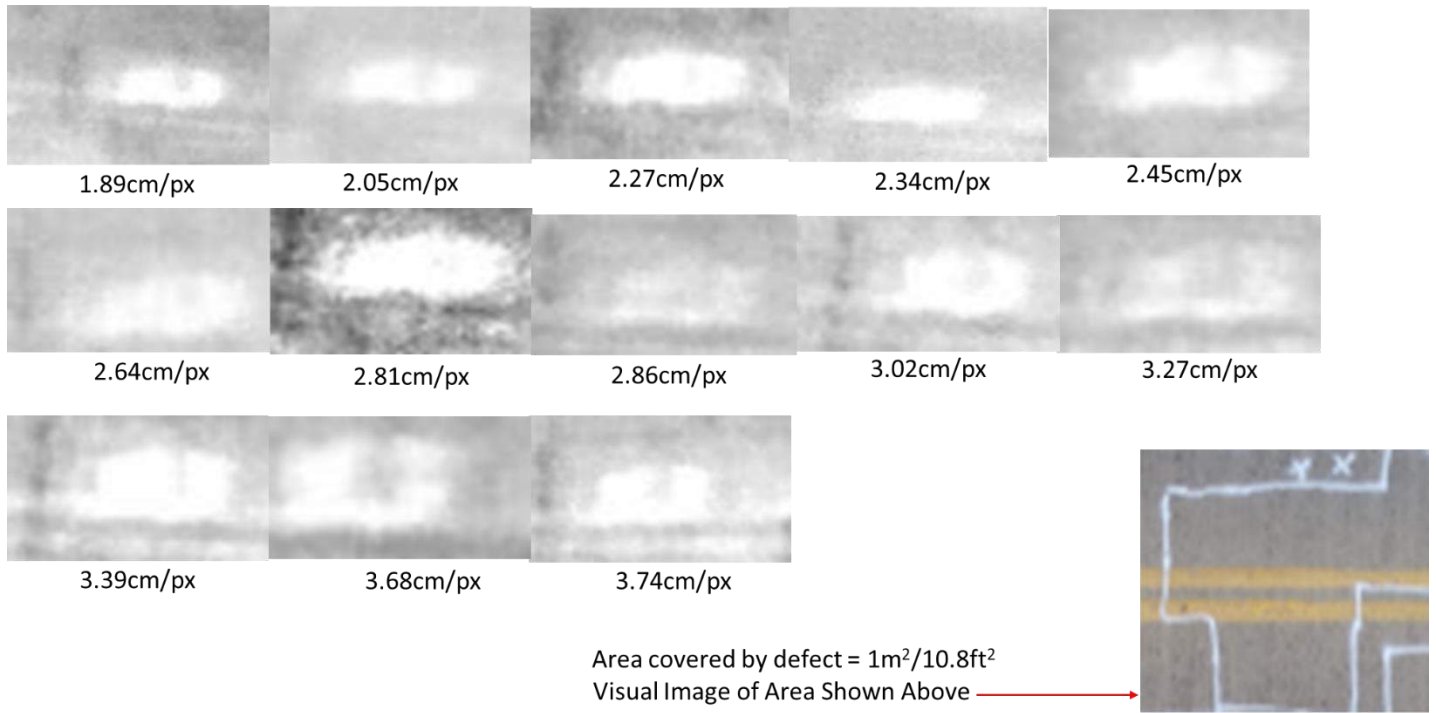
Figure 3.26: Analysis of Thermal Images with Varying GSDs for a Defective Area of 1m^2

1.89cm/px   2.05cm/px   2.27cm/px   2.34cm/px   2.45cm/px

2.64cm/px   2.81cm/px   2.86cm/px   3.02cm/px   3.27cm/px

3.39cm/px   3.68cm/px   3.74cm/px

Area covered by defect = 0.76m^2/8.14ft^2
Visual Image of Area Shown Above
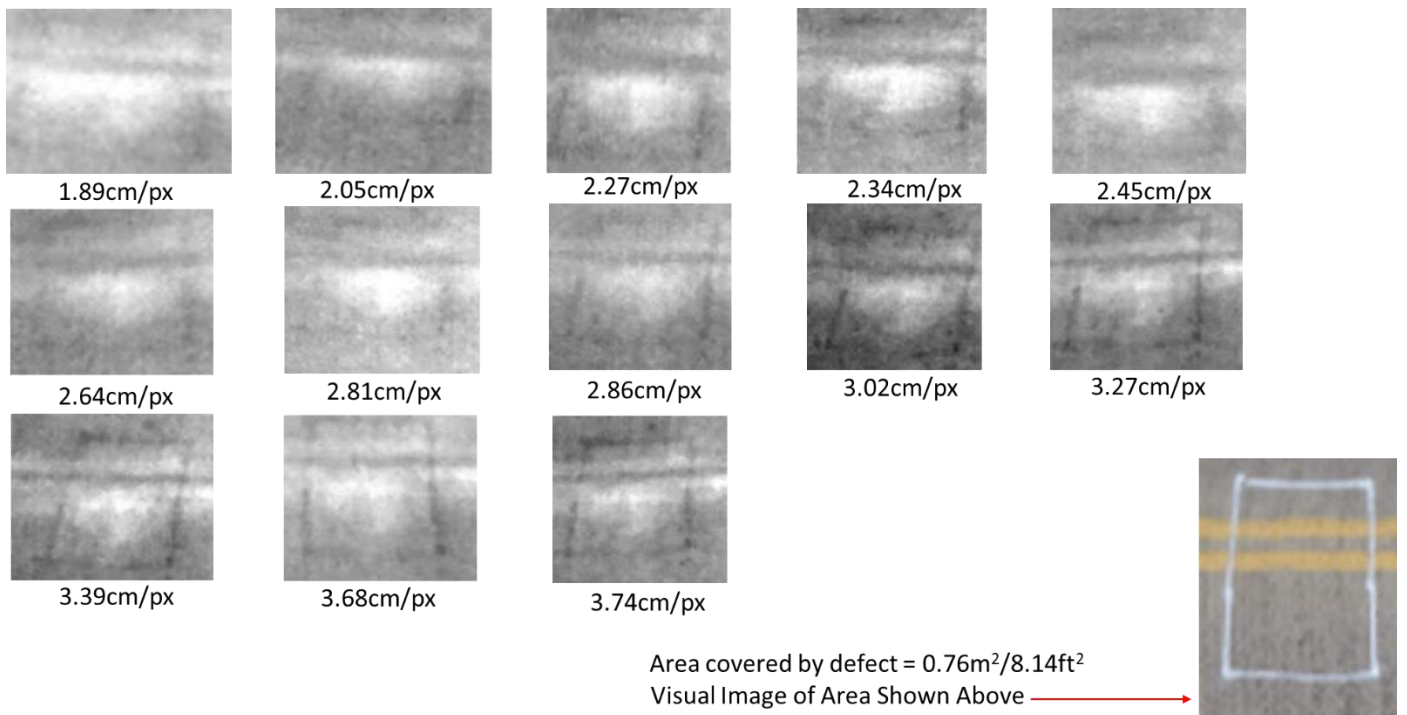
Figure 3.27: Analysis of Thermal Images with Varying GSDs for a Defective Area of 0.76m^2

73

1.89cm/px   2.05cm/px   2.27cm/px   2.34cm/px   2.45cm/px

2.64cm/px   2.81cm/px   2.86cm/px   3.02cm/px   3.27cm/px

3.39cm/px   3.68cm/px   3.74cm/px

Area covered by defect = $0.5m^2/5.38ft^2$
Visual Image of Area Shown Above
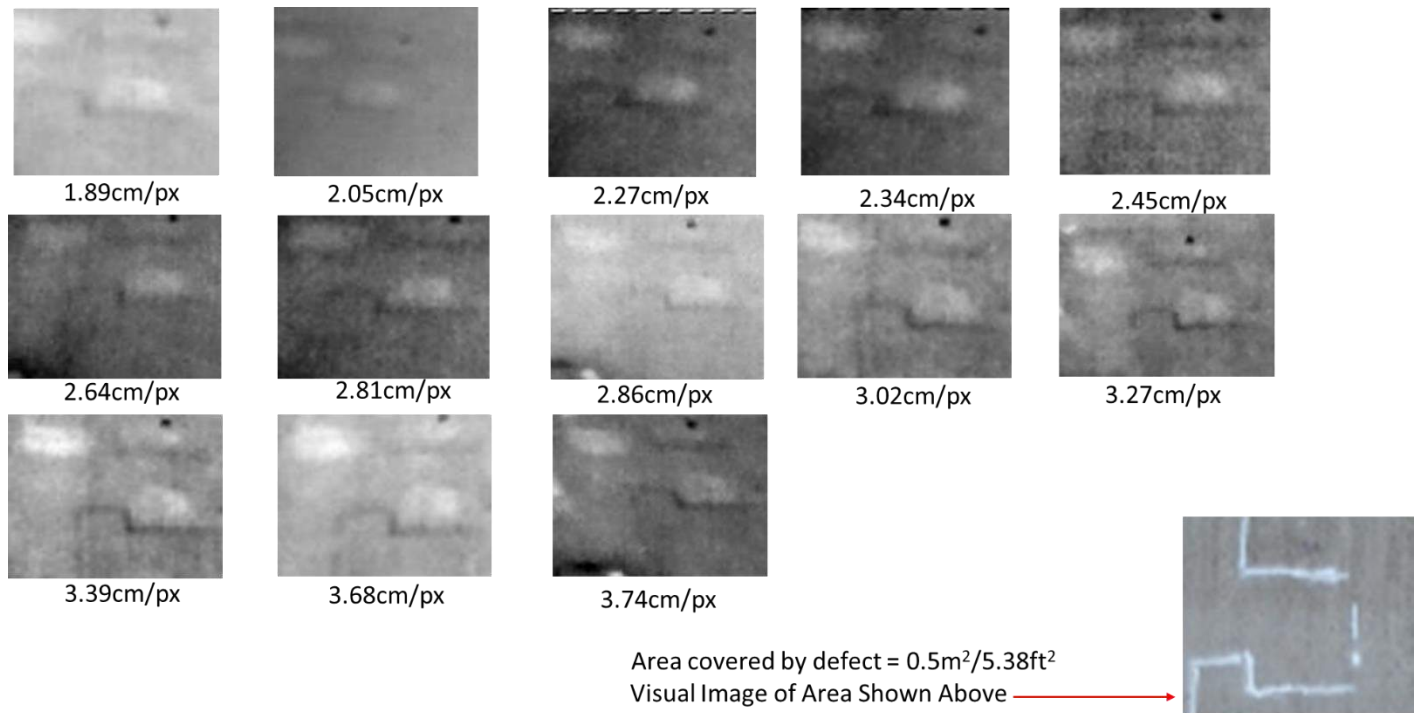
Figure 3.28: Analysis of Thermal Images with Varying GSDs for a Defective Area of $0.5m^2$

1.89cm/px   2.05cm/px   2.27cm/px   2.34cm/px   2.45cm/px

2.64cm/px   2.81cm/px   2.86cm/px   3.02cm/px   3.27cm/px

3.39cm/px   3.68cm/px   3.74cm/px

Area covered by defect = $0.18m^2/1.43ft^2$
Visual Image of Area Shown Above
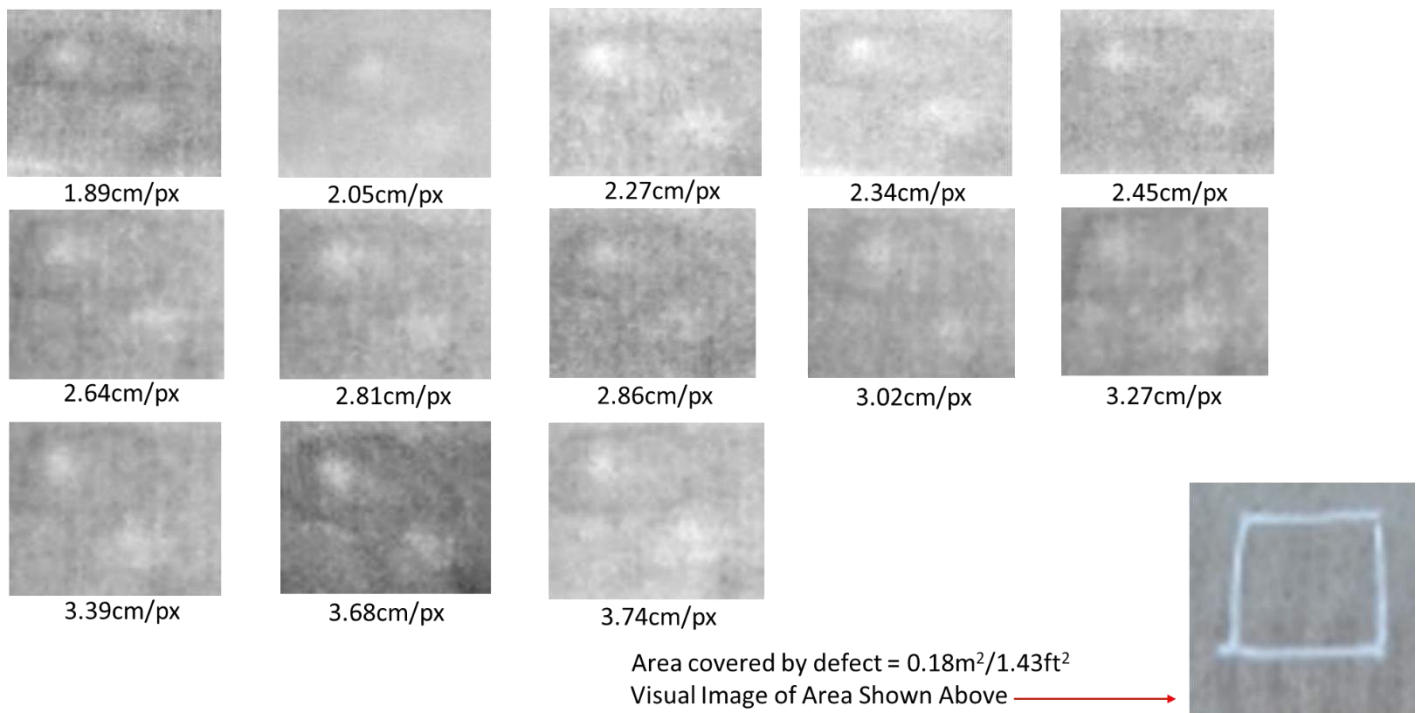
Figure 3.29: Analysis of Thermal Images with Varying GSDs for a Defective Area of $0.18m^2$

Analyzing the data compiled in Figures 3.23 and 3.24, show that most of the defects detected using the 1.89cm/px dataset were also detected using the 3.39cm/px dataset. This shows that thermal images captured at GSDs greater than 1.5cm/px (to negate spot size effect) can still be used to detect unusual temperature changes/defects with relative ease. This is further supported by the data presented in Figures 3.25-3.29. Figure 3.29 shows thermal images with GSDs greater than 1.5cm/px, covering regions greater than 6", can still be used to detect unusual temperature changes/defects.

3.3.2 Image Overlap Percentage

Image overlap percentage is the percentage of overlap between two images, i.e. the amount by which one image includes the area covered by the next image. There are two types of image overlaps in photogrammetry, front overlap and side overlap. The front overlap is the percentage of overlap between consecutive images captured in the same path of flight direction and side overlap is the percentage of overlap between images on consecutive flight paths as shown in Figure 2.34. This section presents the work conducted to derive the equation that calculates the overlap percentage that must be set in the flight planning application to compensate for mapping areas of varying elevations/terrain or with tall structures, as described in Figure 2.35.

3.3.2.1 Overlap Percentage Derivations

Figure 3.30 shows the illustration and the breakdown of the overlap between two nadir images above a structure with a defined height. The illustration in Figure 3.30 aided in deriving the equations below (Equations 44-51).
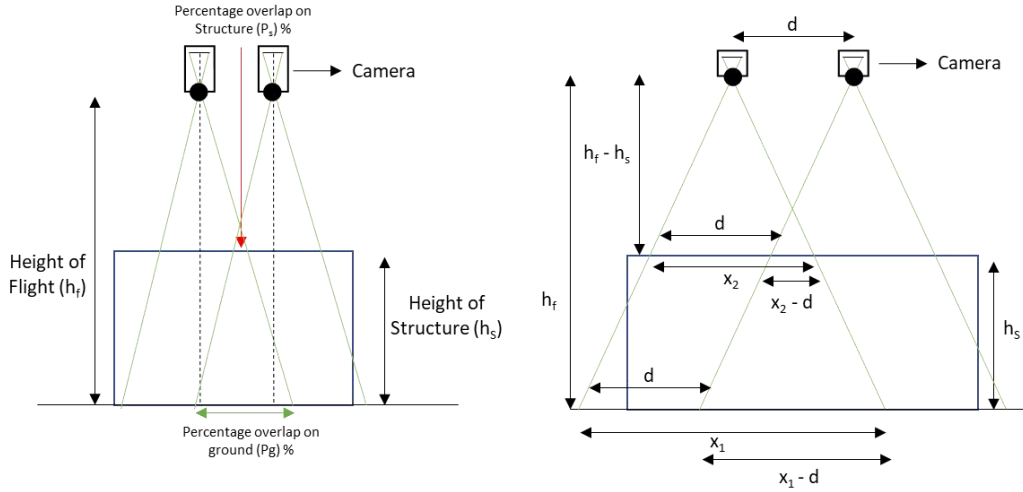
Figure 3.30: Illustration of Image Overlap Above a Tall Structure

$$\frac{x_1}{h_f} = \frac{x_2}{(h_f - h_s)} \qquad\qquad 44$$

$$x_2 = \frac{x_1 \cdot (h_f - h_s)}{h_f} \qquad\qquad 45$$

$$P_S = \frac{x_2 - d}{x_2} \qquad\qquad 46$$

$$P_S = \frac{\dfrac{x_1 \cdot (h_f - h_s)}{h_f} - d}{\dfrac{x_1 \cdot (h_f - h_s)}{h_f}} \qquad\qquad 47$$

$$P_g = \frac{x_1 - d}{x_1} \qquad\qquad 48$$

$$d = x_1\big(1 - P_g\big) \qquad\qquad 49$$

$$P_S = 1 - \frac{\big(1 - P_g\big)h_f}{(h_f - h_s)} \qquad\qquad 50$$

$$P_g = 1 - \frac{(1 - P_S)(h_f - h_s)}{h_f} \qquad\qquad 51$$

The above equations were derived using trigonometric functions. The variables seen in Equations 44-51 are defined as follows:

- h_f: Height at which image is captured or flight height in meters

- h_S: Height of tallest point or structure withing region of interest in meters

- P_S: Desired overlap between images on top of the structure for Equation 51; expected overlap between images on top of the structure for an overlap percentage set with respect to ground (P_g) in the flight planning application for Equation 50 in fractions

- P_g: Overlap that must be set in the flight planning application with respect to the ground compensated for the height change in the region of interest for Equation 51; overlap set in the flight planning application with respect to ground for Equation 50 in fractions

Using Equation 51 users can set the correct overlap percentage in the flight planning application, without overcompensating or under compensating, when mapping regions with tall structures or uneven terrains. Equation 51 was used to plan a mission to map a building where the take-off point was at its base. The height of the structure was approximated to 32m and the flight height was set to 52.3m (to achieve a GSD of 0.8cm/px on top of the structure). To achieve an 80% overlap on top of the structure the overlap on the flight application was set to 92%. Figure 3.31 shows the two consecutive images captured with this plan and the overlap estimated analyzing the images.

Front Overlap (%) = 2.29"/2.76" = 0.829
82.9% Front Overlap
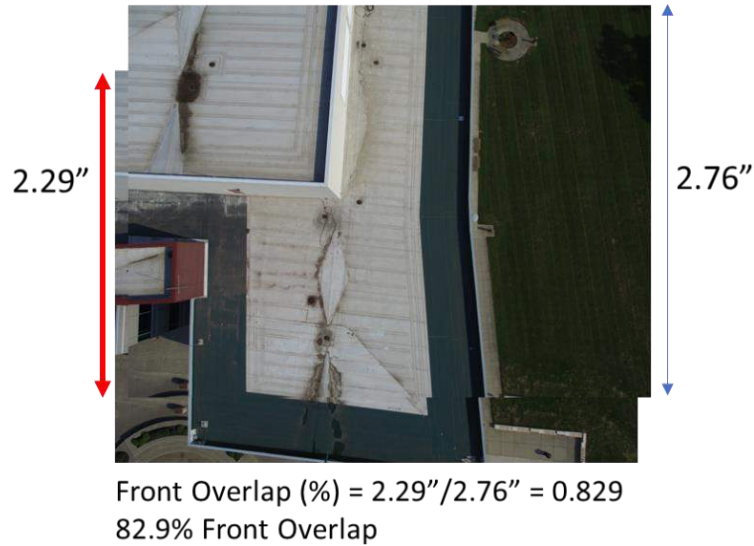
Figure 3.31: Image Overlap Estimation

Current flight planning applications do not have the functionality to automate the sUAS to map sides of buildings or bridges. Users will have to create separate missions at different altitudes that fly in straight lines along the side of the structure to replicate the suggested flight plans that capture the necessary images. Figure 3.32 shows the illustration used to derive the formula to achieve the desired side overlap when the face/side of a structure is mapped. Figure 3.33 shows the illustration used to derive the formula to calculate the height difference between flights to achieve the desired top & bottom overlap when the face/side of a structure is mapped. Using Equations 4 and 51 and Figures 3.32 and 3.33 the following formulas were derived (Equations 52-55).
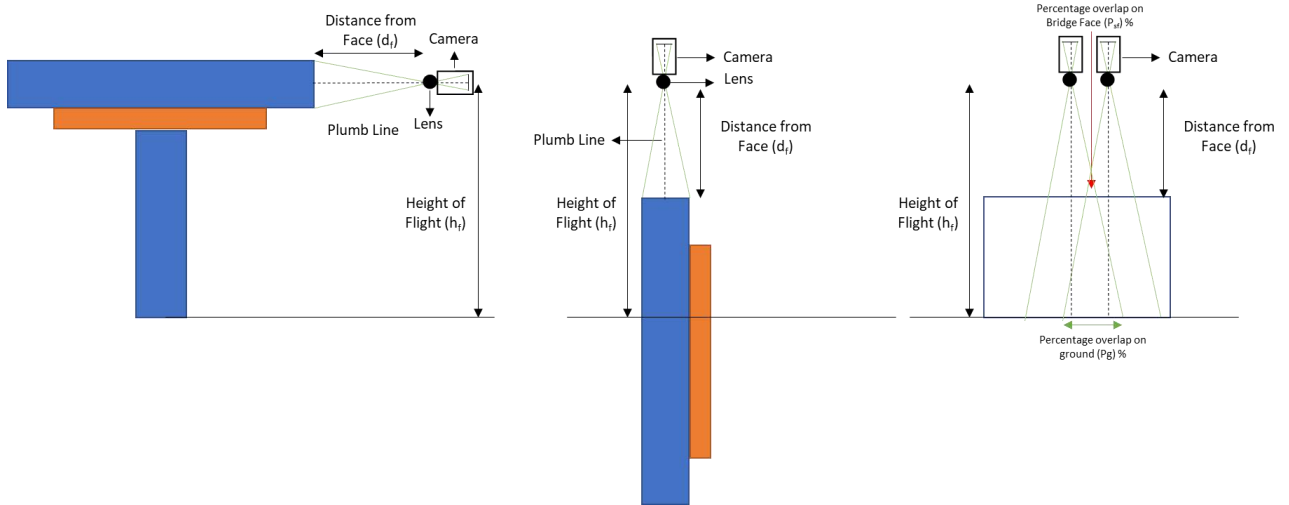
Figure 3.32: Illustration of Image Side Overlap When the Side/Face of a Structure is Mapped
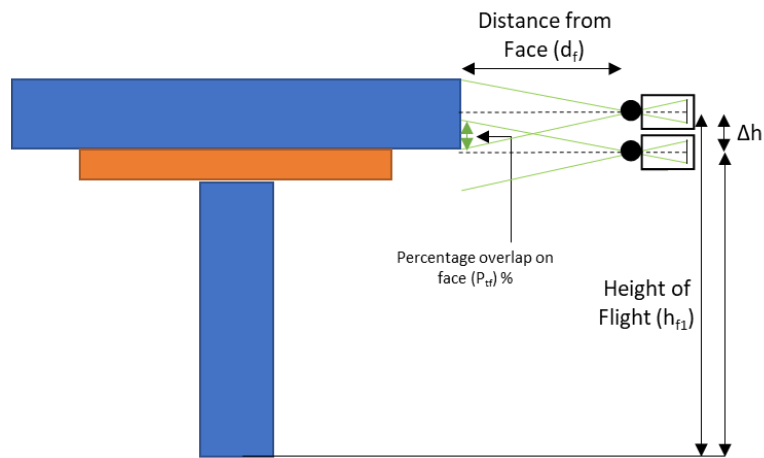
Figure 3.33: Illustration Used to Derive the Height Difference Between Flights to Achieve the Necessary Top & Bottom Overlaps

$$P_g = 1 - \frac{(1 - P_{sf})(d_f)}{h_f} \qquad 52$$

$$D_h = GSD \, . \, image_{height} \qquad 53$$

$$D_h = \frac{d_f \cdot sensor_{height}}{F_R} \qquad 54$$

$$\Delta h = D_h \cdot (1 - P_{tf}) \qquad 55$$

The variables seen in Equations 52-55 are defined as follows:

- h_f: Height at which image is captured or flight height in meters

- d_f: Distance from the face of the structure in meters

- P_{sf}: Desired overlap between images (side) on the face of the structure in fractions

- P_g: Overlap that must be set in the flight planning application with respect to the ground to get the desired side overlap in images of the structure's face in fractions

- P_{tf}: Desired overlap between images (top & bottom) on the face of the structure in fractions

- D_h: Distance covered by the image height in meters

- Δh: Height difference that must be set between two flights to get the desired top & bottom overlap between images in meters

Equations 52 and 55 were used to plan a mission to map the face of a bridge or building where the take-off point is at its base. Using a DJI X5s 15mm camera the flight height was set to 27.5m and the flight was 10m away from the face (to achieve a GSD of 0.2cm/px). To achieve an 80% side overlap on the face of the structure the overlap on the flight application was set to 92% and to achieve a front overlap of the 85% the height difference between two flights was set to 1.3m. Figure 3.34 shows the analyzed images captured with this plan with their overlaps estimated.

Side Overlap (%) = 3.01"/3.68" = 0.817   Top & Bottom Overlap (%) = 3.4"/2.76" = 0.87
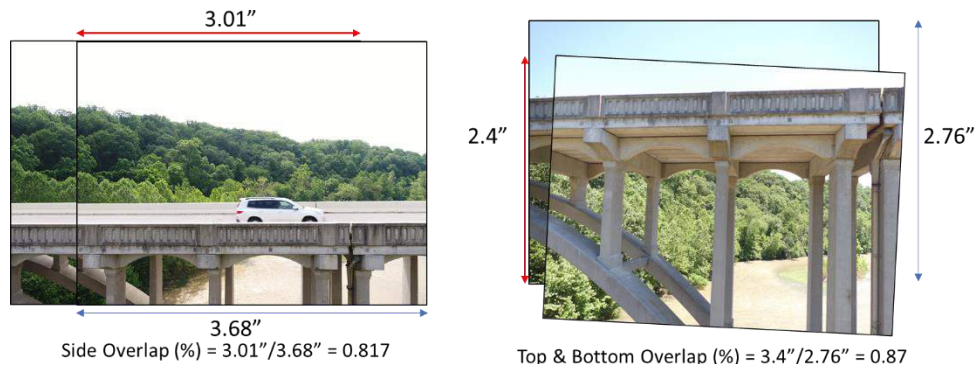
Figure 3.34: Image Overlap Estimations

3.3.3 Camera Triggering Interval

Camera triggering interval is the time elapsed between image capture. This option is available when the mode of capture is set to equal timed mode. This parameter is closely related to flight speed, image height, GSD and image overlap as shown in Equation 5. This section presents the work conducted to identify the effect of camera triggering interval on image capture using the DJI XTR and DJI X5 cameras.

3.3.3.1 Effect of Camera Triggering Interval on Capturing Images

This section presents the results obtained to study the effect of camera triggering interval on capturing images for a given set of flight parameters (GSD, image overlap and speed of flight). The section is divided into five paragraphs where the first three paragraph presents information about the experiment setup and the data captured, the fourth paragraph presents the compiled results, and the fifth paragraph presents the conclusion obtained.

The test was conducted at Air Master RC Flying Park an empty field in North Bend, Ohio. The DJI M100 sUAS and DJI XTR and X5 cameras were used to conduct this study. The minimum triggering interval for the sensor used in the DJI XTR camera (FLIR Tau 2 663) is 4 seconds [37], [79]. Whereas the DJI X5 user manual does not mention a minimum triggering interval for its sensor. The flowchart shown in Figure 3.35 describes the process followed to generate the characteristic surface plot for the DJI XTR and DJI X5 cameras. Figures 3.36 and 3.37 show the characteristic surface plots for the DJI XTR and X5 cameras respectively. Figures 3.38 and 3.39 show DJI XTR and X5's individual hyperplanes for triggering intervals 1 – 5 seconds.
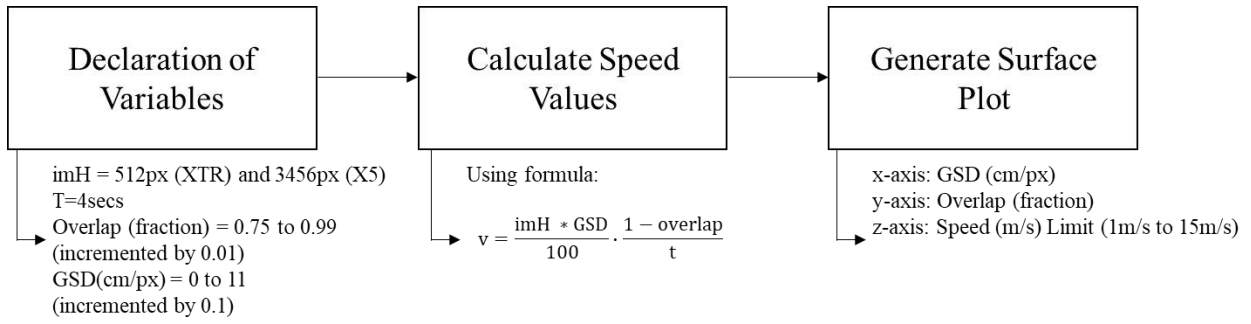
Figure 3.35: Flowchart of the Process Followed to Generate Characteristic Surface Plots
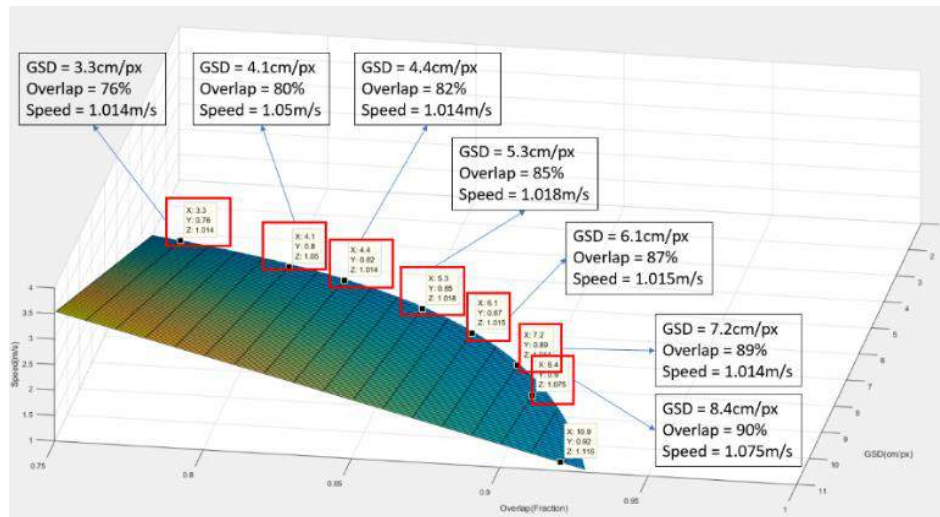
Figure 3.36: Characteristic Surface Plot for the DJI XTR Camera for t = 4sec
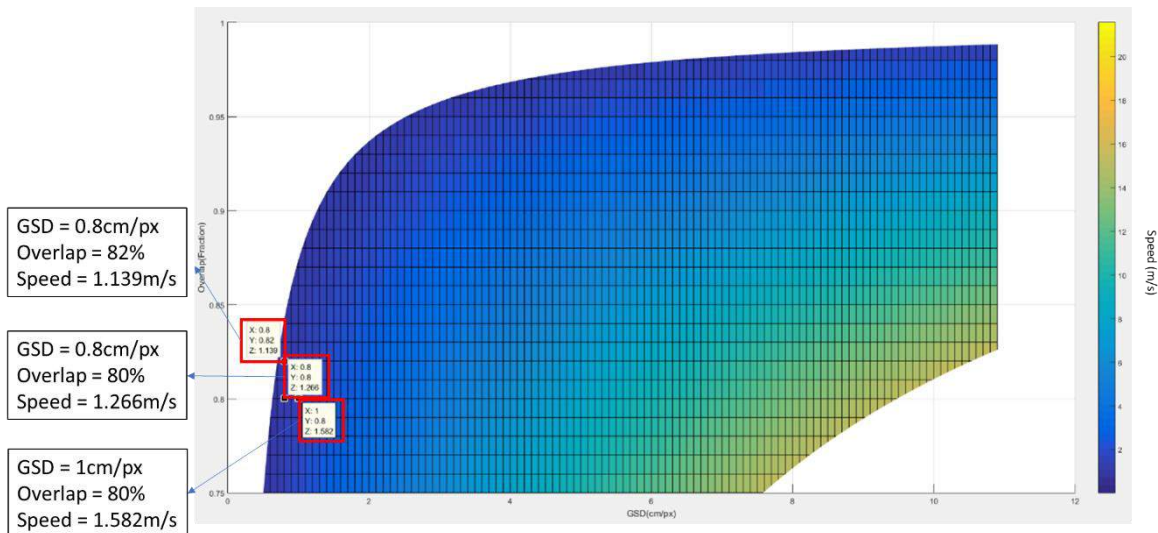
Figure 3.37: Characteristic Surface Plot for the DJI X5 Camera for t=4sec

82
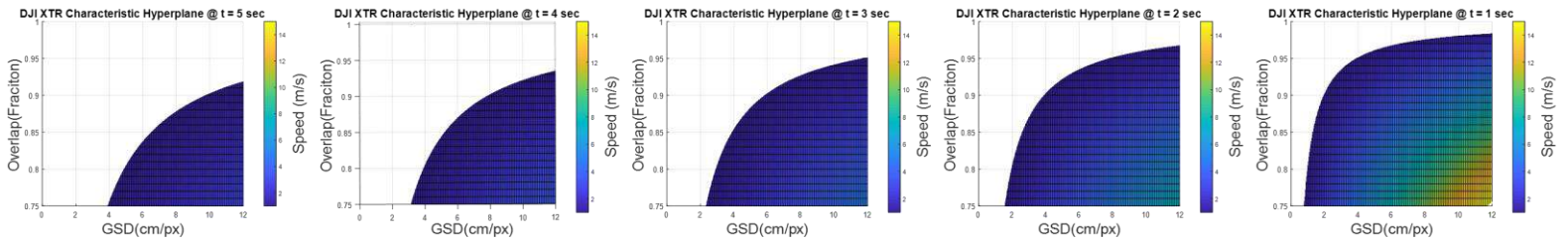
Figure 3.38: DJI XTR's Individual Characteristic Hyperplane for Triggering Intervals 5, 3, 2, and 1 second (left to right)
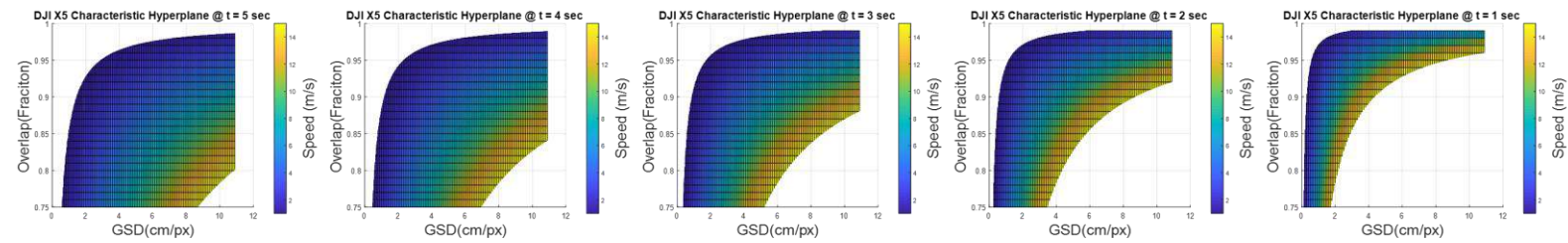
Figure 3.39: DJI X5's Individual Characteristic Hyperplane for Triggering Intervals 5, 3, 2, and 1 second (left to right)

Various flight parameters that lie on the surface plots in Figures 3.38 and 3.39 were selected to generate flight plans for this experiment. Flight parameters that lie on the edge of the plots and at the center of the plots were selected. The objective of the experiment was to record the number and observe the pattern of images captured by the DJI XTR and X5 cameras for varying values of the flight parameters above and below the 4-second surface plot generated. The surface plots for triggering interval of 5 seconds lies below the plot created using 4 seconds, and the other surface plots lie above the 4-second surface plot.

DJI GS Pro, the flight planning application, calculates an approximate number of images that will be captured for the mission designed and this value will be compared to the actual number of images captured. Twenty-eight different flights using varying flight parameters were run using the DJI XTR and X5 cameras. The percentage of images captured with respect to the value estimated by the application was calculated and summarized in a plot. The captured image datasets were also analyzed using an application called GeoSetter. The application allows the user to visualize the position of the images captured on Google Maps and aids in confirming if the images were captured in the pattern as planned.

The number of images captured every mission was recorded and the percentage of images captured with respect to the value estimated by the application was calculated and summarized in the plots shown in Figure 3.40. The pattern of images captured at the various triggering interval was observed using GeoSetter. Figures 3.41 and 3.42 show the GeoSetter screenshots of images captured at triggering intervals from 5 seconds to 1 second (left to right) for the DJI XTR and DJI X5.
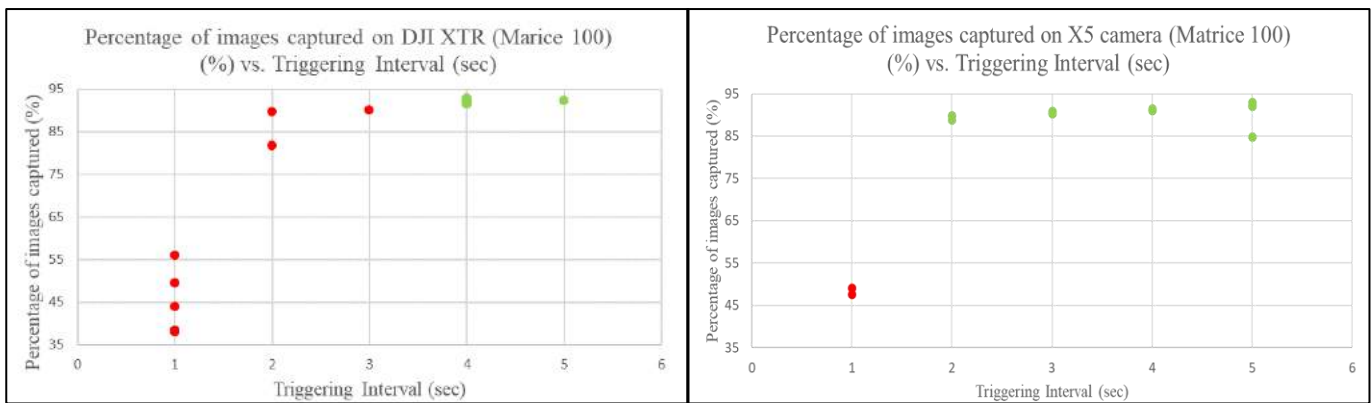
Figure 3.40: Graph of Percentage of Images Captured vs. Triggering Interval; Left: DJI XTR, Right: DJI X5
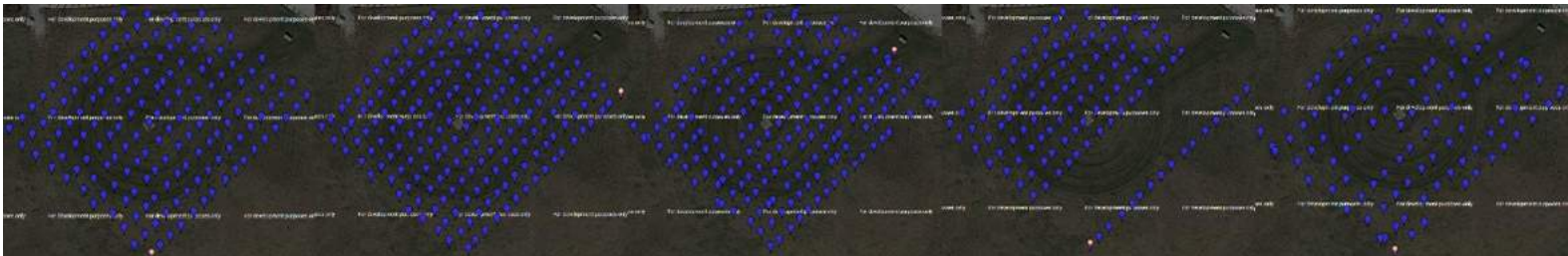
Figure 3.41: GeoSetter Screenshots of the DJI XTR Image Dataset Obtained for Triggering Intervals 5, 4, 3, 2, and 1 Seconds (left to right)
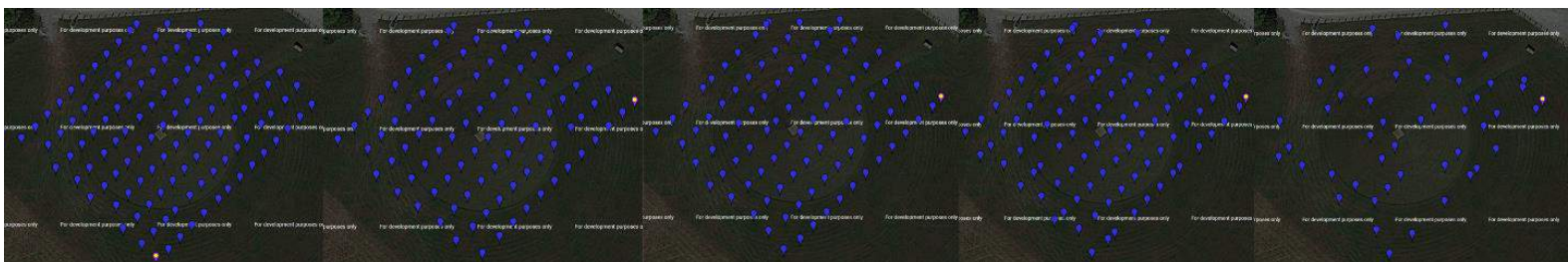
Figure 3.42: GeoSetter Screenshots of the DJI X5 Image Dataset Obtained for Triggering Intervals 5, 4, 3, 2, and 1 Seconds (Left to Right)

From the results obtained, DJI XTR camera requires at least 4 seconds of triggering interval to capture a high percentage of the estimated number of images and for triggering intervals greater than or equal to 4 seconds the percentage of images captured starts to saturate around 93%. Whereas, the DJI X5 camera requires at least 2 seconds of triggering interval to capture a high percentage of the estimated number of images. The screenshots shown in Figures 3.41 and 3.42 clearly indicate the issues in image capture when the triggering interval is not set to a minimum of 4 seconds and 2 seconds for the DJI XTR and DJI X5 cameras respectively. One can observe that the overlap between images start to become inconsistent and rows of images go missing when the correct triggering interval is not set.

3.3.4 Mode of Capture

Hover & capture and equal timed mode are the two modes of capture available in most of the flight planning applications. This section presents the work conducted to identify the effect of the two modes of capture on the accuracies of the 3D point cloud produced using Pix4D Mapper.

3.3.4.1 Effect of Mode of Capture on 3D Point Cloud Accuracies

This section presents the results obtained to study the effect of modes of capture, on the planimetric measurement accuracies, recorded using a 3D point cloud. The section is divided into three paragraphs where the first paragraph presents information about the experiment setup and the data captured, the second paragraph presents the processed output and the compiled accuracy results, and the third paragraph presents the conclusion obtained.

The test was conducted at Air Master RC Flying Park an empty field in North Bend, Ohio. Four targets with distinct centers were laid out in the mapped region. Figure 3.43 shows the measurements between the target centers recorded on-field. Images of the field were captured

85

using the DJI Z3 camera and the DJI M100 sUAS. Images were captured in a parallel to width pattern with a GSD of 1cm/px in the two different modes of capture, keeping all the other flight parameters the same. Figure 3.44 shows screenshots obtained using the GeoSetter application showing the image locations of the two datasets, on a map. The hover & capture mode mission took 8 minutes to complete whereas the equal timed mode took 4 minutes to complete.

On-field Measurements						
Number	1	2	3	4	5	6
Name	D-A	B-C	A-B	C-D	D-B	A-C
Value (ft)	104.30	122.50	139.00	151.40	152.99	209.90
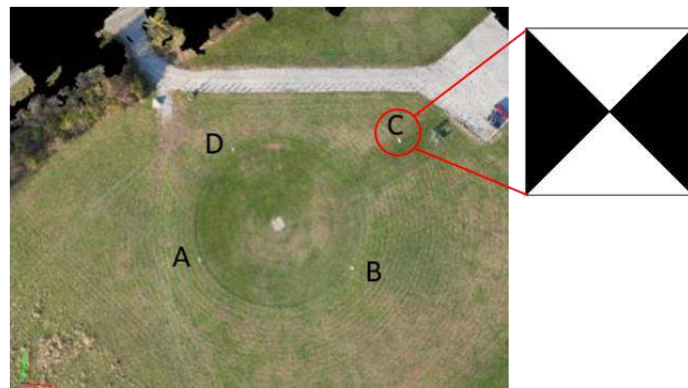
Figure 3.43: Air Masters Mode of Capture Experiment Measurements
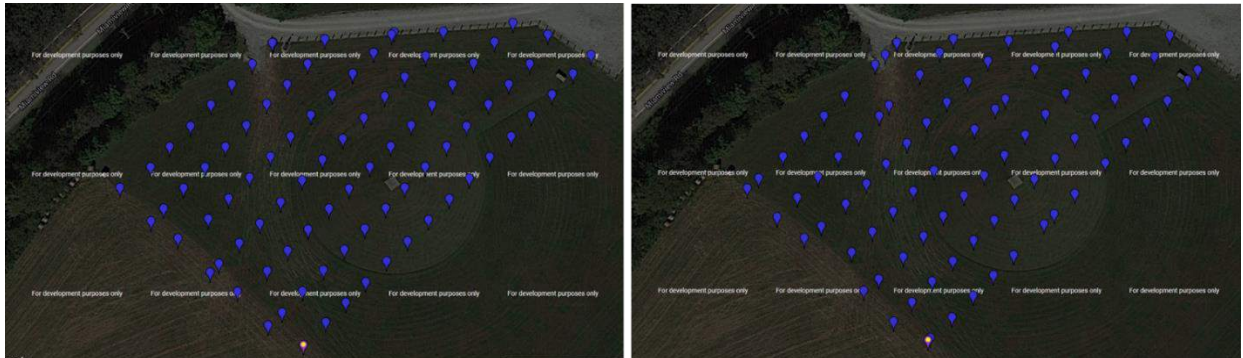
Figure 3.44: Image Locations; Left: Hover & Capture Dataset, Right: Equal Timed Mode Dataset

The datasets were processed separately using Pix4D Mapper without any GCPs and with their geotags. The models were processed using the default 3D model template available on Pix4D Mapper. The generated 3D point clouds met the required quality checks recommended by Pix4D Mapper and were shown in the quality report. The generated 3D point cloud was analyzed by

86

measuring the distance between the centers of targets laid out in the field using the polyline line tool and the computed values were compared to the values recorded on the field. Figure 3.45 shows the 3D point cloud generated using the hover & capture dataset. Figure 3.46 shows the 3D point cloud generated using the equal timed mode dataset. The plot shown in Figure 3.47 shows the individual absolute error measurements and their mean absolute errors.
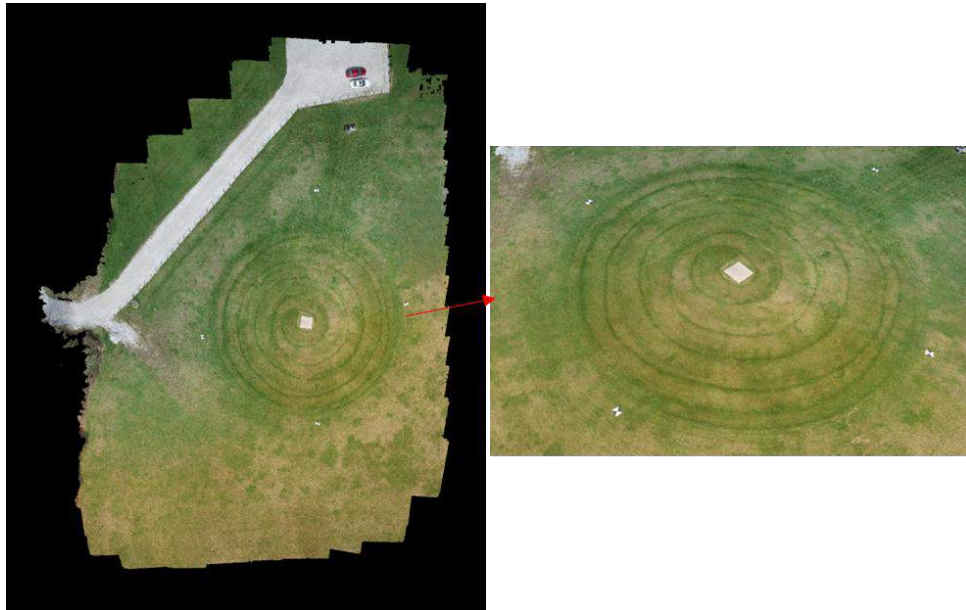
Figure 3.45: 3D Point Cloud Generated Using Hover & Capture Dataset
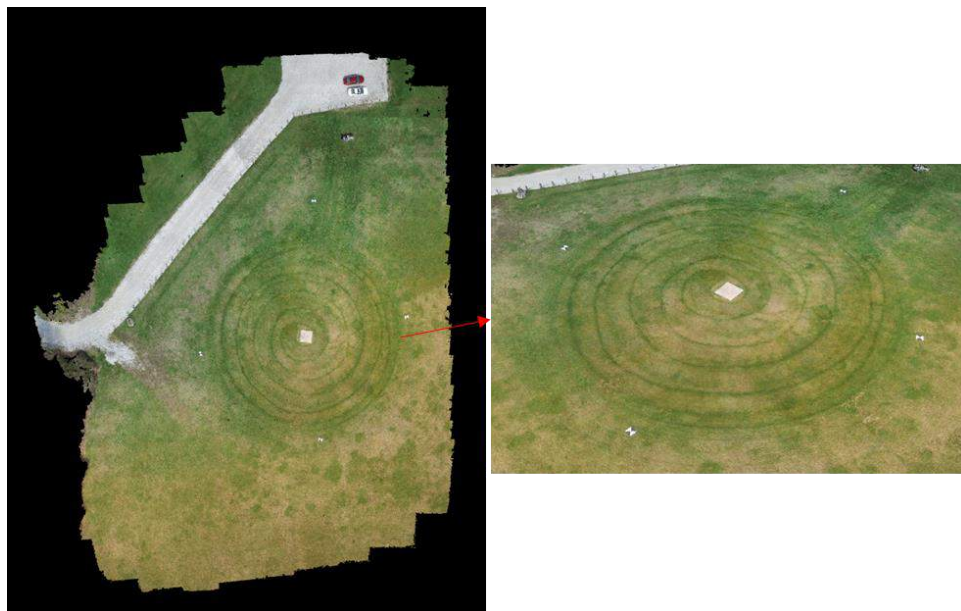
Figure 3.46: 3D Point Cloud Generated Equal Timed Mode Dataset

87

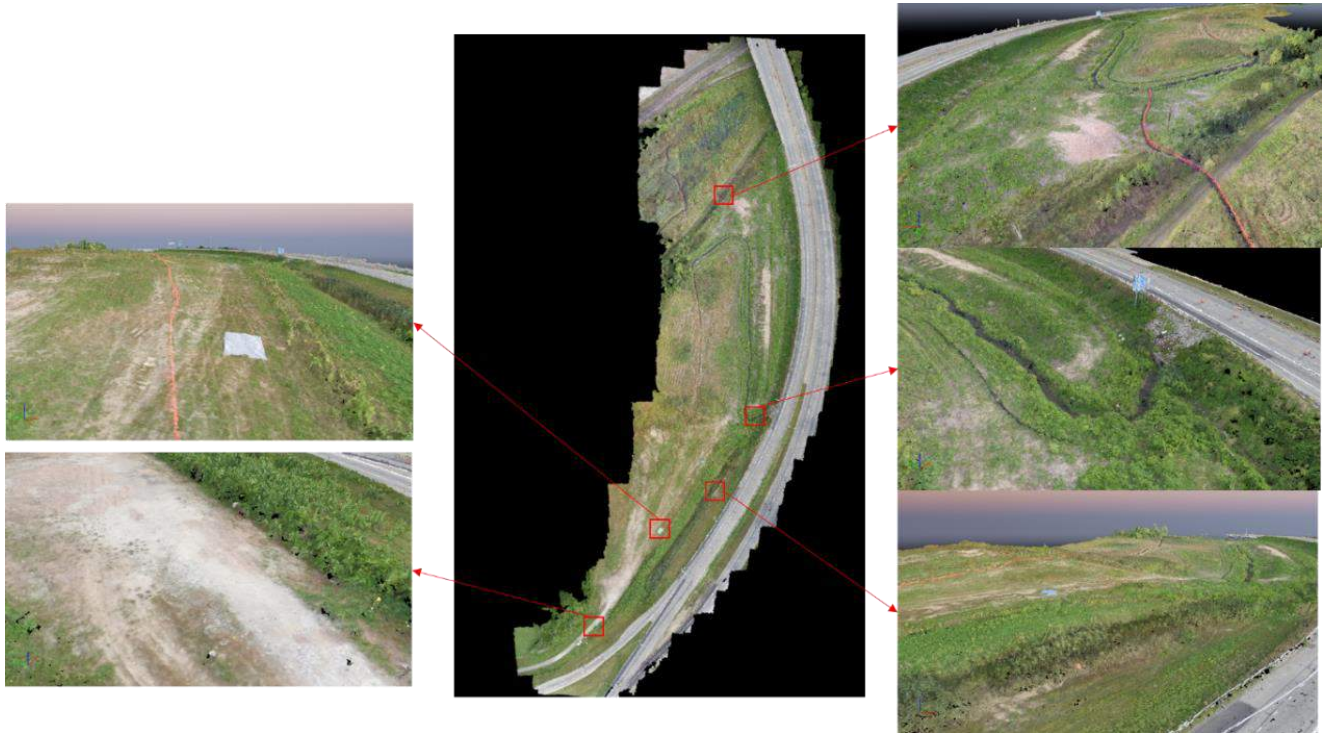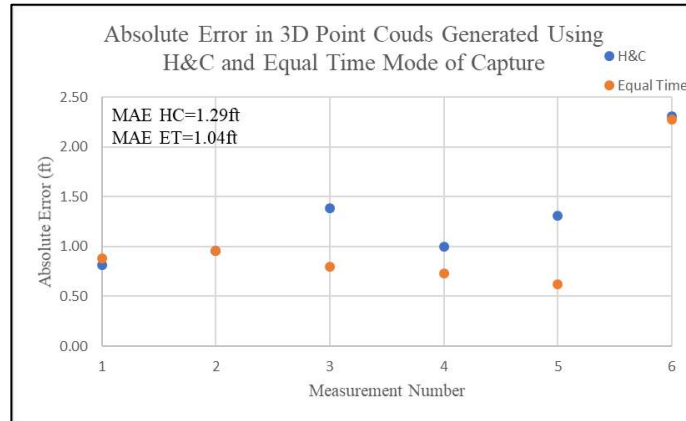Figure 3.47: Absolute Error Measurement Plots of Generated 3D Point Clouds

The results presented in Figure 3.47 show that the individual as well as average error values are relatively lower for the equal timed mode dataset 3D point cloud when compared to the hover & capture dataset 3D point cloud. When the image locations for the two datasets are compared, in Figure 86, the hover & capture mode dataset is more uniform than the equal timed mode. Despite this, the equal timed mode generated better results and as is favored over the hover & capture mode due to the lower mission time.

3.3.5 Pattern of Flight

The flight patterns analyzed in this section are parallel, perpendicular, and grid (the combination of parallel and perpendicular). This section presents the work conducted to identify the effect of these flight patterns on the 3D model accuracies produced using Pix4D Mapper.

3.3.5.1 Effect of Pattern of Flight on 3D Point Cloud Accuracies

This section presents the results obtained to study the effect of patterns of flight, on the planimetric measurement accuracies, recorded using a 3D point cloud. The section is divided into three paragraphs where the first paragraph presents information about the experiment setup and the data captured, the second paragraph presents the processed output and the compiled accuracy results, and the third paragraph presents the conclusion obtained.

The test was conducted at an empty parking lot behind ODOT's District 8 HQ in Lebanon, Ohio. The parking lot had a truck shed where markers with distinct centers were stuck on the sides of the shed. Figure 3.48 shows the illustration of the setup and the on-field measurements between the centers of the markers. Two types of measurements were recorded on the field, horizontal and vertical, and they were compared separately on the 3D point cloud. Images of the shed were captured using the DJI Z3 camera and the DJI M100 sUAS. Images were captured in a parallel (Flight 1) and perpendicular (Flight 2) to width patterns with a GSD of 1cm/px, keeping all the other flight parameters the same. Figure 3.49 shows screenshots obtained using the GeoSetter application showing the image locations of the two datasets, on a map.
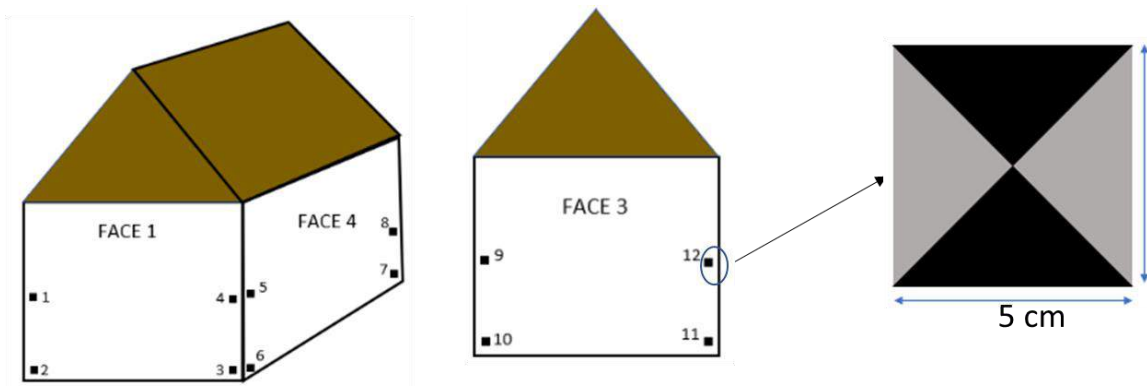
Measurements On-Field

Horizontal Measurements					Vertical Measurements					
Measurement Number					Measurement Number					
Face 1		Face 3	Face 4		Face 1		Face 3		Face 4	
1	2	3	4	5	1	2	3	4	5	6
1-4 (ft)	2-3 (ft)	10-11 (ft)	6-7 (ft)	5-8 (ft)	1-2 (ft)	3-4 (ft)	9-10 (ft)	11-12 (ft)	5-6 (ft)	7-8 (ft)
39.58	39.58	39.60	78.50	78.50	6.66	6.66	6.66	6.66	6.66	6.66

Figure 3.48: Flight Pattern Experiment Setup and On-field Measurements

Figure 3.49: Flight Pattern Experiment Image Locations; Left: Parallel Dataset (Flight 1), Right: Perpendicular Dataset (Flight 2)

The datasets were processed separately using Pix4D Mapper without any GCPs and with their geotags. The models were processed using the default 3D model template available on Pix4D Mapper. The generated 3D point clouds met the required quality checks recommended by Pix4D Mapper and were stated in the quality report. The generated 3D point cloud was analyzed by measuring the distance between the marker centers laid out using the polyline line tool and the computed values were compared to the values recorded on the field. Figure 3.50 shows the 3D point cloud generated using the parallel dataset. Figure 3.51 shows the 3D point cloud generated using the perpendicular dataset. Figure 3.52 shows the 3D point cloud generated using the parallel and perpendicular datasets. The plots shown in Figure 3.53 show the individual absolute error measurements and their mean absolute errors.

90
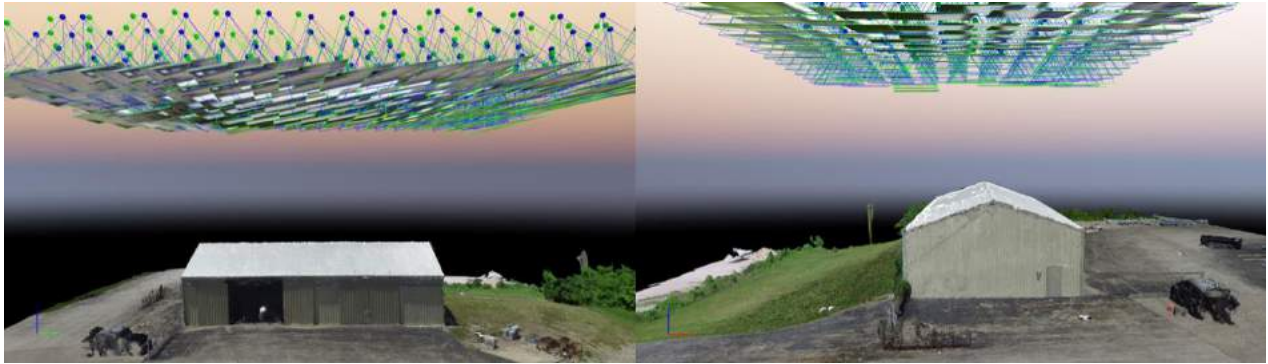
Figure 3.50: Pix4D Mapper 3D Model Generated Using Parallel Image Dataset
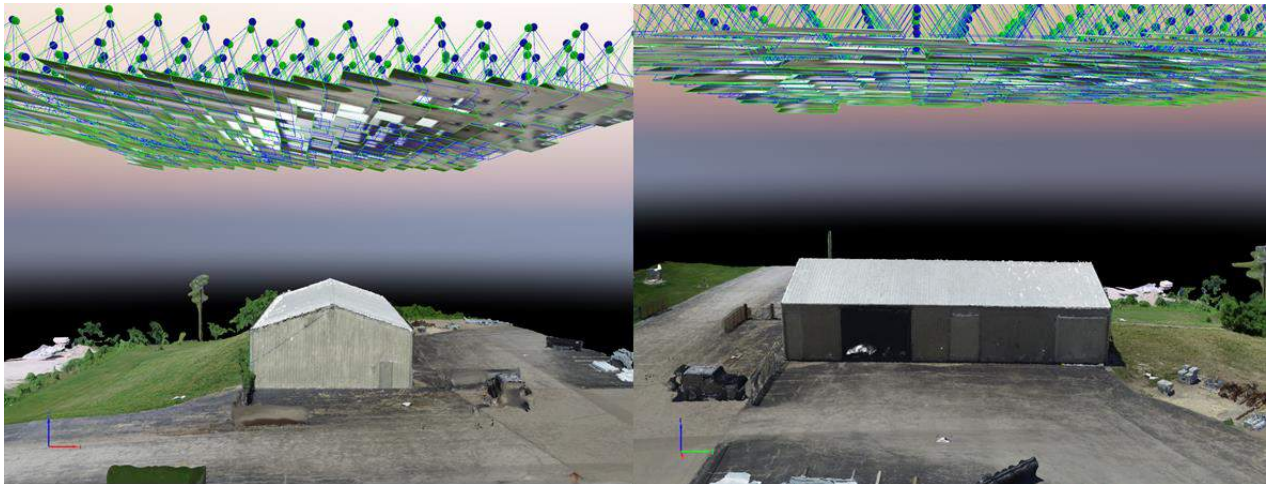
Figure 3.51: Pix4D Mapper 3D Model Generated Using Perpendicular Image Datasets
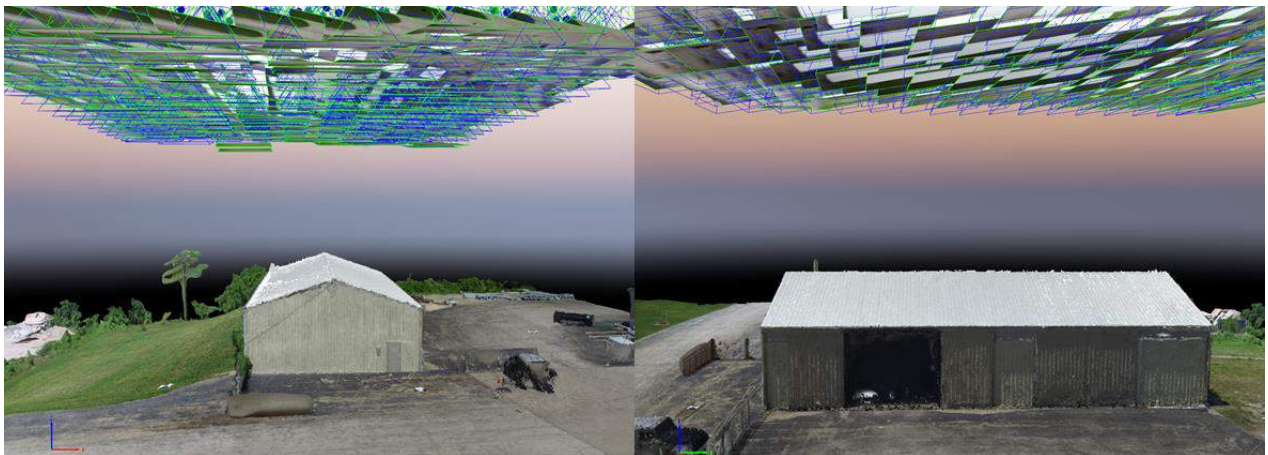
Figure 3.52: Pix4D Mapper 3D Model Generated Using Perpendicular and Parallel Image Dataset
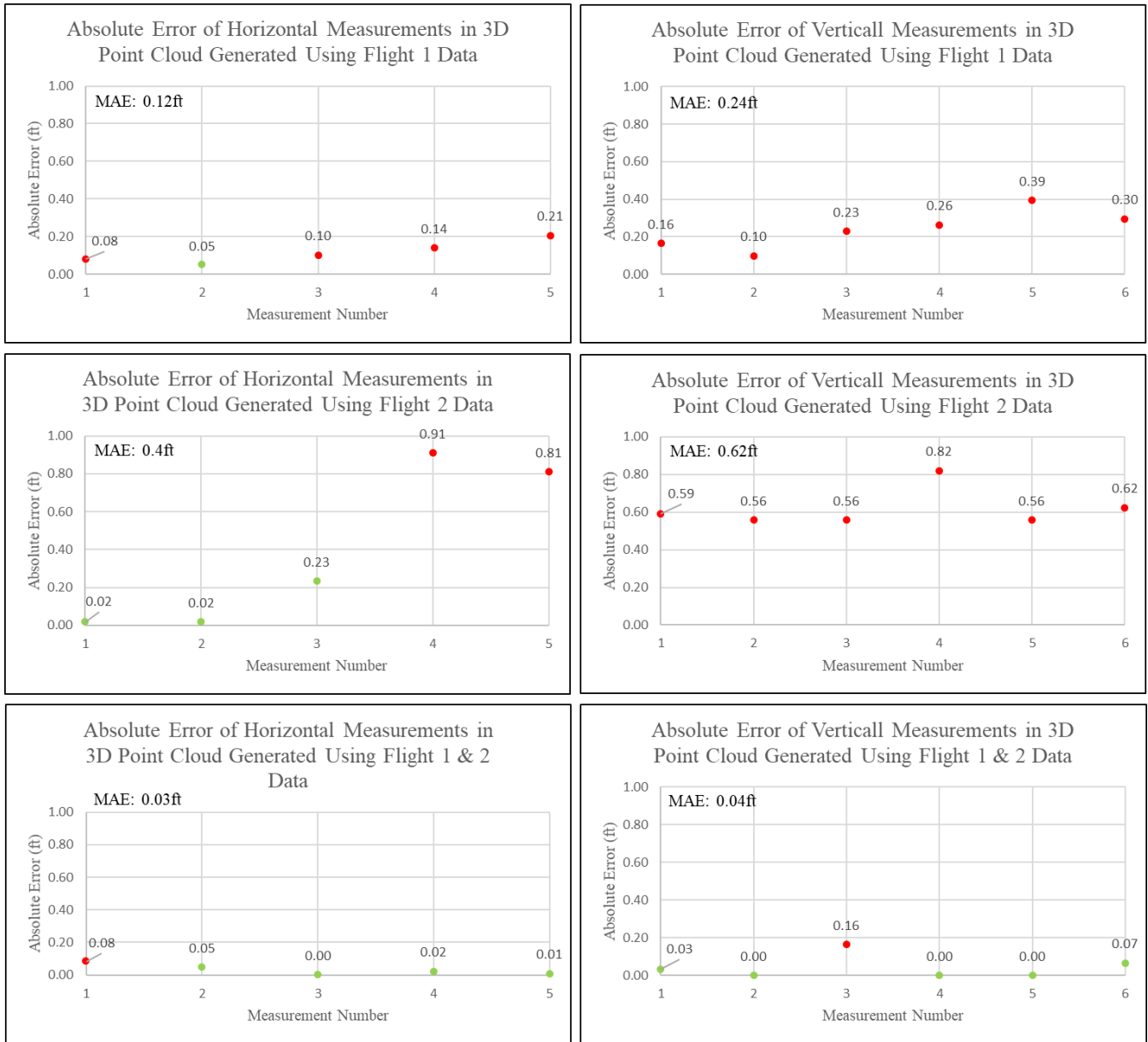
Figure 3.53: Absolute Error Measurement Plots of Generated 3D Point Clouds for the Flight Pattern Experiment

Closely analyzing the point clouds generated using the parallel and perpendicular dataset
(Figures 3.50 and 3.51), the shed re-created in these models look slightly crooked and is
corrected in the 3D point cloud (Figure 3.52) generated using the combination of the two
datasets. This explains the relatively higher errors obtained using the 3D point clouds generated
using individual parallel and perpendicular datasets seen in Figure 3.53 whereas the individual as
well as average error values are lower for the 3D point clouds processed using the combination

of parallel and perpendicular datasets (grid pattern). Therefore, the results obtained through this study suggest that the 3D point clouds of structures generated using a grid dataset are relatively more accurate.

3.4 Data Analysis and Processing

The images captured were analyzed and processed using Pix4D Mapper, Context Capture, FLIR Tools, and GeoSetter. Pix4D Mapper was primarily used to process the images and provides users multiple options to calibrate 3D point clouds. Ground control points, manual tie points, and scale constraints are the main 3D point cloud calibration options. This section presents the work done to document the effect of ground control points and image geotags on the accuracies of 3D point cloud generated using 3D point clouds.

FLIR Tools allow users to analyze thermal images, which include constraining the temperature values recorded, measuring the temperature value of any point in the image, and changing the emissivity values of the image to correct the temperature values based on the material analyzed. This section also presents the work done to derive the formula that can be used to correct the temperature values based on emissivity. The formula can be used, when thermal images are not analyzed using FLIR tools.

3.4.1 Effect of Ground Control Points and Image Geotags

Pix4D Mapper allows users to calibrate 3D point clouds using GCPs. This section presents the results obtained to study the effect of GCPs and image geotags, on the planimetric measurement accuracies, recorded using a 3D point cloud. The section is divided into three paragraphs where the first paragraph presents information about the experiment setup and the data captured, the

second paragraph presents the processed output and the compiled accuracy results, and the third paragraph presents the conclusion obtained.

The test was conducted at an empty field beside i75 in the city of Toledo, Ohio. Five objects of known dimensions were laid out in the mapped region. These objects included vinyl targets of varying sizes and a metal ruler. Figure 3.12 shows the illustrations of these objects along with the measurements recorded on-field and their images. Twelve GCPs points with distinct centers were spray-painted uniformly across the field. These points were recorded by an ODOT surveyor using professional equipment and were referenced in the Ohio north state plane coordinate system. Figure 3.54 shows the images of all the survey points marked on the field. Figure 3.55 shows the map marked with the surveyed points, identified by their numbers. Images of the field were captured using the DJI X5 camera and the DJI M100 sUAS. Images were captured in a grid pattern and with a GSD value of 1cm/px. Figure 3.13 shows the screenshot obtained using the GeoSetter application showing the image locations of the 1cm/px datasets, on a map.

Figure 3.54: Images of the GCPs Marked on the Field for the GCP Experiment

Figure 3.55: Map of the GCPs Marked on the Field

The 1cm/px dataset was processed in two ways using Pix4D Mapper; with GCPs and with image

geotags, and with GCPs and without image geotags. The models were processed using the

default 3D model template available on Pix4D Mapper. The generated 3D point clouds met the

required quality checks recommended by Pix4D Mapper and were stated in the quality report. The generated 3D point cloud was analyzed by measuring the objects laid out in the field using the polyline line tool and the computed values were compared to the values recorded on the field. The plots in Figure 3.56 show the individual absolute error measurements, and their mean absolute and root mean square errors computed using the model without GCPs and with image geotags, with GCPs and with images geotags and with GCPs and without image geotags.
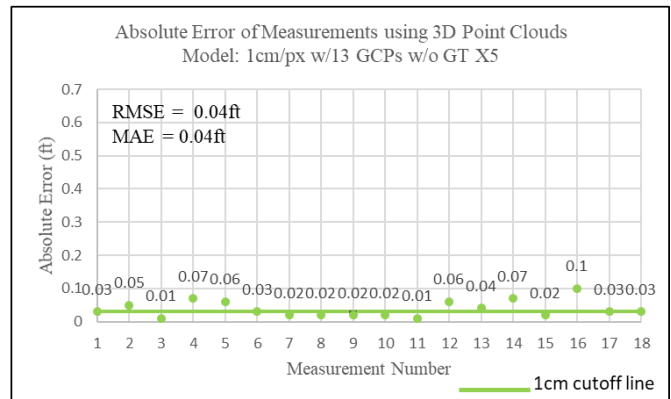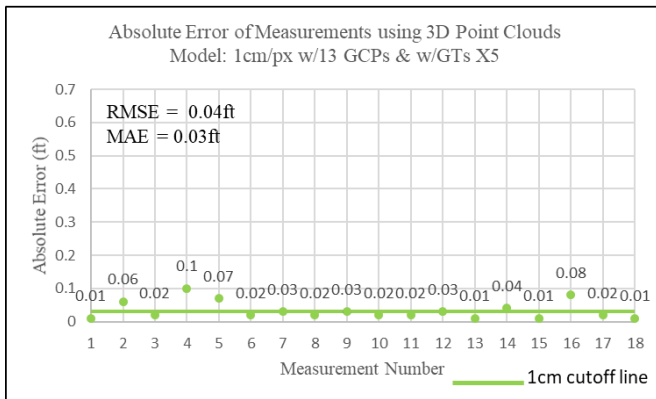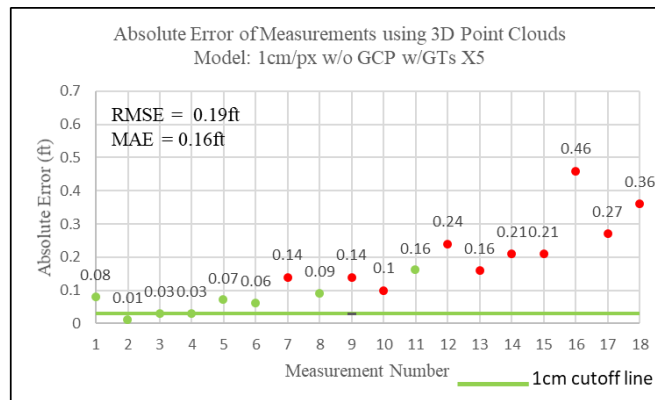
Figure 3.56: Absolute Error Measurement Plots of Generated 3D Point Clouds for the GCP Experiment

Comparing the plots shown in Figure 3.56 clearly show that individual as well as average error values reduce considerably when the 3D point clouds are calibrated using GCPs. As long as the GCPs are distributed uniformly, and are laid out following the rules suggested by Pix4D [41] repeatable results can be achieved. The case study, presented in the following chapters, conducted at Deer Creek, Ohio, investigates the effect of the number of GCPs on the accuracies of 3D point clouds generated using Pix4D Mapper.

3.4.2 Correcting Thermal Images Temperatures Using Emissivity Values

Using Equations 6, 7 and 8 the formulas to correct thermal image temperatures based on emissivity values were derived. Equation 56 was derived using Equations 6 and 7. Substituting Equation 56 in Equation 57 generates Equation 58. Rearranging Equation 58 produces Equation 59, the formula that can be used to correct thermal image temperature values using a new emissivity value.

$$T_{sensor}^4 = \varepsilon_{app}.T_{target,app}^4 + (1 - \varepsilon_{app}).T_{background}^4 \qquad 56$$

$$T_{target} = \sqrt[4]{\frac{T_{sensor}^4 - (1 - \varepsilon_{target}).T_{background}^4}{\varepsilon_{target}}} \qquad 57$$

$$T_{target} = \sqrt[4]{\frac{\varepsilon_{app}.T_{target,app}^4 + (1 - \varepsilon_{app}).T_{background}^4 - (1 - \varepsilon_{target}).T_{background}^4}{\varepsilon_{target}}} \qquad 58$$

$$T_{target} = \sqrt[4]{\frac{\varepsilon_{app}.T_{target,app}^4 + (\varepsilon_{target} - \varepsilon_{app}).T_{background}^4}{\varepsilon_{target}}} \qquad 59$$

The variables seen in Equations 56-59 are defined as follows:

- T_{target}: Corrected temperature of the object based on new emissivity value in kelvin

- $T_{target,app}$: Temperature recorded using the thermal image with old emissivity value in kelvin

- T_{sensor}: Temperature recorded by the sensor after background temperature correction in kelvin

- $T_{background}$: Brightest temperature of the background in kelvin

- ε_{app}: The emissivity value set in the application/camera before thermal image capture

- ε_{target}: The emissivity value of the object in the thermal image for which the temperature is corrected

FLIR tools allow users to correct the temperature values of thermal images using their interface. The application was used to test the derived formula (Equation 59). An image that contains a concrete slab ($\varepsilon = 0.94$), vinyl target ($\varepsilon = 0.95$) and green grass ($\varepsilon = 0.98$) was used for this experiment. Using the spot measurement tool in FLIR tools the temperature of objects in the thermal image with the original emissivity value and the temperature of the objects calculated by the software after the new emissivity value was inputted were recorded and shown in the table in Figure 3.57. The table also shows the temperatures calculated using the derived formula (Equation 59) and the absolute error percentage between the temperature calculated using the application and the temperature calculated using the derived formula.

Emissivity Set on Application	Emissivity of the Object	Temperature Reading on FLIR Tools	Temperature Reading on FLIR w/correct emissivity value	Calculated Temperature Value (using derived formula)	Absolute % Error (FLIR w/correct emissivity-calculated)
0.93	0.94	17.3	17.30	17.26	0.3
0.93	0.94	18.5	18.50	18.44	0.3
0.93	0.94	16.3	16.30	16.27	0.2
0.93	0.94	19.4	19.40	19.33	0.3
0.93	0.94	19.7	19.60	19.63	0.2
0.93	0.94	19.4	19.40	19.33	0.3
0.93	0.95	29.8	29.50	29.47	0.1
0.93	0.95	28.1	27.80	27.80	0.0
0.93	0.95	29.7	29.40	29.38	0.1
0.93	0.95	30.4	30.10	30.06	0.1
0.93	0.95	26.7	26.40	26.43	0.1
0.93	0.95	27.6	27.30	27.31	0.1
0.93	0.98	23.3	22.80	22.80	0.0
0.93	0.98	19.4	19.00	19.08	0.4
0.93	0.98	23.9	23.40	23.37	0.1
0.93	0.98	23	22.50	22.51	0.1
0.93	0.98	22	21.50	21.56	0.3
0.93	0.98	20.4	20.10	20.04	0.3
				Mean of Absolute Error %:	0.2

Figure 3.57: Correcting Thermal Image Temperature Based on Emissivity Value Experiment Results

Analyzing the results obtained in Figure 99, the majority of the errors obtained are negligible and are mainly observed due to rounding. The small error values also indicate that this formula can be used to correct thermal image temperature values when FLIR Tools is not used to analyze thermal images and instead analyzed using a code-based platform.

3.5 Outputs

This section presents information about the different types of outputs that can be generated using Pix4D Mapper with examples of outputs generated for the research work presented in this document. Figure 3.58 shows the flowchart of all the possible outputs, with their file format extensions, that can be generated using Pix4D Mapper and Context Capture. The flow chart also shows three different software, Bentley MicroStation, ArcGIS, and QGIS (commonly used by surveyors), that can be used to view and edit the outputs from Pix4D Mapper and Context Capture or generate new outputs/file types using Pix4D and Context Capture outputs.
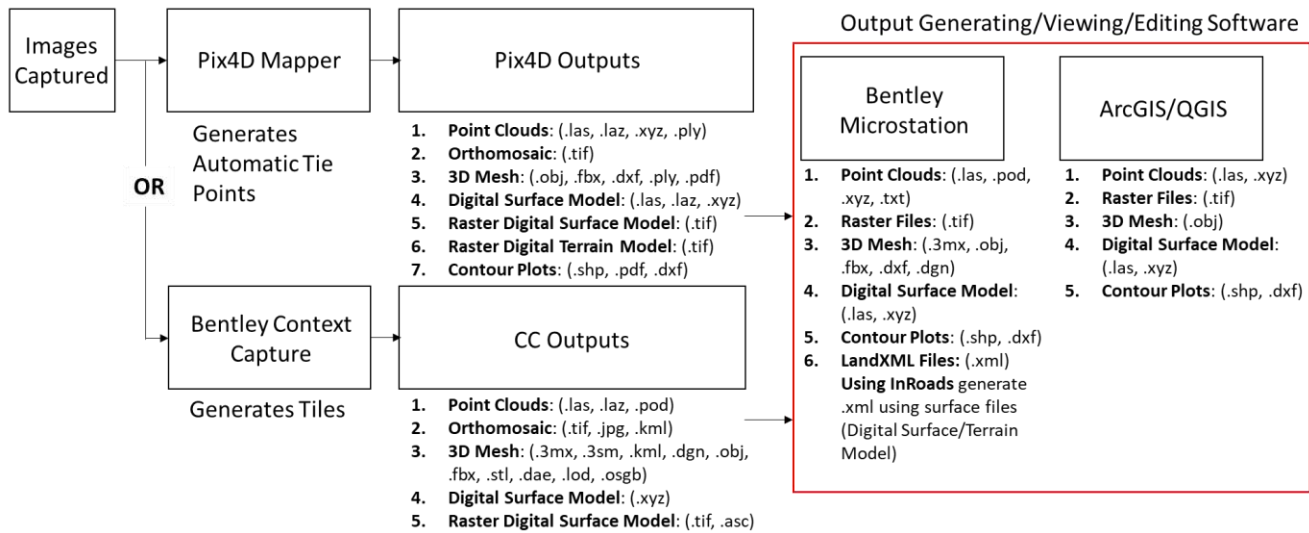
Figure 3.58: Flowchart of Possible Outputs that can be Generated Using Available Software

For the work presented in this document, Pix4D Mapper was primarily used to generate 3D point clouds, 2D orthomosaic, orthofacades and digital surface model (DSM). Whereas Context Capture was primarily used to generate 3D mesh files in their proprietary .3mx file format and Bentley Microstation was used to create the orthofacades using the generated 3D mesh files.

3.5.1 3D Point Clouds

3D point clouds are a set of points generated in space, that reconstruct the geometry of objects mapped. The X, Y and Z position and color information are stored in each point of the 3D point cloud [41]. Pix4D Mapper generates RGB point clouds using the images captured of the object of interest and allows users to visualize, edit and analyze the sparse point cloud generated of the surface mapped [41]. Figure 3.59 shows an example of a 3D point cloud of a work shed. Pix4D Mapper generates 3D point clouds in the .las file format, by default [41].
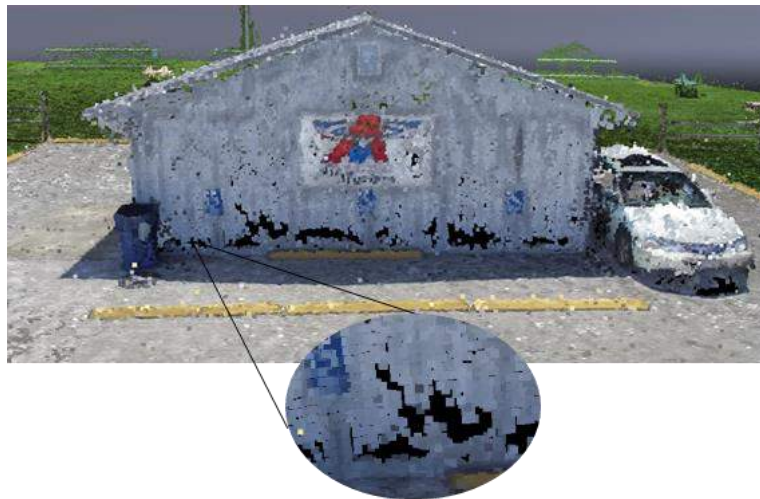
Figure 3.59: 3D Point Cloud of a Work Shed Generated Using Pix4D Mapper

3.5.2 3D Mesh

3D mesh represents the shape and the geometry of object mapped using vertices, edges, faces and texture form the images. Pix4D Mapper generates the 3D mesh files by estimating the surface between triangulated points in the 3D point cloud [41]. Figure 3.60 shows an example of a 3D mesh of a work shed. Pix4D Mapper generated 3D mesh in the .obj file format, by default [41], but can also be exported in the file formats shown in Figure 3.58. Context Capture generates 3D mesh files primarily using the information in the images and the generated 3D

mesh has greater levels of detail when compared to Pix4D Mapper. This comparison is discussed in the following chapters.
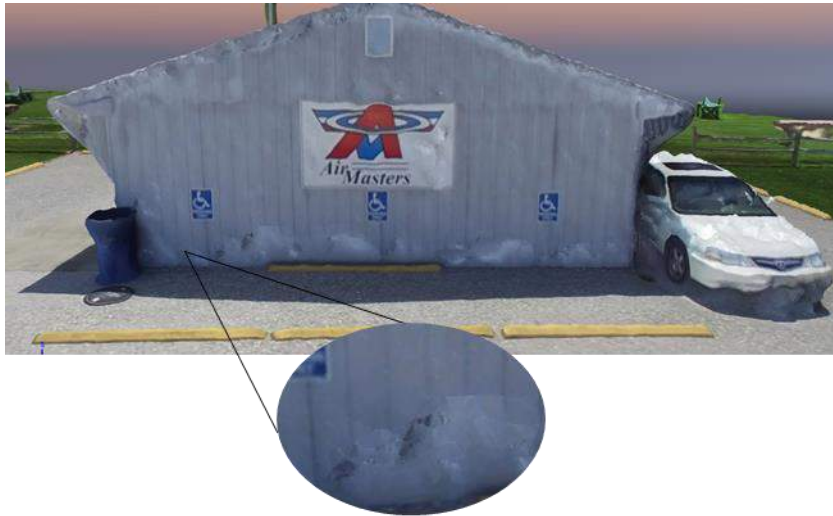
Figure 3.60: 3D Mesh of a Work Shed Generated Using Pix4D Mapper

3.5.3 Orthomosaic

Orthomosaic is an orthorectified 2D map, top view, of the 3D model generated. Pix4D Mapper generates an orthomosaic using the information present in images and 3D point cloud generated [41]. Each point on the orthomosaic contains X, Y, and color information. Orthomosaic allows
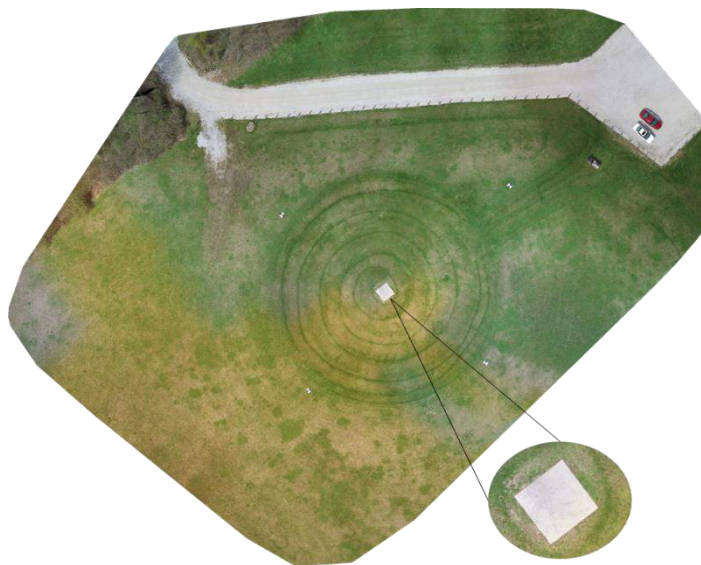
Figure 3.61: 2D Orthomosaic of a Field Generated Using Pix4D Mapper

users to represent large 2D surfaces at a higher resolution. Figure 3.61 shows an example of a 2D orthomosaic of a field.

3.5.4 Orthofacade

Orthofacade is an orthorectified image of a façade of a building or the sides of an object modeled in Pix4D Mapper [41]. Users can generate orthofacades, in Pix4D Mapper by inserting orthoplanes parallel to the side of the object. Figure 3.62 shows the orthoplane added parallel to a bridge segment's façade, in Pix4D Mapper and Figure 3.63 shows the orthofacade generated.
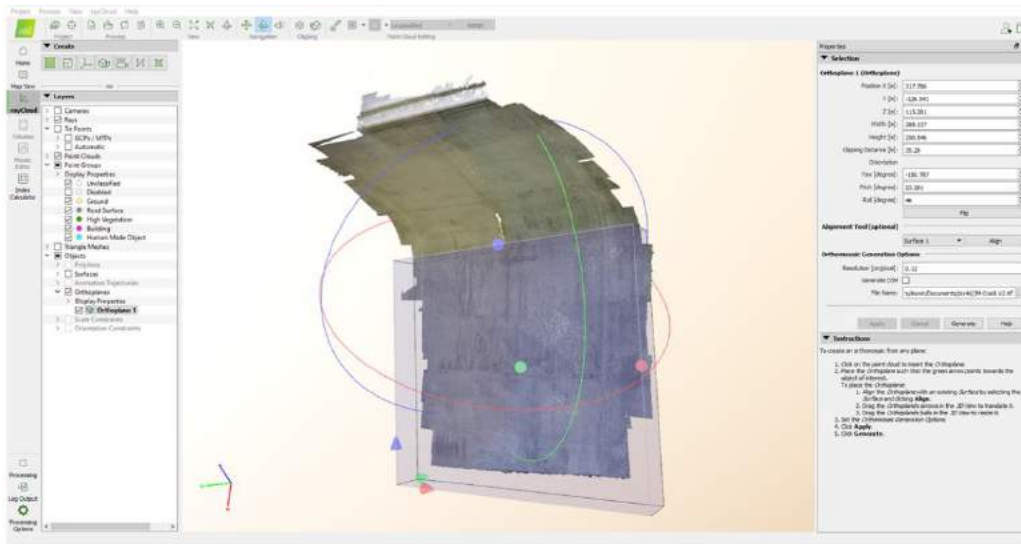
Figure 3.62: Adding Orthoplane Using Pix4D Mapper to Generate the Orthofacade of the Bridge Segment's Facade

Figure 3.63: 2D Orthofacade of a Bridge Segment's Facade

Chapter 4 : Case Studies

To understand the effectiveness of photogrammetry and sUAS in surveying and monitoring infrastructure and construction sites various studies were conducted across the state of Ohio. The map of Ohio, in Figure 4.1, shows the locations of these studies. The following sections present the case study details and the results obtained.
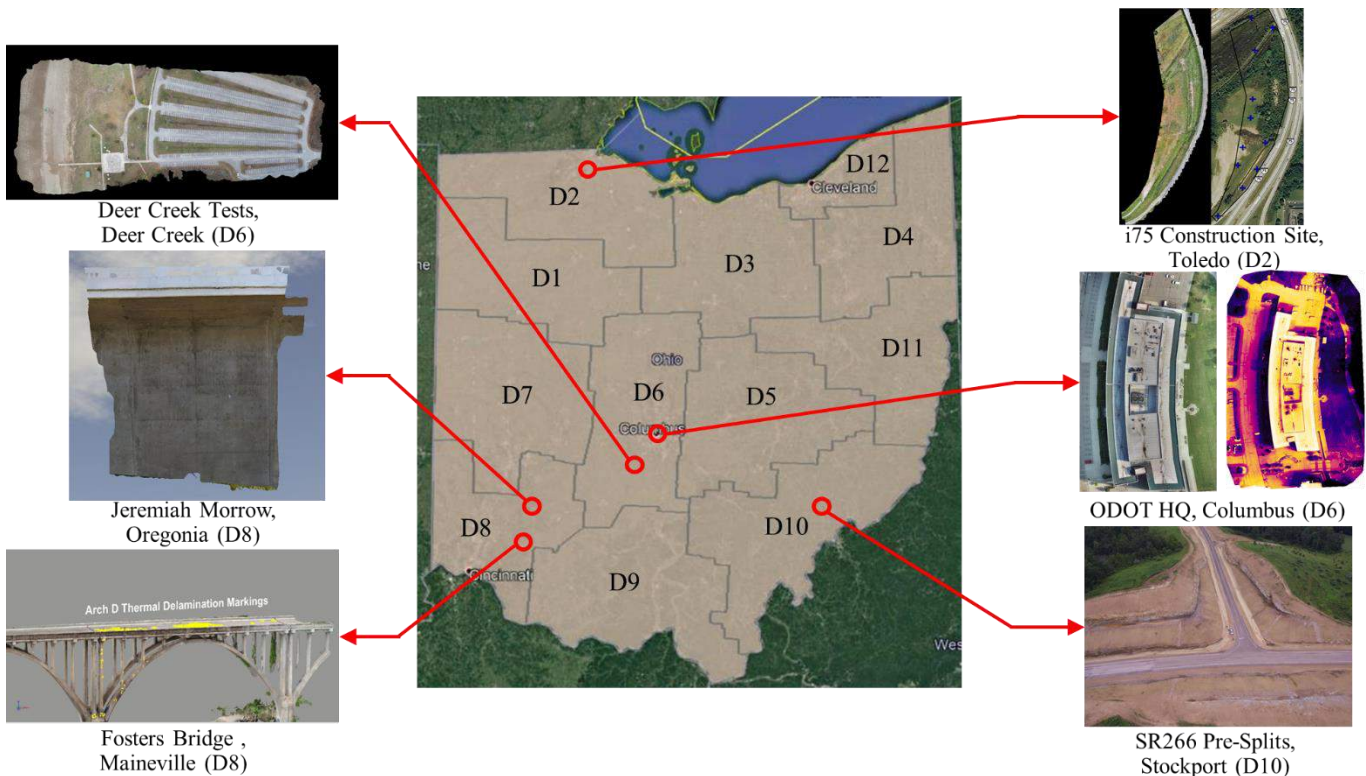
Figure 4.1: Case Study Locations in the State of Ohio

4.1 Case Study 1: SR266 Pre-Split Area Measurement, Stockport D10

This section presents the case study conducted at the intersection of Point Lookout Road and the newly constructed SR266 in Stockport district 10 of the state of Ohio. The objective of this study was to measure the areas of pre-splits at the intersection using a 3D model for the ODOT

surveyors. The areas measured using the 3D model were compared to the values estimated by the ODOT plan sheet and a third-party surveyor.

4.1.1 Flight Plan and Image Capture

The plan sheets of the area mapped were analyzed prior to designing flight plans. Figure 4.2 shows the plan sheet of the project with the area to be mapped circled. Using the information present in the plan sheets a rough schematic of the area mapped was generated and shown in Figure 4.3. The rough schematic aided in dividing the area and estimating the rough positions for the GCPs. The area to be mapped was divided into five regions and 25 GCPs were laid out in the region. The area was divided to efficiently map the region using the sUAS. Using the elevation profiles of the region the flight plans designed considered the elevation changes and these were reflected in the flight heights and the image overlaps set for each mission. Figure 4.4 shows the visual image of the area that was mapped and the takeoff points for the missions.
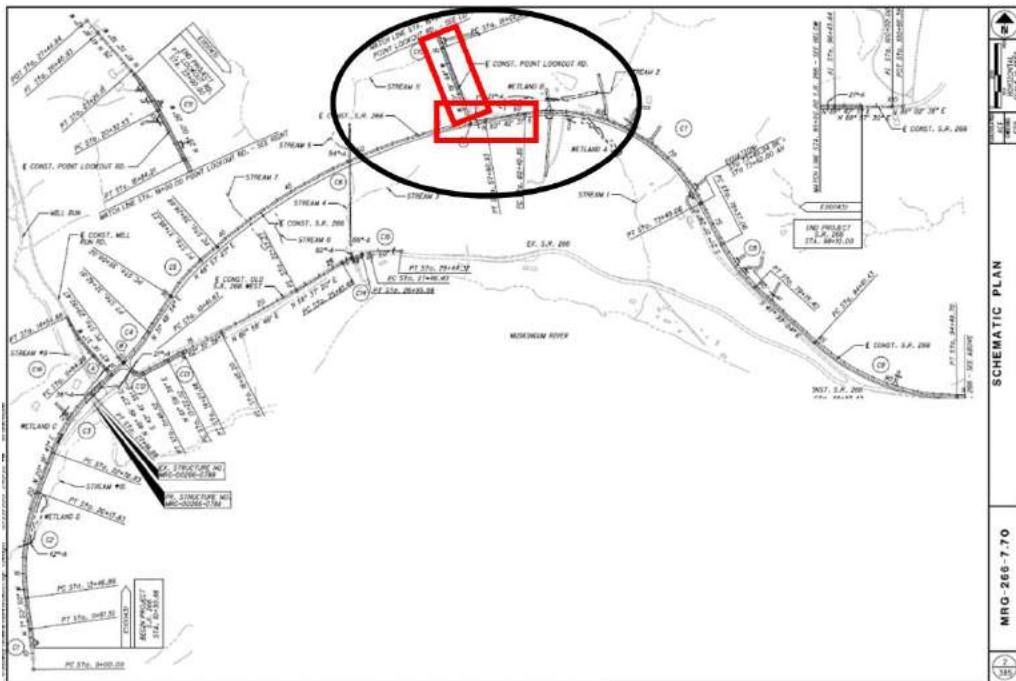
Figure 4.2: Plan Sheet of SR266 Construction Project with Area Mapped Circled
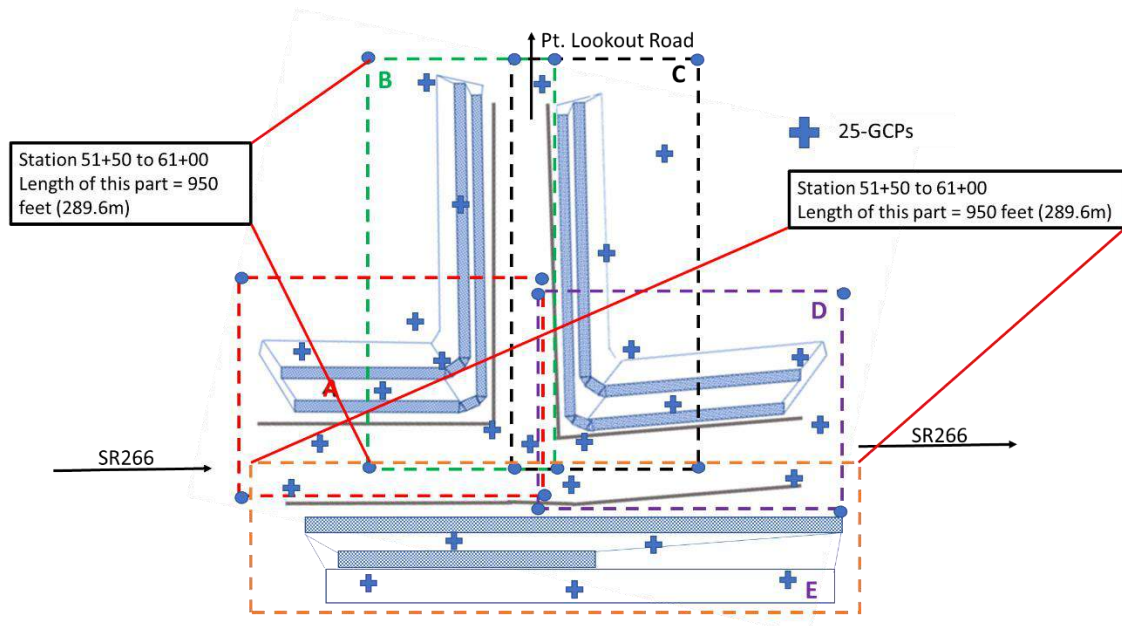
Figure 4.3: Rough Schematic of the Intersection Mapped
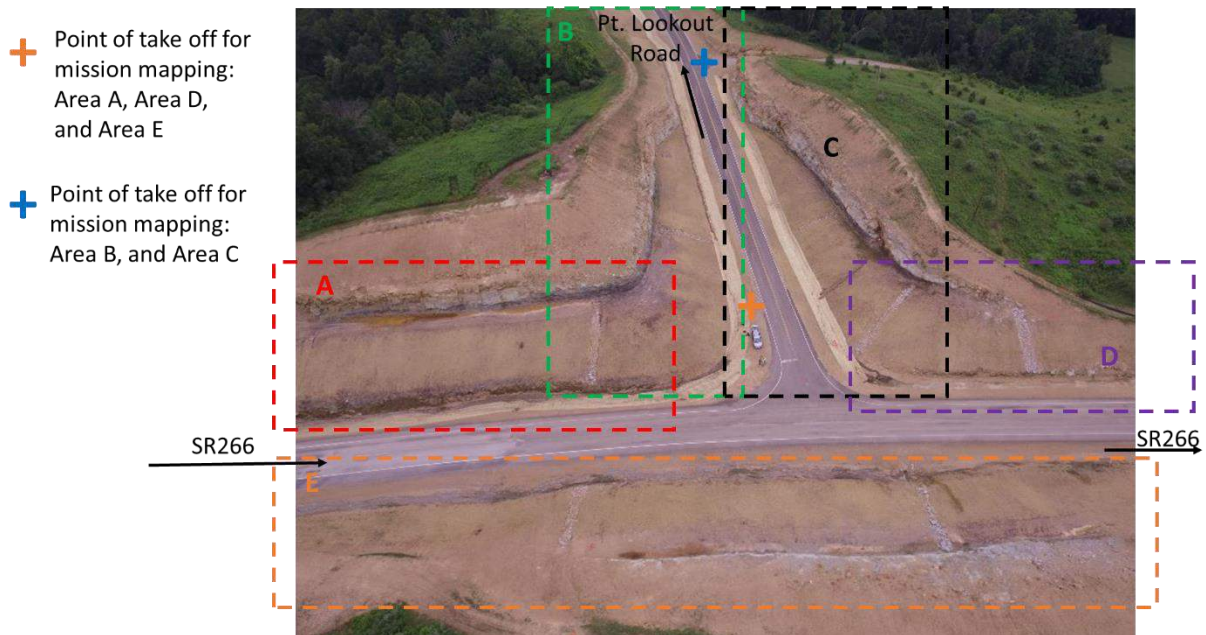
Figure 4.4: Visual Image of the Regions Mapped with sUAS Take Off Point Marked to Compensate for Elevation Changes

The images of the region were captured using DJI Matrice 100 sUAS and the DJI Z3 camera.

The missions were planned on the DJI GS Pro flight planning application, where the mode of

capture was set to equal timed mode and the images were captured in a grid pattern. Figure 4.5

shows the summary of the missions run at the site. The sUAS mapped a total area of 4.47

hectares. Figure 4.6 shows the screenshot of the flight plans for area E of the intersection.

Area	Mission Type	GSD (cm/px)	Altitude (m)	FO/SO(%)	Flight Time	Recorded Photos
A	Parallel	1cm/px	25.5m	93%/93%	1hr 20min	1530
	Perpendicular	1cm/px	25.5m	93%/93%	1hr 30min	1693
B	Parallel	1cm/px	25.5m	93%/93%	1hr	1182
	Perpendicular	1cm/px	25.5m	93%/93%	1hr 10 min	1389
C	Parallel	1cm/px	25.5m	93%/93%	1hr 10 min	1547
	Perpendicular	1cm/px	25.5m	93%/93%	1hr 10 min	1694
D	Parallel	1.1cm/px	28m	93%/93%	30min	779
	Perpendicular	1.1cm/px	28m	93%/93%	30min	748
E	Parallel	1.8cm/px	46m	93%/93%	32min	832
	Perpendicular	1.8cm/px	46m	93%/93%	33min	979

Figure 4.5: Summary of Missions Conducted at SR266 Intersection
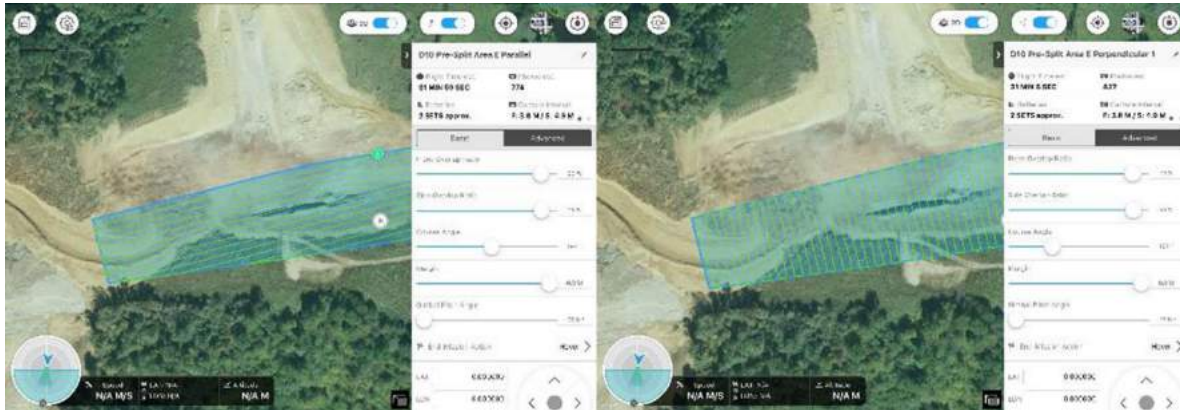
Figure 4.6: Screenshot of Area E Mission Plan on DJI GS Pro

The coordinates of the ground control points laid out in the field were recorded by a surveyor

using survey-grade equipment. The coordinates were also recorded using the RTK system

available on DJI M210 sUAS. When the two sets of coordinates were analyzed, using Google

Earth, a consistent visual shift between them was observed, as shown in Figure 4.7. On further

analysis of the data, it was observed that the distance between the two sets of coordinates was

consistently off by a fixed value. Figure 4.8 shows the difference in values between the

coordinate recorded by the DJI M210 RTK system and the surveyors.
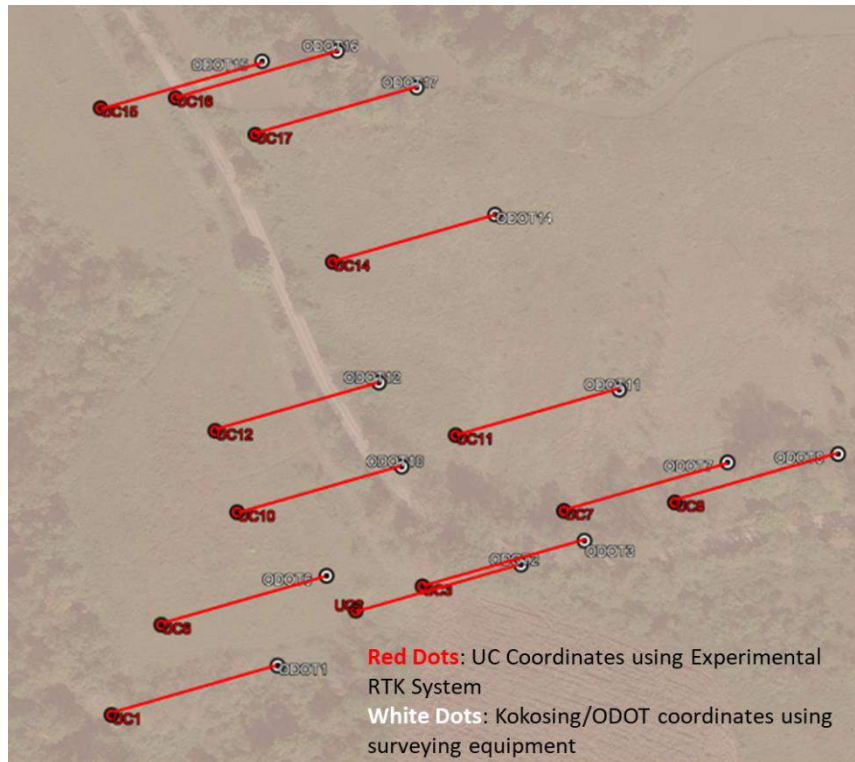
Figure 4.7: Google Earth Screenshot Showing the Shift Between the Coordinates
Recorded Using the RTK System and the Surveyor's Survey Grade Equipment

GCP	Difference in coordinates between University of Cincinnati and Kokosing/ODOT			
	Difference in Northing (feet)	Difference in Easting (feet)	Difference in Altitude (feet)	Distance b/w Kokosing/ODOT and UC coordinates (feet)
1	41.032	192.4556	-14.1724	196.7810534
2	40.9831	192.4646	-14.44	196.7796655
3	40.882	192.5815	-14.2633	196.8729846
6	40.9486	192.5159	-14.2592	196.8226603
7	41.1886	192.3585	-14.2054	196.7188178
8	40.8387	192.667	-14.31	196.9476385
10	40.9875	192.4262	-14.3794	196.7430243
11	41.0316	192.65	-14.3192	196.9711012
12	41.4648	192.5967	-14.1186	197.0096914
14	41.2203	192.7304	-14.2232	197.0891174
15	40.9172	192.2846	-14.4308	196.5898895
16	41.2142	192.4491	-14.2265	196.8127698
17	41.3722	192.8635	-14.3594	197.25108
Mean	41.083 feet	192.542 feet	-14.28518462 feet	196.876 feet
Standard Deviation	0.193 feet	0.1599 feet	0.0986 feet	0.175 feet
	(2.316 inches)	(1.9188 inches)	(1.1832 inches)	(2.1 inches)

Figure 4.8: Analysis of the Coordinates Recorded Using the RTK System and the
Surveyor's Survey Grade Equipment

The shift in coordinates was due to not compensating for the combined scale factor of the project. The coordinates recorded by professional surveyors were multiplied by the combined scale factor seen in the project plan sheet (Figure 4.9). After applying the scale factor, the coordinates recorded by the surveyor shifted to the vicinity of the coordinates recorded using the RTK system, as seen in Figure 4.10.
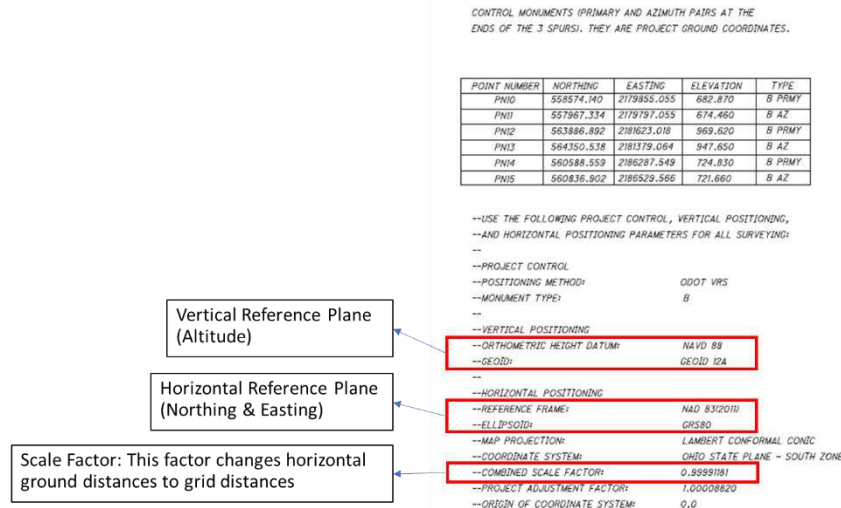
Figure 4.9: SR266 Project Plan Sheet with Coordinate System and Combined Scale Factor Information
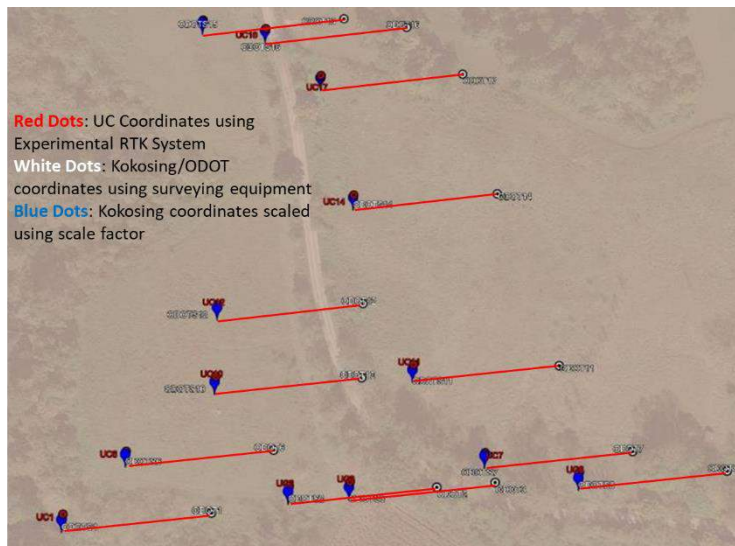
Figure 4.10: Google Earth Screenshot Showing the Shift Between the Coordinates Recorded Using the RTK System and the Surveyor's Survey Grade Equipment, and the Corrected Surveyor Coordinates

4.1.2 Processing and Analysis

The images captured were processed separately based on the area mapped, using Pix4D Mapper.

3D point clouds of the five areas were generated without ground control points. The areas of the

pre-splits were measured using plane and surface markings, and the measured values were

compared to the values estimated using ODOT's plan sheets and the contractor's estimates.

Figures 4.11 – 4.15 show the 3D point clouds, of the respective areas, with the pre-splits marked

by a surface and a plane using Pix4D Mapper.
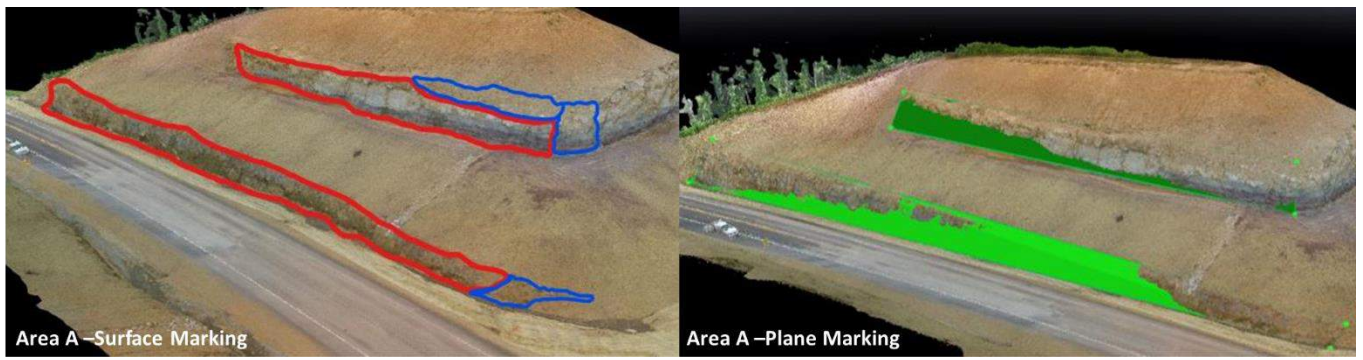
Figure 4.11: 3D Point Cloud of SR266 Area A with Pre-splits Marked; Left: Surface Marking, Right: Plane Marking

Figure 4.12: 3D Point Cloud of SR266 Area B with Pre-splits Marked; Left: Surface Marking, Right: Plane Marking
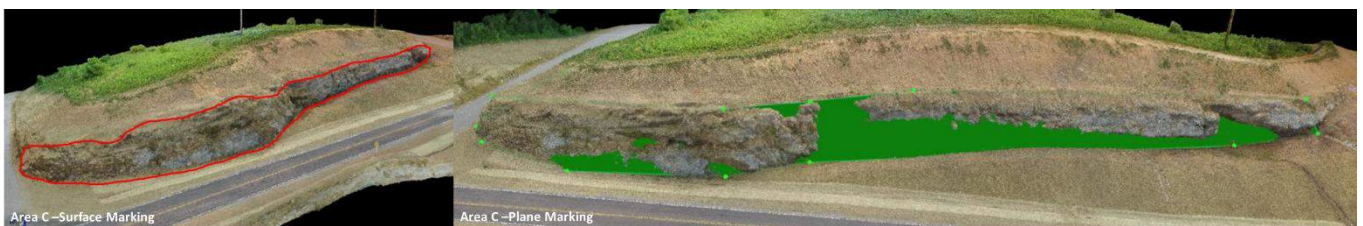
Figure 4.13: 3D Point Cloud of SR266 Area C with Pre-splits Marked; Left: Surface Marking, Right: Plane Marking

Figure 4.14: 3D Point Cloud of SR266 Area D with Pre-splits Marked; Left: Surface Marking, Right: Plane Marking
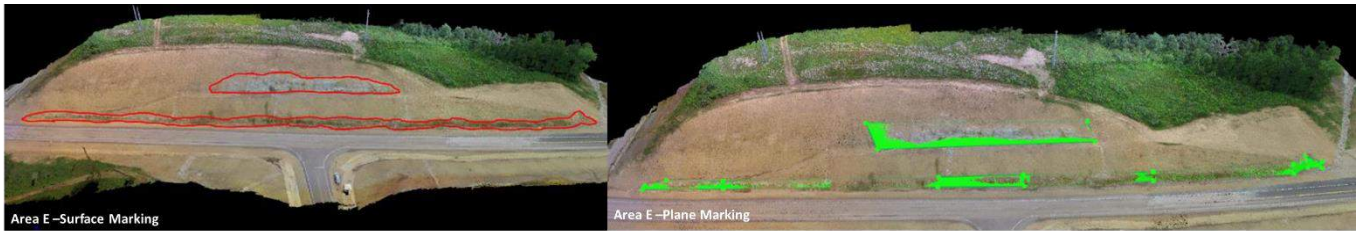
Figure 4.15: 3D Point Cloud of SR266 Area E with Pre-splits Marked; Left: Surface Marking, Right: Plane Marking

4.1.3 Outputs

The areas measured using the surface and plane markings are summarized in the table shown in Figure 4.16. The table shown in Figure 4.17 shows that the areas measured using the 3D point clouds lie between the estimates obtained using ODOT plan sheets and the areas estimated by the contractors.

	w/o GCP (Surface Markings)		w/o GCP (Plane Markings)	
	sq. ft	sq. yd	sq. ft	sq. yd
Upper Cut	4,054.87	450.541	6,487.48	720.83
Lower Cut	6,124.74	680.527	9,302.27	1,033.59
Area A (STA. 53+00 to 57+00) -1	10,179.61	1,131.07	15,789.75	1,754.42
Area B (STA. 10+50 to 16+00) -1	13,061.57	1,451.28	10,088.67	1,120.96
Area C (STA. 10+50 to 16+00) -2	12,819.78	1,424.42	13,165.65	1,462.85
Upper Cut	675.78	75.09	740.73	82.3
Lower Cut	2,109.11	234.35	2,004.27	222.7
Area D (STA. 57+00 to 61+00) -1	2,784.89	309.43	2,745	305
Upper Cut	4,327.73	480.86	8,776.28	975.14
Lower Cut	7,847.81	871.98	10,244.34	1,138.26
Area E (STA. 53+00 to 61+00) -2	12,175.54	1,352.84	19,020.62	2,113.4

Figure 4.16: Areas Measured Using the Point Clouds Generated for the SR266 Case Study

Area as calculated by **ODOT (from project plan sheets)**	SR266 Pre-Split Total Area (Sta.53+00-62+00)	1,744 sy. yd	
	Point Lookout Road Total Area (Sta. 10+50-16+00)	3,044 sq. yd	
	Total Area	4,788 sq. yd	**Difference (surface-ODOT)**
Area as measured by **creating a surface Using 3D model w/o GCP**	SR266 Pre-Split Total Area (Sta.51+50-62+00)	2,793 sq.yd.	1049 sq.yd (+ve)
	Point Lookout Road Total Area (Sta. 10+50-16+00)	2,876 sq. yd.	168 sq. yd (-ve)
	Total Area	5,669 sq.yd.	**Difference (plane-ODOT)**
Area as measured by creating a plane **Using 3D model w/o GCP**	SR266 Pre-Split Total Area (Sta.51-50-62+00)	4,173 sq. yd.	2,429 sq.yd (+ve)
	Point Lookout Road Total Area (Sta. 10+50-16+00)	2,584 sq. yd.	460 sq. yd (-ve)
	Total Area	6,757 sq. yd.	
Area as measure by **Contractor (Approx.)**	Total Area (Sta.51+50-62+00 and Sta.10+50-16+00)	7,288 sq. yd. to 7,788 sq. yd.	

Figure 4.17: Comparison of Areas Measured Using 3D Point Clouds, ODOT Plan Sheets, and Contractor Estimate

4.2 Case Study 2: ODOT HQ Roof Inspection, Columbus D6

This section presents the case study conducted at the ODOT headquarters in Columbus district 6 of the state of Ohio. The objective of this study was to inspect the roof of the building and attempt to construct a 3D model of the building. The roof was inspected using thermal and visual images where the visual images were used to cross-refer the trouble spots identified using thermal images.

4.2.1 Flight Plan and Image Capture

Prior to designing the flight plans for this case study, the building's height was estimated to account for the flight height and image overlap values. Using this information, the missions were planned on DJI GS Pro application and the images of the region were captured using DJI Matrice 100 sUAS and the DJI Z3 visual camera and DJI XTR thermal camera. Images were captured in a grid pattern (parallel and perpendicular) and the mode of capture was set to equal timed mode. Figure 4.18 shows the flight plans generated to capture the visual and thermal images of the building. Figure 4.19 shows the summary of the missions run at the site. The flight parameters

were set to achieve a GSD of 0.8cm/px, and image overlap of 80%, for the visual images, and a

GSD of 4.1cm/px and image overlap of 80%, for the thermal images, on top of the roof.
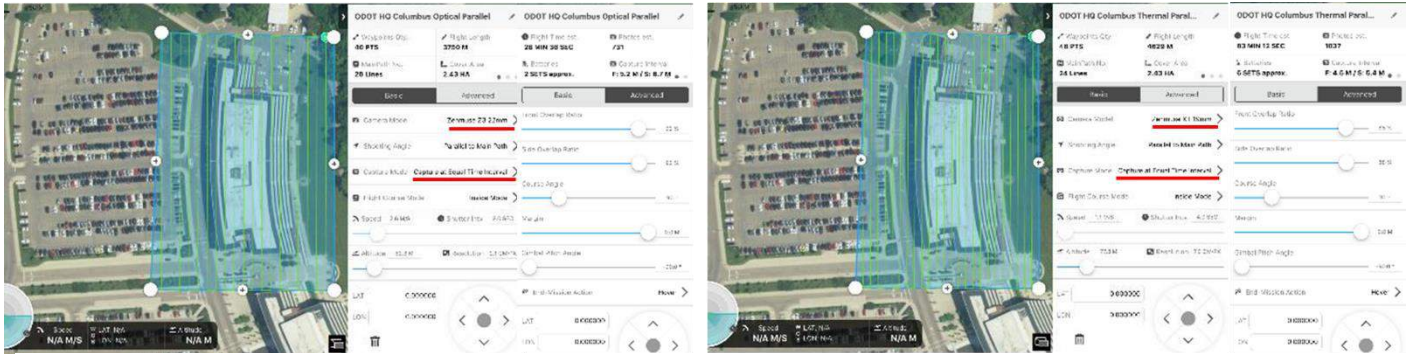
Figure 4.18: Screenshot of the Missions Conducted at ODOT HQ; Left: Visual Parallel, Right: Thermal Parallel

Image	Mission Type	GSD (cm/px)	Altitude (m)	FO/SO(%)	Flight Time	Recorded Photos
Visual	Parallel	2.06cm/px	52.3m	92%/92%	27min	731
	Perpendicular	2.06cm/px	52.3m	92%/92%	29min	791
Thermal	Parallel	6.96cm/px	77.82m	88%/88%	1hr 25min	1037
	Perpendicular	6.96cm/px	77.82m	88%/88%	1hr 25min	1038

Figure 4.19: Summary of Missions Conducted at ODOT Headquarters

Figure 4.20 shows the screenshot of the visual and thermal images captured, on the GeoSetter

application.
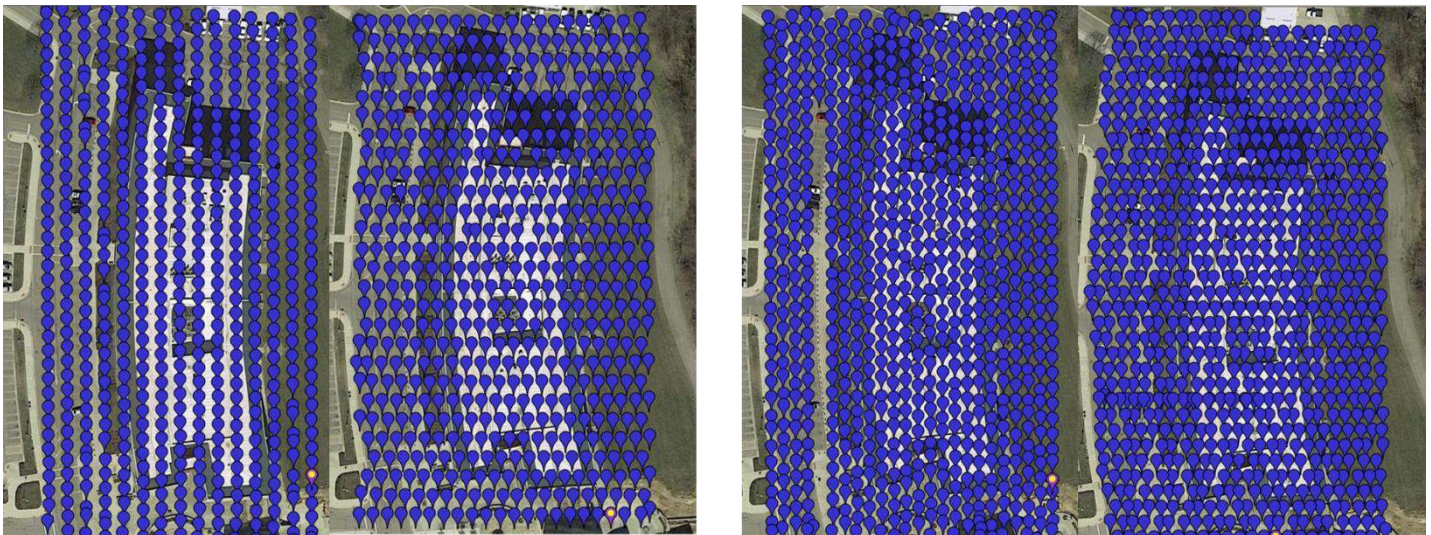
Figure 4.20: Images Captured for the ODOT HQ Case Study; Left: Visual Images, Right: Thermal Images

112

4.2.2 Processing and Analysis

The images captured were processed separately, using Pix4D Mapper. 3D point clouds and 2D orthomosaics using the visual and thermal images were generated without ground control points. The visual and thermal orthomosaics were cross-referenced to identify possible problem spots. Figure 4.21 and 4.22 show the outputs generated using the visual images. Figures 4.23 and 4.24 show the outputs generated using the thermal images.
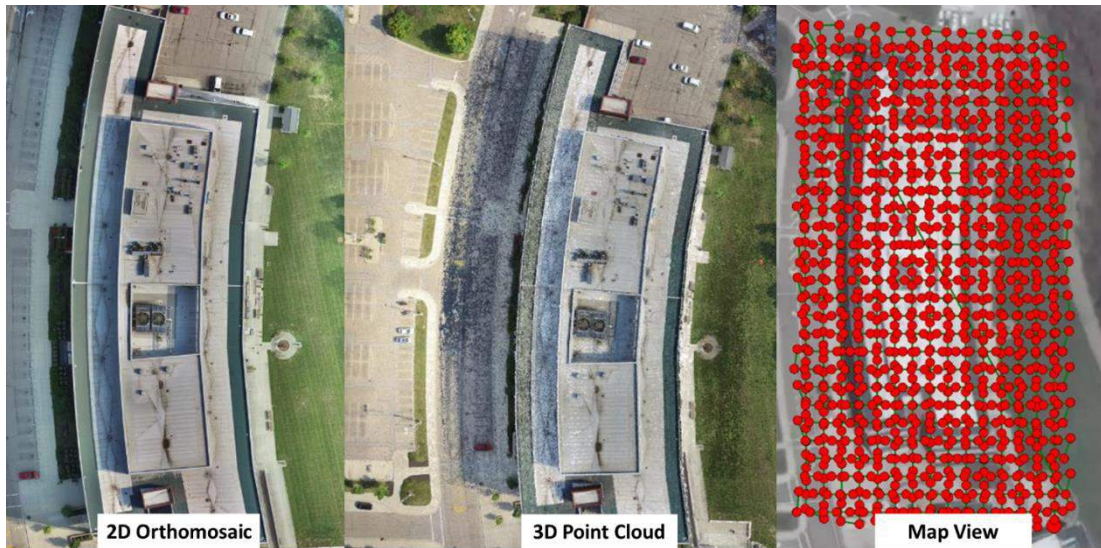
Figure 4.22: Top View of the Outputs Generated on Pix4D Mapper Using the Visual Images; Left: 2D Orthomosaic, Center: 3D Point Cloud, Right: Map View on Pix4D Mapper

Figure 4.21: 3D Views of the 3D Point Cloud Generated Using the Visual Images of ODOT HQ

113
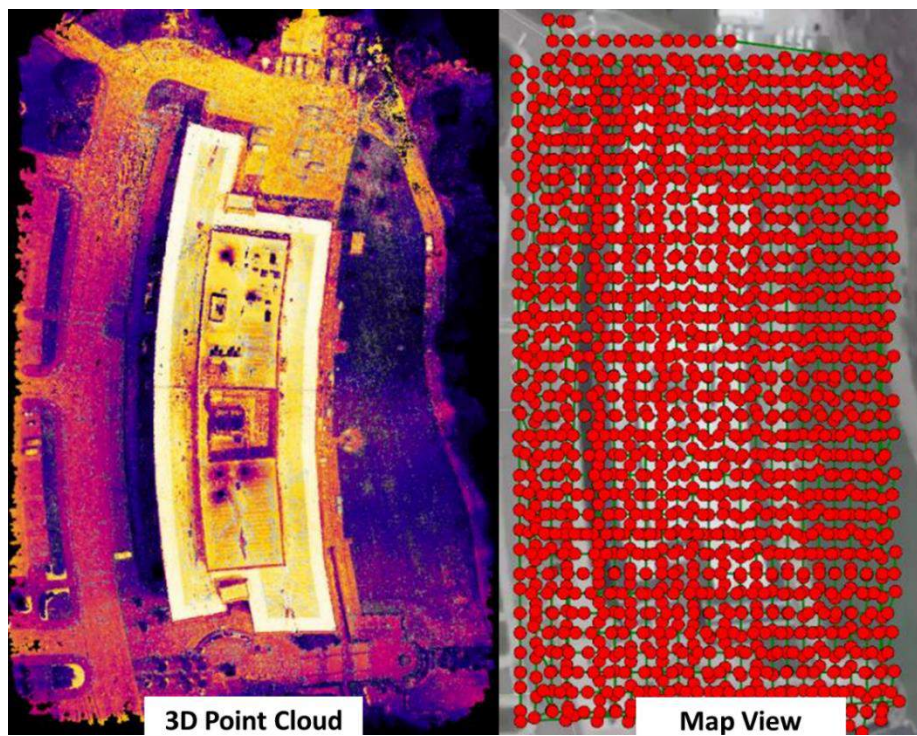
Figure 4.23: Top View of the Outputs Generated on Pix4D Mapper Using the Thermal Images; Left: 3D Point Cloud, Right: Map View on Pix4D Mapper
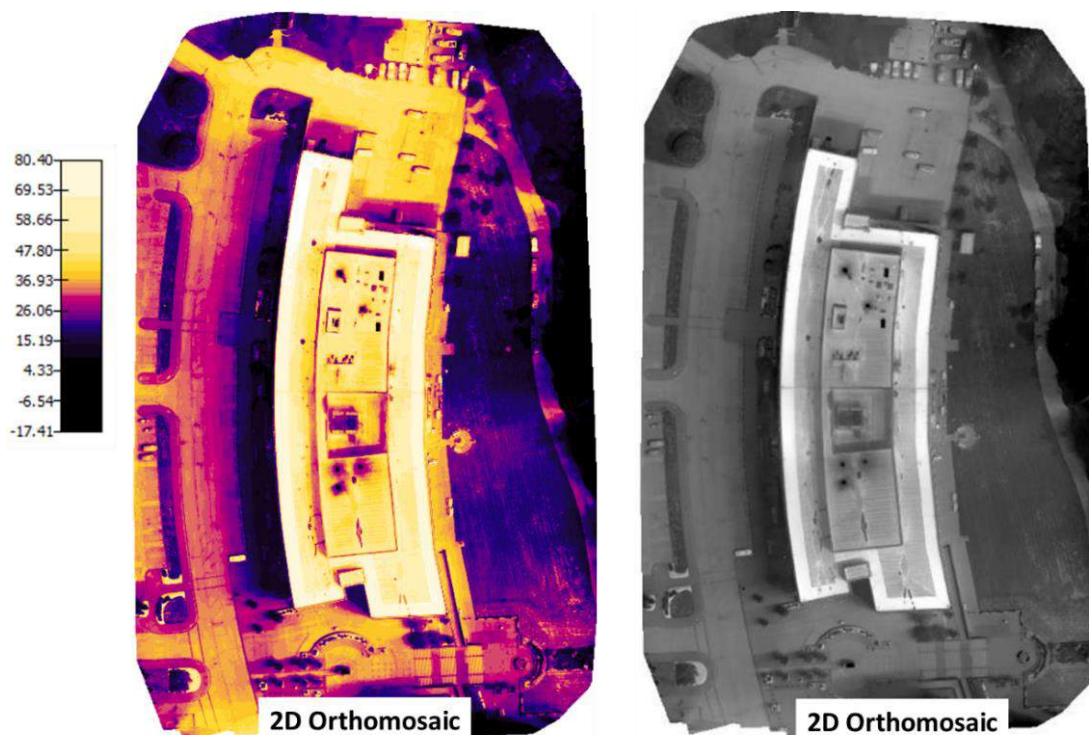
Figure 4.24: Top View of the Outputs Generated on Pix4D Mapper Using the Thermal Images; Left: 2D Orthomosaic with Reflectance Map, Right: 2D Orthomosaic without Reflectance Map

114

Analyzing the thermal orthomosaic it was observed the temperatures recorded varied greatly. This was mainly due to the presence of various objects, in the region mapped, that had a wide range of emissivity values.

4.2.3 Outputs

The thermal and visual orthomosaics were compared side by side (Figure 4.25) and trouble spots were identified and annotated on the Orthomosaic using Pix4D Cloud (Figure 4.26). Pix4D Mapper was also used to conduct an in-depth analysis where regions of interest were drawn on the orthomosaic and the individual images covering the area were analyzed. This also constrained the temperature scale on Pix4D, to the region analyzed (Figure 4.27). Using Pix4D outputs and Pix4D environment, multiple defects on the roof were identified and this helped the inspectors to gain a better understanding of the condition of the roof.

Possible wear in insulation due to its proximity to a drain hole
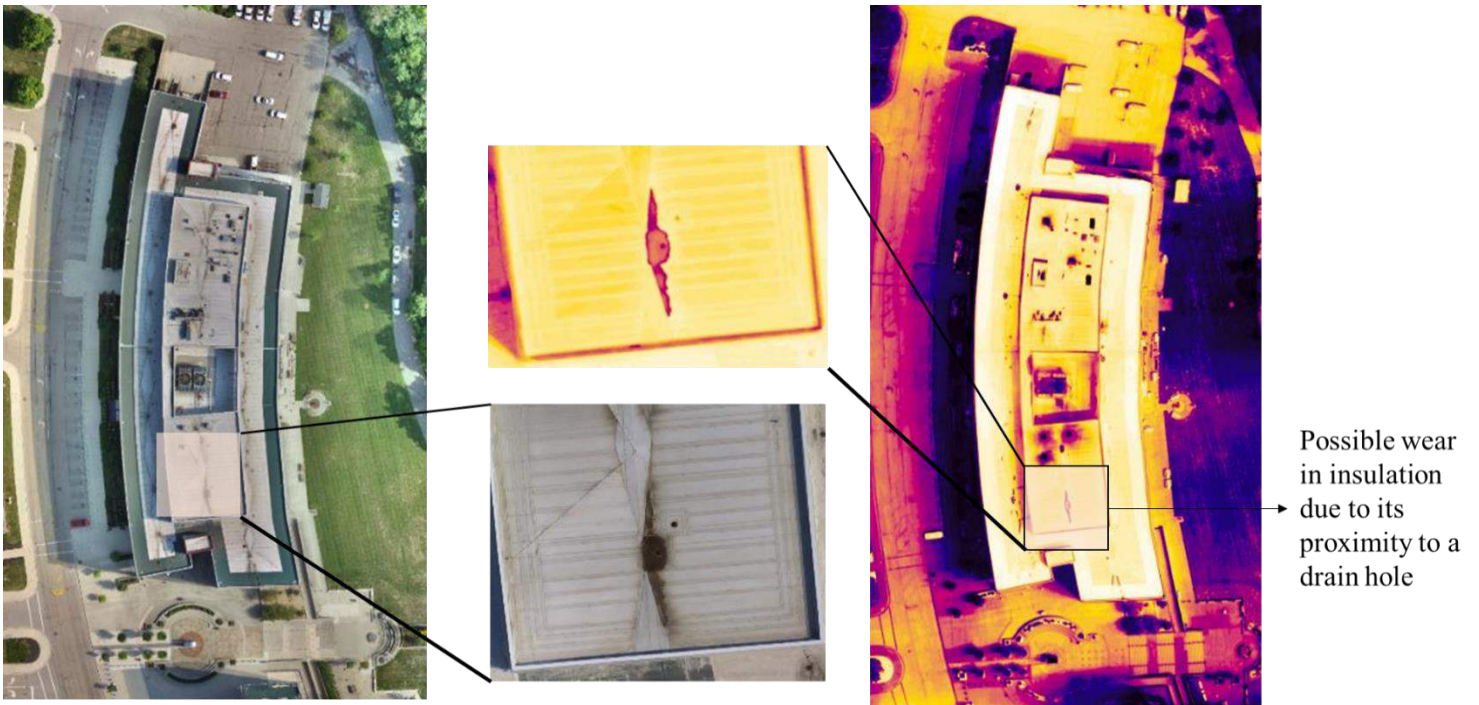
Figure 4.25: Cross Referring Visual and Thermal Images to Identify Problem Spots on the Roof
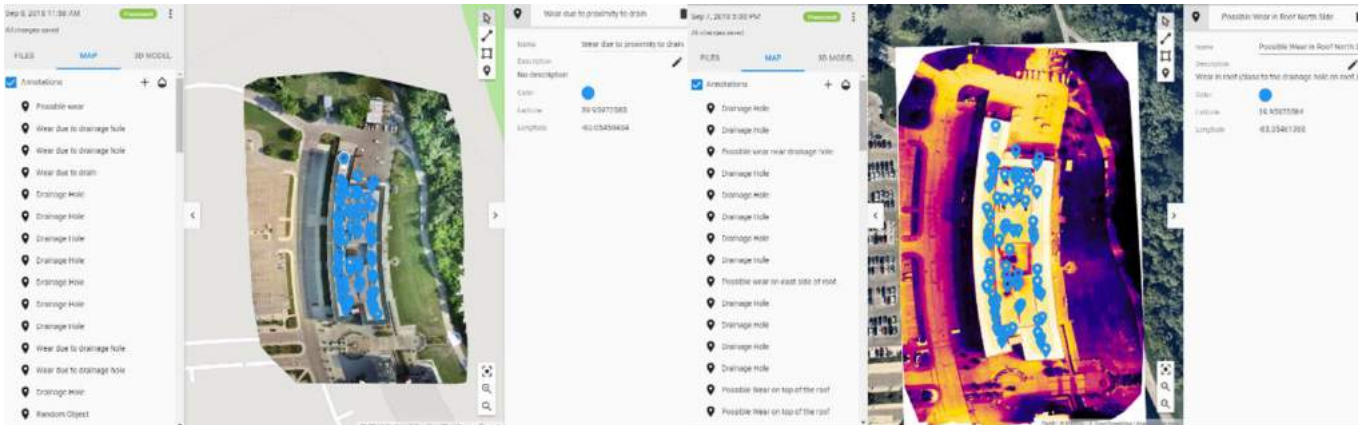
Figure 4.27: Visual and Thermal Orthomosaics Annotated Using Pix4D Cloud
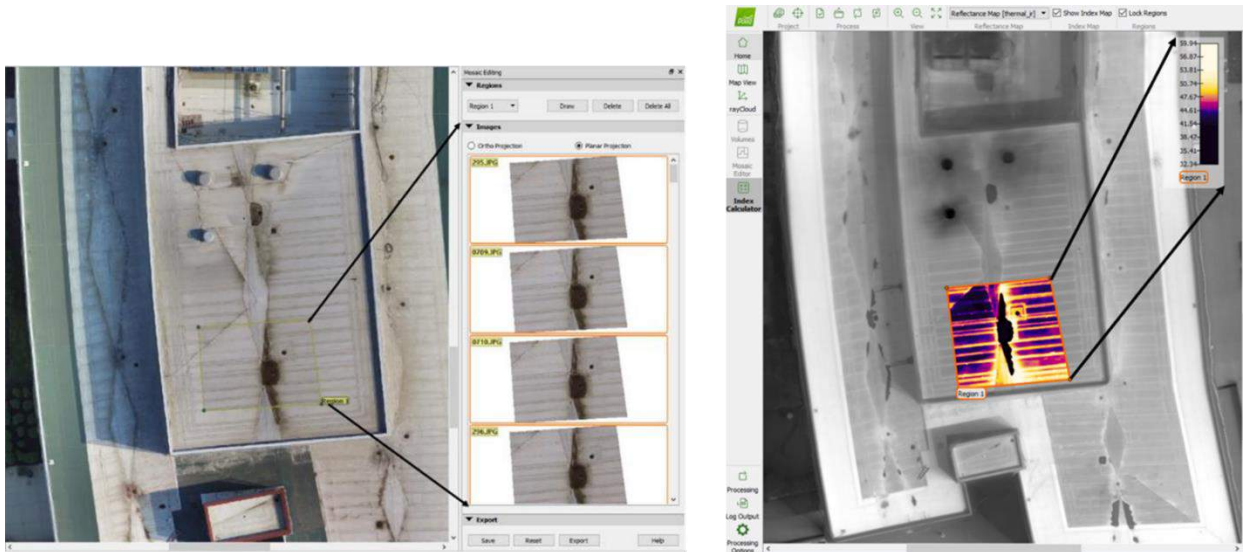
Figure 4.26: Regions of Interest Drawn on Visual and Thermal Orthomosaic on Pix4D Mapper

4.3 Case Study 3: Fosters Bridge Deck Inspection, Maineville D8

This section presents the case study conducted at Fosters Bridge in Maineville district 6 of the state of Ohio. The objective of this study was to map the bridge deck using oblique and nadir thermal images to identify delamination and compare the results obtained using both the datasets to the results obtained using the chain drag method. Thermal and visual images of the deck were captured to cross-refer identified delaminated regions.

4.3.1 Flight Plan and Image Capture

The plan sheets of the bridge were analyzed prior to designing flight plans. Due to issues of accessibility and line of sight, it was decided to map out the decks of spans 4 and 5 (Figure 4.28). For this case study, two types of missions were conducted. The first type involved capturing thermal and visual oblique images of the bridge when the bridge was open and functional. This was achieved by capturing images in a single line along the side of the bridge at different camera angles. The second type involved capturing thermal and visual nadir images when the bridge was closed. This was done when ODOT bridge inspectors closed the bridge for their routine inspections. The inspection was done lane wise while traffic was controlled in the second lane. Bridge inspectors inspected the bridge for delamination using the chain dragging method, and the trouble spots were marked using white paint. The visual nadir images of the marked deck were captured to compare the delamination identified using the nadir thermal images.
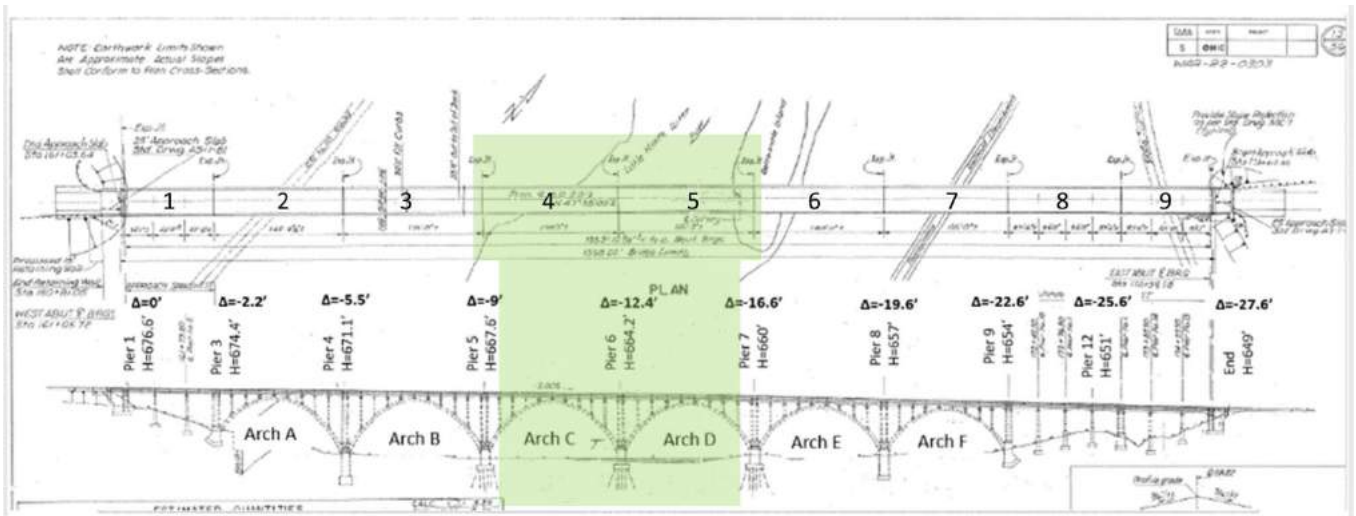
Figure 4.28: Fosters Bridge Plan Sheet

Using the information in the plan sheets a rough scaled illustration was created to understand the oblique thermal and visual image footprints. Thermal and visual images of the bridge deck were captured from both the north and south side of the bridge. DJI Matrice 100 sUAS and DJI XTR

thermal camera and DJI X5 15mm visual cameras were used to capture the images. Figure 4.29

shows the illustrations for the DJI XTR camera that was used to generate the necessary flight

plans. The flight parameters (flight position and camera angle) were set to obtain thermal images

captured with average GSDs of 2.1cm/px (45^0), 2.4cm/px (47^0) and 2.7cm/px (50^0) respectively

and 80% image side overlap and 95% top and bottom image overlap on the bridge deck. Figure

4.30 shows the illustrations for the DJI X5 15mm lens camera that was used to generate the

necessary flight plans. If flight parameters (flight position and camera angle) were set to obtain

visual images with average GSDs of 2.1cm/px (45^0), 2.4cm/px (47^0) and 2.7cm/px (50^0)

respectively and 80% image side overlap and 95% top and bottom image overlap on the bridge

deck. The camera angles on DJI GS Pro is set by changing the gimbal pitch angle option. The

gimbal pitch angle on the application is measured with respect to the horizon and care was taken

to set the required angles on the application. Figure 4.31 shows the flight plans generated to

capture oblique visual and thermal images at an angle of 45^0. Figure 4.32 shows the flight plans

generated to capture nadir visual and thermal images for each lane. Figure 4.33 shows the

summary of the missions run at the site.
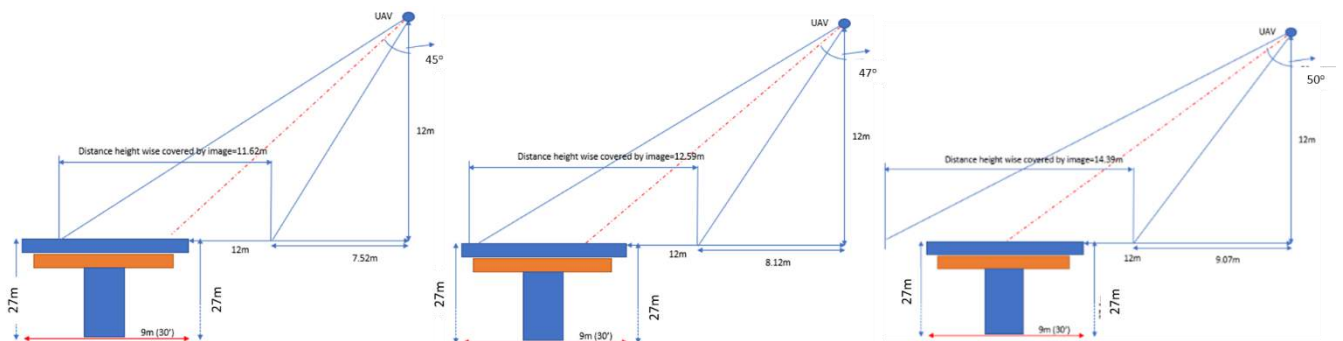
Figure 4.29: DJI XTR Thermal Oblique Image Footprint Illustration; Left: 45^0, Center: 47^0, Right: 50^0

Figure 4.30: DJI X5 Visual Oblique Image Footprint Illustration; Left: 45+, Center: 47^0, Right: 50^0
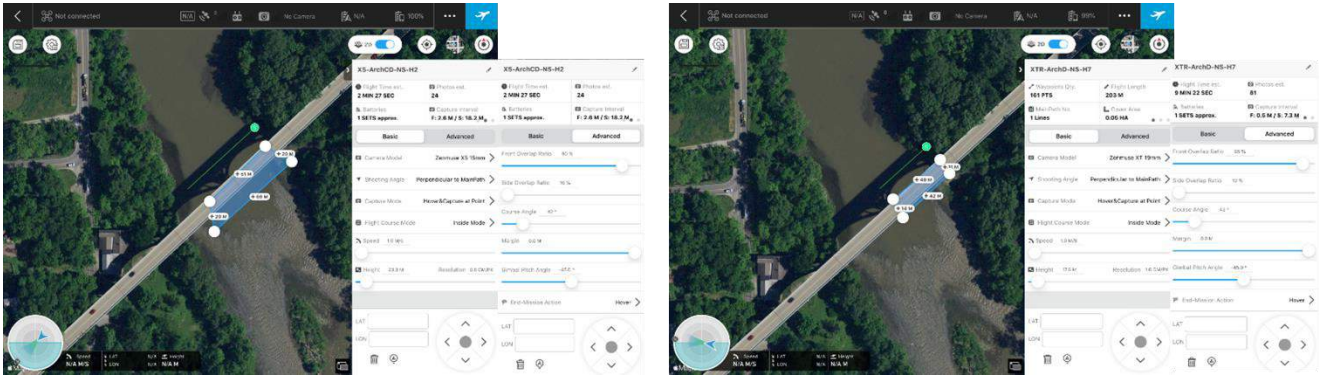
Figure 4.31: DJI GS Pro Flight Plan to Capture Oblique Images for the Fosters Bridge Case Study; Left: Visual Images, Right: Thermal Images
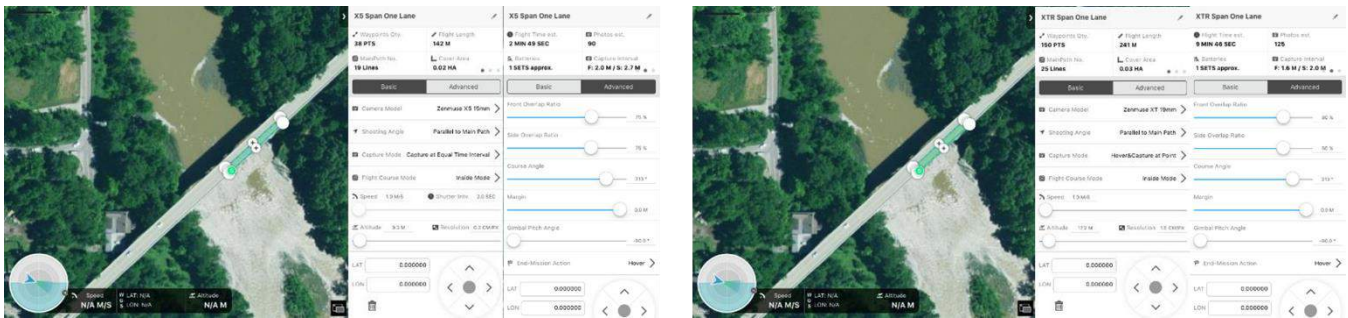
Figure 4.32: DJI GS Pro Flight Plan to Capture Nadir Images for the Fosters Bridge Case Study; Left: Visual Images, Right: Thermal Images

Image	Mission Type	Avg. GSD (cm/px)	Distance from Face/Above Deck (m)	Side Overlap (%)	Flight Time	Recorded Photos
Visual (North and South Sides)	Oblique (45^0)	0.54cm/px	10m/10m	90%	6min	90
	Oblique (47^0)	0.6cm/px	10m/10m	90%	6min	90
	Oblique (50^0)	0.72cm/px	10m/10m	90%	6min	90
Thermal (North and South Sides)	Oblique (45^0)	2.1cm/px	12m/12m	95%	20min	160
	Oblique (47^0)	2.4cm/px	12m/12m	95%	20min	164
	Oblique (50^0)	2.7cm/px	12m/12m	95%	20min	162

Image	Mission Type	Avg. GSD (cm/px)	Altitude (m)	FO/SO (%)	Flight Time	Recorded Photos
Visual	Nadir Parallel	0.2cm/px	9.3m	75%/75%	6min	180
Thermal	Nadir Parallel	1.5cm/px	17.2m	80%/80%	20min	250

Figure 4.33: Summary of Missions Conducted at Fosters Bridge

119

4.3.2 Processing and Analysis

The visual images were processed on Pix4D Mapper and the bridge deck's 3D point cloud and orthomosaic were generated. The outputs, using Pix4D Mapper, were generated without GCPs or scale constraints. Figure 4.34 shows the 3D model of the bridge deck. The thermal images were analyzed using FLIR Tools and Microsoft Word. The contrast of the thermal images was corrected to analyze the temperature differences on the bridge deck easily. The corrected images were laid out side by side on Microsoft Word and the delaminated regions were identified. Figure 4.35 shows the process followed to analyze the thermal images. The detected delaminated regions were then marked on the orthomosaic (Figure 4.36) generated using the 3D point cloud.
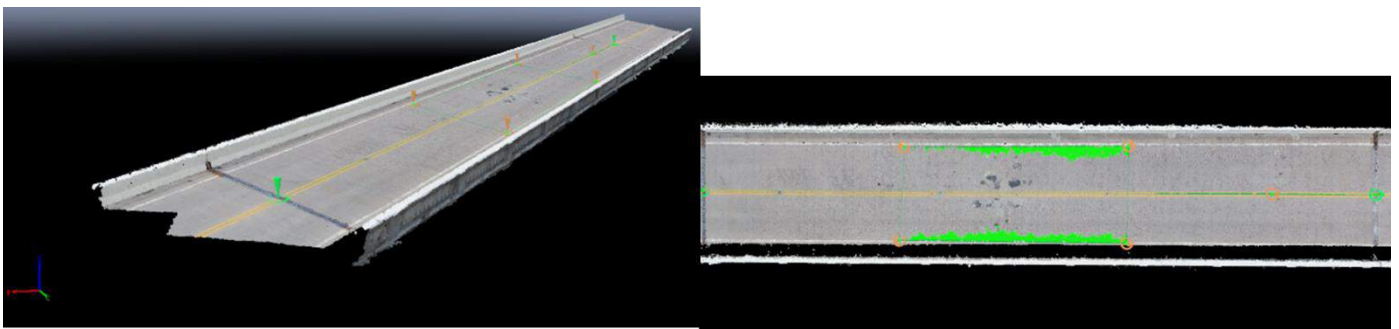
Figure 4.34: 3D Model of Fosters Bridge Deck Spans 4 and 5
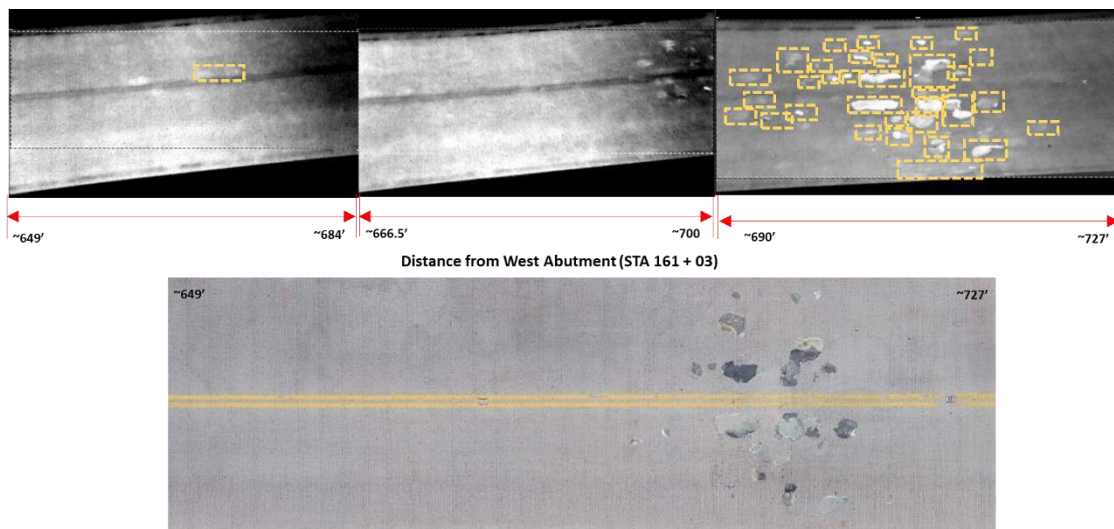
Figure 4.35: Thermal Image Analysis of the Fosters Bridge Deck; Top: Thermal Images Marked, Bottom: Portion of Visual 2D Orthomosaic
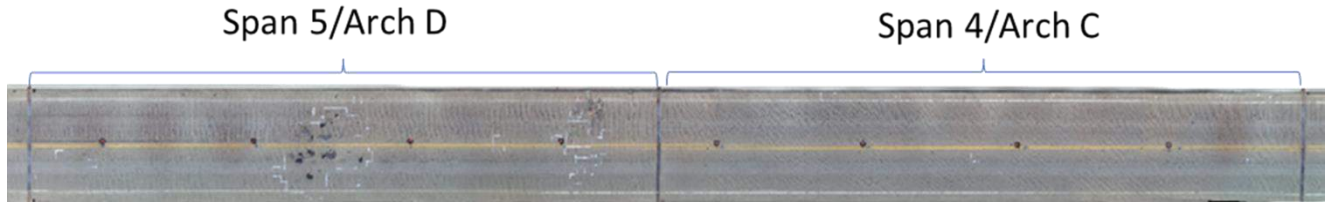
Figure 4.36: Visual 2D Orthomosaic of Fosters Bridge Deck

4.3.3 Outputs

The captured thermal images were analyzed and detected delaminated regions were marked on the visual orthomosaic. Figure 4.37 shows the comparison between the inspector marking and the markings obtained by analyzing the nadir thermal images of Span 4. The figure shows the percentage of area covered by the defects and indicates if the defects were seen or not on the results compared.
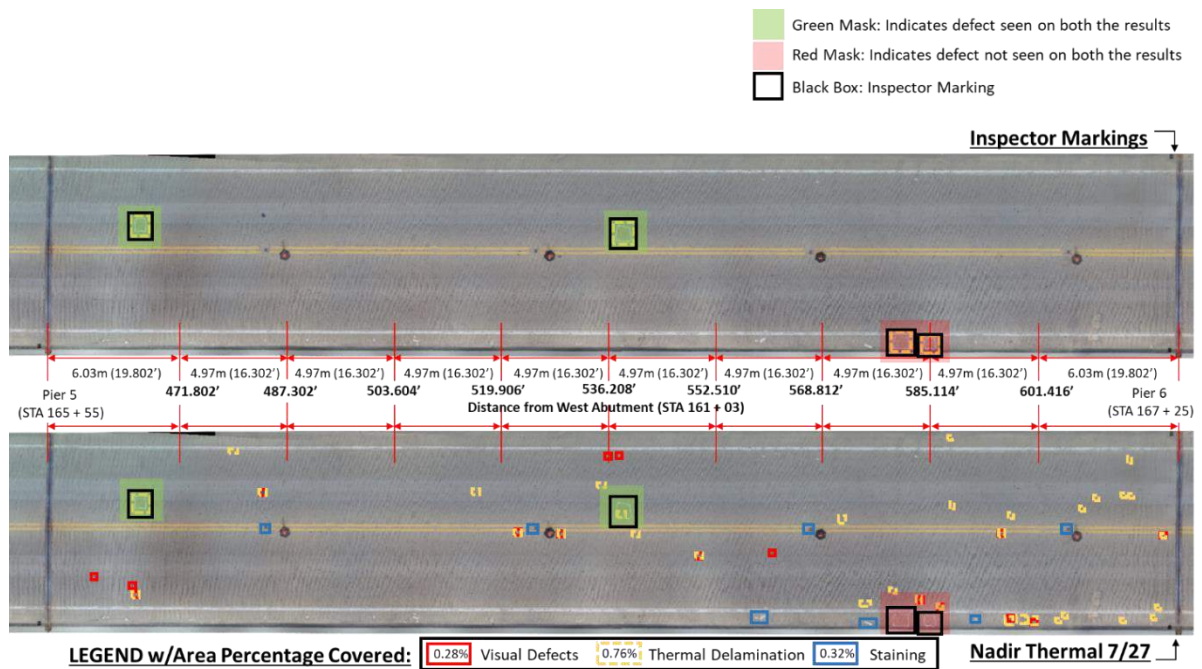
Figure 4.37: Delamination Marking Comparison of Span 4; Top: Inspector Markings, Bottom: Nadir Thermal Images

Figure 4.38 shows the comparison between the inspector marking and the markings obtained by analyzing the oblique thermal images of Span 4. The figure shows the percentage of area covered by the defects and indicates if the defects were seen or not on the results compared.

121
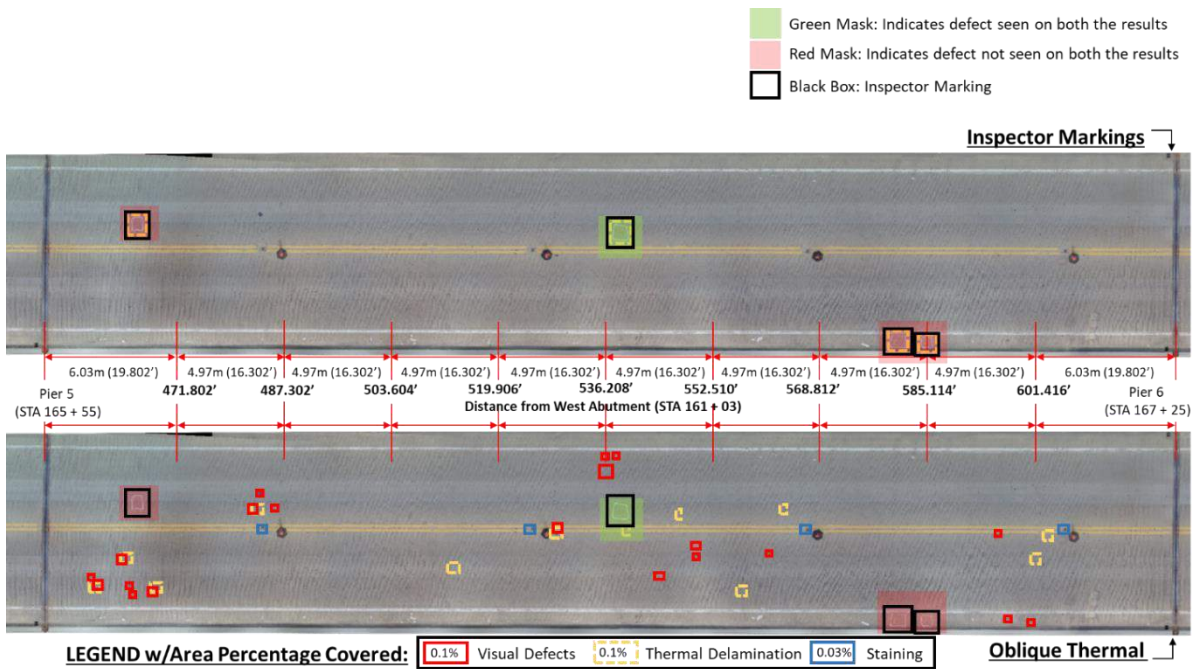
Figure 4.38: Delamination Marking Comparison of Span 4; Top: Inspector Markings, Bottom: Oblique Thermal Images

Figure 4.39 shows the comparison between the markings obtained by analyzing nadir thermal images and oblique thermal images of Span 4. The figure shows the percentage of area covered by the defects and indicates if the defects were seen or not on the results compared.
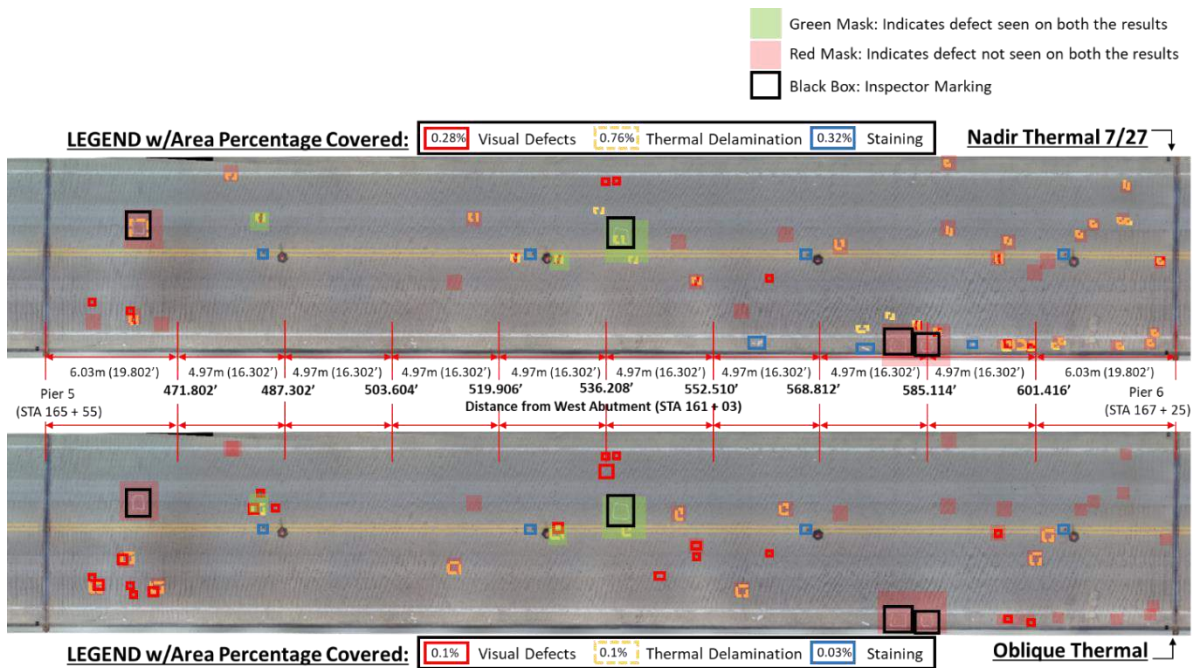
Figure 4.39: Delamination Marking Comparison of Span 4; Top: Nadir Thermal Images, Bottom: Oblique Thermal Images

122

Figure 4.40 shows the comparison between the inspector marking and the markings obtained by analyzing the nadir thermal images of Span 5. The figure shows the percentage of area covered by the defects and indicates if the defects were seen or not on the results compared.
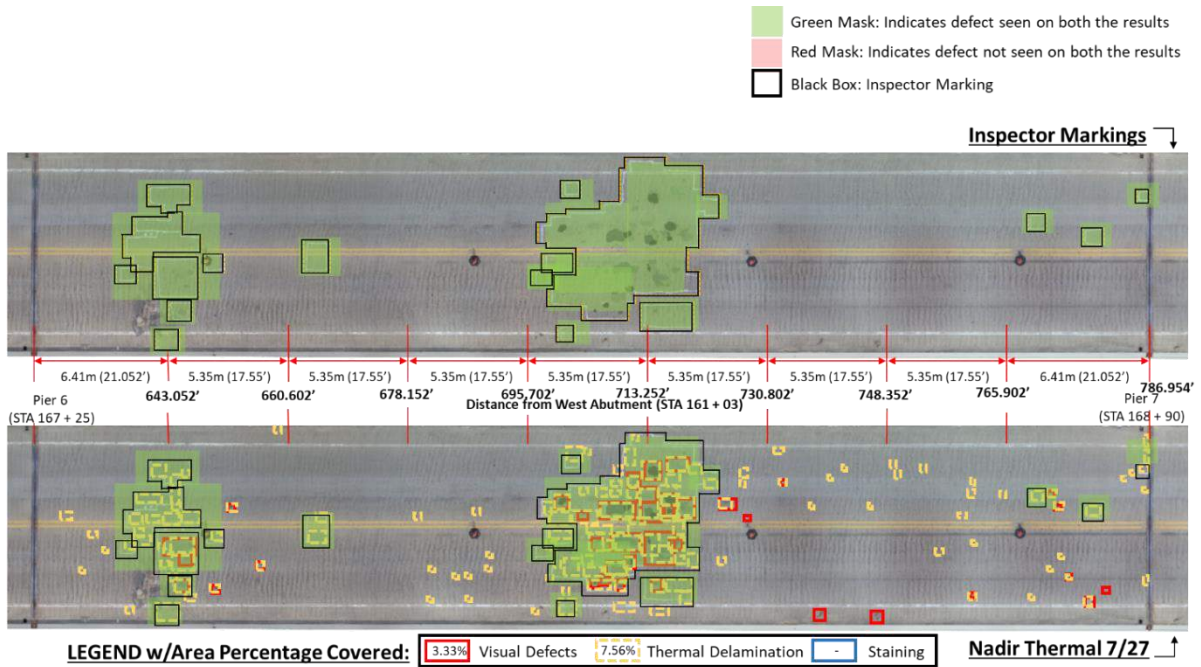
Figure 4.40: Delamination Marking Comparison of Span 5; Top: Inspector Markings, Bottom: Nadir Thermal Images

Figure 4.41 shows the comparison between the inspector marking and the markings obtained by analyzing the oblique thermal images of Span 5. The figure shows the percentage of area covered by the defects and indicates if the defects were seen or not on the results compared.
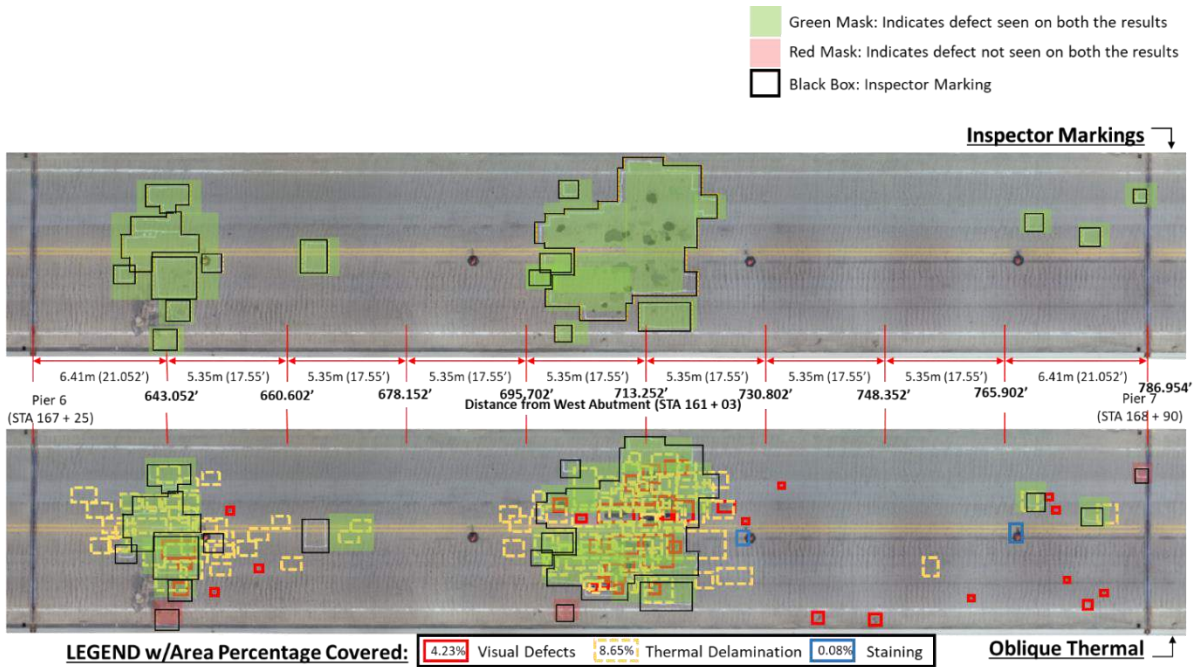
Figure 4.41: Delamination Marking Comparison of Span 5; Top: Inspector Markings, Bottom: Oblique Thermal Images

Figure 4.42 shows the comparison between the markings obtained by analyzing nadir thermal images and oblique thermal images of Span 4. The figure shows the percentage of area covered by the defects and indicates if the defects were seen or not on the results compared.
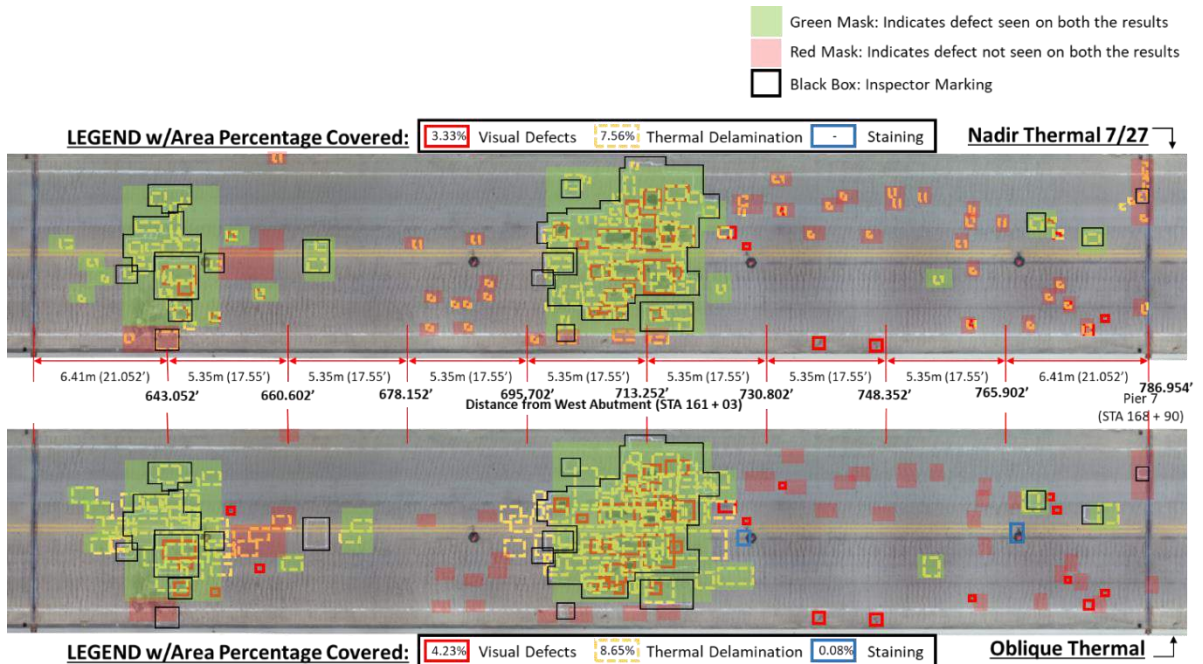
Figure 4.42: Delamination Marking Comparison of Span 5; Top: Nadir Thermal Images, Bottom: Oblique Thermal Images

The results obtained from this study show that a good estimation of delaminated regions can be obtained using oblique thermal images without closing the bridge or obstructing traffic. Analysis of the results shows that few spots marked by the inspector, on Span 4, were not visible in the oblique thermal images captured. Nadir and oblique thermal images captured almost all the marked delaminated regions, but the nadir thermal images were able to capture finer temperature changes when compared to oblique thermal images.

4.4 Case Study 4: Jeremiah Morrow Bridge Segment Modelling, Oregonia D8

This section presents the case study conducted at Jeremiah Morrow bridge in Oregonia district 6 of the state of Ohio. The objective of this study was to generate high-resolution 3D models of the bridge segments, that would allow inspectors to monitor the cracking on bridge segments. Visual images of the bridge segments were captured at GSDs close to 0.3mm/px to generate high-resolution 3D models.

4.4.1 Flight Plan and Image Capture

To capture images with GSDs close to 0.3mm/px the sUAS must be flown close to the bridge, and as it moves closer to a structure the accuracy of the on-board GPS starts to decrease. The decrease in GPS accuracy will affect the positioning of the sUAS midair and as a result, one will not be able to generate automated missions using DJI GS Pro. To obtain the necessary images the sUAS was flown manually. The images of the bridge segments were captured using DJI Matrice 210 sUAS and DJI X5s 45mm camera. The first-person view (FPV) and the ultrasonic sensor on-board the Matrice 210 helped the pilots to maintain the safe and necessary distance from the structure. Given the height of the bridge (~240 feet) these sensors aided in maintaining

the flight perspective during image capture. The bridge segments mapped were identified by an ODOT inspector and are marked in the bridge plan sheet shown in Figure 4.43. Jeremiah Morrow consists of two bridges, northbound and southbound, and the outer segments of both the bridges were mapped in this study. Among the eight segments that were mapped in this study, one of the segments (P2-3D on the southbound bridge) was inspected and the inspector marked all the cracks visible, which was later used to visually check the accuracy of the generated 3D model. The inscriptions on the segment aided to estimate the required GSD for the missions. The measurement 0.012" was inscribed beside the markings on the segment and was used to decide the distance of flight away from the face of the segment. Since the DJI X5s 45mm camera was used to capture images it was decided to fly at 4m away from the face to obtain a GSD of 0.3mm/px. The ultrasonic sensor on the Matrice 210 sUAS was used to maintain the required distance from the segment. The images were captured in the recommended pattern and with enough overlaps. Figure 4.44 shows the positions of the cameras as estimated by Pix4D Mapper.
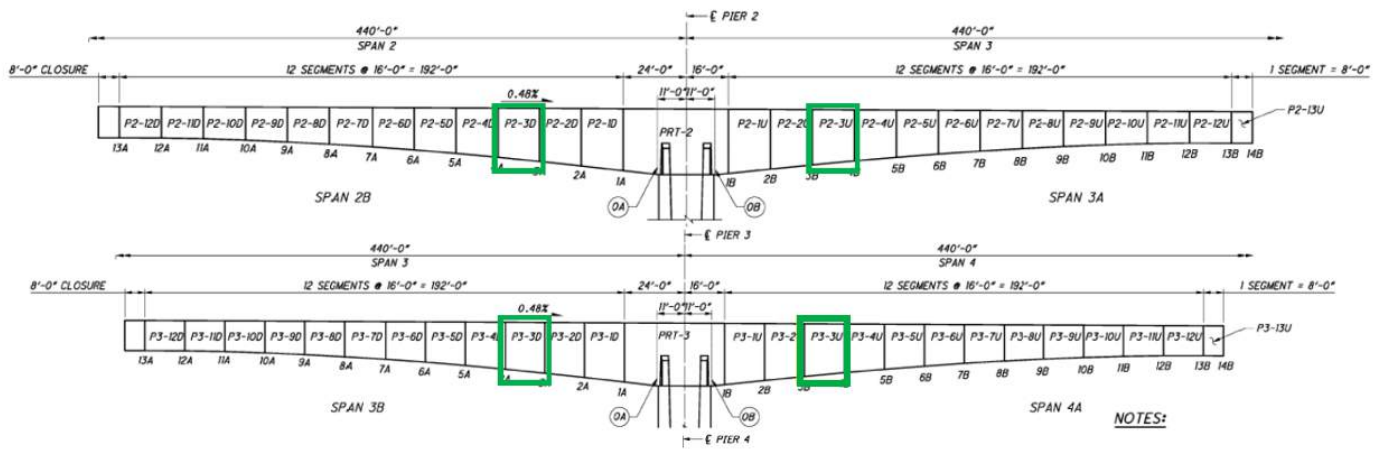
Figure 4.43: Jeremiah Morrow Bridge Segment Plan Sheets with Mapped Segments Marked
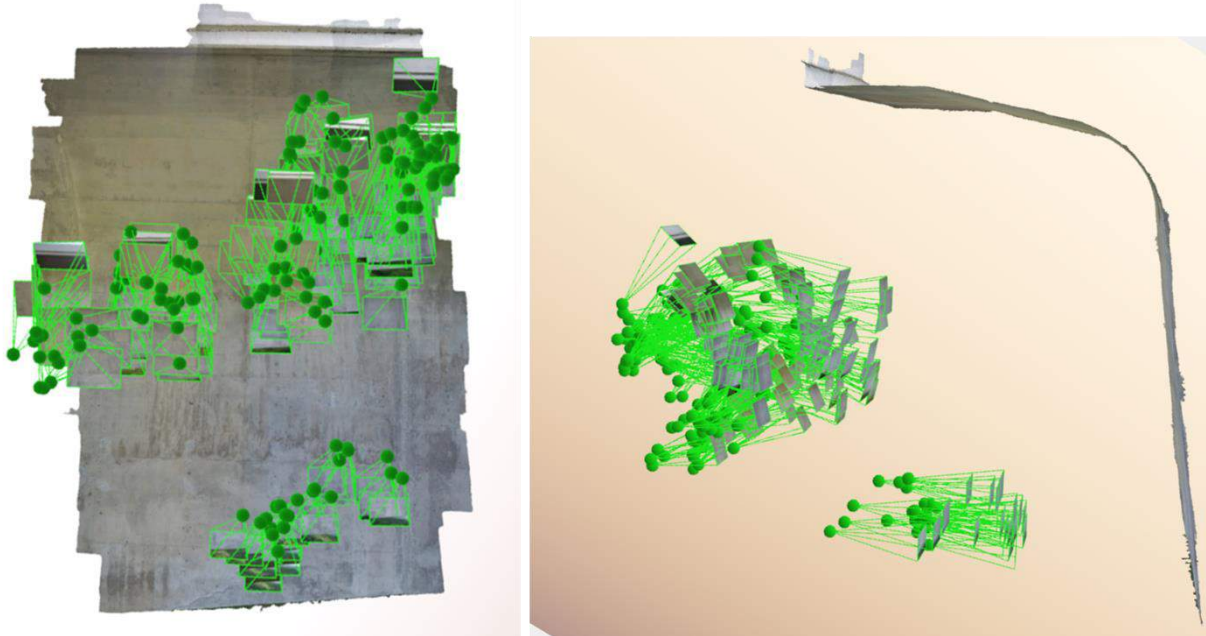
Figure 4.44: Camera Positions Estimated Using Pix4D Mapper

4.4.2 Processing and Analysis

The captured images were first analyzed before processing and images that were blurry or out of focus were removed from the dataset. This was a necessary step since the image capture process was manual. The images of the P2-3D segment on the southbound bridge were processed first using Pix4D Mapper. The initial model was processed using manual tie points (MTP) and without image geotags. Fifteen MTPs were added uniformly along the corners and the center of the dataset. Figure 4.45 shows the 3D point cloud that was generated using the fifteen MTPs and it was seen that a few points along the curve of the segment were not correctly positioned. The green points visible in the 3D point cloud indicates the positions of the MTPs.
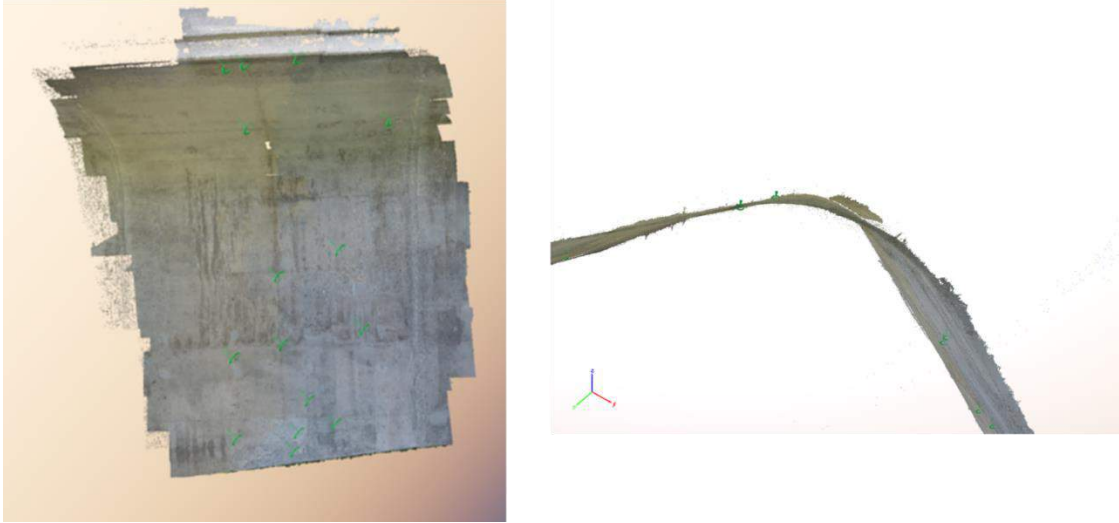
Figure 4.45: Pix4D 3D Point Cloud Generated Using 15 MTPs

The model was reprocessed by adding four more MTPs around the region where the points were not positioned correctly. Figure 4.46 shows the new point cloud generated using nineteen MTPs, and the new point cloud was used to generate the 3D mesh model in the .obj file format (Figure 4.47).
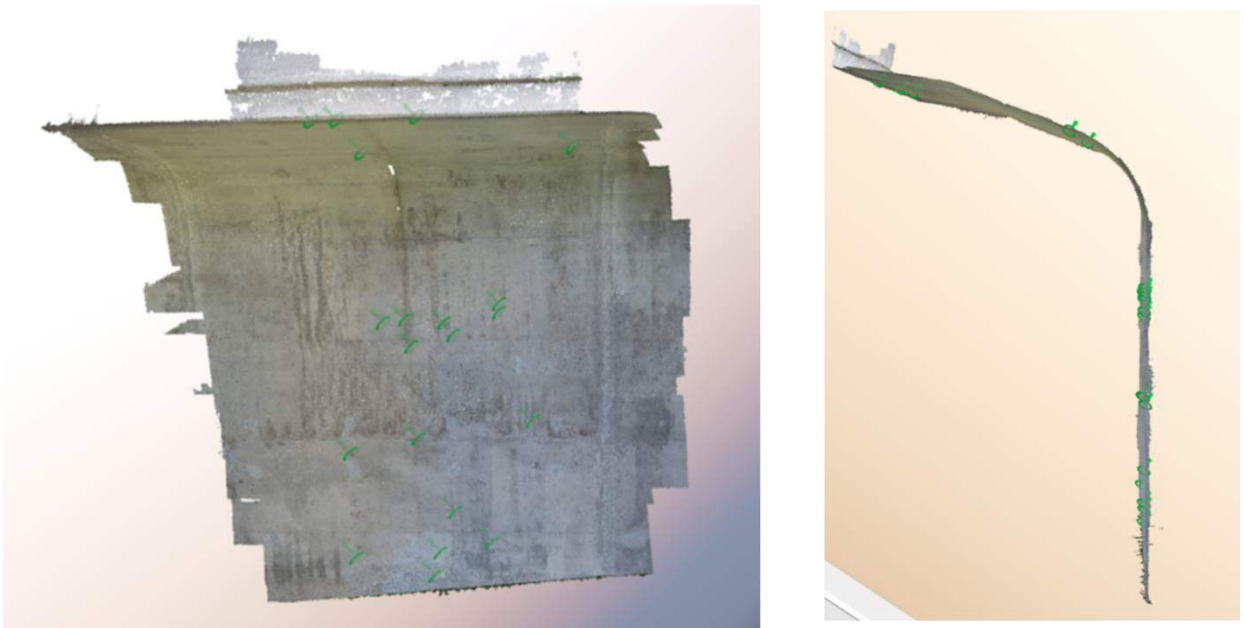
Figure 4.46: Pix4D 3D Point Cloud Generated Using 19 MTPs
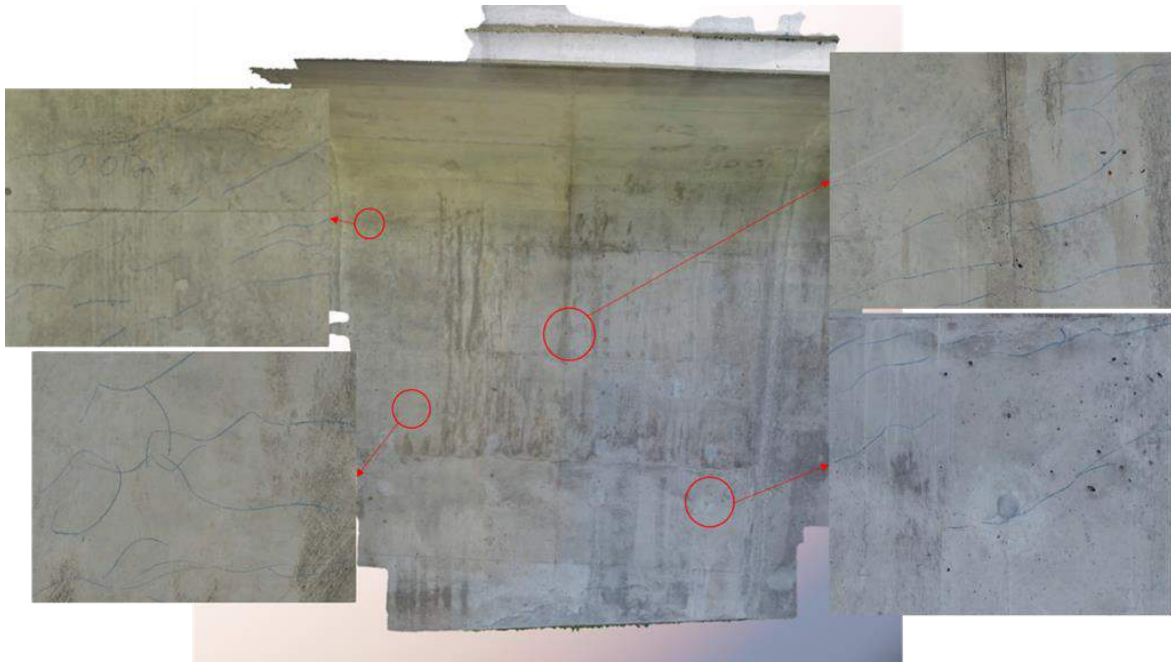
Figure 4.47: Pix4D 3D Mesh Model of Segment P2-3D on the Southbound Bridge

The image dataset, of segment P2-3D on the southbound bridge, was reprocessed using Context
Capture without image geotags and with nineteen MTPs. Figure 4.48 shows the 3D mesh model
generated using Context Capture in the .3mx file format.
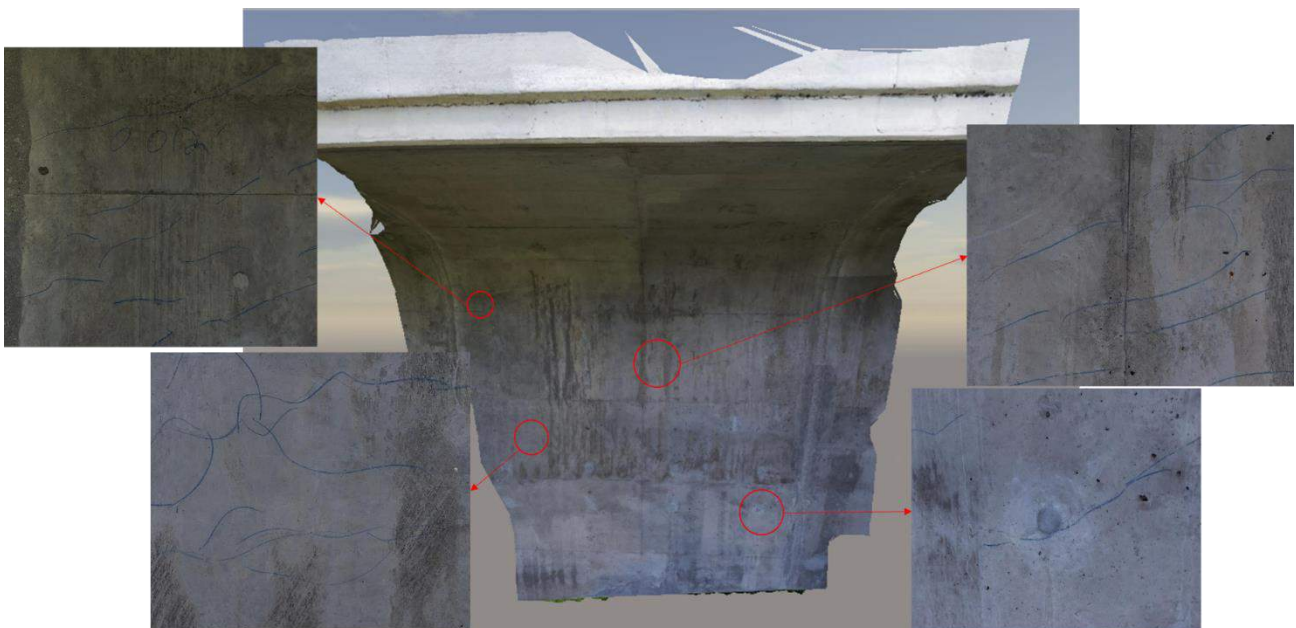
Figure 4.48: Context Capture 3D Mesh Model of Segment P2-3D on the Southbound Bridge

Context Capture was used to generate the 3D mesh model of the segment in three different file formats (obj, .dgn, and .3mx). The quality of the three models was visually compared to find out the best file format (Figure 154). Comparing the models in Figure 4.49 it was evident that the .3mx file format produces the best 3D mesh model. The CAD format (.dgn), and object format (.obj) files are commonly used and can be viewed using multiple third-party applications. Whereas the Context Capture reality mesh format (.3mx) is a proprietary file format and can be only viewed using Bentley products.
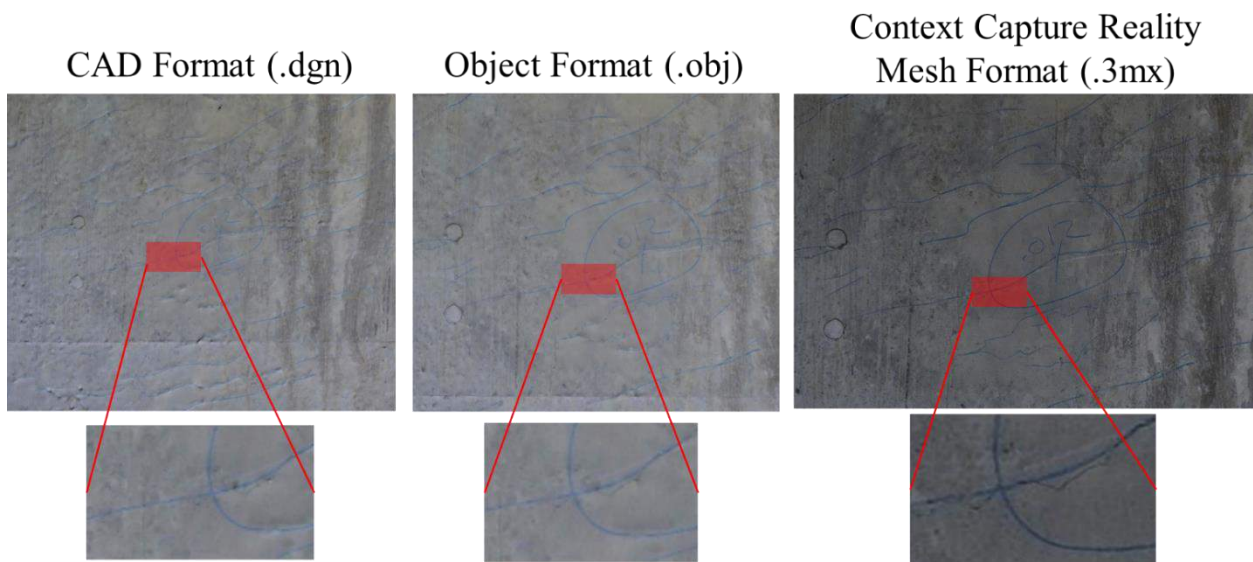
Figure 4.49: Comparison of 3D Mesh Model in Different File Formats; Left: CAD Format (.dgn), Center: Object Format (.obj), Right: Context Capture Reality Mesh Format (.3mx)

4.4.3 Outputs

Using the 3D model of the P2-3D segment on the southbound bridge, the orthofacades of the segments were generated. Figure 4.50 shows the orthofacade generated using Pix4D Mapper's orthoplane tool. The orthofacade of the 3D mesh model generated using Context Capture was created using Bentley's MicroStation. The .3mx mesh file was imported to MicroStation and the orthofacade (Figure 4.51) was generated using the available section tool. The process to generate the segment's orthofacade was easier using Pix4D Mapper.

Figure 4.50: Pix4D Orthofacade of Segment P2-3D on the Southbound Bridge

Figure 4.51: Context Capture Orthofacade of Segment P2-3D on the Southbound Bridge

Given the quality of the 3D mesh model generated using Context Capture, the image dataset of

the remaining segments was processed using Context Capture. The images were processed

without image geotags and MTPs were added uniformly along the corners and the center of the

dataset. Figures 4.52 to 4.58 show the 3D mesh models generated using the remaining dataset.
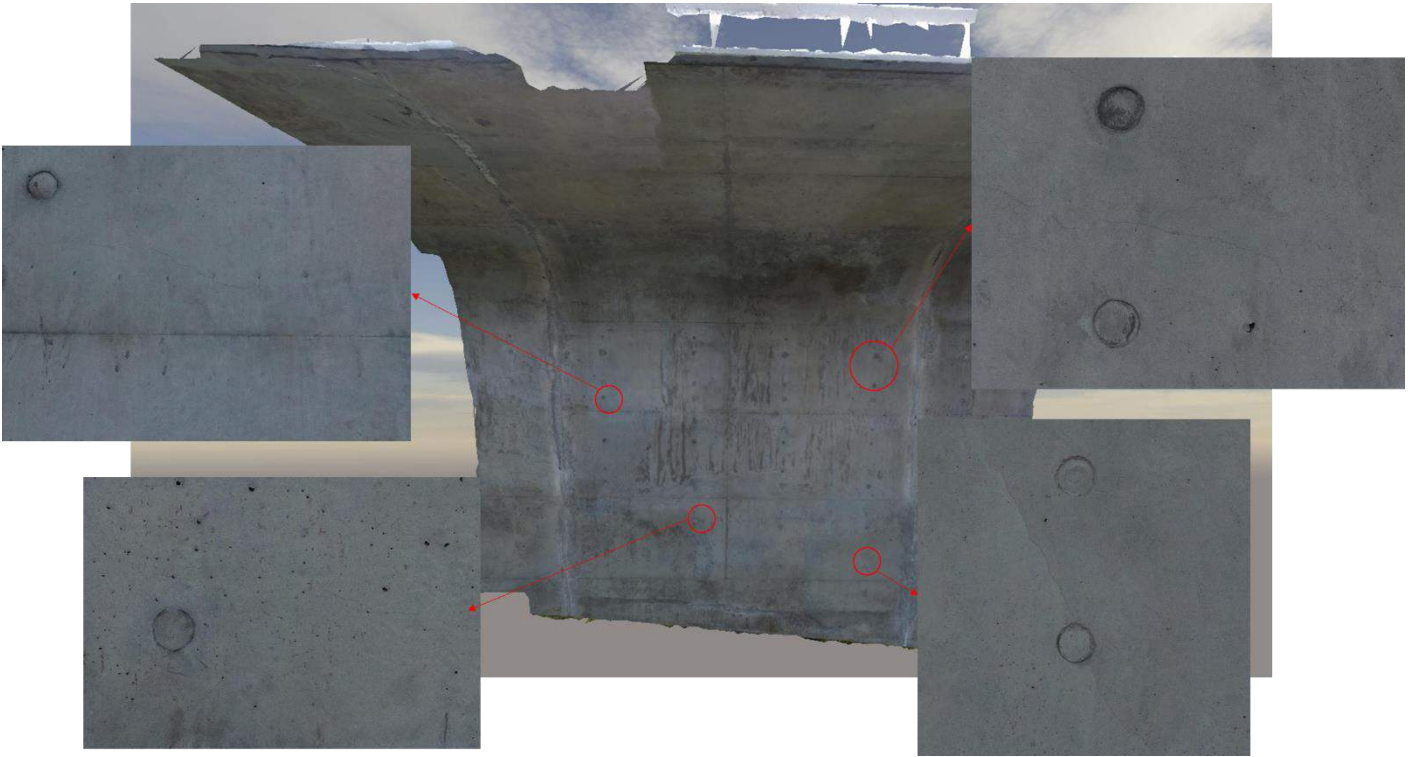
Figure 4.52: Context Capture 3D Mesh Model of Segment P2-3D on the Northbound Bridge

Figure 4.53:Context Capture 3D Mesh Model of Segment P2-3U on the Southbound Bridge
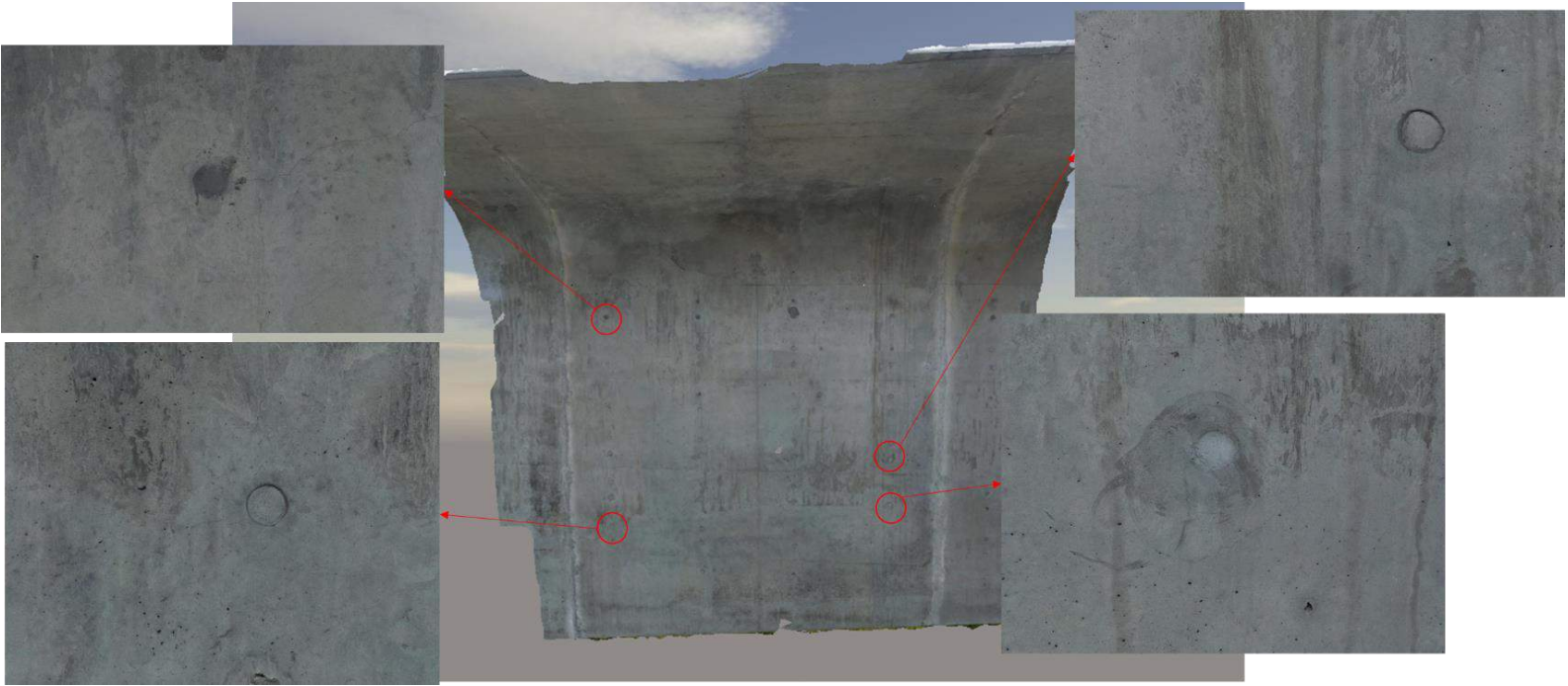
Figure 4.54: Context Capture 3D Mesh Model of Segment P2-3U on the Northbound Bridge

Figure 4.55: Context Capture 3D Mesh Model of Segment P3-3D on the Southbound Bridge
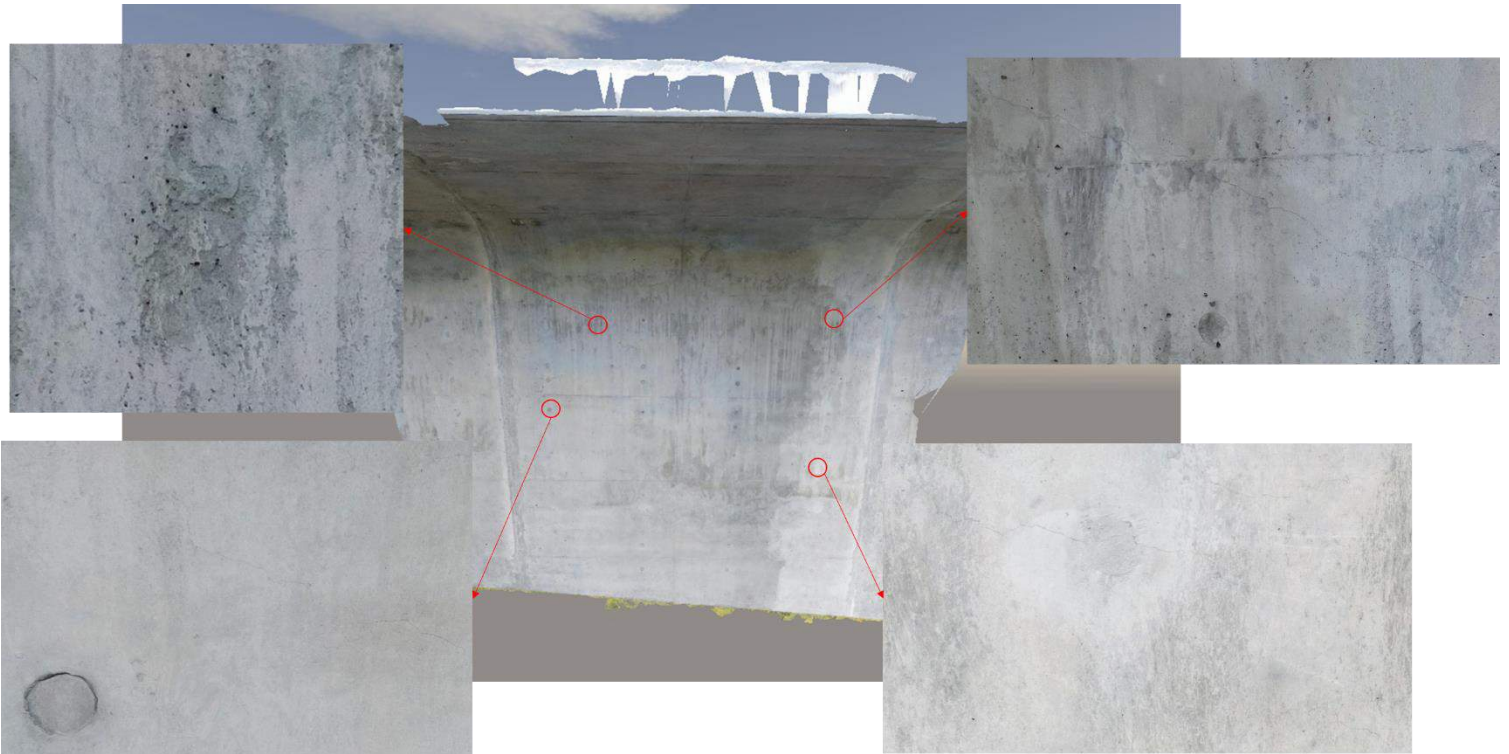
Figure 4.56: Context Capture 3D Mesh Model of Segment P3-3D on the Northbound Bridge

Figure 4.57: Context Capture 3D Mesh Model of Segment P3-3U on the Southbound Bridge
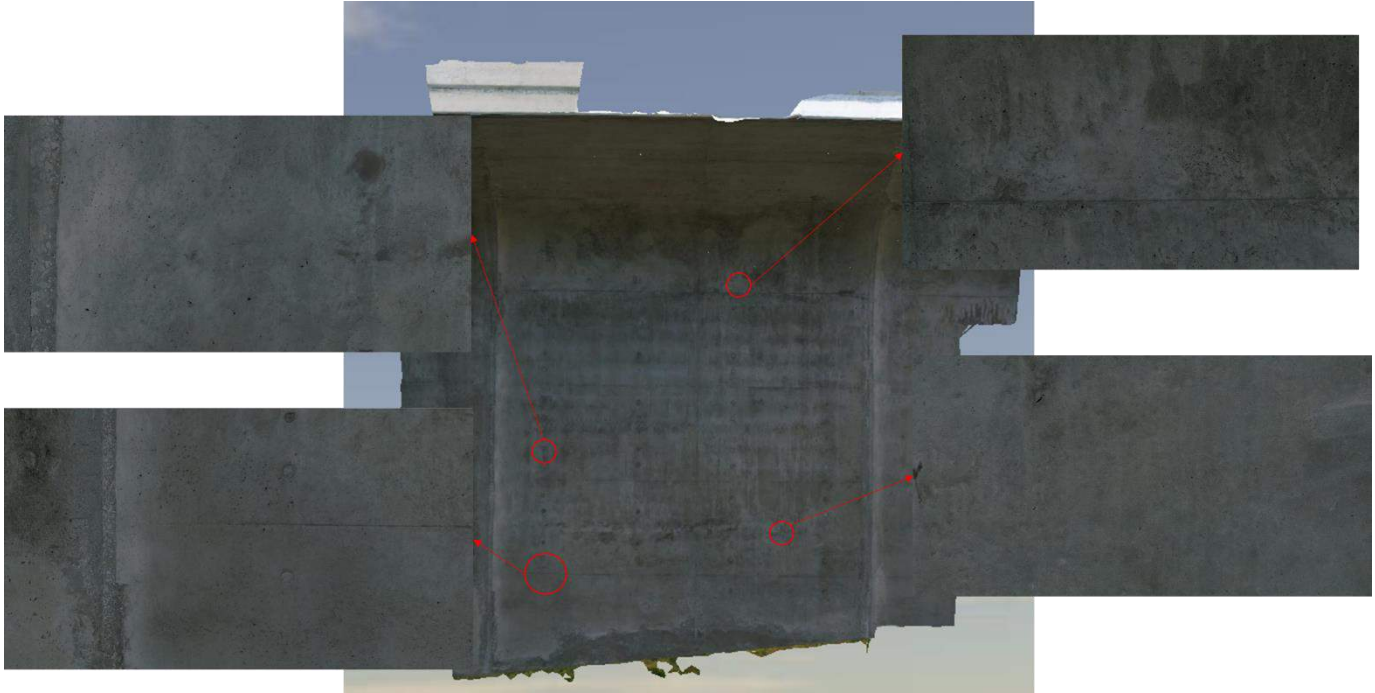
Figure 4.58: Context Capture 3D Mesh Model of Segment P3-3U on the Northbound Bridge

Analyzing the screenshots of the 3D mesh model created using Context Capture (Figure 4.47), one can easily make out the cracks. Given the information inscribed on the segment and the GSD of the images captured, the identified cracks have a width greater than and equal to 0.03mm. The cracks were also visible in the orthofacades generated. The orthofacades can be used to conduct future work on automatic crack detection and identification. To help pilots decide the combination of camera, the distance away from face and the required GSD a lookup chart (Figure 4.59) was created for the DJI Z3, X5, X5s and Z30 cameras. The chart helps users to decide the height or distance away from the object value based on their selection of required GSD and available camera. The lookup chart was created using the information present on a crack comparator card (Figure 4.60). The crack comparator card shown in Figure 4.60 is a tool used by bridge inspectors to measure the crack widths on bridges. The GSD values that lie above the crack comparator card were blacked out in the chart.

135

Color Scale

GSD (mm/px)	Colors
>1.5	
1.5	
1.25	
1	
0.9	
0.8	
0.6	
0.5	
0.4	
0.33	
0.3	
0.2	
0.15	
<0.15	

② Lookup required camera

③ Lookup required height of flight

① Select Desired GSD for the mission

Crack Detection GSD Setting Chart for Z3 X5 (15mm & 45 mm) X5s (15mm & 45 mm) Z30 (varying zoom levels) (mm/px)

Camera / Distance (feet)	Z3	X5 Lens = 15mm	X5 Lens = 45mm	X5s Lens = 15mm	X5s Lens = 45mm	Z30 1	Z30 2	Z30 5	Z30 10	Z30 15	Z30 20	Z30 25	Z30 30
2	0.240	0.153	0.051	0.133	0.044	0.348	0.174	0.070	0.035	0.023	0.017	0.014	0.012
3	0.360	0.229	0.076	0.200	0.067	0.522	0.261	0.104	0.052	0.035	0.026	0.021	0.017
4	0.480	0.305	0.102	0.266	0.089	0.696	0.348	0.139	0.070	0.046	0.035	0.028	0.023
5	0.600	0.381	0.127	0.333	0.111	0.869	0.435	0.174	0.087	0.058	0.043	0.035	0.029
6	0.720	0.458	0.153	0.399	0.133	1.043	0.522	0.209	0.104	0.070	0.052	0.042	0.035
7	0.840	0.534	0.178	0.466	0.155	1.217	0.609	0.243	0.122	0.081	0.061	0.049	0.041
8	0.959	0.610	0.203	0.533	0.178	1.391	0.696	0.278	0.139	0.093	0.070	0.056	0.046
9	1.079	0.687	0.229	0.599	0.200	1.565	0.782	0.313	0.156	0.104	0.078	0.063	0.052
10	1.199	0.763	0.254	0.666	0.222	1.739	0.869	0.348	0.174	0.116	0.087	0.070	0.058
15	1.799	1.144	0.381	0.999	0.333	2.608	1.304	0.522	0.261	0.174	0.130	0.104	0.087
20	2.399	1.526	0.509	1.332	0.444	3.478	1.739	0.696	0.348	0.232	0.174	0.139	0.116
25	2.998	1.907	0.636	1.664	0.555	4.347	2.174	0.869	0.435	0.290	0.217	0.174	0.145
30	3.598	2.289	0.763	1.997	0.666	5.217	2.608	1.043	0.522	0.348	0.261	0.209	0.174
35	4.198	2.670	0.890	2.330	0.777	6.086	3.043	1.217	0.609	0.406	0.304	0.243	0.203
40	4.797	3.052	1.017	2.663	0.888	6.955	3.478	1.391	0.696	0.464	0.348	0.278	0.232
45	5.397	3.433	1.144	2.996	0.999	7.825	3.912	1.565	0.782	0.522	0.391	0.313	0.261
50	5.997	3.814	1.271	3.329	1.110	8.694	4.347	1.739	0.869	0.580	0.435	0.348	0.290
55	6.597	4.196	1.399	3.662	1.221	9.564	4.782	1.913	0.956	0.638	0.478	0.383	0.319
60	7.196	4.577	1.526	3.995	1.332	10.433	5.217	2.087	1.043	0.696	0.522	0.417	0.348
65	7.796	4.959	1.653	4.328	1.443	11.303	5.651	2.261	1.130	0.754	0.565	0.452	0.377
70	8.396	5.340	1.780	4.661	1.554	12.172	6.086	2.434	1.217	0.811	0.609	0.487	0.406
75	8.995	5.722	1.907	4.993	1.664	13.041	6.521	2.608	1.304	0.869	0.652	0.522	0.435
80	9.595	6.103	2.034	5.326	1.775	13.911	6.955	2.782	1.391	0.927	0.696	0.556	0.464
85	10.195	6.484	2.161	5.659	1.886	14.780	7.390	2.956	1.478	0.985	0.739	0.591	0.493
90	10.794	6.866	2.289	5.992	1.997	15.650	7.825	3.130	1.565	1.043	0.782	0.626	0.522
95	11.394	7.247	2.416	6.325	2.108	16.519	8.260	3.304	1.652	1.101	0.826	0.661	0.551
100	11.994	7.629	2.543	6.658	2.219	17.389	8.694	3.478	1.739	1.159	0.869	0.696	0.580

Figure 4.59: Crack Detection Case Study Lookup Chart

Figure 4.60: Crack Comparator Card Used by Bridge Engineers to Measure Crack Widths

4.5 Case Study 5: i75 Construction Site Tests, Toledo D2

This section presents the case study conducted at the i75 construction site in Toledo district 2 of the state of Ohio. The primary objective of this study was to generate a 3D point cloud with an accuracy of 0.1' in the horizontal and vertical frame of reference. The construction site was also used to test the effect of GSDs, GCPs, sUAS, and image geotags on 3D point cloud accuracies.

4.5.1 Flight Plan and Image Capture

The region mapped was an open field (future construction site) that lies between i75 in Toledo and a private property. The public property boundary lines were first located before the flight plans were designed. The images of the field were captured using DJI Matrice 100 and Matrice 210 RTK sUAS and DJI X5 15mm and X5s 15mm cameras. Objects (vinyl targets and metal ruler) of known measurements, were laid out in the field to test the accuracies of the outputs generated. Figure 4.61 shows the measurements of the objects laid out and their illustrations and images. Twelve GCPs were spray painted, using a stencil, on the ground and were distributed uniformly across the region mapped. The coordinates of the GCP centers were recorded by a surveyor using survey-grade equipment. The coordinates were referenced in the NAD83 2011 Ohio north horizontal coordinate system and in the NAVD88 Geoid 12A vertical coordinate system. Figure 4.62 shows the location of the GCPs on the region mapped and the boundary line that indicates the area accessible to the public. Figure 4.63 shows the images of the twelve GCPs marked on the field.

On-field Measurements																	
Number	1	2	3	4	5	6	7	8	9	10	11	12	13	14	15	16	17	18
Name	S1 - S2	S2-S3	S3-S4	S4-S1	Long	Small	M1 - M2	M2-M3	M3-M4	M4-M1	M2 1-M2 2	M2 2-M2 3	M2 3-M2 4	M2 4-M2 1	L1-L2	L2-L3	L3-L4	L4-L1
Value (ft)	2.58	2.6	2.63	2.58	2	1.33	9.67	7.83	9.88	7.67	7.75	9.65	7.71	9.71	12.1	19.79	12.17	19.81
Object	Small Target				Metal Ruler		Medium Target 1				Medium Target 2				Large Target			
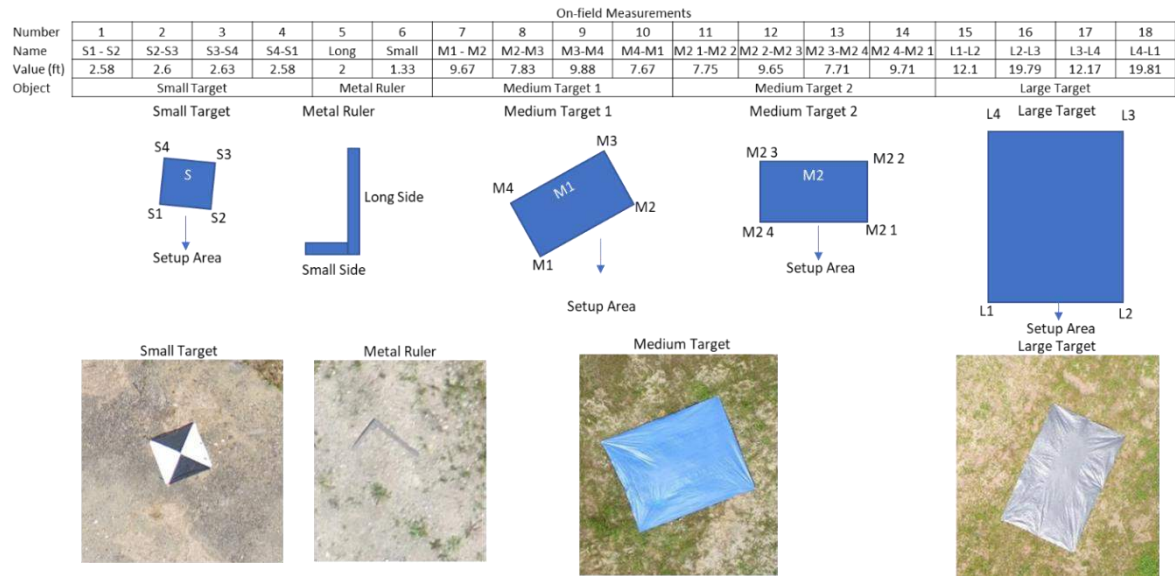
Figure 4.61: Measurement of Objects Laid Out in the Region Mapped for the i75 Construction Site Case Study

Figure 4.62: Locations of the GCPs Marked on the Region Mapped for the i75 Construction Site Case Study

138

Figure 4.63: Images of the GCPs Marked on the Field for the i75 Construction Site Case Study

Images were captured in a grid pattern, with 1cm/px and 2cm/px GSDs and with 75 % image overlaps, using the Matrice 100 sUAS and DJI X5 15mm camera. Images were also captured in a grid pattern, with 1cm/px GSD and 75% image overlap, using the Matrice 210 RTK sUAS and DJI X5s 15mm camera. Figure 4.64 shows a summary of all the missions conducted at the i75 construction site. Figure 4.65 shows the locations of all the images captured for the i75 construction site study.

		Mission 1	Mission 2	Mission 3
sUAS		Matrice 100	Matrice 100	Matrice 210 RTK
Camera		X5 15mm	X5 15mm	X5S 15mm
	Resolution	16MP	16MP	21MP
	Resolution (WxH)	4608px x 3456px	4608px x 3456px	5280px x 3956px
Flight Type		Grid Pattern	Grid Pattern	Grid Pattern
Ground Sampling Distance (GSD)		1cm/px	2cm/px	1cm/px
Flight Height (m)		38m (125ft)	80m (320ft)	45m
Total Flight Time		50min	15min	40min
Total Number of Batteries		4	2	4
Total Number of Photos		1280	337	930
Total Number of GCPs		12	12	12

Figure 4.64: Summary of the Missions Conducted for the i75 Construction Site Case Study

139

Figure 4.65: Location of the Images Captured for the i75 Construction Site Study; Left: 1cm/px Dataset Using X5, center: 2cm/px Dataset Using X5, Right: 1cm/px Dataset Using X5s

4.5.2 Processing and Analysis

The images captured at the i75 construction site were processed using Pix4D Mapper in multiple ways using the default 3D model template. The images captured in each mission were processed separately without GCPs and with image geotags, with GCPs and with image geotags, and finally with GCPs and without image geotags. The measurements of the objects laid out in the field were measured using the point clouds generated in this case study. These measurements were analyzed separately to understand the effect of varying GSDs, GCPs, various sUAS and image geotags on 3D point cloud accuracies. Figure 4.66 shows the point clouds generated without GCPs using the combined (grid) dataset from each mission.
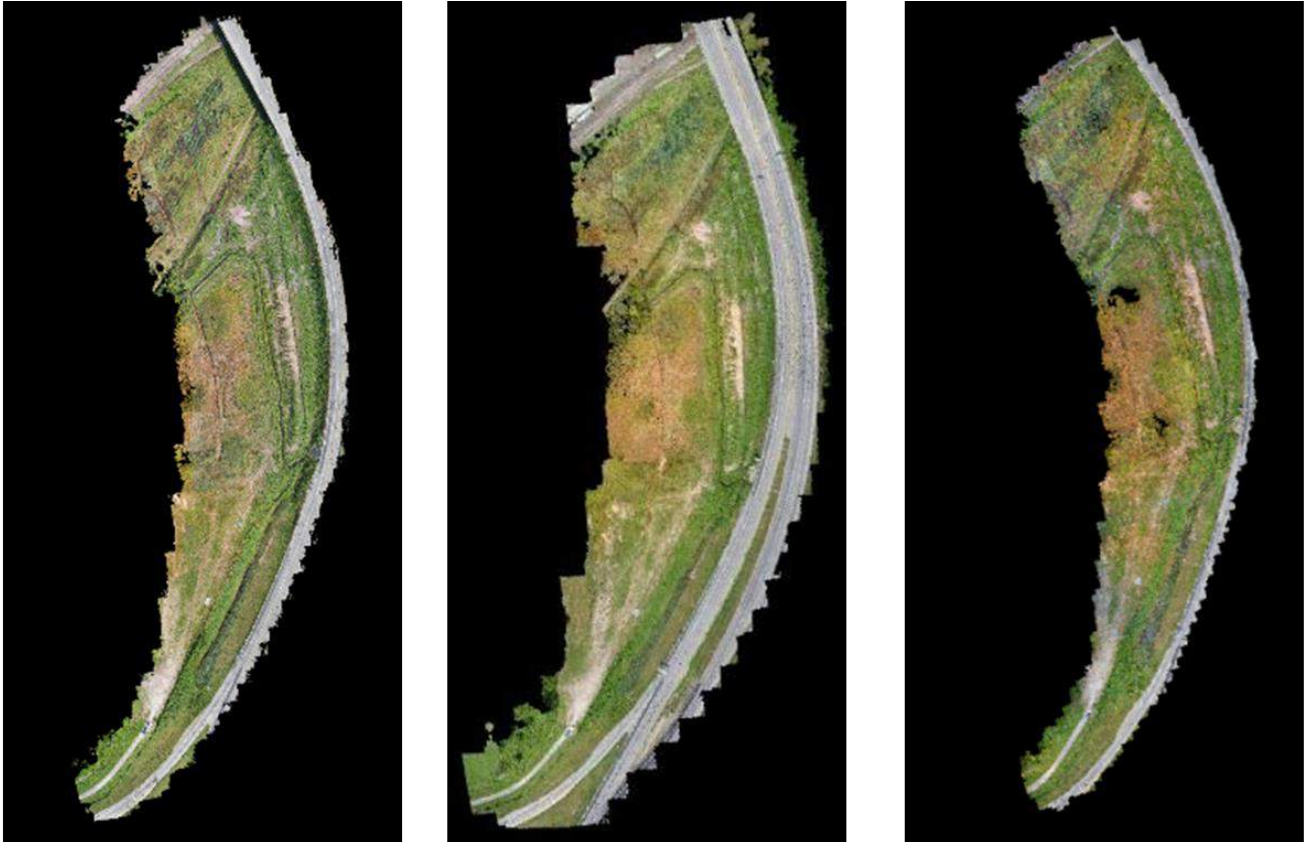
M100 & X5 (1cm/px GSD)   M100 & X5 (2cm/px GSD)   M210 & X5s (1cm/px GSD)

Figure 4.66: 3D Point Clouds Generated Using the Dataset Captured for the i75 Construction Site Case Study; Left: 3D Point Cloud Processed Using X5 1cm/px Dataset, Center: 3D Point Cloud Processed Using X5 2cm/px Dataset, Right: 3D Point Cloud Processed Using X5s

4.5.3 Outputs

The generated 3D point clouds were analyzed by measuring the objects laid out in the field using the polyline line tool and the computed values were compared to the values recorded on the field. The plots in Figure 4.67 show the individual absolute error measurements, and their mean absolute and root mean square errors of the 3D point clouds generated using the 1cm/px data, captured using the DJI Matrice 100 sUAS and DJI X5 15mm camera, without GCPs and with image geotags, with GCPs and images geotags and with GCPs and without image geotags.

141
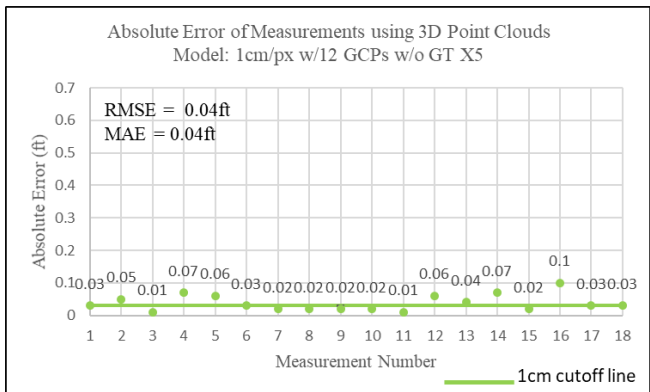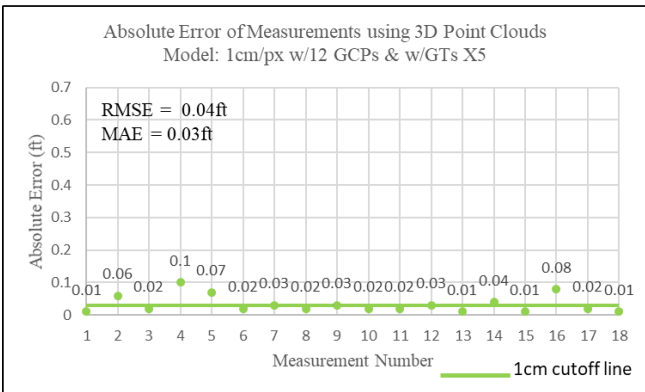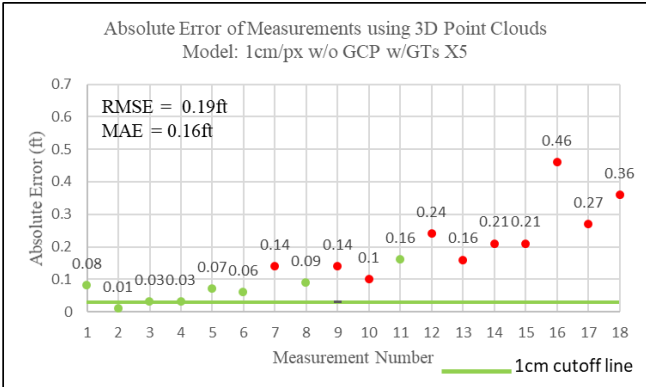
Figure 4.67: Absolute Error Measurement Plots of the 3D Point Clouds Generated Using the 1cm/px GSD Dataset Obtained Using DJI Matrice 100 and DJI X5 15mm; Top: 3D Point Cloud Generated Without GCPs and With Image Geotags, Bottom Left: 3D Point Cloud Generated With GCPs and with Image Geotags, Bottom Right: 3D Point Cloud Generated Without GCPs and with Image Geotags

The plots in Figure 4.68 show the individual absolute error measurements, and their mean absolute and root mean square errors of the 3D point clouds generated using the 2cm/px data, captured using the DJI Matrice 100 sUAS and DJI X5 15mm camera, without GCPs and with image geotags, with GCPs and images geotags and with GCPs and without image geotags.
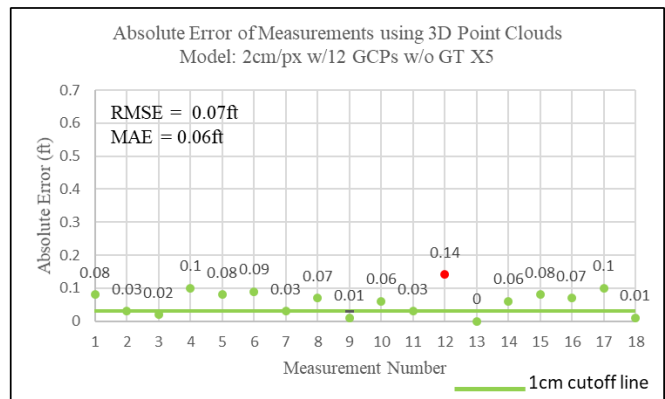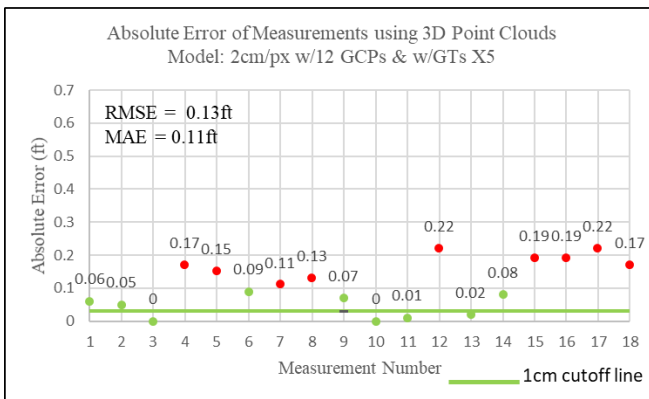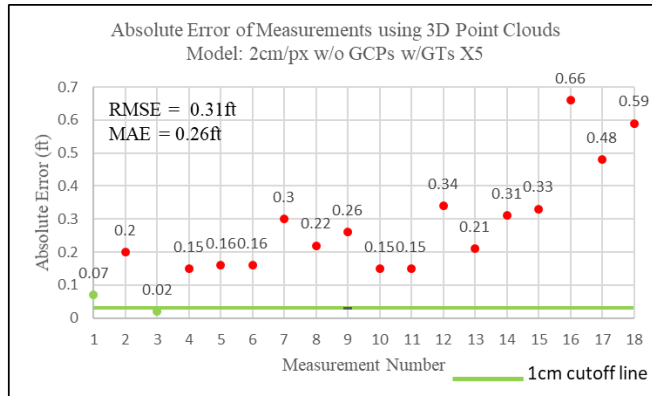
Figure 4.68: Absolute Error Measurement Plots of the 3D Point Clouds Generated Using the 2cm/px GSD Dataset Obtained Using DJI Matrice 100 and DJI X5 15mm; Top: 3D Point Cloud Generated Without GCPs and With Image Geotags, Bottom Left: 3D Point Cloud Generated With GCPs and with Image Geotags, Bottom Right: 3D Point Cloud Generated Without GCPs and with Image Geotags

The plots in Figure 4.69 show the individual absolute error measurements, and their mean absolute and root mean square errors of the 3D point clouds generated using the 1cm/px data, captured using the DJI Matrice 210 RTK sUAS and DJI X5s 15mm camera, without GCPs and with image geotags, with GCPs and images geotags and with GCPs and without image geotags.
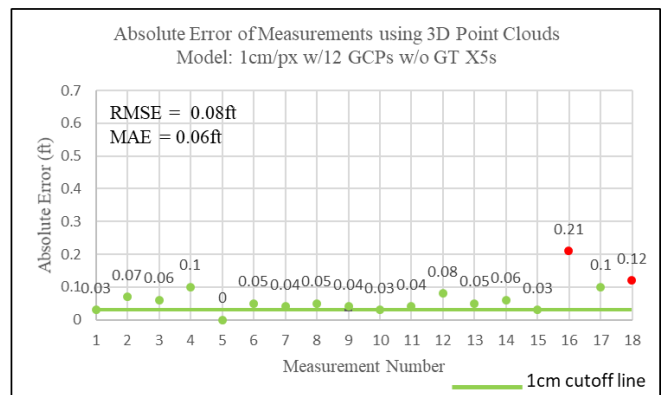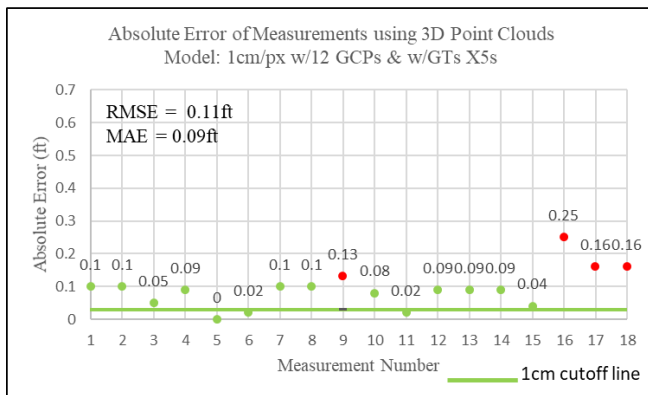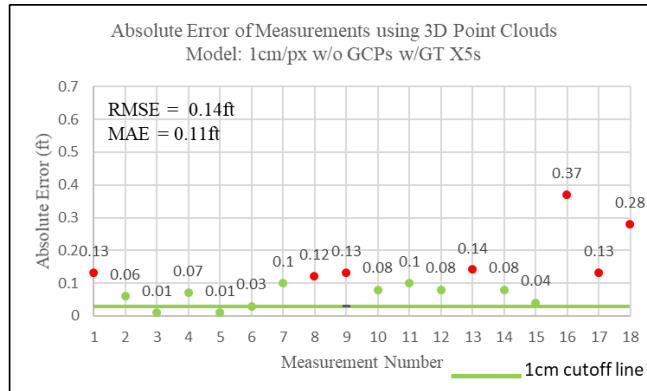
Figure 4.69: Absolute Error Measurement Plots of the 3D Point Clouds Generated Using the 2cm/px GSD Dataset Obtained Using DJI Matrice 210 RTK and DJI X5s 15mm; Top: 3D Point Cloud Generated Without GCPs and With Image Geotags, Bottom Left: 3D Point Cloud Generated With GCPs and with Image Geotags, Bottom Right: 3D Point Cloud Generated Without GCPs and with Image Geotags

To study the effect of varying GSDs on the accuracy of 3D point clouds, the absolute error measurement plots in Figures 4.67 and 4.68 were compared. Comparing the results compiled for the models generated without GCPs and with image geotags, one can clearly see that the mean and RMSE errors increase as the GSD value increases. The effect of using GCPs to calibrate 3D point clouds can be seen in Figures 4.67 to 4.69. The plots of the models generated with GCPs and image geotags clearly show smaller error values when compared to the plots for the models generated without GCPs. It can also be seen that the errors recorded using the model generated with the 1cm/px dataset and GCPs have errors within the ranges acceptable by ODOT surveyors [75]. Given the small error values recorded using the model generated using the 1cm/px dataset

144

with GCPs and image geotags, the point cloud was edited to remove tall vegetations and noise.

Figure 4.70 shows the edited 3D point cloud generated using the 1cm/px dataset and with GCPs.
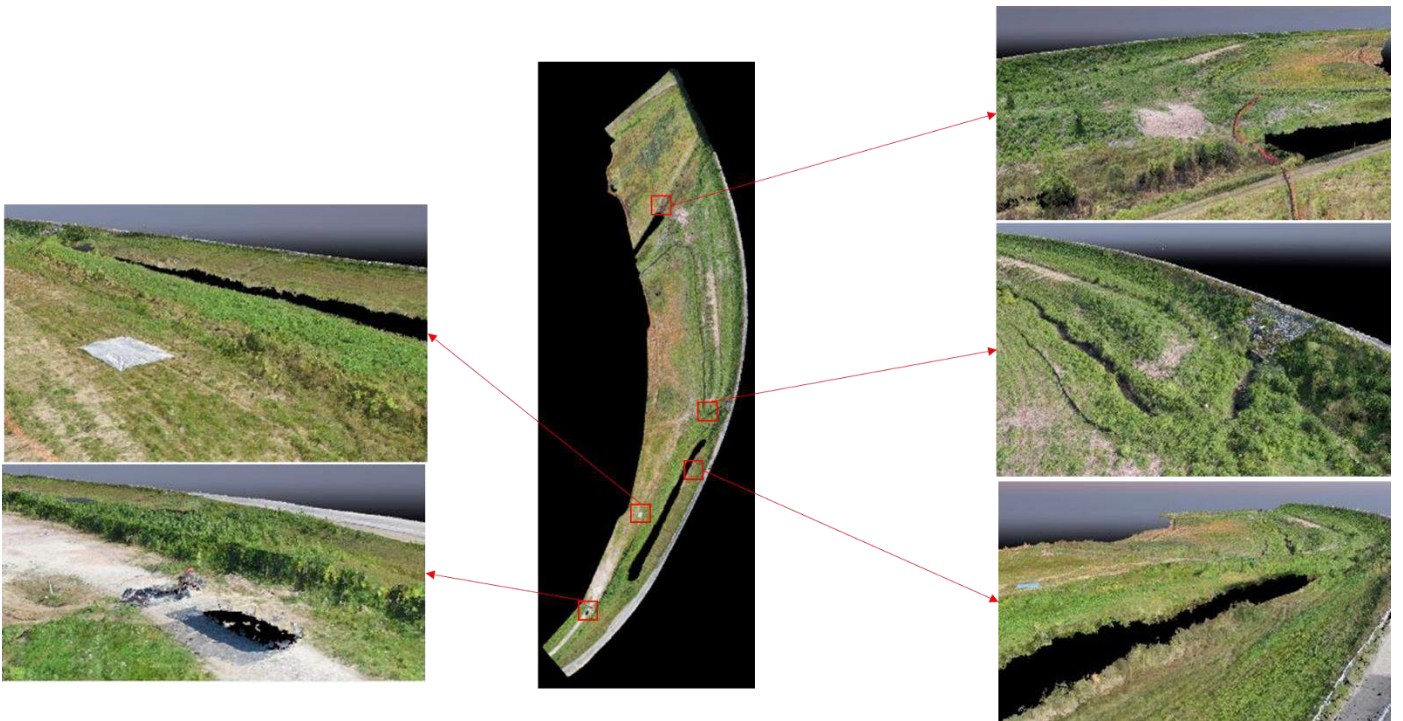
Figure 4.70: Edited 3D Point Cloud Generated Using the 1cm/px Dataset with GCPs Captured for the i75 Construction Site Case Study

Figure 4.71 shows the 3D mesh file generated using the edited 3D point cloud shown in Figure 4.70.
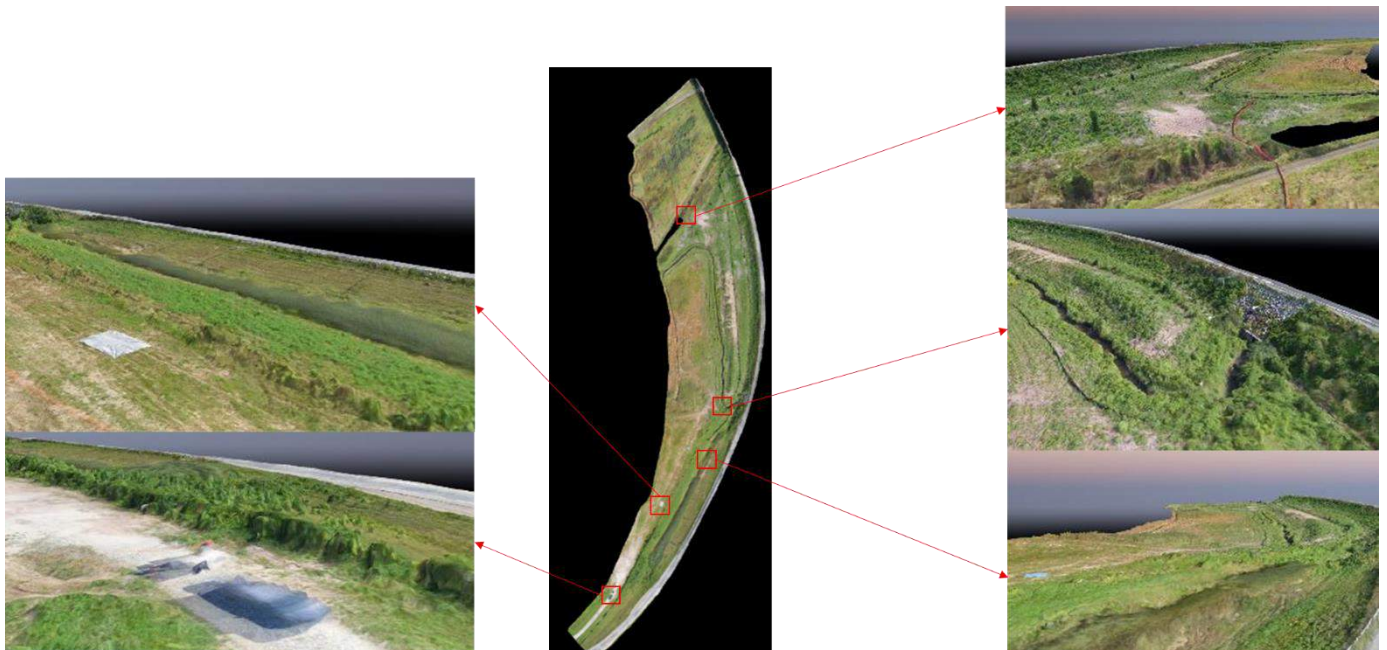
Figure 4.71: Edited 3D Mesh Generated Using the 1cm/px Dataset with GCPs Captured for the i75 Construction Site Case Study

The effect of image geotags can be since by comparing the error plots generated for the models with and without image geotags and with GCPs. The effect of image geotags can be seen clearly in the model generated using the 2cm/px dataset captured using the Matrice 100 sUAS and X5 camera. Removing the geotags helped improve the accuracy of the produced 3D point cloud. Whereas, removing the geotags from the images captured at a GSD of 1cm/px did not impact the calculated errors. The dataset captured using the DJI Matrice 210 RTK helps improve the accuracy of the generated 3D point cloud by a small factor. This is seen when the plots (plot of 3D point cloud generated using image geotags and without GCPs) in Figures 4.67 and 4.69 are compared.

4.6 Case Study 6: Deer Creek Park Tests, Deer Creek D6

This section presents the case study conducted at Deer Creek Park in Deer Creek district 2 of the state of Ohio. The primary objective of this study was to record the accuracies of the 3D point clouds generated using images captured with DJI Phantom 4 RTK sUAS. The sUAS has the capability to connect to Ohio's VRS system which helps improve the positioning of the vehicle in midair. The study documents the effect of a varying number of GCPs, GSDs, and pattern of image capture on the accuracies of the 3D point clouds generated using the DJI Phantom 4 RTK dataset.

4.6.1 Flight Plan and Image Capture

Deer Creek Park is a test site frequently used by ODOT surveyors to test their survey grade equipment. From their studies, certain regions within the park were identified to produce surveying results of good quality. One such region is marked in yellow in the map shown in Figure 4.72.
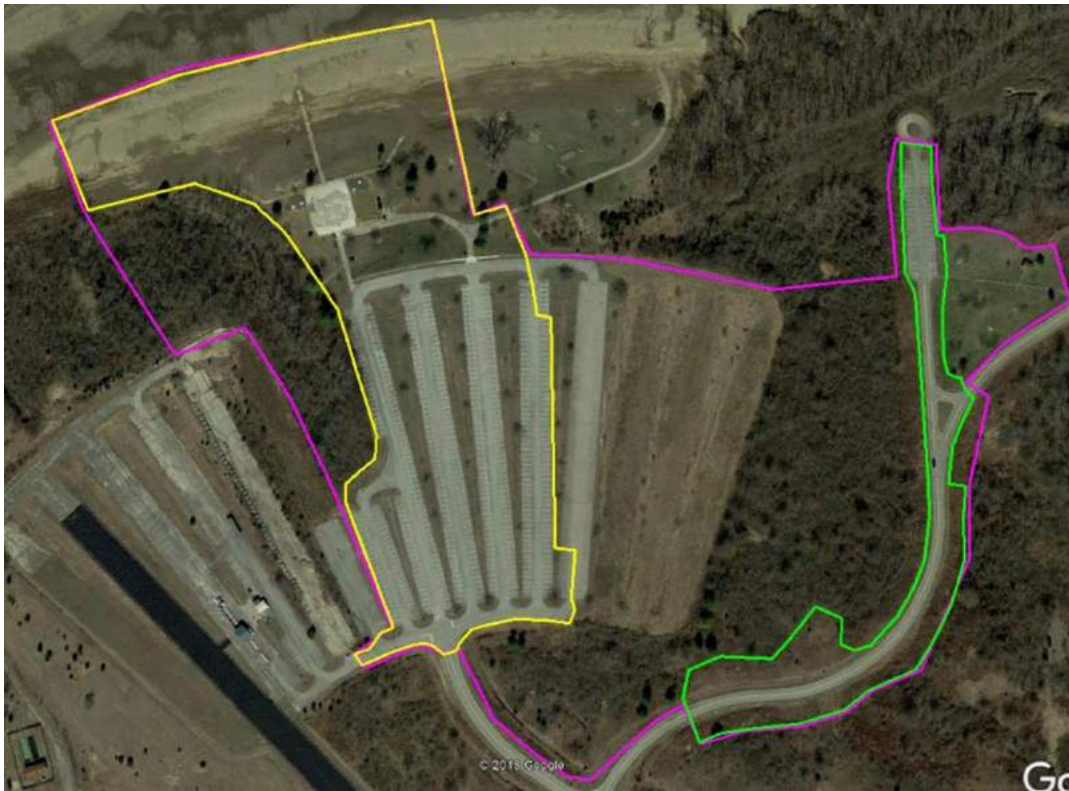
Figure 4.72: Deer Creek Park Regions Used by ODOT Surveyors to Test Their Surveying Equipment

A region that lies inside the yellow boundary was selected to conduct the study (Figure 4.73).
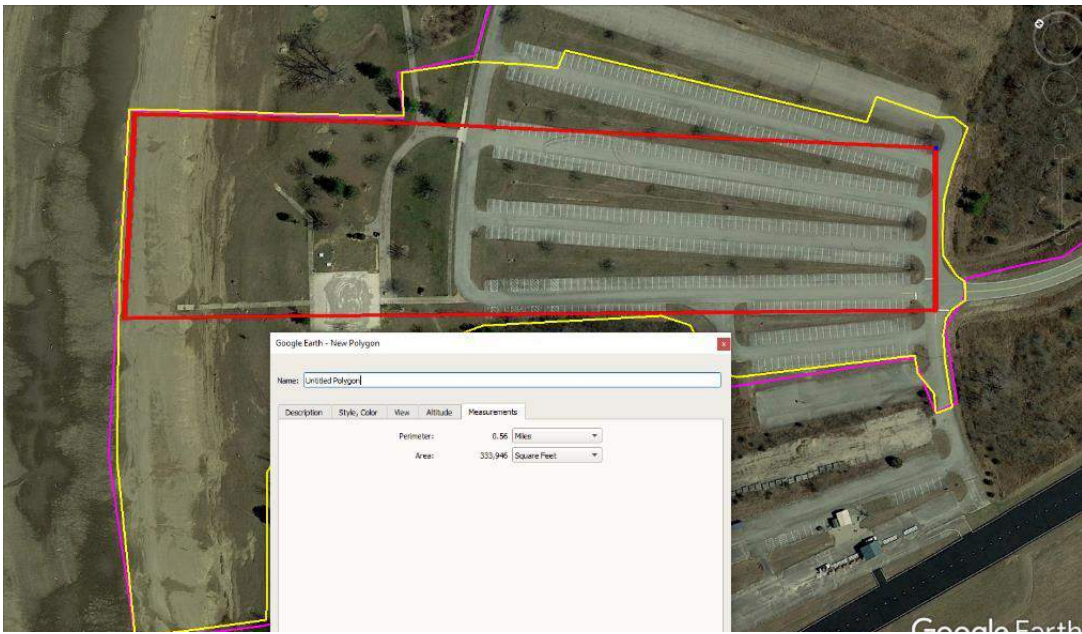
Figure 4.73: Region Selected Within the Yellow Boundary Line to Conduct the Study

The selected region was divided into a grid of thirty cells to determine the location of vinyl targets, whose centers were used as GCPs and checkpoints. Figure 4.74 shows the proposed positions of the vinyl targets in the region mapped. Fifteen of the vinyl targets were selected to be used as GCPs and the remaining fifteen were used as checkpoints (Figure 4.75).

Figure 4.74: Proposed Positions of the Vinyl Targets in the Mapped Region

Figure 4.75: Map of the Region Mapped with Vinyl Targets Designated as GCPs and Check Points

148

The positions of the targets that were going to be used as GCPs, were selected following Pix4D recommendations. The selected GCPs were distributed uniformly on the mapped region. The coordinates of the target centers were recorded by an ODOT surveyor using survey-grade equipment. The coordinates were recorded in the NAD83 2011 Ohio South horizontal coordinate system and in the NAVD88 Geoid 12A vertical coordinate system. The coordinates were also recorded in the ellipsoid reference system (WGS84). Figure 4.76 shows the actual positions of the targets laid out and the targets selected as GCPs and checkpoints. Figure 4.77 shows the table with the coordinates of the target centers. On the day of the test thirty-one targets were laid out and analyzing the image dataset it was observed that target AT22 was not secured properly and was ignored for this study.

Figure 4.76: Actual Positions of the Vinyl Targets and Targets Selected as GCPs and Check Points

Point Name	Northing (ft)	Easting (ft)	Elevation (ft)		Latitude (degree)	Longitude (degree)	Ellipsoid Ht. (m)
AT01	589477.358	1764235.313	853.594		39d36'58.39647"	-83d13'30.35252"	745.721
AT02	589629.3	1764180.219	850.499		39d36'59.89377"	-83d13'31.07215"	742.629
AT03	589706.907	1764146.42	848.727		39d37'00.65810"	-83d13'31.51203"	740.858
AT04	589769.573	1764115.355	847.343		39d37'01.27497"	-83d13'31.91544"	739.476
AT05	589532.287	1764152.46	851.552		39d36'58.93276"	-83d13'31.41692"	743.683
AT06	589597.591	1764112.308	849.91		39d36'59.57499"	-83d13'31.93672"	742.043
AT07	589679.243	1764079.857	847.674		39d37'00.37940"	-83d13'32.35978"	739.808
AT08	589707.423	1764047.227	847.742		39d37'00.65532"	-83d13'32.77965"	739.878
AT09	589827.365	1764013.004	845.279		39d37'01.83801"	-83d13'33.22930"	737.417
AT10	589877.8	1763950.375	843.073		39d37'02.33149"	-83d13'34.03481"	735.213
AT11	589978.856	1763922.651	840.272		39d37'03.32805"	-83d13'34.39948"	732.413
AT12	590040.422	1763927.019	842.88		39d37'03.93687"	-83d13'34.34999"	735.022
AT13	590045.194	1763774.171	839.578		39d37'03.97187"	-83d13'36.30373"	731.727
AT14	590103.913	1763876.155	839.126		39d37'04.56032"	-83d13'35.00651"	731.27
AT15	590011.368	1763708.931	840.446		39d37'03.63238"	-83d13'37.13395"	732.598
AT16	589409.929	1764127.614	854.046		39d36'57.72150"	-83d13'31.72186"	746.178
AT17	589532.044	1764057.364	851.264		39d36'58.92281"	-83d13'32.63210"	743.399
AT18	589608.662	1764004.608	849.498		39d36'59.67585"	-83d13'33.31413"	741.636
AT19	589738.785	1763911.762	846.627		39d37'00.95451"	-83d13'34.51396"	738.769
AT20	589825.346	1763896.941	844.367		39d37'01.80884"	-83d13'34.71225"	736.509
AT21	589907.895	1763796.775	842.896		39d37'02.61672"	-83d13'36.00075"	735.043
AT22	590120.126	1763613.711	841.204		39d37'04.69968"	-83d13'38.36196"	733.36
AT23	590147.851	1763752.273	839.963		39d37'04.98471"	-83d13'36.59412"	732.113
AT24	590262.55	1763817.609	827.064		39d37'06.12351"	-83d13'35.77099"	719.21
AT25	590389.017	1763748.78	819.338		39d37'07.36794"	-83d13'36.66356"	711.488
AT26	590482.688	1763650.295	810.828		39d37'08.28587"	-83d13'37.93177"	702.983
AT27	590308.994	1763658.912	823.242		39d37'06.56990"	-83d13'37.80377"	715.396
AT28	590246.549	1763547.378	824.648		39d37'05.94387"	-83d13'39.22265"	716.807
AT29	590368.789	1763472.601	810.854		39d37'07.14603"	-83d13'40.19082"	703.016
AT30	590414.085	1763589.275	812.314		39d37'07.60299"	-83d13'38.70449"	704.471
AT31	589825.577	1764088.815	846.132		39d37'01.82636"	-83d13'32.26034"	738.266

Figure 4.77: Coordinates of the Vinyl Targets Placed in the Region of Study

Images of the region were captured using the DJI Phantom 4 RTK sUAS connected to the Ohio VRS system. Four missions were conducted where the first three missions captured images in a grid pattern with 80% image overlap and GSDs of 0.75cm/px, 1cm/px and 1.25cm/px. The fourth mission was a terrain awareness mission where the Phantom 4 sUAS changed its flight altitude with the terrain to obtain images with fixed GSD and image overlap values. To conduct the terrain awareness mission the digital terrain model of the area mapped was uploaded to the sUAS. The sUAS corrects its altitude stepwise at each pass if there is a terrain change. Figure 4.78 shows the location of the images captured for the Deer Creek study. Figure 4.79 shows the summary of all the missions conducted at Deer Creek Park.
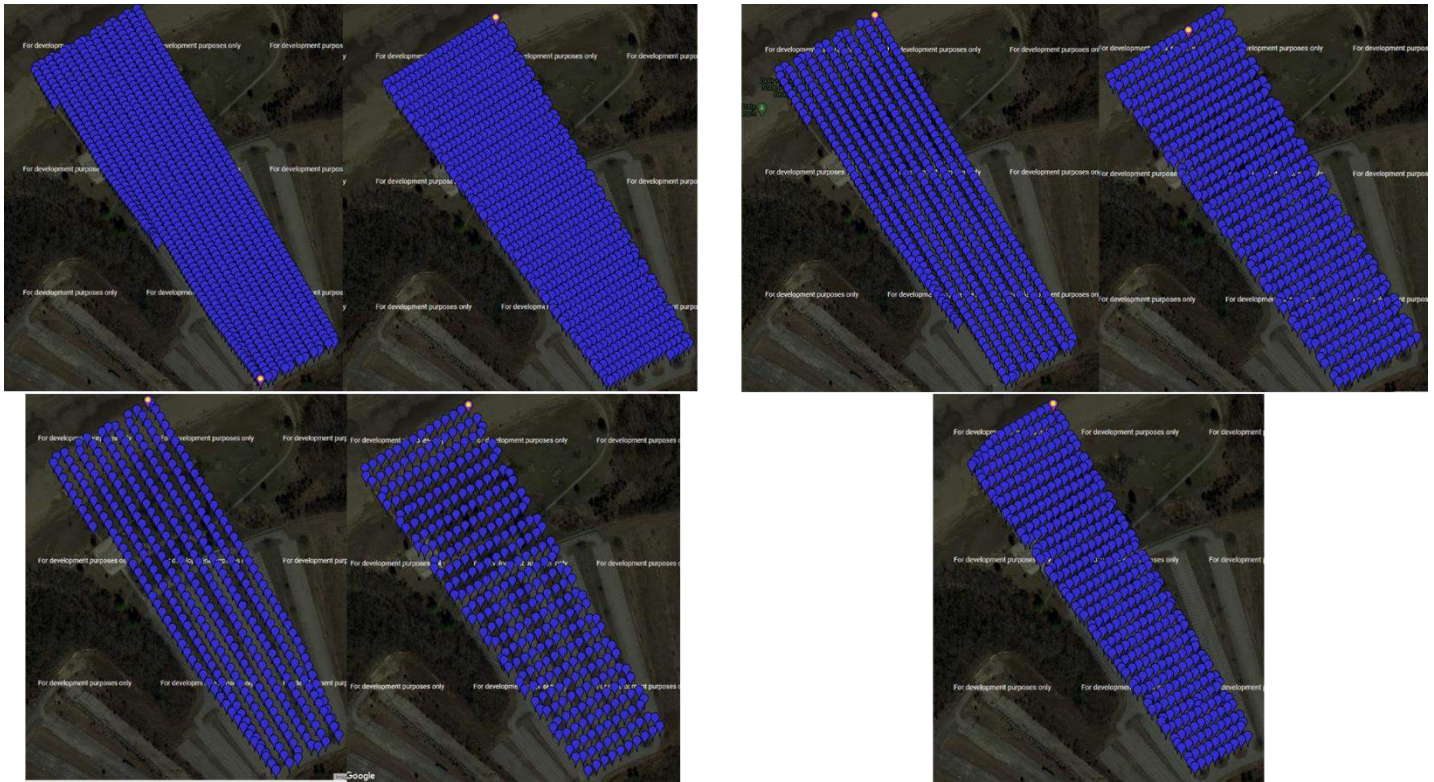
Figure 4.78: Locations of Images Captured for Deer Creek Study; Top Left: 0.75cm/px Dataset, Top Right: 1cm/px Dataset, Bottom Left: 2cm/px Dataset, Bottom Right: 1cm/px Terrain Awareness Dataset

		Mission 1	Mission 2	Mission 3	Mission 4
sUAS		DJI Phantom 4 RTK	DJI Phantom 4 RTK	DJI Phantom 4 RTK	DJI Phantom 4 RTK
Camera		Phantom 4	Phantom 4	Phantom 4	Phantom 4
	Resolution	20MP	20MP	20MP	20MP
	Resolution (WxH)	5472px x 3648px	5472px x 3648px	5472px x 3648px	5472px x 3648px
Flight Type		Grid Pattern	Grid Pattern	Grid Pattern	Perpendicular Terrain Awareness
Ground Sampling Distance (GSD)		0.75cm/px	1cm/px	1.25cm/px	1cm/px
Flight Height (m)		27m (88.6ft)	36m (118.1ft)	46m (151ft)	28m to 40m (91.9ft to 131.2ft)
FO/SO (%)		80%/80%	80%/80%	80%/80%	80%/80%
Total Number of Photos		1910	1068	691	435

Figure 4.79: Summary of the Missions Conducted for the Deer Creek Park Case Study

151

4.6.2 Processing and Analysis

The images obtained in each mission were processed separately using Pix4D Mapper and the 3D point clouds generated were analyzed separately by comparing the computed point cloud coordinates of the checkpoint target centers with the coordinates recorded by the ODOT surveyor. The error values in pixels were also calculated by dividing the measured errors by the average GSD of the 3D point cloud (refer Appendix A). The point cloud was referenced in the NAD83 2011 Ohio south horizontal coordinate reference system and the vertical coordinates system was set to arbitrary on Pix4D Mapper. When the vertical coordinate system is set to arbitrary and the model is processed with GCPs, Pix4D Mapper uses the GCP's altitude to reference the model's altitude. When the vertical coordinate system is set to arbitrary and the model is processed without GCPs, Pix4D Mapper uses the image's vertical coordinate system to reference the model's altitude. The 0.75cm/px dataset (parallel and perpendicular) were processed together and separately without GCPs and with 14 GCPs. The 1cm/px dataset (parallel and perpendicular) were processed together and separately without GCPs and with 14, 12, 11, 9, 7, 5, and 3 GCPs. The 1cm/px terrain awareness dataset was processed without GCPs and with 14 GCPs. The 1.25cm/px dataset (parallel and perpendicular) were processed together and separately without GCPs and with 14 GCPs. Figure 4.80 shows the 3D point cloud generated using the 1cm/px grid dataset and 14 GCPs. Figures 4.81 to 4.86 show the map of the targets used as GCPs for the 12, 11, 9, 7, 5, and 3 GCP models respectively.

Figure 4.80: 3D Point Cloud Generated Using the 1cm/px Grid Dataset of the Region Mapped in Deer Creek Park

Figure 4.81: Positions of the Targets as GCPs for the 12 GCPs 3D point Cloud

Figure 4.82: Positions of the Targets as GCPs for the 11 GCPs 3D point Cloud

Figure 4.83: Positions of the Targets as GCPs for the 9 GCPs 3D point Cloud

154

Figure 4.84: Positions of the Targets as GCPs for the 7 GCPs 3D point Cloud

Figure 4.85: Positions of the Targets as GCPs for the 5 GCPs 3D point Cloud

Figure 4.86: Positions of the Targets as GCPs for the 3 GCPs 3D point Cloud

4.6.3 Outputs

The pointwise error plots calculated for all the models processed in this study are documented in Appendix A. The RMSE values obtained for each of the models were compared to understand the effect of the number of GCPs, GSD values, and pattern of flight on the accuracies of 3D point clouds. Analyzing the error values obtained for each checkpoint in the models processed it was observed that checkpoint AT20 consistently had higher error values and was thus not included to calculate the RMSE values for the models. Figure 4.87 shows the RMSE plots of the easting, northing and altitude values for the 3D point clouds generated using a 1cm/px grid dataset with 0, 3, 5, 7, 9, 11, 12, and 14 GCPs.
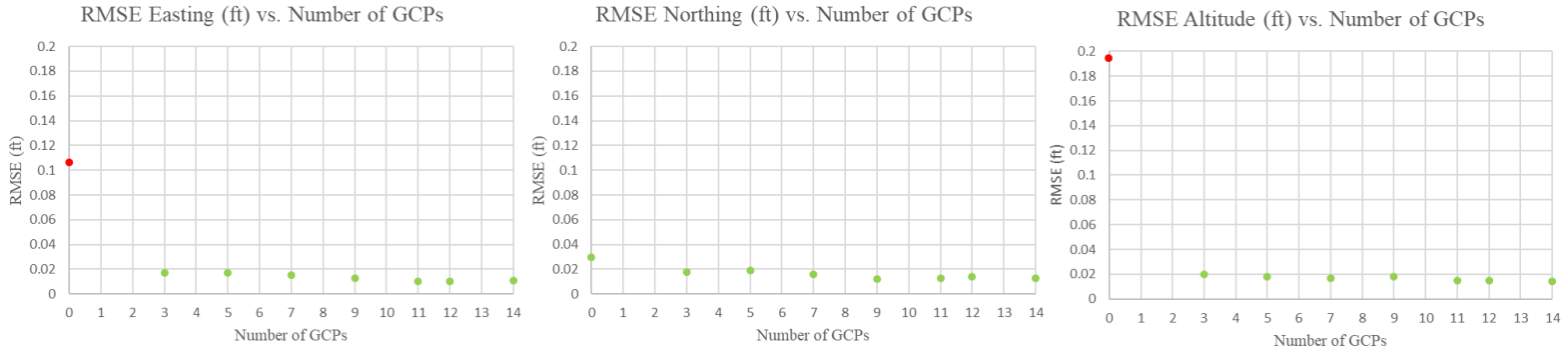
Figure 4.87: RMSE Plots of Easting, Northing, and Altitude of the 3D Point Clouds Generated Using 1cm/px Grid Dataset with 0, 3, 5, 7, 9, 11, 12, and 14 GCPs

The plots in Figure 4.87 shows, an accurate 3D point cloud, with errors close to 0.02ft, can be generated with a minimum of 3 GCPs (distributed uniformly) using images captured with the Phantom 4 RTK sUAS connected to the VRS.

Figure 4.88 shows the RMSE plots of the easting, northing and altitude values for the 3D point clouds generated using 0.75cm/px, 1cm/px, and 1.25cm/px grid dataset without GCPs.
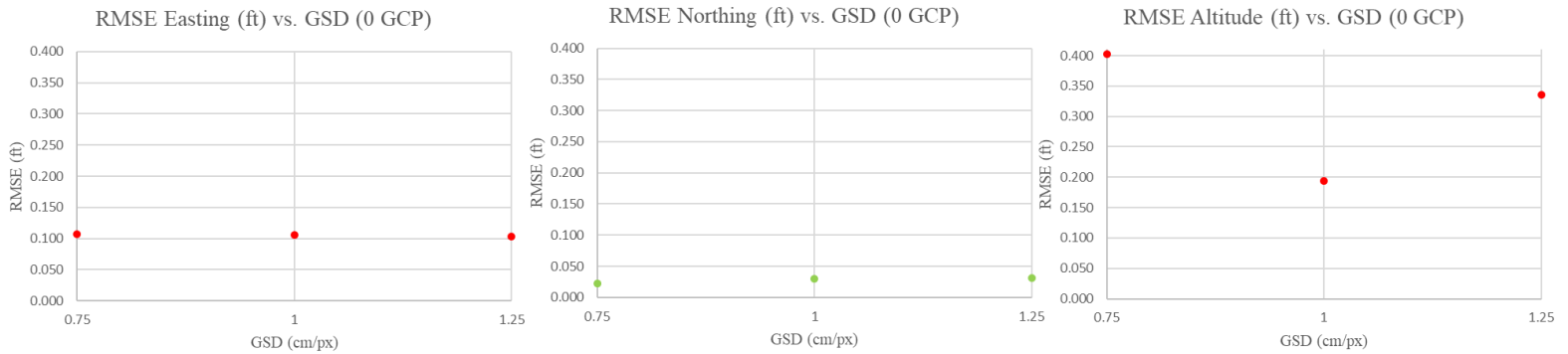
Figure 4.88: RMSE Plots of Easting, Northing, and Altitude of the 3D Point Clouds Generated Using 0.75cm/px, 1cm/px, and 1.25cm/px Grid Dataset Without GCPs

The plots in Figure 4.88 show that similar error values in easting, northing and altitude were obtained using the three different GSD datasets. The similar errors observed could be due to the very similar GSD values of the images used to generate the 3D point clouds. It was also observed that the error values in the northing direction were close to 0.02 ft without any GCP calibration.

157

Figure 4.89 shows the RMSE plots of the easting, northing and altitude values for the 3D point clouds generated using 0.75cm/px, 1cm/px, and 1.25cm/px grid dataset with 14 GCPs.
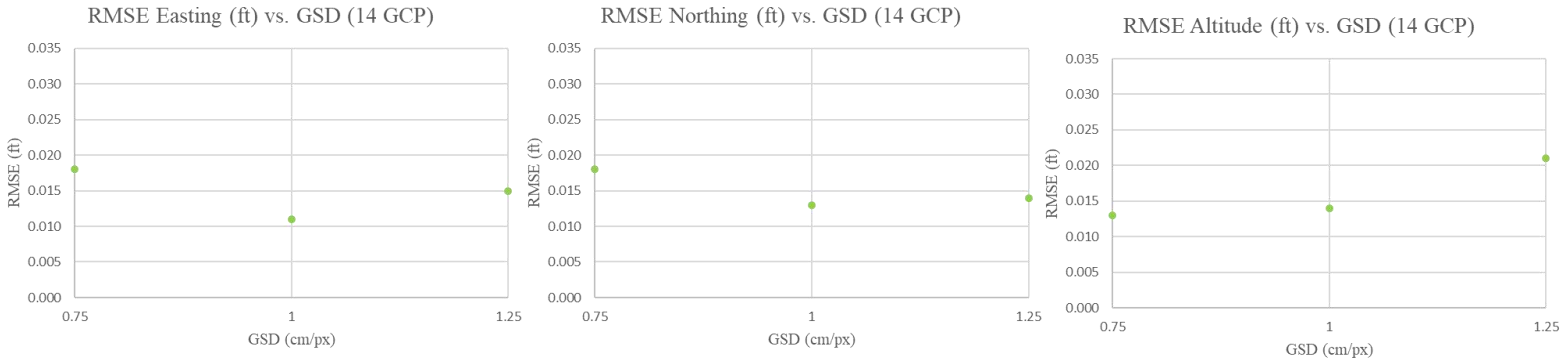
Figure 4.89: RMSE Plots of Easting, Northing, and Altitude of the 3D Point Clouds Generated Using 0.75cm/px, 1cm/px, and 1.25cm/px Grid Dataset 14 GCPs

The plots in Figure 4.89 show that adding 14 GCPs helped in reducing the errors seen in the plots in Figure 4.88. The error values in the easting, northing, and altitude directions were close to 0.02 ft.

Figure 4.90 shows the RMSE plots of the easting, northing and altitude values for the 3D point clouds generated using 0.75cm/px, 1cm/px, and 1.25cm/px grid, parallel, and perpendicular dataset without GCPs.
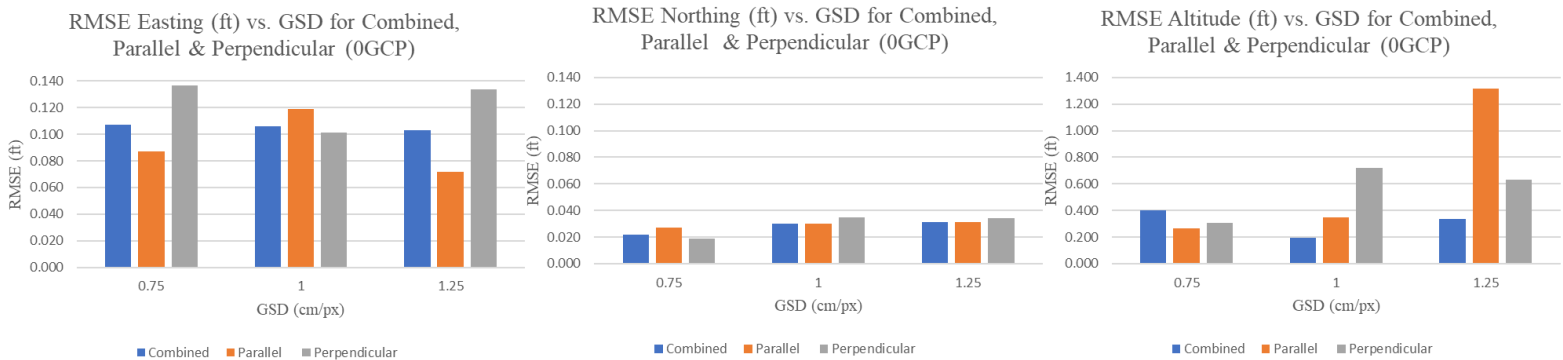
Figure 4.90: RMSE Plots of Easting, Northing, and Altitude of the 3D Point Clouds Generated Using 0.75cm/px, 1cm/px and 1.25cm/px Grid, Parallel and Perpendicular Datasets Without GCPs

The plots in Figure 4.90 show that for most of the cases generating 3D point clouds using the combined dataset generates similar or smaller error values when compared to errors computed using the models generated separately (parallel and perpendicular dataset). It was also observed

158

that the error values in the northing direction were still close to 0.02ft for the models processed

using the combined datasets and without any GCP calibration.

 Figure 4.91 shows the RMSE plots of the easting, northing and altitude values for the 3D point

clouds generated using 0.75cm/px, 1cm/px, and 1.25cm/px grid, parallel, and perpendicular

dataset with 14 GCPs.
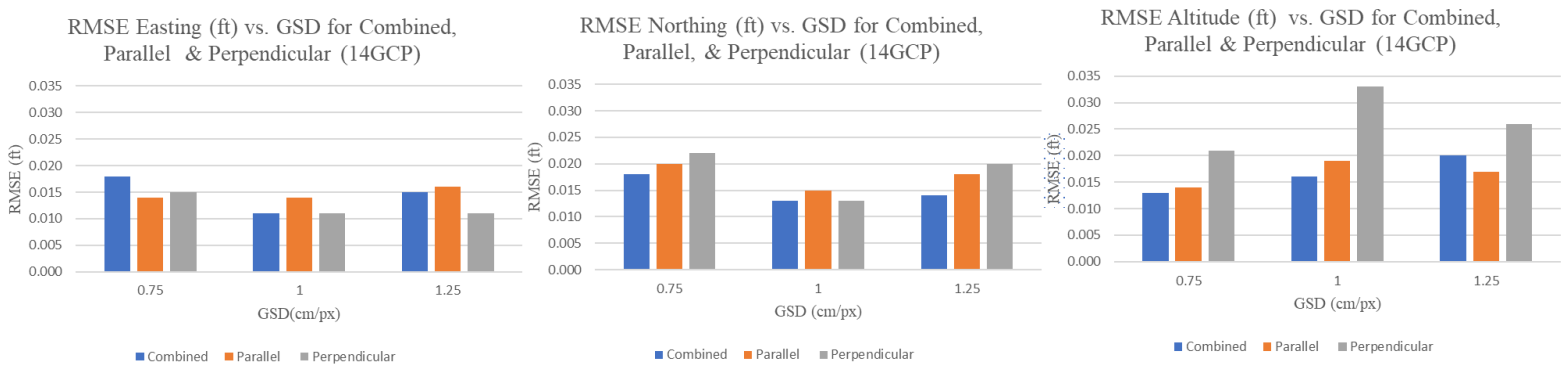
Figure 4.91: RMSE Plots of Easting, Northing, and Altitude of the 3D Point Clouds Generated Using 0.75cm/px, 1cm/px and 1.25cm/px Grid, Parallel and Perpendicular Datasets 14 GCPs

The plots in Figure 4.91 show that adding 14 GCPs helped in reducing the errors irrespective of

the dataset used. Calibrating the models with 14 GCPs bought the errors close 0.02ft. The pattern

of image capture did not have any impact on the errors calculated for the easting and northing

values but helped reduce the errors calculated for the altitude values.

Figure 4.92 shows the RMSE plots of the easting, northing and altitude values for the 3D point

clouds generated using 1cm/px perpendicular and 1cm/px terrain awareness datasets with 14

GCPs and without GCPs.
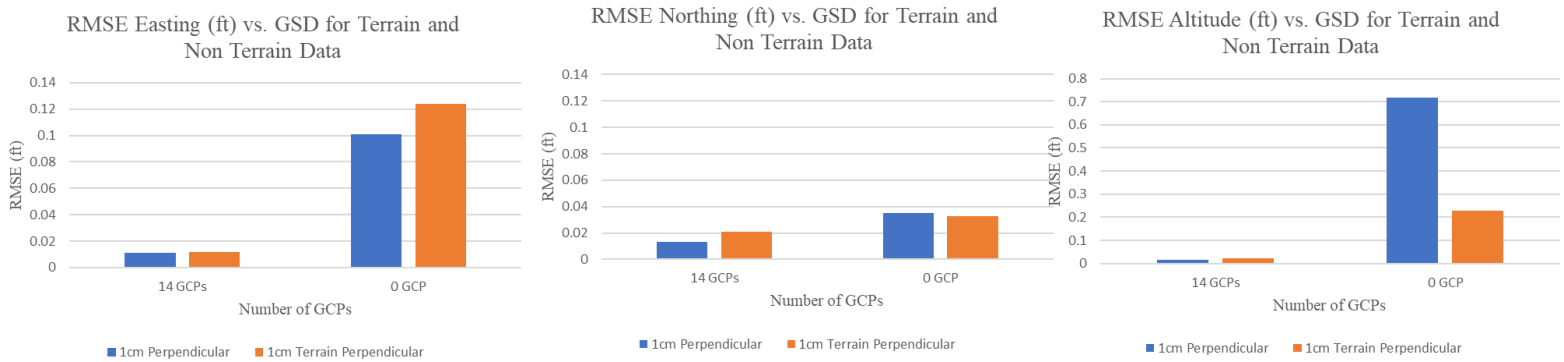
Figure 4.92: RMSE Plots of Easting, Northing, and Altitude of the 3D Point Clouds Generated Using 1cm/px Perpendicular and 1cm/px Terrain Awareness Datasets With 14 GCPS and Without GCPs

The plots in Figure 4.92 show that the 3D point cloud generated, without GCPs, using the 1cm/px terrain awareness data has relatively better accuracies in the northing and altitude directions compared to the 3D point cloud generated using the 1cm/px non-terrain awareness dataset. However, these errors reduce to values close 0.02ft when the models are calibrated using 14 GCPs.

Chapter 5 : Conclusion and Future Work

This chapter presents the conclusions drawn from the research conducted to investigate the applications of sUAS and photogrammetry to monitor and inspect structural health and construction sites. This chapter also presents the scope for potential future work that falls in line with the work presented in this document.

5.1 Conclusion

This section elucidates the conclusions derived from the research work presented in this document. Various experiments and case studies were conducted to understand the effectiveness

of sUAS and photogrammetry tools to inspect and monitor structure health and construction sites.

The effect of various photogrammetry factors on 3D point clouds was investigated and was presented in Chapter 3. It was seen that GSD, camera triggering interval, patterns of flight, and GCPs influence the accuracies of 3D point clouds. As the GSD increases it was seen that the accuracies of 3D point clouds decrease. Camera triggering interval influences image capture and entering incorrect triggering intervals leads to errors in image capture. When mapping structures, processing images captured in a grid pattern helps to fix distortions that would be seen otherwise and at the same time improve the accuracies of the 3D point cloud. Including GCPs, surveyed by a professional using survey-grade equipment, in a project helps to calibrate 3D point clouds and improve its accuracies tremendously. The equations derived to calculate the GSDs of pixels that lie along the center and the edges of a nadir and oblique image helped understand the relation between the GSD per pixel and pixel location. Moreover, the derived GSD equations for oblique images were used to calculate oblique image footprints which proved to be useful to plan missions that required the use of oblique images. The equations derived to calculate corrected image overlaps when mapping regions that have a structure proved to be useful when planning missions for the ODOT HQ case study presented in this document.

The case studies presented in this document show the benefits of using sUAS and photogrammetry tools to aid in the inspection of construction sites, monitor building health, and inspect bridge decks and facades by generating 3D and 2D outputs of high quality and accuracies. The case study conducted at the SR266 construction site show the use of sUAS and photogrammetry to calculate areas and preserve the information in the form of an interactive 3D model. The case study conducted at ODOT headquarters shows the benefits of thermal imaging

and photogrammetry to monitor building health and generate high-quality outputs that can be later used to help in modifications/renovations. The case study conducted at bridges shows the benefits of sUAS and photogrammetry to help in monitoring bridge health without obstructing traffic and help bridge inspectors ease the inspection process by producing realistic and high-resolution 3D models of bridge segments.

The work presented in this thesis provides the necessary information to utilize sUAS and photogrammetry efficiently to aid in the inspection and monitoring of infrastructure health and construction sites. Moving forward, the challenge would be to use the information presented in this document to build applications and tools that would help end-users to easily digest the information present in the outputs.

5.2 Future Work

This section presents a few areas of research that can be considered for future work that falls within the scope of the research work presented.

5.2.1 Mission Planner Application

The information present in this document and general information regarding inspecting bridges and construction sites will be restructured as a standard operating procedure manual. Given the growing popularity and accessibility of mobile phones and applications, the standard operating procedures created can be converted into an interactive mobile application. A functional, proof of concept, Android application called Mission Planner was created to achieve the stated objectives. Figure 5.1 shows screenshots of the application. The initial version of the application would generate specific instructions, based on users' requirements, to aid in planning missions to map structures, using the DJI GS Pro flight planning application. The application also saved

these instructions as PDF files for later reference. Moreover, the application also had information regarding popular sUAS cameras, calculators to help in creating efficient flight plans, and the standard operating procedure documents. Work can be done to improve the existing mission planner application's functionality in the following ways:

1. Ability to connect to various sUAS and camera systems and upload generated flight plans

2. Automatically generate recommended flight plans based on user selection

Figure 5.1: Mission Planner Android Application Version 1

5.2.2 Crack Detection

In the case study conducted at Jeremiah Morrow bridge, it was shown that one can generate 2D orthofacades that show cracks, with widths greater than 0.3mm. Manually identifying and marking these cracks is a tedious process. Using the generated high-quality outputs one can work on developing a crack detection and identification algorithm that would help to identify the cracks present in the image and generate a report. Figure 5.2 shows the preliminary work conducted to detect and identify cracks.
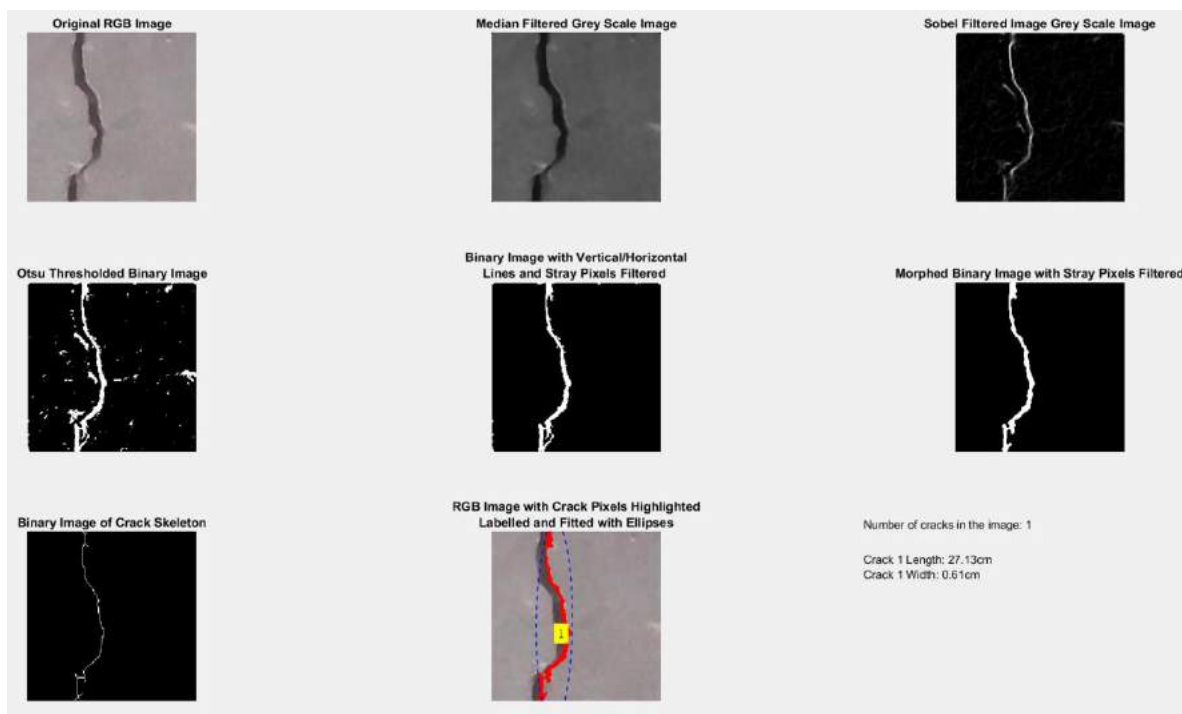
Figure 5.2: Preliminary Work Conducted to Identify and Detect Cracks

5.2.3 Point Cloud Post Processing

Research can be conducted on post-processing point clouds generated by the photogrammetry tools. The post-processing may include but not limited to:

1. Filtering noise and vegetation from point clouds

2. Point cloud classification

3. Converting point clouds to other file formats like digital surface model, digital terrain model or LandXML

References

[1]   A. Alani, M. Aboutalebi, and G. Kilic, "Integrated health assessment strategy using NDT for reinforced concrete bridges," *NDT E Int.*, vol. 61, pp. 80–94, 2014.

[2]   J. Valença, I. Puente, E. Júlio, H. González-Jorge, and P. Arias-Sánchez, "Assessment of cracks on concrete bridges using image processing supported by laser scanning survey," *Constr. Build. Mater.*, vol. 146, pp. 668–678, 2017.

[3]   T. Schenk, "Introduction to Photogrammetry," *Dep. Civ. Environ. Eng. Geod. Sci. Ohio State Univ.*, pp. 79–95, 2005.

[4]   D. G. Low, "Distinctive image features from scale-invariant keypoints," *Int. J. Comput. Vis.*, pp. 91–110, 2004.

[5]   W. Linder, *Digital Photogrammetry: A Practical Course*. 2016.

[6]   M. A. Fonstad, J. T. Dietrich, B. C. Courville, J. L. Jensen, and P. E. Carbonneau, "Topographic structure from motion: A new development in photogrammetric measurement," *Earth Surf. Process. Landforms*, vol. 38, no. 4, pp. 421–430, 2013.

[7]   M. J. Westoby, J. Brasington, N. F. Glasser, M. J. Hambrey, and J. M. Reynolds, "'Structure-from-Motion' photogrammetry: A low-cost, effective tool for geoscience applications," *Geomorphology*, vol. 179, pp. 300–314, 2012.

[8]   B. Triggs, P. McLauchlan, R. Hartley, and A. Fitzgibbon, "Bundle Adjustment A Modern

Synthesis," 2000.

[9]   J. McCarthy, "Multi-image photogrammetry as a practical tool for cultural heritage survey and community engagement," *J. Archaeol. Sci.*, vol. 43, no. 1, pp. 175–185, 2014.

[10]   N. Snavely, S. M. Seitz, and R. Szeliski, "Modeling the world from Internet photo collections," *Int. J. Comput. Vis.*, vol. 80, no. 2, pp. 189–210, 2008.

[11]   D. Turner, A. Lucieer, and C. Watson, "An Automated Technique for Generating Georectified Mosaics from Ultra-High Resolution Unmanned Aerial Vehicle (UAV) Imagery , Based on Structure from Motion (SfM) Point Clouds," pp. 1392–1410, 2012.

[12]   T. Luhman, S. Robson, S. Kyle, and I. Harley, *Close Range Photogrammetry*. .

[13]   C. Duke, "Evalutaion of Photogrammetry at Different Scales," 2018.

[14]   S. Martın, H. Uzkeda, J. Poblet, M. Bulnes, and R. Rubio, "Construction of accurate geological cross-sections along trenches , cliffs and mountain slopes using photogrammetry," vol. 51, pp. 90–100, 2013.

[15]   J. Pecoraro, C. Harper, D. Ph, C. Wang, and D. Ph, "Unmanned Aircraft Systems in Construction and Agriculture : Uses , Benefits , Challenges , and Why Companies Choose to Invest," 2017.

[16]   F. H. A. (FHWA), "Unmanned Aerial Systems (UAS)," 2019. [Online]. Available: https://www.fhwa.dot.gov/innovation/everydaycounts/edc_5/uas.cfm.

[17]   B. Coifman, M. McCord, R. Mishalani, and K. Redmill, "Surface Transportation Surveillance from Unmanned Aerial Vehicles."

[18]   A. Chiddarwar, "Application Of Computer Vision Algorithms For Uninterrupted Traffic

Monitoring Based On Aerial Images And Videos."

[19]   E. A. Carroll and D. B. Rathbone, "Using an Unmanned Airborne Data Acquisition
        System (ADAS) for Traffic Surveillance, Monitoring, and Management." pp. 145–157,
        17-Nov-2002.

[20]   A. M. Zietara, "Creating Digital Elevation Model (DEM) based on ground points
        extracted from classified aerial images obtained from Unmanned Aerial Vehicle (UAV
        )," *Nor. Univ. Sci. Technol. Fac. Eng. Dep. Civ. Environ. Eng.*, no. June, pp. 1–98, 2017.

[21]   DJI, "DJI," 2019. [Online]. Available: https://www.dji.com/.

[22]   DJI, "Matrice 100," 2019. [Online]. Available: https://www.dji.com/matrice100.

[23]   DJI, "Matrice 200 Sereis." [Online]. Available: https://www.dji.com/matrice-200-series.

[24]   DJI, "Phantom 4 RTK," 2019. [Online]. Available: https://www.dji.com/matrice-200-
        series.

[25]   DJI, "DJI Matrice 100 User Manual," 2016.

[26]   DJI, "Zenmuse Z3," 2019. [Online]. Available: https://www.dji.com/zenmuse-z3.

[27]   DJI, "Zenmuse X5," 2019. [Online]. Available: https://www.dji.com/zenmuse-x5.

[28]   DJI, "Zenmuse Z30," 2019. [Online]. Available: https://www.dji.com/zenmuse-z30.

[29]   DJI, "Zenmuse XT," 2019. [Online]. Available: https://www.dji.com/zenmuse-xt.

[30]   DJI, "Matrice 210 RTK User Manual," 2017.

[31]   DJI, "Zenmuse X5s," 2019. [Online]. Available: https://www.dji.com/zenmuse-x5s.

[32]   DJI, "Phantom 4 RTK User Manual," 2018.

[33]   DJI, *Zenmuse Z3 User Manual*. DJI, 2016.

[34]   DJI, *Zenmuse X5 User Manual*. DJI, 2015.

[35]   DJI, *Zenmuse X5s User Manual*. DJI, 2018.

[36]   DJI, *Zenmuse Z30 User Manual*. DJI, 2018.

[37]   DJI, *Zenmuse XT User Manual*. DJI, 2016.

[38]   B. Atkins, "Field of View - Rectilinear and Fishye Lenses," 2017. [Online]. Available:
        http://www.bobatkins.com/photography/technical/field_of_view.html.

[39]   Pix4D, "Pix4D," 2019. [Online]. Available: https://www.pix4d.com/.

[40]   Pix4D, "Hardware Case Study," 2017. [Online]. Available:
        https://support.pix4d.com/hc/en-us/articles/115003928846-Hardware-case-study.

[41]   Pix4D, *Pix4D Mapper User Manual*. Lausanne: Pix4D, 2017.

[42]   Intel, "Intel® Core^{TM} i7-8700K Processor," 2017. [Online]. Available:
        https://www.intel.com/content/www/us/en/products/processors/core/core-vpro/i7-
        8700k.html.

[43]   NVIDIA, "GeForce GTX 1060," 2017. [Online]. Available: https://www.nvidia.com/en-
        us/geforce/products/10series/geforce-gtx-1060/.

[44]   Samsung, "SSD 960 Pro NvME M.2 512GB," 2017. [Online]. Available:
        https://www.samsung.com/us/computing/memory-storage/solid-state-drives/ssd-960-pro-
        m-2-512gb-mz-v6p512bw/.

[45] Western Digital, "WD Black Performance Desktop Hard Drive," 2017. [Online].

Available: https://shop.westerndigital.com/products/internal-drives/wd-black-desktop-

sata-hdd#WD5003AZEX.

[46] DJI, "DJI GS Pro," 2019. [Online]. Available: https://www.dji.com/ground-station-pro.

[47] DJI, *DJI GS Pro User Manual*. DJI, 2017.

[48] F. Schmidt, "GeoSetter," 2020. [Online]. Available: https://geosetter.de/en/main-en/.

[49] Microsoft, "Microsoft Word," 2020. [Online]. Available: https://products.office.com/en-

us/word.

[50] Google, "Googel Earth," 2020. [Online]. Available: https://www.google.com/earth/.

[51] Pix4D, "Pix4D Mapper," 2020. [Online]. Available:

https://www.pix4d.com/product/pix4dmapper-photogrammetry-software.

[52] Bentley, "Bentley Context Capture," 2020. [Online]. Available:

https://www.bentley.com/en/products/brands/contextcapture.

[53] QGIS, "QGIS," 2020. [Online]. Available: https://www.qgis.org/en/site/.

[54] Ohio Department of Transporation, "Manual of Bridge Inspection (ORC 5501.47)," vol.

2014, p. 300, 2014.

[55] Pix4D, "Vertical Datum of GCP in NAV88," 2017. [Online]. Available:

https://community.pix4d.com/t/vertical-datum-of-gcp-in-nav88-which-vertical-coordinate-

system-should-i-use/4072.

[56] Bentley, "Context Capture User Guide," 2020. [Online]. Available:

https://docs.bentley.com/LiveContent/web/ContextCapture Help-v9/en/GUID-E71D0658-82CD-46F3-B400-17F95A3939EE.html.

[57]   FLIR, "FLIR Tools," 2018. .

[58]   Pix4D, "Vertical vs oblique imagery," 2018. [Online]. Available: https://support.pix4d.com/hc/en-us/articles/202559859-Vertical-vs-oblique-imagery.

[59]   P. D. Paul R. Wolf, P. D. Bon A. Dewitt, and P. D. Benjamin E. Wilkinson, *Elements of Photogrammetry with Applications in GIS, Fourth Edition*. New York: McGraw-Hill Education, 2014.

[60]   Pix4D, "Accuracy of Pix4D ouputs," 2018. [Online]. Available: https://support.pix4d.com/hc/en-us/articles/202558889-Accuracy-of-Pix4D-outputs.

[61]   Drone Deploy, "Seven Ways to Improve the Accuracy of Your Drone Maps," 2017. [Online]. Available: https://blog.dronedeploy.com/seven-ways-to-improve-the-accuracy-of-your-drone-maps-9d3161f05956.

[62]   K. Jl, "What is the 'overlapping'? And why is it so critical in 3D reconstruction?," 2017. [Online]. Available: https://blog.altizure.com/what-does-overlap-really-mean-in-3d-modelling-cf8d321bf25.

[63]   Drone Deploy, "Mapping varied elevations, tall buildings or trees," 2019. [Online]. Available: https://support.dronedeploy.com/docs/mapping-varied-elevations-tall-buildings-or-trees.

[64]   R. Usamentiaga, P. Venegas, J. Guerediaga, L. Vega, J. Molleda, and F. G. Bulnes, "Infrared thermography for temperature measurement and non-destructive testing,"

Sensors (Switzerland), vol. 14, no. 7, pp. 12305–12348, 2014.

[65] K. Vaghefi, T. M. Ahlborn, D. K. Harris, and C. N. Brooks, "Combined Imaging
      Technologies for Concrete Bridge Deck Condition Assessment," *J. Perform. Constr.
      Facil.*, vol. 29, no. 4, pp. 1–8, 2015.

[66] Radio2Space, "Components of Electromagnetic Spectrum," *2013*. [Online]. Available:
      https://www.radio2space.com/components-of-electromagnetic-spectrum/.

[67] Apogee Instruments, "Emissivity Correction for Infrared Radiometer Sensors," 2007.
      [Online]. Available: https://www.apogeeinstruments.com/emissivity-correction-for-
      infrared-radiometer-sensors/.

[68] ASTM, "ASTM International," 2020. [Online]. Available: https://www.astm.org/.

[69] FLIR, "FLIR," 2020. [Online]. Available: https://www.flir.com/.

[70] ASTM, "Standard Test Method for Detecting Delaminations in Bridge Decks Using
      Infrared Thermography," p. 3, 2013.

[71] FLIR, "FLIR Technical Note," p. 2, 2010.

[72] Pix4D, "Getting GCPs on the field or through other sources," 2020. [Online]. Available:
      https://support.pix4d.com/hc/en-us/articles/202557489-Step-1-Before-Starting-a-Project-
      4-Getting-GCPs-on-the-field-or-through-other-sources-optional-but-recommended.

[73] Ohio Department of Natural Resources, "Latitude-Longitude Grid, UTM Zone Boundary
      and State Plane Coordinate System Zone BOundary," 2008.

[74] National Oceanic And Atmospheric Administration, "Vertical Datum Transformation,"
      2020. [Online]. Available: https://vdatum.noaa.gov/.

[75]   Office of CADD & Mapping Service Ohio, "Survey & Mapping Specifications," 2016.

[76]   FLUKE, "62 MAX Mini Infrared Thermometer," 2020. [Online]. Available: https://www.fluke.com/en-us/product/temperature-measurement/ir-thermometers/fluke-62-max.

[77]   Engineering Toolbox, "Emissivity Coefficients Materials," 2003. [Online]. Available: https://www.engineeringtoolbox.com/emissivity-coefficients-d_447.html.

[78]   Engineering Toolbox, "Emissivity Coefficients for some common Materials," 2003. [Online]. Available: https://www.engineeringtoolbox.com/radiation-heat-emissivity-d_432.html.

[79]   FLIR, "Datasheet FLIR Tau2," 2016.

Chapter 6 : Appendix
A. Case Study 6: Deer Creek Park Tests, Deer Creek D6

Figure 6.1 shows the error data compiled for the 3D point cloud generated using the 0.75 cm/px

combined dataset with 14 GCPs.

Pointwise Difference Point Cloud			
Number	Point Name	Delta Easting (X) ft	Delta Northing (Y) ft	Delta Elevation (Z) ft
1	AT02	-0.003	-0.015	-0.019
2	AT04	-0.003	-0.013	-0.006
3	AT05	0.009	0.006	0.007
4	AT07	-0.007	0.012	0.005
5	AT08	0.005	0.006	0.003
6	AT09	0.003	0.018	-0.006
7	AT10	0.01	-0.005	0
8	AT12	-0.009	0.014	0.011
9	AT13	0	0.015	0.008
10	AT17	0.008	-0.016	0.022
11	AT20	-0.114	0.016	0.092
12	AT21	-0.05	-0.011	-0.006
13	AT23	-0.034	0.018	0.023
14	AT25	0.008	0.009	0.01
15	AT28	0.014	0.05	0.028
16	AT30	0.021	0.015	-0.007

Errors in Pixels for Point Cloud			
Number	Point Name	Delta Easting (X) px	Delta Northing (Y) px	Delta Elevation (Z) px
1	AT02	0.117	0.586	0.742
2	AT04	0.117	0.508	0.234
3	AT05	0.352	0.234	0.274
4	AT07	0.274	0.469	0.195
5	AT08	0.195	0.234	0.117
6	AT09	0.117	0.703	0.234
7	AT10	0.391	0.195	0.000
8	AT12	0.352	0.547	0.430
9	AT13	0.000	0.586	0.313
10	AT17	0.313	0.625	0.860
11	AT20	4.455	0.625	3.595
12	AT21	1.954	0.430	0.234
13	AT23	1.329	0.703	0.899
14	AT25	0.313	0.352	0.391
15	AT28	0.547	1.954	1.094
16	AT30	0.821	0.586	0.274

	Delta Easting (ft)	Delta Northing (ft)	Delta Elevation (ft)
Mean of Absolute Error	0.019	0.015	0.016
Std. Deviation	0.033	0.017	0.025
Variance	0.001	0.000	0.001
RMSE (16 Points)	0.033	0.018	0.026
RMSE (15 Points)	0.018	0.018	0.013

Figure 6.1: Error Data Compiled for the 3D Point Cloud Generated Using the 0.75cm/px Grid Dataset with 14 GCPs

Figure 6.2 shows the error data compiled for the 3D point cloud generated using the 0.75 cm/px

combined dataset with 0 GCPs.

		Pointwise Difference Point Cloud		
Number	Point Name	Delta Easting (X) ft	Delta Northing (Y) ft	Delta Elevation (Z) ft
1	AT02	0.106	-0.031	-0.084
2	AT04	0.106	-0.031	-0.076
3	AT05	0.118	-0.008	-0.052
4	AT07	0.101	-0.004	-0.061
5	AT08	0.113	-0.01	-0.066
6	AT09	0.112	0.004	-0.083
7	AT10	0.119	-0.014	-0.076
8	AT12	0.102	0.011	-0.068
9	AT13	0.109	0.014	-0.065
10	AT17	0.119	-0.029	-0.032
11	AT20	-0.015	0.006	0.002
12	AT21	0.055	-0.014	-0.084
13	AT23	0.077	0.018	-0.046
14	AT25	0.124	0.005	-0.044
15	AT28	0.131	0.055	-0.048
16	AT30	0.143	0.014	-0.068

		Errors in Pixels for Point Cloud		
Number	Point Name	Delta Easting (X) px	Delta Northing (Y) px	Delta Elevation (Z) px
1	AT02	4.142	1.211	3.282
2	AT04	4.142	1.211	2.970
3	AT05	4.611	0.313	2.032
4	AT07	3.947	0.156	2.384
5	AT08	4.416	0.391	2.579
6	AT09	4.377	0.156	3.243
7	AT10	4.650	0.547	2.970
8	AT12	3.986	0.430	2.657
9	AT13	4.259	0.547	2.540
10	AT17	4.650	1.133	1.250
11	AT20	0.586	0.234	0.078
12	AT21	2.149	0.547	3.282
13	AT23	3.009	0.703	1.798
14	AT25	4.846	0.195	1.719
15	AT28	5.119	2.149	1.876
16	AT30	5.588	0.547	2.657

	Delta Easting (ft)	Delta Northing (ft)	Delta Elevation (ft)
Mean of Absolute Error	0.099	0.017	0.153
Std. Deviation	0.039	0.022	0.371
Variance	0.001	0.000	0.138
RMSE (16 Points)	0.104	0.022	0.391
RMSE (15 Points)	0.107	0.022	0.403

Pointwise Difference Between Point Cloud and Surveyor (0.75cm Combined w/ 0GCPs)

Figure 6.3: Error Data Compiled for the 3D Point Cloud Generated Using the 0.75cm/px Grid Dataset with 0 GCPs

Figure 6.3 shows the error data compiled for the 3D point cloud generated using the 0.75 cm/px parallel dataset with 14 GCPs.

		Pointwise Difference Point Cloud		
Number	Point Name	Delta Easting (X) ft	Delta Northing (Y) ft	Delta Elevation (Z) ft
1	AT02	-0.006	-0.023	-0.012
2	AT04	-0.006	-0.018	-0.005
3	AT05	0.009	0.005	0
4	AT07	-0.006	0.016	0.014
5	AT08	0.007	0.011	0.007
6	AT09	0.005	0.017	-0.011
7	AT10	0.012	0	0.013
8	AT12	-0.013	0.005	0.011
9	AT13	0.009	0.016	-0.001
10	AT17	0.015	-0.008	0.021
11	AT20	-0.111	0.029	0.085
12	AT21	0.014	-0.02	-0.009
13	AT23	-0.029	0.019	0.033
14	AT25	-0.004	0.002	-0.007
15	AT28	0.026	0.057	0.037
16	AT30	0.013	0.019	0

		Errors in Pixels for Point Cloud		
Number	Point Name	Delta Easting (X) px	Delta Northing (Y) px	Delta Elevation (Z) px
1	AT02	0.234	0.899	0.469
2	AT04	0.234	0.703	0.195
3	AT05	0.352	0.195	0.000
4	AT07	0.234	0.625	0.547
5	AT08	0.274	0.430	0.274
6	AT09	0.195	0.664	0.430
7	AT10	0.469	0.000	0.508
8	AT12	0.508	0.195	0.430
9	AT13	0.352	0.625	0.039
10	AT17	0.586	0.313	0.821
11	AT20	4.338	1.133	3.322
12	AT21	0.547	0.782	0.352
13	AT23	1.133	0.742	1.290
14	AT25	0.156	0.078	0.274
15	AT28	1.016	2.227	1.446
16	AT30	0.508	0.742	0.000

	Delta Easting (ft)	Delta Northing (ft)	Delta Elevation (ft)
Mean of Absolute Error	0.018	0.017	0.017
Std. Deviation	0.031	0.020	0.025
Variance	0.001	0.000	0.001
RMSE (16 Points)	0.031	0.021	0.026
RMSE (15 Points)	0.014	0.020	0.016

Pointwise Difference Between Point Cloud and Surveyor (0.75cm Parallel w/14GCP)

Figure 6.2: Error Data Compiled for the 3D Point Cloud Generated Using the 0.75cm/px Parallel Dataset with 14 GCPs

Figure 6.4 shows the error data compiled for the 3D point cloud generated using the 0.75 cm/px parallel dataset with 0 GCPs.

174

Pointwise Difference Point Cloud				
Number	Point Name	Delta Easting (X) ft	Delta Northing (Y) ft	Delta Elevation (Z) ft
1	AT02	0.072	-0.045	0.205
2	AT04	0.078	-0.045	0.209
3	AT05	0.087	-0.009	0.224
4	AT07	0.077	-0.006	0.242
5	AT08	0.09	-0.011	0.232
6	AT09	0.09	-0.003	0.213
7	AT10	0.098	-0.013	0.247
8	AT12	0.078	-0.001	0.241
9	AT13	0.097	0.014	0.247
10	AT17	0.1	-0.021	0.256
11	AT20	-0.029	0.017	0.321
12	AT21	0.052	0.004	0.247
13	AT23	0.06	0.019	0.275
14	AT25	0.089	0.009	0.331
15	AT28	0.11	0.069	0.334
16	AT30	0.105	0.031	0.373

Errors in Pixels for Point Cloud				
Number	Point Name	Delta Easting (X) px	Delta Northing (Y) px	Delta Elevation (Z) px
1	AT02	2.814	1.758	8.011
2	AT04	3.048	1.758	8.167
3	AT05	3.400	0.352	8.753
4	AT07	3.009	0.234	9.457
5	AT08	3.517	0.430	9.066
6	AT09	3.517	0.117	8.323
7	AT10	3.830	0.508	9.652
8	AT12	3.048	0.039	9.418
9	AT13	3.790	0.547	9.652
10	AT17	3.908	0.821	10.004
11	AT20	1.133	0.664	12.544
12	AT21	2.032	0.156	9.652
13	AT23	2.345	0.742	10.746
14	AT25	3.478	0.352	12.934
15	AT28	4.298	2.696	13.052
16	AT30	4.103	1.211	14.576

	Delta Easting (ft)	Delta Northing (ft)	Delta Elevation (ft)
Mean of Absolute Error	0.082	0.020	0.262
Std. Deviation	0.033	0.028	0.051
Variance	0.001	0.001	0.003
RMSE (16 Points)	0.085	0.027	0.267
RMSE (15 Points)	0.087	0.027	0.263

Pointwise Difference Between Point Cloud and Surveyor
(0.75cm Parallel w/ 0GCPs)
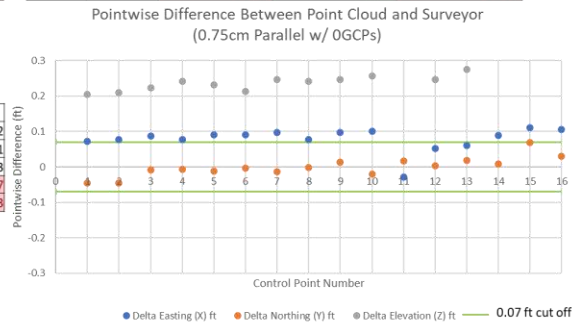
Figure 6.4: Error Data Compiled for the 3D Point Cloud Generated Using the 0.75cm/px Parallel Dataset with 0 GCPs

Figure A.5 shows the error data compiled for the 3D point cloud generated using the 0.75 cm/px perpendicular dataset with 14 GCPs.

Pointwise Difference Point Cloud				
Number	Point Name	Delta Easting (X) ft	Delta Northing (Y) ft	Delta Elevation (Z) ft
1	AT02	0.003	0.001	-0.021
2	AT04	0.002	0.003	-0.001
3	AT05	0.012	0.016	0.013
4	AT07	-0.007	0.019	0.002
5	AT08	0.006	0.011	0.005
6	AT09	0.002	0.028	0.005
7	AT10	0.01	-0.007	-0.007
8	AT12	-0.009	0.023	0.016
9	AT13	-0.008	0.01	0.015
10	AT17	0.001	-0.018	0.02
11	AT20	-0.124	0.006	0.073
12	AT21	-0.019	-0.056	-0.04
13	AT23	-0.039	0.013	0.014
14	AT25	0.019	0.009	-0.003
15	AT28	0.006	0.033	0.021
16	AT30	0.021	0.005	-0.049

Errors in Pixels for Point Cloud				
Number	Point Name	Delta Easting (X) px	Delta Northing (Y) px	Delta Elevation (Z) px
1	AT02	0.117	0.039	0.821
2	AT04	0.078	0.117	0.039
3	AT05	0.469	0.625	0.508
4	AT07	0.274	0.742	0.078
5	AT08	0.234	0.430	0.195
6	AT09	0.078	1.094	0.195
7	AT10	0.391	0.274	0.274
8	AT12	0.352	0.899	0.625
9	AT13	0.313	0.391	0.586
10	AT17	0.039	0.703	0.782
11	AT20	4.846	0.234	2.853
12	AT21	0.742	2.188	1.563
13	AT23	1.524	0.508	0.547
14	AT25	0.742	0.352	0.117
15	AT28	0.234	1.290	0.821
16	AT30	0.821	0.195	1.915

	Delta Easting (ft)	Delta Northing (ft)	Delta Elevation (ft)
Mean of Absolute Error	0.018	0.016	0.019
Std. Deviation	0.034	0.021	0.027
Variance	0.001	0.000	0.001
RMSE (16 Points)	0.034	0.021	0.027
RMSE (15 Points)	0.015	0.022	0.020

Pointwise Difference Between Point Cloud and Surveyor
(0.75cm Perpendicular w/14GCP)
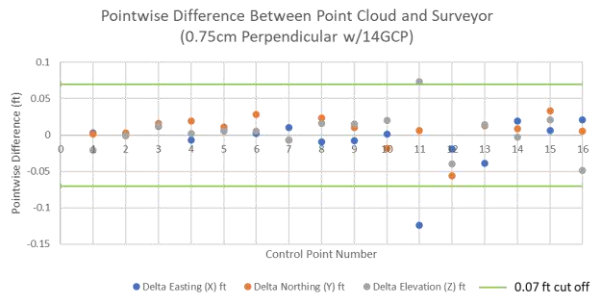
Figure 6.5: Error Data Compiled for the 3D Point Cloud Generated Using the 0.75cm/px Perpendicular Dataset with 14 GCPs

175

Figure A.6 shows the error data compiled for the 3D point cloud generated using the 0.75 cm/px perpendicular dataset with 0 GCPs.

		Pointwise Difference Point Cloud		
Number	Point Name	Delta Easting (X) ft	Delta Northing (Y) ft	Delta Elevation (Z) ft
1	AT02	0.14	-0.015	-0.29
2	AT04	0.137	-0.016	-0.285
3	AT05	0.151	0	-0.25
4	AT07	0.128	0	-0.282
5	AT08	0.138	-0.009	-0.284
6	AT09	0.134	0.013	-0.298
7	AT10	0.139	-0.016	-0.316
8	AT12	0.122	0.022	-0.29
9	AT13	0.121	0.009	-0.295
10	AT17	0.14	-0.034	-0.245
11	AT20	0	-0.006	-0.234
12	AT21	0.06	-0.032	-0.33
13	AT23	0.095	0.012	-0.285
14	AT25	0.164	-0.009	-0.336
15	AT28	0.157	0.039	-0.343
16	AT30	0.185	-0.005	-0.429

		Errors in Pixels for Point Cloud		
Number	Point Name	Delta Easting (X) px	Delta Northing (Y) px	Delta Elevation (Z) px
1	AT02	5.471	0.586	11.332
2	AT04	5.354	0.625	11.137
3	AT05	5.901	0.000	9.769
4	AT07	5.002	0.000	11.020
5	AT08	5.393	0.352	11.098
6	AT09	5.236	0.508	11.645
7	AT10	5.432	0.625	12.348
8	AT12	4.767	0.860	11.332
9	AT13	4.728	0.352	11.528
10	AT17	5.471	1.329	9.574
11	AT20	0.000	0.234	9.144
12	AT21	2.345	1.250	12.895
13	AT23	3.712	0.469	11.137
14	AT25	6.409	0.352	13.130
15	AT28	6.135	1.524	13.403
16	AT30	7.229	0.195	16.764

	Delta Easting (ft)	Delta Northing (ft)	Delta Elevation (ft)
Mean of Absolute Error	0.126	0.015	0.300
Std. Deviation	0.044	0.019	0.046
Variance	0.002	0.000	0.002
RMSE (16 Points)	0.133	0.019	0.303
RMSE (15 Points)	0.137	0.019	0.307

Pointwise Difference Between Point Cloud and Surveyor (0.75cm/px Perpendicular w/ 0GCPs)

Figure 6.6: Error Data Compiled for the 3D Point Cloud Generated Using the 0.75cm/px Perpendicular Dataset with 0 GCPs

Figure A.7 shows the error data compiled for the 3D point cloud generated using the 1 cm/px combined dataset with 14 GCPs.

		Pointwise Difference Point Cloud		
Number	Point Name	Delta Easting (X) ft	Delta Northing (Y) ft	Delta Elevation (Z) ft
1	AT02	0.001	-0.013	-0.018
2	AT04	-0.005	-0.006	0.013
3	AT05	0.016	0.012	-0.005
4	AT07	-0.004	0.012	0.009
5	AT08	0.006	0.007	-0.012
6	AT09	0.008	0.012	-0.007
7	AT10	0.012	-0.009	0.003
8	AT12	-0.01	0.009	0.028
9	AT13	0.003	0.001	-0.012
10	AT17	0.011	-0.019	-0.002
11	AT20	-0.115	0.01	0.099
12	AT21	-0.005	0.002	0
13	AT23	-0.028	0.009	0
14	AT25	0.008	0.005	0.02
15	AT28	-0.002	0.032	0.028
16	AT30	0.006	0.014	-0.001

		Errors in Pixels for Point Cloud		
Number	Point Name	Delta Easting (X) px	Delta Northing (Y) px	Delta Elevation (Z) px
1	AT02	0.029	0.377	0.523
2	AT04	0.145	0.174	0.377
3	AT05	0.464	0.348	0.145
4	AT07	0.116	0.348	0.261
5	AT08	0.174	0.203	0.348
6	AT09	0.232	0.348	0.203
7	AT10	0.348	0.261	0.087
8	AT12	0.290	0.261	0.813
9	AT13	0.087	0.029	0.348
10	AT17	0.319	0.552	0.058
11	AT20	3.338	0.290	2.874
12	AT21	0.145	0.058	0.000
13	AT23	0.813	0.261	0.000
14	AT25	0.232	0.145	0.581
15	AT28	0.058	0.929	0.813
16	AT30	0.174	0.406	0.029

	Delta Easting (ft)	Delta Northing (ft)	Delta Elevation (ft)
Mean of Absolute Error	0.015	0.011	0.016
Std. Deviation	0.031	0.012	0.028
Variance	0.001	0.000	0.001
RMSE (16 Points)	0.031	0.013	0.028
RMSE (15 Points)	0.011	0.013	0.014

Pointwise Difference Between Point Cloud and Surveyor (1cm Combined w/14GCP)

Figure 6.7: Error Data Compiled for the 3D Point Cloud Generated Using the 1cm/px Grid Dataset with 14 GCPs

176

Figure A.8 shows the error data compiled for the 3D point cloud generated using the 1 cm/px combined dataset with 12 GCPs.

	Pointwise Difference Point Cloud			
Number	Point Name	Delta Easting (X) ft	Delta Northing (Y) ft	Delta Elevation (Z) ft
1	AT02	0.001	-0.01	-0.018
2	AT04	-0.005	-0.004	0.013
3	AT05	0.016	0.015	-0.007
4	AT07	-0.004	0.014	0.008
5	AT08	0.006	0.009	-0.011
6	AT09	0.008	0.014	-0.006
7	AT10	0.012	-0.007	0.003
8	AT12	-0.01	0.011	0.028
9	AT13	0.003	0.004	-0.012
10	AT17	0.009	-0.016	-0.001
11	AT20	-0.115	0.012	0.099
12	AT21	0	0.002	-0.001
13	AT23	-0.027	0.012	0.001
14	AT25	0.011	0.007	0.026
15	AT28	0.001	0.036	0.032
16	AT30	0.008	0.015	0.004

	Errors in Pixels for Point Cloud			
Number	Point Name	Delta Easting (X) px	Delta Northing (Y) px	Delta Elevation (Z) px
1	AT02	0.029	0.290	0.523
2	AT04	0.145	0.116	0.377
3	AT05	0.464	0.435	0.203
4	AT07	0.116	0.406	0.232
5	AT08	0.174	0.261	0.319
6	AT09	0.232	0.406	0.174
7	AT10	0.348	0.203	0.087
8	AT12	0.290	0.319	0.813
9	AT13	0.087	0.116	0.348
10	AT17	0.261	0.464	0.029
11	AT20	3.338	0.348	2.874
12	AT21	0.000	0.058	0.029
13	AT23	0.784	0.348	0.029
14	AT25	0.319	0.203	0.755
15	AT28	0.029	1.045	0.929
16	AT30	0.232	0.435	0.116

	Delta Easting (ft)	Delta Northing (ft)	Delta Elevation (ft)
Mean of Absolute Error	0.015	0.012	0.017
Std. Deviation	0.031	0.012	0.028
Variance	0.001	0.000	0.001
RMSE (16 Points)	0.030	0.014	0.029
RMSE (15 Points)	0.010	0.014	0.015

Pointwise Difference Between Point Cloud and Surveyor (1cm Combined w/12GCPs)
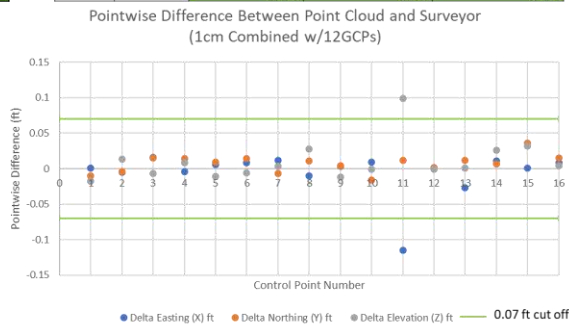
Figure 6.8: Error Data Compiled for the 3D Point Cloud Generated Using the 1cm/px Grid Dataset with 12 GCPs

Figure A.9 shows the error data compiled for the 3D point cloud generated using the 1 cm/px combined dataset with 11 GCPs.

	Pointwise Difference Point Cloud			
Number	Point Name	Delta Easting (X) ft	Delta Northing (Y) ft	Delta Elevation (Z) ft
1	AT02	0	-0.014	-0.016
2	AT04	-0.006	-0.011	0.018
3	AT05	0.015	0.013	-0.005
4	AT07	-0.005	0.01	0.01
5	AT08	0.006	0.004	-0.008
6	AT09	0.009	0.008	-0.005
7	AT10	0.013	-0.012	0.003
8	AT12	-0.008	0.008	0.027
9	AT13	0.004	0.001	-0.013
10	AT17	0.009	-0.018	0
11	AT20	-0.114	0.008	0.099
12	AT21	0	-0.002	-0.002
13	AT23	-0.026	0.01	0
14	AT25	0.011	0.006	0.027
15	AT28	0.001	0.034	0.031
16	AT30	0.008	0.014	0.004

	Errors in Pixels for Point Cloud			
Number	Point Name	Delta Easting (X) px	Delta Northing (Y) px	Delta Elevation (Z) px
1	AT02	0.000	0.406	0.464
2	AT04	0.174	0.319	0.523
3	AT05	0.435	0.377	0.145
4	AT07	0.145	0.290	0.290
5	AT08	0.174	0.116	0.232
6	AT09	0.261	0.232	0.145
7	AT10	0.377	0.348	0.087
8	AT12	0.232	0.232	0.784
9	AT13	0.116	0.029	0.377
10	AT17	0.261	0.523	0.000
11	AT20	3.309	0.232	2.874
12	AT21	0.000	0.058	0.058
13	AT23	0.755	0.290	0.000
14	AT25	0.319	0.174	0.784
15	AT28	0.029	0.987	0.900
16	AT30	0.232	0.406	0.116

	Delta Easting (ft)	Delta Northing (ft)	Delta Elevation (ft)
Mean of Absolute Error	0.015	0.011	0.017
Std. Deviation	0.031	0.013	0.028
Variance	0.001	0.000	0.001
RMSE (16 Points)	0.030	0.013	0.029
RMSE (15 Points)	0.010	0.013	0.015

Pointwise Difference Between Point Cloud and Surveyor (1cm Combined w/11GCPs)
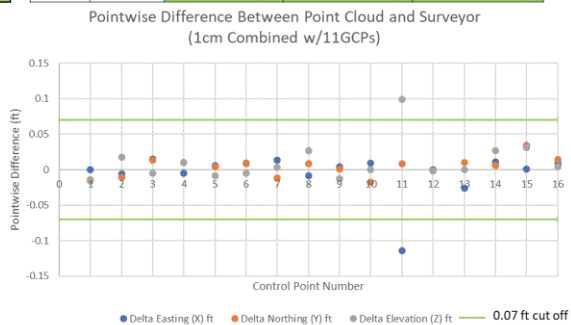
Figure 6.9: Error Data Compiled for the 3D Point Cloud Generated Using the 1cm/px Grid Dataset with 11 GCPs

177

Figure A.10 shows the error data compiled for the 3D point cloud generated using the 1 cm/px combined dataset with 9 GCPs.

Pointwise Difference Point Cloud

Number	Point Name	Delta Easting (X) ft	Delta Northing (Y) ft	Delta Elevation (Z) ft
1	AT02	0.006	-0.016	-0.014
2	AT04	0	-0.013	0.017
3	AT05	0.021	0.011	-0.003
4	AT07	0.002	0.006	0.009
5	AT08	0.012	0.001	-0.012
6	AT09	0.013	0.006	-0.007
7	AT10	0.016	-0.014	0.002
8	AT12	-0.006	0.006	0.028
9	AT13	0.007	-0.001	-0.009
10	AT17	0.019	-0.019	0.003
11	AT20	-0.112	0.004	0.096
12	AT21	0.002	-0.004	-0.003
13	AT23	-0.023	0.007	0.008
14	AT25	0.017	0	0.04
15	AT28	0.006	0.029	0.037
16	AT30	0.013	0.011	0.012

Errors in Pixels for Point Cloud

Number	Point Name	Delta Easting (X) px	Delta Northing (Y) px	Delta Elevation (Z) px
1	AT02	0.174	0.464	0.406
2	AT04	0.000	0.377	0.493
3	AT05	0.610	0.319	0.087
4	AT07	0.058	0.174	0.261
5	AT08	0.348	0.029	0.348
6	AT09	0.377	0.174	0.203
7	AT10	0.464	0.406	0.058
8	AT12	0.174	0.174	0.813
9	AT13	0.203	0.029	0.261
10	AT17	0.552	0.552	0.087
11	AT20	3.251	0.116	2.787
12	AT21	0.058	0.116	0.087
13	AT23	0.668	0.203	0.232
14	AT25	0.493	0.000	1.161
15	AT28	0.174	0.842	1.074
16	AT30	0.377	0.319	0.348

	Delta Easting (ft)	Delta Northing (ft)	Delta Elevation (ft)
Mean of Absolute Error	0.017	0.009	0.019
Std. Deviation	0.032	0.012	0.028
Variance	0.001	0.000	0.001
RMSE (16 Points)	0.031	0.012	0.030
RMSE (15 Points)	0.013	0.012	0.018

Pointwise Difference Between Point Cloud and Surveyor (1cm Combined w/9GCPs)

Figure 6.10: Error Data Compiled for the 3D Point Cloud Generated Using the 1cm/px Grid Dataset with 9 GCPs

Figure A.11 shows the error data compiled for the 3D point cloud generated using the 1 cm/px combined dataset with 7 GCPs.

Pointwise Difference Point Cloud

Number	Point Name	Delta Easting (X) ft	Delta Northing (Y) ft	Delta Elevation (Z) ft
1	AT02	0.007	-0.028	-0.008
2	AT04	0.005	-0.027	0.014
3	AT05	0.022	0.004	0.002
4	AT07	0.005	-0.005	0.009
5	AT08	0.016	-0.011	-0.014
6	AT09	0.018	-0.003	-0.011
7	AT10	0.021	-0.022	-0.002
8	AT12	-0.003	0	0.026
9	AT13	0.009	-0.008	-0.016
10	AT17	0.023	-0.028	0.007
11	AT20	-0.107	-0.003	0.094
12	AT21	0.006	-0.011	-0.007
13	AT23	-0.021	0.001	0.003
14	AT25	0.02	-0.004	0.039
15	AT28	0.006	0.024	0.034
16	AT30	0.014	0.008	0.012

Errors in Pixels for Point Cloud

Number	Point Name	Delta Easting (X) px	Delta Northing (Y) px	Delta Elevation (Z) px
1	AT02	0.203	0.813	0.232
2	AT04	0.145	0.784	0.406
3	AT05	0.639	0.116	0.058
4	AT07	0.145	0.145	0.261
5	AT08	0.464	0.319	0.406
6	AT09	0.523	0.087	0.319
7	AT10	0.610	0.639	0.058
8	AT12	0.087	0.000	0.755
9	AT13	0.261	0.232	0.464
10	AT17	0.668	0.813	0.203
11	AT20	3.106	0.087	2.729
12	AT21	0.174	0.319	0.203
13	AT23	0.610	0.029	0.087
14	AT25	0.581	0.116	1.132
15	AT28	0.174	0.697	0.987
16	AT30	0.406	0.232	0.348

	Delta Easting (ft)	Delta Northing (ft)	Delta Elevation (ft)
Mean of Absolute Error	0.019	0.012	0.019
Std. Deviation	0.031	0.014	0.027
Variance	0.001	0.000	0.001
RMSE (16 Points)	0.030	0.015	0.029
RMSE (15 Points)	0.015	0.016	0.017

Pointwise Difference Between Point Cloud and Surveyor (1cm Combined w/7GCPs)

Figure 6.11: Error Data Compiled for the 3D Point Cloud Generated Using the 1cm/px Grid Dataset with 7 GCPs

Figure A.12 shows the error data compiled for the 3D point cloud generated using the 1 cm/px combined dataset with 5 GCPs.

Pointwise Difference Point Cloud					Errors in Pixels for Point Cloud				
Number	Point Name	Delta Easting (X) ft	Delta Northing (Y) ft	Delta Elevation (Z) ft	Number	Point Name	Delta Easting (X) px	Delta Northing (Y) px	Delta Elevation (Z) px
1	AT02	0.008	-0.033	-0.001	1	AT02	0.232	0.958	0.029
2	AT04	0.007	-0.034	0.02	2	AT04	0.203	0.987	0.581
3	AT05	0.023	0.001	0.008	3	AT05	0.668	0.029	0.232
4	AT07	0.008	-0.011	0.016	4	AT07	0.232	0.319	0.464
5	AT08	0.018	-0.018	-0.007	5	AT08	0.523	0.523	0.203
6	AT09	0.021	-0.011	-0.007	6	AT09	0.610	0.319	0.203
7	AT10	0.024	-0.029	0	7	AT10	0.697	0.842	0.000
8	AT12	0.003	-0.005	0.027	8	AT12	0.087	0.145	0.784
9	AT13	0.014	-0.012	-0.014	9	AT13	0.406	0.348	0.406
10	AT17	0.027	-0.031	0.015	10	AT17	0.784	0.900	0.435
11	AT20	-0.106	-0.011	0.095	11	AT20	3.077	0.319	2.758
12	AT21	0.008	-0.016	-0.004	12	AT21	0.232	0.464	0.116
13	AT23	-0.016	-0.003	0.004	13	AT23	0.464	0.087	0.116
14	AT25	0.024	-0.004	0.039	14	AT25	0.697	0.116	1.132
15	AT28	0.008	0.021	0.033	15	AT28	0.232	0.610	0.958
16	AT30	0.016	0.007	0.012	16	AT30	0.464	0.203	0.348

	Delta Easting (ft)	Delta Northing (ft)	Delta Elevation (ft)
Mean of Absolute Error	0.021	0.015	0.019
Std. Deviation	0.032	0.015	0.026
Variance	0.001	0.000	0.001
RMSE (16 Points)	0.031	0.019	0.029
RMSE (15 Points)	0.017	0.019	0.018

Figure 6.12: Error Data Compiled for the 3D Point Cloud Generated Using the 1cm/px Grid Dataset with 5 GCPs

Figure A.13 shows the error data compiled for the 3D point cloud generated using the 1 cm/px combined dataset with 0 GCPs.

Pointwise Difference Point Cloud					Errors in Pixels for Point Cloud				
Number	Point Name	Delta Easting (X) ft	Delta Northing (Y) ft	Delta Elevation (Z) ft	Number	Point Name	Delta Easting (X) px	Delta Northing (Y) px	Delta Elevation (Z) px
1	AT02	0.109	-0.017	0.172	1	AT02	3.164	0.493	4.993
2	AT04	0.106	-0.017	0.201	2	AT04	3.077	0.493	5.835
3	AT05	0.124	0.012	0.18	3	AT05	3.600	0.348	5.225
4	AT07	0.106	0.006	0.194	4	AT07	3.077	0.174	5.632
5	AT08	0.117	0	0.17	5	AT08	3.396	0.000	4.935
6	AT09	0.121	0.007	0.173	6	AT09	3.512	0.203	5.022
7	AT10	0.125	-0.011	0.181	7	AT10	3.629	0.319	5.254
8	AT12	0.106	0.015	0.194	8	AT12	3.077	0.435	5.632
9	AT13	0.109	0.009	0.152	9	AT13	3.164	0.261	4.412
10	AT17	0.122	-0.019	0.183	10	AT17	3.541	0.552	5.312
11	AT20	-0.005	0.008	0.275	11	AT20	0.145	0.232	7.983
12	AT21	0.062	0.028	0.186	12	AT21	1.800	0.813	5.399
13	AT23	0.077	0.025	0.162	13	AT23	2.235	0.726	4.703
14	AT25	0.117	0.049	0.253	14	AT25	3.396	1.422	7.344
15	AT28	0.079	0.059	0.229	15	AT28	2.293	1.713	6.648
16	AT30	0.09	0.066	0.252	16	AT30	2.613	1.916	7.315

	Delta Easting (ft)	Delta Northing (ft)	Delta Elevation (ft)
Mean of Absolute Error	0.098	0.022	0.197
Std. Deviation	0.033	0.026	0.036
Variance	0.001	0.001	0.001
RMSE (16 Points)	0.103	0.029	0.200
RMSE (15 Points)	0.106	0.030	0.194

Figure 6.13: Error Data Compiled for the 3D Point Cloud Generated Using the 1cm/px Grid Dataset with 0 GCPs

179

Figure A.14 shows the error data compiled for the 3D point cloud generated using the 1 cm/px parallel dataset with 14 GCPs.

Pointwise Difference Point Cloud					Errors in Pixels for Point Cloud			
Number	Point Name	Delta Easting (X) ft	Delta Northing (Y) ft	Delta Elevation (Z) ft	Number	Point Name	Delta Easting (X) px	Delta Northing (Y) px	Delta Elevation (Z) px
1	AT02	-0.006	-0.019	-0.009	1	AT02	0.174	0.552	0.261
2	AT04	-0.016	-0.007	0.008	2	AT04	0.464	0.203	0.232
3	AT05	0.009	0.007	-0.005	3	AT05	0.261	0.203	0.145
4	AT07	-0.008	0.018	0.002	4	AT07	0.232	0.523	0.058
5	AT08	0.004	0.014	0.001	5	AT08	0.116	0.406	0.029
6	AT09	0	0.014	-0.012	6	AT09	0.000	0.406	0.348
7	AT10	0.011	-0.003	0.005	7	AT10	0.319	0.087	0.145
8	AT12	-0.02	0.003	0.042	8	AT12	0.581	0.087	1.219
9	AT13	0.002	0.005	-0.01	9	AT13	0.058	0.145	0.290
10	AT17	0.004	-0.015	-0.026	10	AT17	0.116	0.435	0.755
11	AT20	-0.109	0.013	0.09	11	AT20	3.164	0.377	2.613
12	AT21	0.014	0.004	-0.004	12	AT21	0.406	0.116	0.116
13	AT23	-0.032	0.009	-0.006	13	AT23	0.929	0.261	0.174
14	AT25	-0.004	-0.005	0.018	14	AT25	0.116	0.145	0.523
15	AT28	0.024	0.044	0.046	15	AT28	0.697	1.277	1.335
16	AT30	0.006	0.009	-0.007	16	AT30	0.174	0.261	0.203

	Delta Easting (ft)	Delta Northing (ft)	Delta Elevation (ft)
Mean of Absolute Error	0.017	0.012	0.018
Std. Deviation	0.030	0.015	0.029
Variance	0.001	0.000	0.001
RMSE (16 Points)	0.030	0.015	0.029
RMSE (15 Points)	0.014	0.015	0.019

Figure 6.14: Error Data Compiled for the 3D Point Cloud Generated Using the 1cm/px Parallel Dataset with 14 GCPs

Figure A.15 shows the error data compiled for the 3D point cloud generated using the 1 cm/px parallel dataset with 0 GCPs.

Pointwise Difference Point Cloud					Errors in Pixels for Point Cloud			
Number	Point Name	Delta Easting (X) ft	Delta Northing (Y) ft	Delta Elevation (Z) ft	Number	Point Name	Delta Easting (X) px	Delta Northing (Y) px	Delta Elevation (Z) px
1	AT02	0.109	-0.005	-0.041	1	AT02	3.164	0.145	1.190
2	AT04	0.101	-0.011	-0.031	2	AT04	2.932	0.319	0.900
3	AT05	0.131	0.029	-0.043	3	AT05	3.803	0.842	1.248
4	AT07	0.114	0.013	-0.044	4	AT07	3.309	0.377	1.277
5	AT08	0.125	0.018	-0.051	5	AT08	3.629	0.523	1.480
6	AT09	0.123	0.02	-0.073	6	AT09	3.571	0.581	2.119
7	AT10	0.134	0.011	-0.066	7	AT10	3.890	0.319	1.916
8	AT12	0.11	0.024	-0.022	8	AT12	3.193	0.697	0.639
9	AT13	0.126	0.032	-0.084	9	AT13	3.658	0.929	2.438
10	AT17	0.136	0.004	-0.068	10	AT17	3.948	0.116	1.974
11	AT20	0.009	0.026	0.007	11	AT20	0.261	0.755	0.203
12	AT21	0.088	0.054	0.933	12	AT21	2.555	1.568	27.084
13	AT23	0.094	0.034	-0.064	13	AT23	2.729	0.987	1.858
14	AT25	0.123	0.017	-0.021	14	AT25	3.571	0.493	0.610
15	AT28	0.123	0.068	0.938	15	AT28	3.571	1.974	27.229
16	AT30	0.139	0.027	-0.058	16	AT30	4.035	0.784	1.684

|	Delta Easting (ft)	Delta Northing (ft)	Delta Elevation (ft)
Mean of Absolute Error	0.112	0.025	0.159
Std. Deviation	0.031	0.020	0.336
Variance	0.001	0.000	0.113
RMSE (16 Points)	0.116	0.030	0.334
RMSE (15 Points)	0.119	0.030	0.345

Figure 6.15: Error Data Compiled for the 3D Point Cloud Generated Using the 1cm/px Parallel Dataset with 0 GCPs

Figure A.16 shows the error data compiled for the 3D point cloud generated using the 1 cm/px perpendicular dataset with 14 GCPs.

Pointwise Difference Point Cloud				
Number	Point Name	Delta Easting (X) ft	Delta Northing (Y) ft	Delta Elevation (Z) ft
1	AT02	0.005	-0.004	-0.028
2	AT04	0.002	0.006	0.017
3	AT05	0.02	0.016	-0.014
4	AT07	-0.004	0.016	0.015
5	AT08	0.004	0.01	-0.021
6	AT09	0.01	0.017	0.005
7	AT10	0.011	-0.011	0.01
8	AT12	-0.007	0.01	0.024
9	AT13	0.003	-0.001	-0.016
10	AT17	0.006	-0.024	0.002
11	AT20	-0.12	0.011	0.1
12	AT21	-0.008	-0.002	-0.004
13	AT23	-0.028	0.01	0.004
14	AT25	0.011	0.006	0.018
15	AT28	-0.008	0.025	0.029
16	AT30	0.008	0.013	-0.002

Errors in Pixels for Point Cloud				
Number	Point Name	Delta Easting (X) px	Delta Northing (Y) px	Delta Elevation (Z) px
1	AT02	0.145	0.116	0.813
2	AT04	0.058	0.174	0.493
3	AT05	0.581	0.464	0.406
4	AT07	0.116	0.464	0.435
5	AT08	0.116	0.290	0.610
6	AT09	0.290	0.493	0.145
7	AT10	0.319	0.319	0.290
8	AT12	0.203	0.290	0.697
9	AT13	0.087	0.029	0.464
10	AT17	0.174	0.697	0.058
11	AT20	3.483	0.319	2.903
12	AT21	0.232	0.058	0.116
13	AT23	0.813	0.290	0.116
14	AT25	0.319	0.174	0.523
15	AT28	0.232	0.726	0.842
16	AT30	0.232	0.377	0.058

	Delta Easting (ft)	Delta Northing (ft)	Delta Elevation (ft)
Mean of Absolute Error	0.016	0.011	0.019
Std. Deviation	0.032	0.012	0.029
Variance	0.001	0.000	0.001
RMSE (16 Points)	0.032	0.013	0.030
RMSE (15 Points)	0.011	0.013	0.017

Figure 6.16: Error Data Compiled for the 3D Point Cloud Generated Using the 1cm/px Perpendicular Dataset with 14 GCPs

Figure A.17 shows the error data compiled for the 3D point cloud generated using the 1 cm/px perpendicular dataset with 0 GCPs.

Pointwise Difference Point Cloud				
Number	Point Name	Delta Easting (X) ft	Delta Northing (Y) ft	Delta Elevation (Z) ft
1	AT02	0.114	-0.018	-0.665
2	AT04	0.111	-0.012	-0.643
3	AT05	0.128	0.005	-0.646
4	AT07	0.106	0	-0.645
5	AT08	0.114	-0.008	-0.683
6	AT09	0.121	0	-0.677
7	AT10	0.121	-0.026	-0.689
8	AT12	0.107	0.007	-0.703
9	AT13	0.101	-0.007	-0.777
10	AT17	0.115	-0.032	-0.632
11	AT20	-0.012	-0.006	-0.59
12	AT21	0.05	0.008	-0.704
13	AT23	0.065	0.02	-0.763
14	AT25	0.11	0.071	-0.822
15	AT28	0.034	0.051	-0.796
16	AT30	0.059	0.091	-0.856

Errors in Pixels for Point Cloud				
Number	Point Name	Delta Easting (X) px	Delta Northing (Y) px	Delta Elevation (Z) px
1	AT02	3.278	0.518	19.122
2	AT04	3.192	0.345	18.489
3	AT05	3.681	0.144	18.576
4	AT07	3.048	0.000	18.547
5	AT08	3.278	0.230	19.639
6	AT09	3.479	0.000	19.467
7	AT10	3.479	0.748	19.812
8	AT12	3.077	0.201	20.215
9	AT13	2.904	0.201	22.342
10	AT17	3.307	0.920	18.173
11	AT20	0.345	0.173	16.965
12	AT21	1.438	0.230	20.243
13	AT23	1.869	0.575	21.940
14	AT25	3.163	2.042	23.636
15	AT28	0.978	1.466	22.889
16	AT30	1.697	2.617	24.614

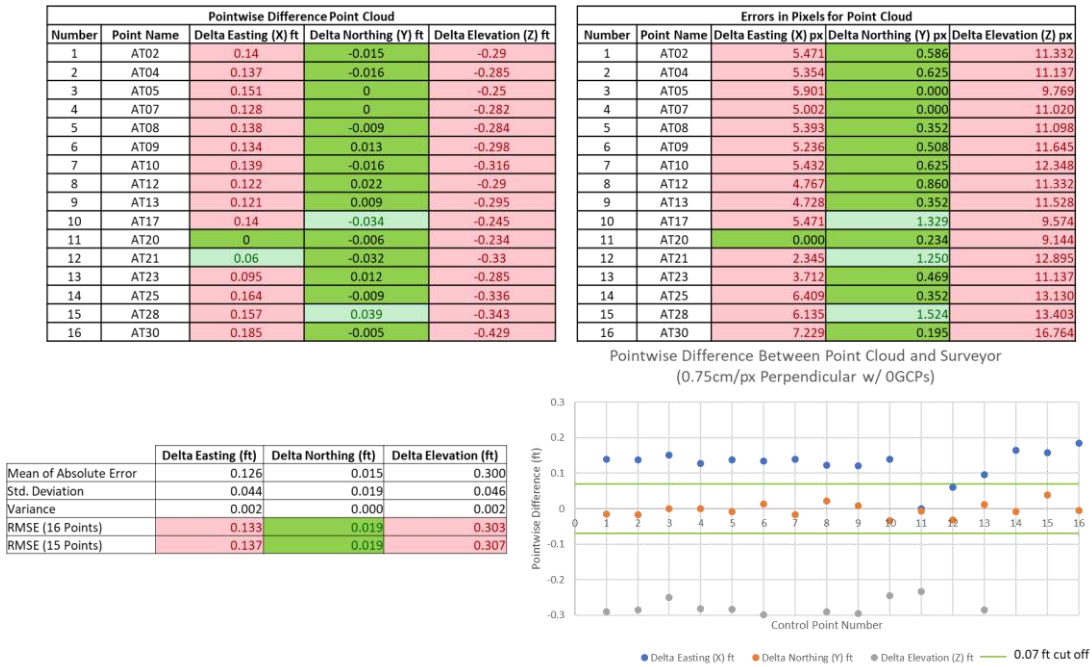|	Delta Easting (ft)	Delta Northing (ft)	Delta Elevation (ft)
Mean of Absolute Error	0.092	0.023	0.706
Std. Deviation	0.039	0.034	0.076
Variance	0.002	0.001	0.006
RMSE (16 Points)	0.098	0.034	0.709
RMSE (15 Points)	0.101	0.035	0.717

Figure 6.17: Error Data Compiled for the 3D Point Cloud Generated Using the 1cm/px Perpendicular Dataset with 0 GCPs

Figure A.18 shows the error data compiled for the 3D point cloud generated using the 1 cm/px terrain awareness dataset with 14 GCPs.

Pointwise Difference Point Cloud

Number	Point Name	Delta Easting (X) ft	Delta Northing (Y) ft	Delta Elevation (Z) ft
1	AT02	-0.001	0.001	-0.013
2	AT04	0.002	0.004	-0.002
3	AT05	0.012	0.023	-0.014
4	AT07	-0.003	0.018	0.012
5	AT08	0.015	0.014	-0.004
6	AT09	0.008	0.027	0.008
7	AT10	0.015	-0.008	0.023
8	AT12	-0.002	-0.003	0.01
9	AT13	0.012	-0.012	-0.017
10	AT17	0	-0.01	0.051
11	AT20	-0.119	0.008	0.098
12	AT21	-0.004	-0.057	-0.045
13	AT23	-0.029	0.012	0.002
14	AT25	0.013	0	0.016
15	AT28	0.001	0.034	0.018
16	AT30	0.014	0.001	0.044

Errors in Pixels for Point Cloud

Number	Point Name	Delta Easting (X) px	Delta Northing (Y) px	Delta Elevation (Z) px
1	AT02	0.028	0.028	0.367
2	AT04	0.056	0.113	0.056
3	AT05	0.339	0.649	0.395
4	AT07	0.085	0.508	0.339
5	AT08	0.423	0.395	0.113
6	AT09	0.226	0.762	0.226
7	AT10	0.423	0.226	0.649
8	AT12	0.056	0.085	0.282
9	AT13	0.339	0.339	0.480
10	AT17	0.000	0.282	1.439
11	AT20	3.358	0.226	2.766
12	AT21	0.113	1.609	1.270
13	AT23	0.818	0.339	0.056
14	AT25	0.367	0.000	0.452
15	AT28	0.028	0.960	0.508
16	AT30	0.395	0.028	1.242

	Delta Easting (ft)	Delta Northing (ft)	Delta Elevation (ft)
Mean of Absolute Error	0.016	0.015	0.024
Std. Deviation	0.033	0.021	0.033
Variance	0.001	0.000	0.001
RMSE (16 Points)	0.032	0.021	0.034
RMSE (15 Points)	0.012	0.021	0.024

**Pointwise Difference Between Point Cloud and Surveyor (1cm Terrain w/14GCP)**

Figure 6.18: Error Data Compiled for the 3D Point Cloud Generated Using the 1cm/px Terrain Awareness Dataset with 14 GCPs

Figure A.19 shows the error data compiled for the 3D point cloud generated using the 1 cm/px terrain awareness dataset with 0 GCPs.

Pointwise Difference Point Cloud

Number	Point Name	Delta Easting (X) ft	Delta Northing (Y) ft	Delta Elevation (Z) ft
1	AT02	0.112	-0.03	-0.211
2	AT04	0.14	-0.034	-0.221
3	AT05	0.121	0.015	-0.208
4	AT07	0.126	-0.003	-0.212
5	AT08	0.142	-0.017	-0.233
6	AT09	0.142	-0.006	-0.248
7	AT10	0.133	-0.027	-0.239
8	AT12	0.127	0.009	-0.226
9	AT13	0.135	0.013	-0.243
10	AT17	0.129	-0.026	-0.189
11	AT20	0.002	0.001	-0.188
12	AT21	0.068	-0.036	-0.275
13	AT23	0.1	0.024	-0.246
14	AT25	0.14	0.053	-0.21
15	AT28	0.101	0.058	-0.211
16	AT30	0.114	0.064	-0.227

Errors in Pixels for Point Cloud

Number	Point Name	Delta Easting (X) px	Delta Northing (Y) px	Delta Elevation (Z) px
1	AT02	3.161	0.847	5.955
2	AT04	3.951	0.960	6.237
3	AT05	3.415	0.423	5.870
4	AT07	3.556	0.085	5.983
5	AT08	4.008	0.480	6.576
6	AT09	4.008	0.169	6.999
7	AT10	3.754	0.762	6.745
8	AT12	3.584	0.254	6.378
9	AT13	3.810	0.367	6.858
10	AT17	3.641	0.734	5.334
11	AT20	0.056	0.028	5.306
12	AT21	1.919	1.016	7.761
13	AT23	2.822	0.677	6.943
14	AT25	3.951	1.496	5.927
15	AT28	2.850	1.637	5.955
16	AT30	3.217	1.806	6.406

	Delta Easting (ft)	Delta Northing (ft)	Delta Elevation (ft)
Mean of Absolute Error	0.114	0.026	0.224
Std. Deviation	0.036	0.033	0.023
Variance	0.001	0.001	0.001
RMSE (16 Points)	0.120	0.032	0.225
RMSE (15 Points)	0.124	0.033	0.228

Pointwise Difference Between Point Cloud and Surveyor (1cm Terrain w/0GCPs)

Figure 6.19: Error Data Compiled for the 3D Point Cloud Generated Using the 1cm/px Terrain Awareness Dataset with 0 GCPs

Figure A.20 shows the error data compiled for the 3D point cloud generated using the 1.25 cm/px combined dataset with 14 GCPs.
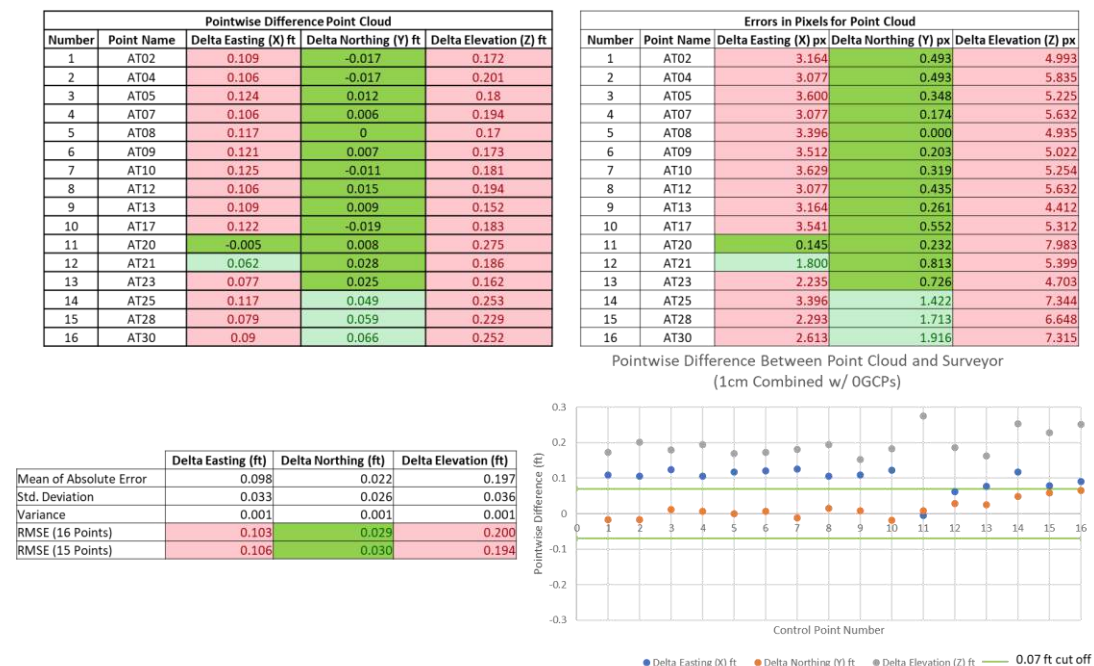
	Pointwise Difference Point Cloud			
Number	Point Name	Delta Easting (X) ft	Delta Northing (Y) ft	Delta Elevation (Z) ft
1	AT02	-0.005	-0.01	-0.02
2	AT04	-0.001	-0.01	-0.013
3	AT05	0.01	0.008	-0.002
4	AT07	-0.003	0.016	-0.027
5	AT08	0.004	0.007	0.006
6	AT09	0.014	0.019	-0.014
7	AT10	0.014	-0.013	-0.008
8	AT12	-0.005	0.006	0.027
9	AT13	0.019	-0.007	0.005
10	AT17	0.007	-0.007	-0.024
11	AT20	-0.106	0.011	0.097
12	AT21	-0.036	-0.023	0.002
13	AT23	-0.027	0.008	0.007
14	AT25	0.001	-0.002	-0.062
15	AT28	0.004	0.034	0.002
16	AT30	0.012	0.012	-0.01

	Errors in Pixels for Point Cloud			
Number	Point Name	Delta Easting (X) px	Delta Northing (Y) px	Delta Elevation (Z) px
1	AT02	0.112	0.224	0.448
2	AT04	0.022	0.224	0.291
3	AT05	0.224	0.179	0.045
4	AT07	0.067	0.359	0.605
5	AT08	0.090	0.157	0.134
6	AT09	0.314	0.426	0.314
7	AT10	0.314	0.291	0.179
8	AT12	0.112	0.134	0.605
9	AT13	0.426	0.157	0.112
10	AT17	0.157	0.157	0.538
11	AT20	2.376	0.247	2.174
12	AT21	0.807	0.515	0.045
13	AT23	0.605	0.179	0.157
14	AT25	0.022	0.045	1.390
15	AT28	0.090	0.762	0.045
16	AT30	0.269	0.269	0.224

	Delta Easting (ft)	Delta Northing (ft)	Delta Elevation (ft)
Mean of Absolute Error	0.017	0.012	0.020
Std. Deviation	0.030	0.014	0.033
Variance	0.001	0.000	0.001
RMSE (16 Points)	0.030	0.014	0.032
RMSE (15 Points)	0.015	0.014	0.021

Pointwise Difference Between Point Cloud and Surveyor (1.25cm Combined w/14GCPs)

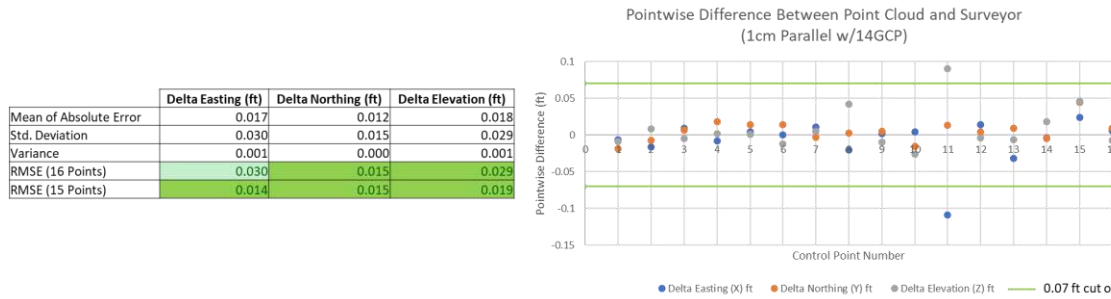● Delta Easting (X) ft   ● Delta Northing (Y) ft   ● Delta Elevation (Z) ft   —— 0.07 ft cut off
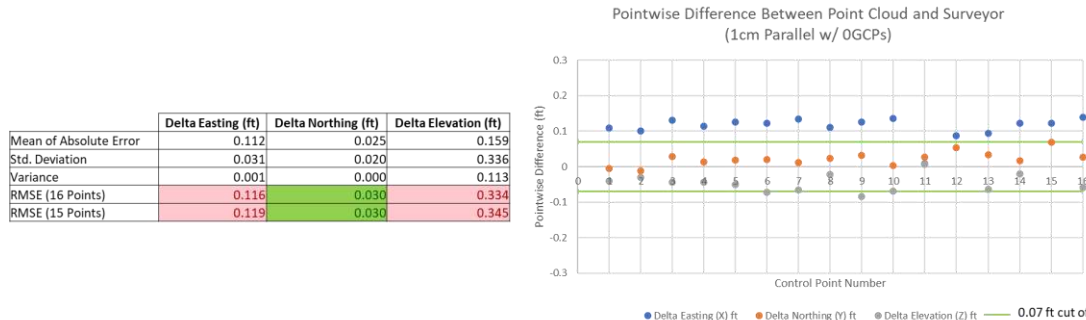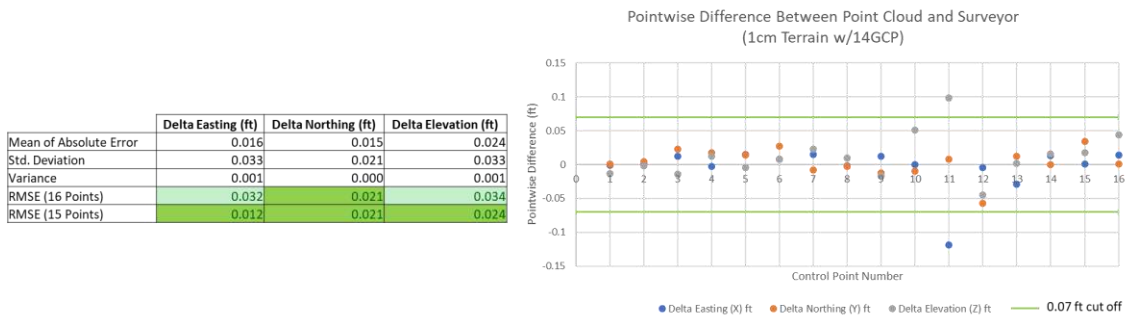
Figure 6.20: Error Data Compiled for the 3D Point Cloud Generated Using the 1.25cm/px Grid Dataset with 14 GCPs

Figure A.21 shows the error data compiled for the 3D point cloud generated using the 1.25 cm/px combined dataset with 0 GCPs.

	Pointwise Difference Point Cloud			
Number	Point Name	Delta Easting (X) ft	Delta Northing (Y) ft	Delta Elevation (Z) ft
1	AT02	0.101	-0.048	-0.312
2	AT04	0.106	-0.05	-0.333
3	AT05	0.118	-0.023	-0.289
4	AT07	0.103	-0.022	-0.34
5	AT08	0.109	-0.03	-0.31
6	AT09	0.119	-0.018	-0.346
7	AT10	0.114	-0.043	-0.349
8	AT12	0.099	-0.01	-0.314
9	AT13	0.115	-0.021	-0.331
10	AT17	0.118	-0.041	-0.305
11	AT20	-0.011	-0.021	-0.238
12	AT21	0.056	-0.044	-0.334
13	AT23	0.069	-0.001	-0.327
14	AT25	0.098	0	-0.413
15	AT28	0.092	0.035	-0.341
16	AT30	0.101	0.02	-0.361

	Errors in Pixels for Point Cloud			
Number	Point Name	Delta Easting (X) px	Delta Northing (Y) px	Delta Elevation (Z) px
1	AT02	2.264	1.076	6.992
2	AT04	2.376	1.121	7.463
3	AT05	2.645	0.515	6.477
4	AT07	2.308	0.493	7.620
5	AT08	2.443	0.672	6.948
6	AT09	2.667	0.403	7.754
7	AT10	2.555	0.964	7.822
8	AT12	2.219	0.224	7.037
9	AT13	2.577	0.471	7.418
10	AT17	2.645	0.919	6.836
11	AT20	0.247	0.471	5.334
12	AT21	1.255	0.986	7.486
13	AT23	1.546	0.022	7.329
14	AT25	2.196	0.000	9.256
15	AT28	2.062	0.784	7.642
16	AT30	2.264	0.448	8.091

	Delta Easting (ft)	Delta Northing (ft)	Delta Elevation (ft)
Mean of Absolute Error	0.096	0.027	0.328
Std. Deviation	0.033	0.024	0.037
Variance	0.001	0.001	0.001
RMSE (16 Points)	0.099	0.031	0.330
RMSE (15 Points)	0.103	0.031	0.335

Pointwise Difference Between Point Cloud and Surveyor (1.25cm Combined w/0GCPs)

● Delta Easting (X) ft   ● Delta Northing (Y) ft   ● Delta Elevation (Z) ft   —— 0.07 ft cut off

Figure 6.21: Error Data Compiled for the 3D Point Cloud Generated Using the 1.25cm/px Grid Dataset with 0 GCPs

183

Figure A.22 shows the error data compiled for the 3D point cloud generated using the 1.25 cm/px parallel dataset with 14 GCPs.

Pointwise Difference Point Cloud

Number	Point Name	Delta Easting (X) ft	Delta Northing (Y) ft	Delta Elevation (Z) ft
1	AT02	-0.007	-0.018	-0.028
2	AT04	-0.007	-0.011	-0.018
3	AT05	0.015	0.006	-0.001
4	AT07	-0.003	0.016	-0.033
5	AT08	0.006	0.013	0.012
6	AT09	0.012	0.018	-0.016
7	AT10	0.011	-0.012	0
8	AT12	-0.009	-0.001	0.03
9	AT13	0.03	-0.002	-0.005
10	AT17	0.009	-0.008	-0.023
11	AT20	-0.094	0.021	0.097
12	AT21	0.028	-0.041	0.016
13	AT23	-0.03	0.01	-0.004
14	AT25	-0.014	-0.008	-0.099
15	AT28	0.006	0.04	-0.034
16	AT30	0.007	0.011	-0.034

Errors in Pixels for Point Cloud

Number	Point Name	Delta Easting (X) px	Delta Northing (Y) px	Delta Elevation (Z) px
1	AT02	0.156	0.400	0.623
2	AT04	0.156	0.245	0.400
3	AT05	0.334	0.133	0.022
4	AT07	0.067	0.356	0.734
5	AT08	0.133	0.289	0.267
6	AT09	0.267	0.400	0.356
7	AT10	0.245	0.267	0.000
8	AT12	0.200	0.022	0.667
9	AT13	0.667	0.044	0.111
10	AT17	0.200	0.178	0.512
11	AT20	2.091	0.467	2.158
12	AT21	0.623	0.912	0.356
13	AT23	0.667	0.222	0.089
14	AT25	0.311	0.178	2.203
15	AT28	0.133	0.890	0.756
16	AT30	0.156	0.245	0.756

	Delta Easting (ft)	Delta Northing (ft)	Delta Elevation (ft)
Mean of Absolute Error	0.018	0.015	0.028
Std. Deviation	0.029	0.019	0.041
Variance	0.001	0.000	0.002
RMSE (16 Points)	0.028	0.018	0.040
RMSE (15 Points)	0.016	0.018	0.033

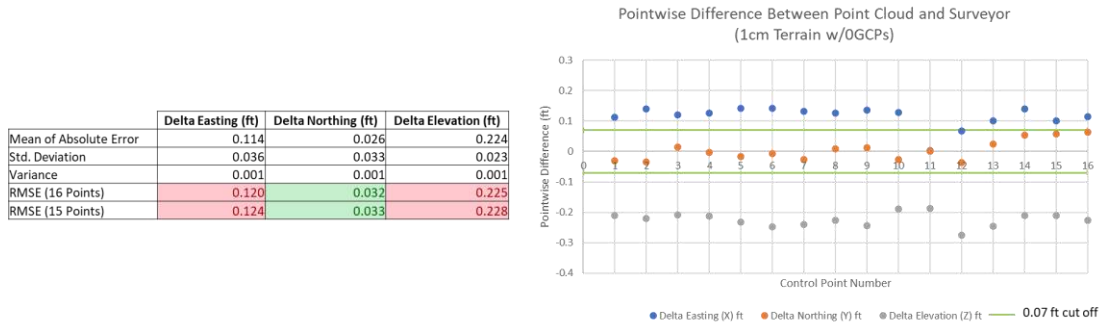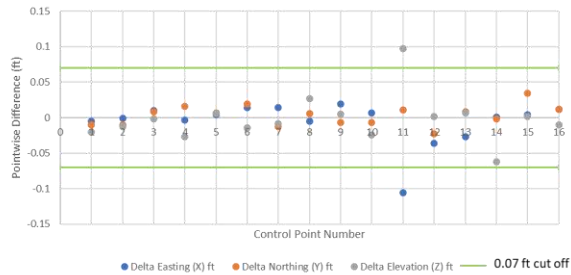Pointwise Difference Between Point Cloud and Surveyor (1.25cm Parallel w/14GCP)

Figure 6.22: Error Data Compiled for the 3D Point Cloud Generated Using the 1.25cm/px Parallel Dataset with 14 GCPs

Figure A.23 shows the error data compiled for the 3D point cloud generated using the 1.25 cm/px parallel dataset with 0 GCPs.

Pointwise Difference Point Cloud

Number	Point Name	Delta Easting (X) ft	Delta Northing (Y) ft	Delta Elevation (Z) ft
1	AT02	0.063	-0.055	-1.261
2	AT04	0.062	-0.056	-1.29
3	AT05	0.089	-0.023	-1.21
4	AT07	0.07	-0.02	-1.283
5	AT08	0.077	-0.024	-1.237
6	AT09	0.083	-0.019	-1.3
7	AT10	0.08	-0.04	-1.298
8	AT12	0.057	-0.017	-1.272
9	AT13	0.093	-0.011	-1.3
10	AT17	0.09	-0.038	-1.219
11	AT20	-0.028	-0.009	-1.176
12	AT21	0.041	-0.029	-1.247
13	AT23	0.038	0.002	-1.3
14	AT25	0.052	-0.016	-1.542
15	AT28	0.076	0.042	-1.414
16	AT30	0.076	0.003	-1.508

Errors in Pixels for Point Cloud

Number	Point Name	Delta Easting (X) px	Delta Northing (Y) px	Delta Elevation (Z) px
1	AT02	1.412	1.233	28.261
2	AT04	1.390	1.255	28.911
3	AT05	1.995	0.515	27.118
4	AT07	1.569	0.448	28.754
5	AT08	1.726	0.538	27.723
6	AT09	1.860	0.426	29.135
7	AT10	1.793	0.896	29.090
8	AT12	1.277	0.381	28.508
9	AT13	2.084	0.247	29.135
10	AT17	2.017	0.852	27.320
11	AT20	0.628	0.202	26.356
12	AT21	0.919	0.650	27.947
13	AT23	0.852	0.045	29.135
14	AT25	1.165	0.359	34.559
15	AT28	1.703	0.941	31.690
16	AT30	1.703	0.067	33.797

	Delta Easting (ft)	Delta Northing (ft)	Delta Elevation (ft)
Mean of Absolute Error	0.067	0.025	1.304
Std. Deviation	0.030	0.024	0.101
Variance	0.001	0.001	0.010
RMSE (16 Points)	0.070	0.030	1.307
RMSE (15 Points)	0.072	0.031	1.316

Pointwise Difference Between Point Cloud and Surveyor (1.25cm Parallel w/ 0GCPs)
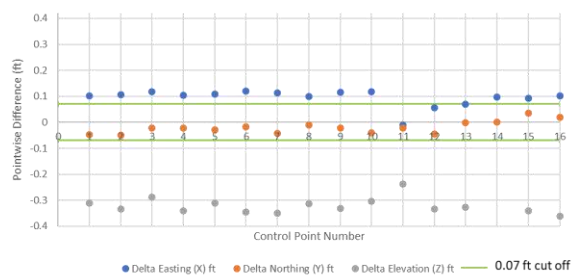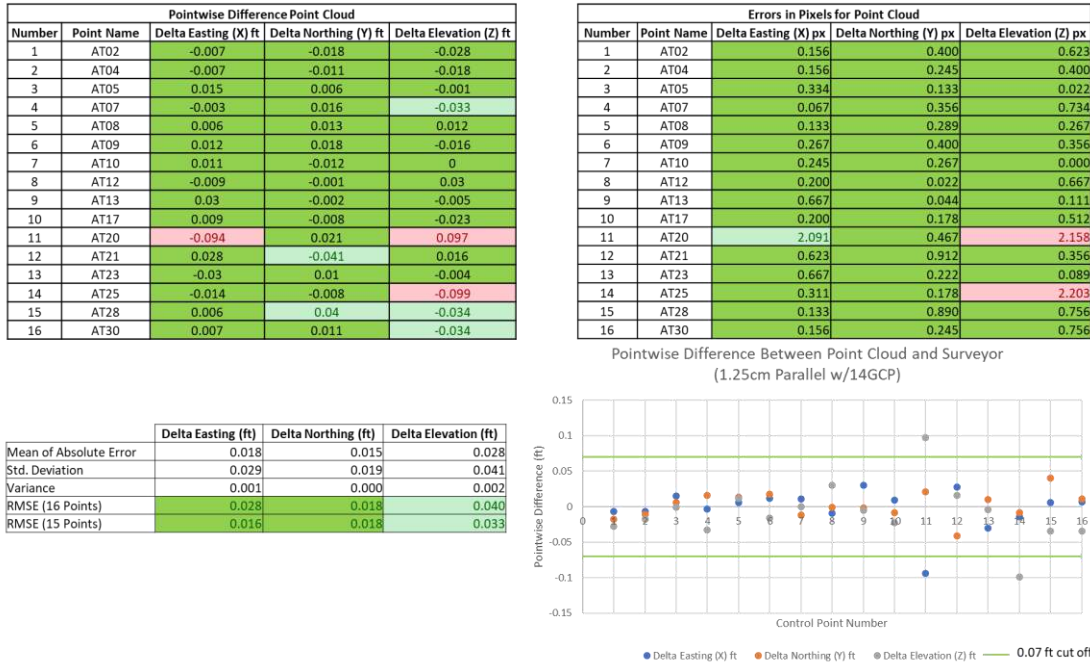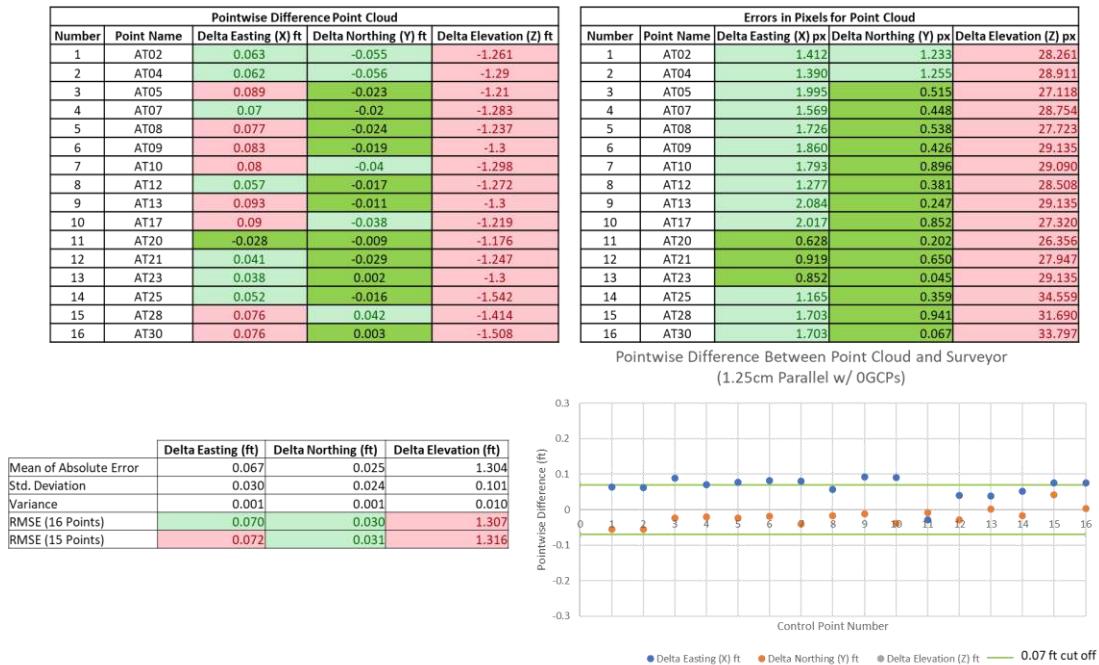
Figure 6.23: Error Data Compiled for the 3D Point Cloud Generated Using the 1.25cm/px Parallel Dataset with 0 GCPs

184

Figure A.22 shows the error data compiled for the 3D point cloud generated using the 1.25 cm/px perpendicular dataset with 14 GCPs.

		Pointwise Difference Point Cloud		
Number	Point Name	Delta Easting (X) ft	Delta Northing (Y) ft	Delta Elevation (Z) ft
1	AT02	0.002	-0.002	-0.01
2	AT04	0.004	-0.001	-0.008
3	AT05	0.006	0.009	-0.006
4	AT07	-0.002	0.018	-0.022
5	AT08	0.002	0.006	-0.004
6	AT09	0.015	0.024	-0.012
7	AT10	0.016	-0.014	-0.014
8	AT12	0	0.008	0.028
9	AT13	0.009	-0.013	-0.001
10	AT17	0	-0.009	-0.02
11	AT20	-0.118	0.003	0.093
12	AT21	-0.001	-0.058	-0.043
13	AT23	-0.025	0.006	0.001
14	AT25	0.019	0.005	-0.068
15	AT28	-0.007	0.024	-0.008
16	AT30	0.011	0.017	-0.035

		Errors in Pixels for Point Cloud		
Number	Point Name	Delta Easting (X) px	Delta Northing (Y) px	Delta Elevation (Z) px
1	AT02	0.044	0.044	0.222
2	AT04	0.089	0.022	0.178
3	AT05	0.133	0.200	0.133
4	AT07	0.044	0.400	0.489
5	AT08	0.044	0.133	0.089
6	AT09	0.334	0.534	0.267
7	AT10	0.356	0.311	0.311
8	AT12	0.000	0.178	0.623
9	AT13	0.200	0.289	0.022
10	AT17	0.000	0.200	0.445
11	AT20	2.625	0.067	2.069
12	AT21	0.022	1.290	0.957
13	AT23	0.556	0.133	0.022
14	AT25	0.423	0.111	1.513
15	AT28	0.156	0.534	0.178
16	AT30	0.245	0.378	0.779

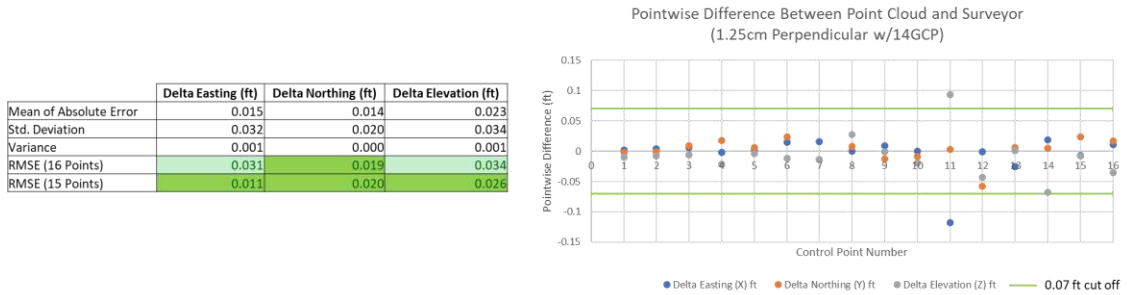|	Delta Easting (ft)	Delta Northing (ft)	Delta Elevation (ft)
Mean of Absolute Error	0.015	0.014	0.023
Std. Deviation	0.032	0.020	0.034
Variance	0.001	0.000	0.001
RMSE (16 Points)	0.031	0.019	0.034
RMSE (15 Points)	0.011	0.020	0.026

Figure 6.24: Error Data Compiled for the 3D Point Cloud Generated Using the 1.25cm/px Perpendicular Dataset with 14 GCPs

Figure A.23 shows the error data compiled for the 3D point cloud generated using the 1.25 cm/px perpendicular dataset with 0 GCPs.

		Pointwise Difference Point Cloud		
Number	Point Name	Delta Easting (X) ft	Delta Northing (Y) ft	Delta Elevation (Z) ft
1	AT02	0.137	-0.041	-0.559
2	AT04	0.143	-0.043	-0.594
3	AT05	0.142	-0.022	-0.546
4	AT07	0.135	-0.02	-0.604
5	AT08	0.138	-0.033	-0.595
6	AT09	0.151	-0.011	-0.625
7	AT10	0.149	-0.039	-0.646
8	AT12	0.142	0.003	-0.603
9	AT13	0.136	-0.02	-0.644
10	AT17	0.139	-0.044	-0.568
11	AT20	0.007	-0.026	-0.535
12	AT21	0.077	-0.048	-0.659
13	AT23	0.103	0.008	-0.631
14	AT25	0.157	0.03	-0.745
15	AT28	0.106	0.04	-0.679
16	AT30	0.135	0.05	-0.732

		Errors in Pixels for Point Cloud		
Number	Point Name	Delta Easting (X) px	Delta Northing (Y) px	Delta Elevation (Z) px
1	AT02	3.048	0.912	12.437
2	AT04	3.181	0.957	13.215
3	AT05	3.159	0.489	12.148
4	AT07	3.004	0.445	13.438
5	AT08	3.070	0.734	13.238
6	AT09	3.359	0.245	13.905
7	AT10	3.315	0.868	14.372
8	AT12	3.159	0.067	13.416
9	AT13	3.026	0.445	14.328
10	AT17	3.092	0.979	12.637
11	AT20	0.156	0.578	11.903
12	AT21	1.713	1.068	14.662
13	AT23	2.292	0.178	14.039
14	AT25	3.493	0.667	16.575
15	AT28	2.358	0.890	15.107
16	AT30	3.004	1.112	16.286

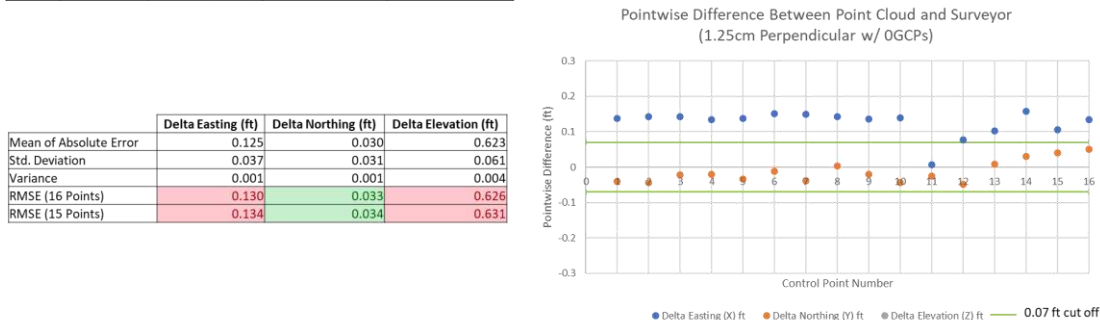|	Delta Easting (ft)	Delta Northing (ft)	Delta Elevation (ft)
Mean of Absolute Error	0.125	0.030	0.623
Std. Deviation	0.037	0.031	0.061
Variance	0.001	0.001	0.004
RMSE (16 Points)	0.130	0.033	0.626
RMSE (15 Points)	0.134	0.034	0.631

Figure 6.25: Error Data Compiled for the 3D Point Cloud Generated Using the 1.25cm/px Perpendicular Dataset with 0 GCPs

185